

6.7 GHZ METHANOL MASERS: PROPERTIES,
ASSOCIATIONS AND TRACERS OF GALACTIC
STRUCTURE

A Dissertation

Presented to the Faculty of the Graduate School

of Cornell University

in Partial Fulfillment of the Requirements for the Degree of

Doctor of Philosophy

by

Jagadheep Dhanasekara Pandian

January 2007

© 2007 Jagadheep Dhanasekara Pandian

ALL RIGHTS RESERVED

6.7 GHz METHANOL MASERS: PROPERTIES, ASSOCIATIONS AND TRACERS OF GALACTIC STRUCTURE

Jagadheep Dhanasekara Pandian, Ph.D.

Cornell University 2007

The 6.7 GHz transition of methanol is the strongest of methanol masers, and is the second strongest maser transition ever observed in the Milky Way. There is strong theoretical and observational evidence that the masers trace an early phase of massive star formation. The lack of association of these masers with other astronomical objects such as low-mass young stellar objects (YSOs) and late type stars, and their high brightness temperatures makes them excellent tools to detect and study massive star formation across our Galaxy. The preponderance of massive stars along the spiral arms of galaxies also imply the potential utility of these methanol masers to study the spiral structure of our Galaxy.

In this dissertation, we present a study of 6.7 GHz methanol masers and their properties based on the Arecibo Methanol Maser Galactic Plane Survey (AMGPS), a sensitive blind survey carried out with the Arecibo radio telescope. To carry out this study, we built a receiver for Arecibo that could process signals between 6 and 8 GHz. The high sensitivity of the cooled receiver and the large collecting area of Arecibo made AMGPS the most sensitive blind survey to date for 6.7 GHz methanol masers, and resulted in the detection of 86 methanol masers, 48 of which are new detections.

The distribution of methanol masers as a function of Galactic latitude and the

statistics of their multi-wavelength counterparts show our data to be consistent with the hypothesis of 6.7 GHz methanol masers being associated with massive YSOs. Using the detection statistics of AMGPS, we estimate the minimum number of methanol masers in the Galaxy to be 1125. The $l - v$ diagram of the AMGPS sample shows the tangent point of the Carina-Sagittarius spiral arm to be around 49.6° , and suggests occurrence of massive star formation along the extension of the Crux-Scutum arm. A Gaussian component analysis of methanol masers shows the mean line-width to be 0.38 km s^{-1} which is more a factor of two larger than what is reported in the literature. We also find no evidence that faint methanol masers have different properties than their bright counterparts.

BIOGRAPHICAL SKETCH

Jagadheep Dhanasekara Pandian was born during the early morning hours of February 19, 1978, although for reasons unknown to the author, the date of birth in the birth certificate was put down as February 18, 1978. He is the only child of Jansi Rani and Dhanasekara Pandian. After being born in Tiruchirapalli located in the state of Tamil Nadu in India, he was raised in Trivandrum (now renamed as Thiruvananthapuram), the capital city of the neighboring state of Kerala. He did his kindergarten through high-school in Loyola school, where the Indian Certificate of Secondary Education (ICSE) and Indian Secondary Certificate (ISC) curricula made him adept in English.

Following high-school, he took the Joint Entrance Examination (JEE), from the results of which he secured admission to the Indian Institute of Technology Madras (IIT-M) with a major in Aerospace Engineering (in India, the major is assigned during admission based on merit). Since he topped the class at the end of the first year, he was allowed to switch the major to Electrical Engineering. The author has fond memories of Saarang festivities, being dunked into the hostel pond during the Holi festival, spending several hours at stretches playing computer games with his friends during the second year when the course work was relatively light, and wasting quite a few nights on meaningless debates with fellow students.

The course work in IIT-M was very rigorous, with the peak workload in the fifth semester comprising of 26 credits spread over six courses and three labs. The faculty were also very strict in grading and did not hesitate to fail as much as one-third of the 81 student class in some courses. While the academic life was hard on the students, they gave the author a thorough understanding of Fourier, Laplace and Z-transforms, and signal processing techniques, which would prove invaluable

during the course of his Ph.D.

While the author was interested in Astronomy since childhood, the idea of pursuing a career in the subject did not occur to him until the final year. Since it was too late to take the Physics subject test in GRE, he applied to various graduate schools which had inter-disciplinary programs between Electrical Engineering and Astronomy. He accepted the offer of Cornell University, where he joined the graduate program of Electrical Engineering in August 2000. A few courses in Astronomy, Experimental Astronomy (ASTRO 410) in particular, made him more interested than ever to pursue a career in Astronomy. At the end of Spring 2001, with the encouragement of his current adviser Paul Goldsmith, he made a formal change of department from Electrical Engineering to Astronomy and Space Sciences.

The long-term desire of the author, to pursue observations of the night sky were fulfilled when he joined the Cornell Astronomical Society (CAS) which runs the Fuertes Observatory housing a 12-inch f/15 refracting telescope. With his enthusiasm, and the help of other club members, he became an expert in the night sky and the use of the telescope to find deep sky objects. He has been in charge of the facility for three years during which time he coordinated telescope and building maintenance with the department of Astronomy. He has overseen numerous outreach activities at the observatory for the general public, school children and 4-H groups.

The author has also been involved with “Curious about Astronomy? Ask an Astronomer” service run by graduate students in the department. He helped redesign the website in 2002, and has answered over a 1000 questions on various topics. He has also helped with other outreach projects such as Expanding Your Horizons (EYH) and Focus for Teens.

Jagadheep leaves Cornell to start a postdoctoral position at the Max Planck Institute for Radio Astronomy in Bonn, Germany. He will work with Karl Menten in millimeter and submillimeter astronomy.

*This thesis is dedicated to my parents
and the Self which is a silent witness
to all the happenings in the Universe.*

ACKNOWLEDGEMENTS

First and foremost, I want to thank my adviser Paul Goldsmith. He engineered my entry into the field of Astronomy and gave me the opportunity to do radio astronomy instrumentation. Without his constant endeavors to obtain the low noise amplifiers utilizing Indium Phosphide transistors, and to secure observing time at the Arecibo telescope, C-Band High receiver would not have come into existence, and the Arecibo Methanol Maser Galactic Plane Survey would not have come to fruition. Paul also allowed me to work independently on my own time scales, which had made me a more responsible person with respect to my research.

I also wish to thank the other members of my committee, Éanna Flanagan, Gordon Stacey and Yervant Terzian for their support during my thesis. Special thanks to Jim Cordes, Steve Eikenberry and Jim Houck for introducing me to astronomical research, which honed my signal processing skills and was in part responsible for my changing discipline from Electrical Engineering to Astronomy.

I thank Bob Brown who as director of NAIC supported me financially and my liberal travel schedule, especially to Arecibo. My heartfelt gratitude to Jill Tarbell who was responsible for arranging travel, doing the paperwork for reimbursement, and numerous other favors during my time here. I also thank Phyllis Sutliff and Wendy Turner for ensuring that I got paid. Thanks to Lynn Baker and German Cortes for helping with the receiver design, and to Kurt Kabelac and David Overbaugh for useful tips regarding mechanical design, and for machining most of the parts for the receiver. Special thanks to Bill Hoffman who took care of a number of maintenance issues at the Fuertes observatory, and made me comfortable in Space Sciences. I thank Tom Shannon, Gerry Stasavage and Dan Wilcox for taking care of computer issues.

I thank Rajagopalan Ganesan and Gomathi Thai for making me feel at home in Arecibo and inviting me for excellent dinners. Many thanks to Phil Perillat for the useful discussions on telescope systematics and data reduction techniques, and to Arun Venkataraman for taking care of computer issues at Arecibo. Thanks to Antonio Nolla and José Rosa for making me feel as part of the electronics group while at Arecibo. I also thank all the telescope operators at Arecibo for making sure that everything worked well during observations, and for sharing occasional light moments which especially helped endure observing at ungodly hours. I also thank Barbara Catinella, Paulo Freire, Jonathan Friedman, Emmanuel Momjian, Shikha Raizada and Hien Vo for organizing fun activities at Arecibo, providing entertainment and a break from the isolation at the observatory.

Thanks to all my fellow graduate students at Cornell with special mention to my incoming classmates. I will not mention any names, as I will inevitably miss some people and give them heartbreak. I extend special thanks to Patrick Taylor who helped me out on numerous occasions. Special mention to my colleagues who shared the work room: Di Li, Yvonne Tang and Marko Krco. It was great sharing each other's work and having stimulating conversations. Thanks to my room-mates during my time here: Bharath Rangarajan, Yegnaswamy Sermadevi and Manoj Srinivasan. I didn't always appreciate you at the time, but I learned several lessons from you.

My other interests and activities outside academics have helped me to remain sane during my time here. Special thanks to Attila Elteto and Edgar Bonet for teaching me the night sky, and training me to use the telescope at Fuertes Observatory. Since then, I have enjoyed amateur astronomy with other members of the club, especially Tanja Bode, Guanhan Chew, Mike Roman, Shianne Beer and

Art Samplaski. I thank you all for the fun time we had together. I also want to mention Alan Ominsky, who at the Southern Cayuga Central School observatory revealed the beauty of deep sky observing from relatively pristine skies, free from significant light pollution.

Many thanks to Jaiganesh Balakrishnan who introduced me to bird watching, and took me on many field trips all over central New York. I also thank David Chernoff for the trips to Montezuma wildlife refuge and Derby Hill Observatory, although all our attempts to watch hawk migration ended in failure due to unfavorable winds and weather conditions.

And finally my parents. Without your constant support and patient ear during the rough times, this thesis would have never happened. You have taught me what loving, caring and sharing are all about and there are no words that can express my gratitude to you.

TABLE OF CONTENTS

1	Introduction	1
2	Astronomical Masers: an Overview	4
2.1	Introduction	4
2.2	Phenomenological Maser Theory	5
2.2.1	Rate Equations	5
2.2.2	Population Inversion	7
2.2.3	Unsaturated masers	8
2.2.4	Saturated masers	10
2.2.5	Radiative transfer in masers	12
2.3	Effects of Geometry: Beaming	13
2.3.1	Beaming in Unsaturated Masers	15
2.3.2	Beaming in Saturated Masers	16
2.4	Pumping Mechanisms	17
2.5	Conclusions	19
3	The Energy Structure of the Methanol Molecule	20
3.1	The Symmetric Rotor	21
3.2	The Asymmetric Rotor	23
3.3	Hindered Torsional Motions in Symmetric Rotors	25
3.4	Hindered Torsional Motions in Asymmetric Rotors	30
3.5	Application to Methanol	31
4	Methanol Masers	38
4.1	An Overview of Methanol Masers	38
4.2	6.7 GHz Methanol Masers	39
4.2.1	Pumping of 6.7 and 12.2 GHz Methanol Masers	41
4.3	6.7 GHz Methanol Masers and Massive Star Formation	43
5	The 6–8 GHz C-Band High receiver at Arecibo	48
5.1	Introduction	48
5.2	The Ortho-Mode Transducer	54
5.3	The Feed Horn	60
5.4	The Thermal Break	67
5.5	Low Noise Amplifiers	72
5.6	Remainder of the Signal Path	75
5.7	Dewar Design	76
5.7.1	Dewar Dimensions	77
5.7.2	Heat Loads	78
5.7.2.1	Radiative Heat Loads	78
5.7.2.2	Conductive Heat Loads	79
5.7.2.3	Heat load on the 70 K stage	80

5.7.2.4	Heat load on the 15 K stage	84
5.7.2.5	Choice of Refrigerator	87
5.7.3	Mechanical design of the dewar	88
5.7.4	Additional Design Considerations	90
5.8	Receiver Noise Temperature	92
5.9	Overall System Performance	93
5.10	Conclusions	94
6	The Arecibo Methanol Maser Galactic Plane Survey–I: Data	97
6.1	Introduction	97
6.2	Observations	98
6.3	Results	102
6.4	Notes on selected sources	130
6.5	Discussion	133
6.6	Conclusions	136
7	The Arecibo Methanol Maser Galactic Plane Survey–II: Statistical and Multi-wavelength Counterpart Analysis	137
7.1	The Sample	137
7.2	Distribution in the Galaxy	137
7.3	Implications for Galactic Structure	140
7.4	The Number of Methanol Masers in the Galaxy	144
7.5	Line Properties: Gaussian Analysis	146
7.6	Counterparts at Other Wavelengths	151
8	Ongoing and Future Work	170
8.1	Probing Galactic Structure Using 6.7 GHz Methanol Masers	170
8.1.1	The Kinematic Distance Ambiguity	170
8.1.2	Resolving the Kinematic Distance Ambiguity–I	172
8.1.3	Application to 6.7 GHz Methanol Masers	174
8.1.4	Resolving the Kinematic Distance Ambiguity–II	176
8.2	6.7 GHz Methanol Masers in M33	178
8.3	Obtaining Accurate Positions for 6.7 GHz Methanol Masers	183
8.4	Linking 6.7 GHz Methanol Masers and Massive Star Formation . .	183
A	Waveguide Calibration	186
A.1	S-parameters	186
A.2	Measurement of S-parameters	189
A.3	One-port Error Model	190
A.4	Two-port Error Model	194
A.4.1	Two-port waveguide calibration	196
A.5	Experimental Demonstration of Waveguide Calibration	197
B	Gaussian Component Analysis	202

LIST OF TABLES

3.1	Moments of inertia for the methanol molecule	32
4.1	A sample of masing transitions in methanol masers.	40
5.1	Calculated overall Antenna Parameters at the input flange of the Arecibo radio telescope's feed horn.	66
5.2	Emissivities of surfaces used in dewar construction (data taken from White & Meeson 1968).	79
5.3	Thermal conductivity data for common materials used in dewar components.	81
5.4	Refrigeration capacity of refrigerator models commonly used in cryogenic dewars.	88
6.1	Methanol masers discovered in the Arecibo Methanol Maser Galac- tic Plane Survey (AMGPS). The columns show the source name, celestial coordinates, velocity range of emission, velocity of peak emission, peak flux density, integrated flux density, epoch of obser- vation and the reference for discovery.	105
6.2	Previously published data compared with our data for known de- tections.	125
7.1	IRAS, MSX and NVSS counterparts to methanol masers discovered in AMGPS.	154
7.2	Multi-wavelength counterparts within 1' to methanol masers dis- covered in AMGPS.	159
B.1	Gaussian Components of source 34.82+0.35.	203
B.2	Gaussian Components of source 35.25-0.24.	203
B.3	Gaussian Components of source 35.39+0.02	206
B.4	Gaussian Components of source 35.40+0.03	206
B.5	Gaussian Components of source 36.02-0.20.	206
B.6	Gaussian Components of source 36.64-0.21.	210
B.7	Gaussian Components of source 36.90-0.41.	210
B.8	Gaussian Components of source 36.92+0.48.	210
B.9	Gaussian Components of source 37.02-0.03.	214
B.10	Gaussian Components of source 37.38-0.09.	214
B.11	Gaussian Components of source 37.74-0.12.	217
B.12	Gaussian Components of source 37.76-0.19.	217
B.13	Gaussian Components of source 37.77-0.22.	220
B.14	Gaussian Components of source 38.08-0.27.	220
B.15	Gaussian Components of source 38.26-0.20.	223
B.16	Gaussian Components of source 38.56+0.15.	223
B.17	Gaussian Components of source 38.60-0.21.	226

B.18	Gaussian Components of source	38.66+0.08.	228
B.19	Gaussian Components of source	38.92-0.36.	228
B.20	Gaussian Components of source	39.39-0.14.	231
B.21	Gaussian Components of source	39.54-0.38.	231
B.22	Gaussian Components of source	40.62-0.14.	234
B.23	Gaussian Components of source	40.94-0.04.	236
B.24	Gaussian Components of source	41.08-0.13.	236
B.25	Gaussian Components of source	41.12-0.11.	239
B.26	Gaussian Components of source	41.12-0.22.	239
B.27	Gaussian Components of source	41.16-0.20.	242
B.28	Gaussian Components of source	41.27+0.37.	242
B.29	Gaussian Components of source	41.58+0.04.	242
B.30	Gaussian Components of source	41.87-0.10.	246
B.31	Gaussian Components of source	43.08-0.08.	246
B.32	Gaussian Components of source	43.17-0.00.	249
B.33	Gaussian Components of source	43.18-0.01.	249
B.34	Gaussian Components of source	44.31+0.04.	252
B.35	Gaussian Components of source	44.64-0.52.	252
B.36	Gaussian Components of source	45.07+0.13.	255
B.37	Gaussian Components of source	45.44+0.07.	255
B.38	Gaussian Components of source	45.49+0.13.	258
B.39	Gaussian Components of source	45.57-0.12.	258
B.40	Gaussian Components of source	46.07+0.22.	261
B.41	Gaussian Components of source	48.89-0.17.	261
B.42	Gaussian Components of source	48.90-0.27.	261
B.43	Gaussian Components of source	48.99-0.30.	265
B.44	Gaussian Components of source	49.62-0.36.	267
B.45	Gaussian Components of source	50.78+0.15.	269
B.46	Gaussian Components of source	52.92+0.41.	271
B.47	Gaussian Components of source	53.04+0.11.	271
B.48	Gaussian Components of source	53.14+0.07.	274
B.49	Gaussian Components of source	53.62+0.04.	274

LIST OF FIGURES

2.1	An illustration of the beaming effect in masers.	14
2.2	An illustration of a collisional pump in HCO^+ molecule.	18
3.1	Schematic structure of the methanol molecule.	20
3.2	The coordinate system used in the symmetric rotor problem. . . .	22
3.3	Partial energy level diagram for <i>A</i> methanol.	36
3.4	Partial energy level diagram for <i>E</i> methanol.	37
5.1	Aerial view of the Arecibo radio telescope.	50
5.2	A schematic showing the optics at the Arecibo radio telescope. . .	51
5.3	A schematic of the fineline ortho-mode transducer (OMT).	55
5.4	Measured return loss of the OMT.	56
5.5	Measured insertion loss of the OMT.	57
5.6	Measured cross-polarization isolation of the OMT.	58
5.7	Measured isolation between the two output ports of the OMT. . . .	59
5.8	Calculated E_{VERT} projected on a cross section of the corrugated horn at 7 GHz	61
5.9	Calculated horn input reflection coefficient as a function of frequency	62
5.10	Calculated and measured radiation patterns at 6 GHz.	63
5.11	Calculated and measured radiation patterns at 7 GHz.	64
5.12	Calculated and measured radiation patterns at 8 GHz.	65
5.13	Schematic of a thermal break with a choke groove.	68
5.14	A coaxial waveguide can be treated as a rolled up thin rectangular waveguide.	69
5.15	LNA module with covers removed.	73
5.16	WBA13 MMIC used in the amplifier.	73
5.17	Measured gain and noise temperature at 12 K at 4 different bias settings for a typical LNA of the type used in the receiver.	74
5.18	Schematic of the receiver showing the signal path from the feed horn to the exterior of the dewar.	75
5.19	Layout of the major components of the receiver.	77
5.20	Top view of the dewar layout.	78
5.21	The thermal conductivity of 304 stainless steel as a function of temperature.	80
5.22	The correction factor K in equation (5.13). L , D and t are the length, diameter and the thickness of the dewar wall respectively. .	89
5.23	The specific heat of Aluminum as a function of temperature.	91
5.24	Measured receiver noise temperature.	93
5.25	Normalized beam response mapped as a function of offsets in az- imuth and zenith-angle.	95
5.26	Beam profiles in azimuth and zenith angle.	96
6.1	The Arecibo telescope gain as a function of zenith angle.	100

6.2	Performance of the automated signal extraction algorithm.	102
6.3	The region mapped by AMGPS.	103
6.4	Spectra of methanol masers detected in AMGPS.	113
6.5	The highly variable source 41.87–0.10.	131
6.6	Distribution of flux densities of methanol masers in AMGPS. . . .	135
7.1	Distribution of methanol masers as a function of Galactic longitude.	138
7.2	Distribution of methanol masers as a function of Galactic latitude.	139
7.3	$l-v$ diagram of methanol masers of AMGPS along with the spiral arm model of Vallee (1995).	142
7.4	$l-v$ diagram of methanol masers of AMGPS along with the NE2001 spiral arm model.	143
7.5	An example of a complex spectrum and an attempted Gaussian fit.	148
7.6	The distribution of FWHM linewidths.	150
7.7	The color-color diagram for IRAS sources associated with 6.7 GHz methanol masers.	166
8.1	The radial velocity of a source at fixed Galactic longitude as a function of distance from the Sun.	171
8.2	An illustration of using absorption lines to resolve the kinematic distance ambiguity.	173
8.3	Recombination line data for source 58.75+0.65	176
8.4	The sum of aligned spectra for 14 GMCs in M33: Spectrum A. . .	180
8.5	The sum of aligned spectra for 14 GMCs in M33: Spectrum B. . .	181
A.1	Schematic of a two-port network.	187
A.2	Voltage waves in a two-port network	188
A.3	One-port error model.	190
A.4	Two-port error model.	195
A.5	S-Band feed horn response with mistuned waveguide to coaxial line adapter.	198
A.6	S-Band feed horn data with waveguide calibration applied.	199
A.7	S-Band feed horn data calibrated internally in the VNA.	200
A.8	Overlay of the S-Band feed horn data calibrated internally and externally.	201
B.1	Gaussian component fit to source 34.82+0.35.	204
B.2	Gaussian component fit to source 35.25–0.24	205
B.3	Gaussian component fit to source 35.39+0.02	207
B.4	Gaussian component fit to source 35.40+0.03.	208
B.5	Gaussian component fit to source 36.02–0.20.	209
B.6	Gaussian component fit to source 36.64–0.21.	211
B.7	Gaussian component fit to source 36.90–0.41.	212
B.8	Gaussian component fit to source 36.92+0.48.	213
B.9	Gaussian component fit to source 37.02–0.03.	215

B.10	Gaussian component fit to source	37.38–0.09.	216
B.11	Gaussian component fit to source	37.74–0.12.	218
B.12	Gaussian component fit to source	37.76–0.19.	219
B.13	Gaussian component fit to source	37.77–0.22.	221
B.14	Gaussian component fit to source	38.08–0.27.	222
B.15	Gaussian component fit to source	38.26–0.20.	224
B.16	Gaussian component fit to source	38.56+0.15.	225
B.17	Gaussian component fit to source	38.60–0.21.	227
B.18	Gaussian component fit to source	38.66+0.08.	229
B.19	Gaussian component fit to source	38.92–0.36.	230
B.20	Gaussian component fit to source	39.39–0.14.	232
B.21	Gaussian component fit to source	39.54–0.38.	233
B.22	Gaussian component fit to source	40.62–0.14.	235
B.23	Gaussian component fit to source	40.94–0.04.	237
B.24	Gaussian component fit to source	41.08–0.13.	238
B.25	Gaussian component fit to source	41.12–0.11.	240
B.26	Gaussian component fit to source	41.12–0.22.	241
B.27	Gaussian component fit to source	41.16–0.20.	243
B.28	Gaussian component fit to source	41.27+0.37.	244
B.29	Gaussian component fit to source	41.58+0.04.	245
B.30	Gaussian component fit to source	41.87–0.10.	247
B.31	Gaussian component fit to source	43.08–0.08.	248
B.32	Gaussian component fit to source	43.17–0.00.	250
B.33	Gaussian component fit to source	43.18–0.01.	251
B.34	Gaussian component fit to source	44.31+0.04.	253
B.35	Gaussian component fit to source	44.64–0.52.	254
B.36	Gaussian component fit to source	45.07+0.13.	256
B.37	Gaussian component fit to source	45.44+0.07.	257
B.38	Gaussian component fit to source	45.49+0.13.	259
B.39	Gaussian component fit to source	45.57–0.12.	260
B.40	Gaussian component fit to source	46.07+0.22.	262
B.41	Gaussian component fit to source	48.89–0.17.	263
B.42	Gaussian component fit to source	48.90–0.27.	264
B.43	Gaussian component fit to source	48.99–0.30.	266
B.44	Gaussian component fit to source	49.62–0.36.	268
B.45	Gaussian component fit to source	50.78+0.15.	270
B.46	Gaussian component fit to source	52.92+0.41.	272
B.47	Gaussian component fit to source	53.04+0.11.	273
B.48	Gaussian component fit to source	53.14+0.07.	275
B.49	Gaussian component fit to source	53.62+0.04.	276

Chapter 1

Introduction

The stellar population in galaxies is usually dominated by low mass stars. However, the high mass stars, though few in number, have a much more profound impact on the environment within the galaxy compared to their low mass counterparts. High mass stars have fierce stellar winds, output intense ultraviolet radiation that create HII regions, and eventually end their lives in massive supernova explosions that briefly outshine the entire host galaxy.

In spite of the importance of massive stars, our understanding of their formation process is very limited compared to that of the formation of low mass stars. Several factors contribute to this: Massive stars remain deeply embedded in the parent molecular cloud for a significant period of time beyond their arrival at the zero age main sequence which is in part due to the short timescales involved in the formation and evolution of massive stars. Regions undergoing massive star formation are more distant and heavily obscured (occasionally even in mid infrared wavelengths). Further, the tendency of massive stars to form in clusters, and their strong interaction with their environment make the interpretation of observational data difficult.

The first observational signposts of high mass star formation are thought to be hot molecular cores. These objects have sizes $\lesssim 0.1$ pc, densities $\gtrsim 10^6$ cm $^{-3}$, and temperatures $\gtrsim 100$ K. Although the details of successive steps in the evolutionary process are not well understood, it is apparent that the hot protostar will eventually begin to ionize the ambient gas, and create a hypercompact HII region. The hypercompact HII region has a size of about 0.003 pc, and an extremely high

emission measure ($\gtrsim 10^{10} \text{ pc cm}^{-6}$). Due to the large free-free optical depth at centimeter wavelengths, the peak flux density from the bremsstrahlung radiation of ionized gas in the hypercompact HII region occurs at millimeter wavelengths, meaning that the objects are often undetectable at longer wavelengths. As time progresses and the shock wave from the hypercompact HII region expands into increasingly dilute ambient gas, the size of the region increases, the optical depth decreases, and the source becomes visible at centimeter wavelengths as an ultra-compact HII region (sizes $\lesssim 0.1 \text{ pc}$, densities $\gtrsim 10^4 \text{ cm}^{-3}$, emission measures $\gtrsim 10^7 \text{ pc cm}^{-6}$).

A fruitful line of research in recent years to detect and probe regions of massive star formation has been the study of molecular masers, especially those of water (H_2O), OH, and methanol (CH_3OH). For instance, ammonia observations of Codella et al. (1997) suggest that water maser emission in massive star forming regions arise from hot molecular cores. Since masers are extremely bright, single dish surveys can detect regions undergoing massive star formation that are otherwise difficult to discover.

This dissertation focuses on the 6668 MHz maser transition of methanol, which is found to be a very strong maser in regions of massive star formation. Since methanol masers were discovered much later than water and OH masers, and thus studied for a much shorter period of time, their place in the star formation process is not as well understood. Our understanding of the 6.7 GHz methanol maser is further limited due to the dearth of large telescopes that have receivers to detect this line. Prior to 2004, no large telescope in the United States had a receiver that could process signals at 6.7 GHz. Thus all research on the 6.7 GHz methanol maser has been carried out by telescopes in Europe and Australia.

To change this scenario, we built a broadband receiver for the 305 m Arecibo radio telescope that could detect radiation between 6 and 8 GHz. The instrument when installed in the telescope in Feb. 2004, gave Arecibo continuous frequency coverage between 1.1 GHz and 10 GHz. There was also considerable effort by the National Astronomy and Ionosphere Center (NAIC) staff to improve the surface accuracy of all reflectors in the system to improve the performance of the telescope at high frequencies ($\nu > 6$ GHz). Following the installation of the receiver, we carried out a large survey for 6.7 GHz methanol masers in a region of the Galactic plane that is visible from Arecibo. The combination of the high sensitivity of the receiver, and the large collecting area of the telescope made our survey the most sensitive blind survey carried out to date.

The organization of this dissertation is as follows: §2 describes the phenomenological maser theory and discusses unsaturated and saturated masers, beaming of maser emission, and pumping mechanisms. These theoretical aspects of masers are mostly from Elitzur (1992). §3 covers an overview of the methanol molecule, and explains the origin of its complex spectrum. In §4, the observational aspects of methanol masers with specific reference to 6.7 GHz and 12.2 GHz masers are described. §5 describes the 6 to 8 GHz receiver that we built for the Arecibo radio telescope. §6 and §7 describe the Arecibo Methanol Maser Galactic Plane Survey (AMGPS) and the results from the survey. Finally, §8 describes ongoing and future work related to the subject.

Chapter 2

Astronomical Masers: an Overview

2.1 Introduction

Stimulated radiation, which is generated in the laboratory with elaborate, special equipment occurs naturally in interstellar space. Maser emission was discovered when simultaneous measurement of four OH lines showed that the population distribution among the four levels was not in thermal equilibrium resulting in anomalous radiation patterns (Weinreb et al. 1963; Weaver et al. 1965). It soon became evident that equilibrium distributions of level populations are the exception rather than the norm in interstellar clouds, a result of the very low densities. In general, the level populations are not in local thermodynamic equilibrium (LTE), which implies that ratios of level populations are not determined by the kinetic temperature of the gas. Departures from LTE may occasionally result in population inversion, which results in maser amplification. Maser emission in interstellar space has been detected in a number of molecules like OH, H₂O, SiO, CH₃OH, NH₃, HCOH, CH and HCN.

In this chapter, we overview the theory behind microwave stimulated emission. The phenomenological theory of maser emission, saturation of masers, geometric beaming effects and pumping mechanisms are reviewed in the following sections. Most of the material presented below is taken from Elitzur (1992).

2.2 Phenomenological Maser Theory

2.2.1 Rate Equations

Consider a two level system with energy separation ΔE . Let N_1 and N_2 denote the number density of particles in the two levels. Then, the rate equations are,

$$\frac{\partial N_1}{\partial t} = -\frac{\partial N_2}{\partial t} = N_2(C_{21} + A_{21}) - N_1 C_{12} + \bar{J}(N_2 B_{21} - N_1 B_{12}) \quad (2.1)$$

Here, B_{12} , B_{21} and A_{21} are the Einstein coefficients, \bar{J} describes the radiation field and C_{12} and C_{21} are the collision rates. The various coefficients obey the relations

$$g_1 C_{12} = g_2 C_{21} e^{-\Delta E/kT} \quad (2.2)$$

$$g_1 B_{12} = g_2 B_{21} \quad (2.3)$$

$$A_{21} = \frac{2h\nu^3}{c^2} B_{21} \quad (2.4)$$

where g_1 and g_2 are the statistical weights of the two levels.

The rate equations above will never produce population inversion because they only describe particle exchange between two levels with rates that obey detailed balance equations. Population inversion can occur only as a result of particles cycling through other levels. A description of the maser effect requires a generalization of the rate equations that describe system gains and losses due to population exchange with other levels that do not directly interact with maser radiation.

To describe this interaction, for each of the two maser levels we introduce a loss rate Γ_i (s^{-1}) and a pump rate per unit volume P_i ($\text{cm}^{-3}\text{s}^{-1}$). Also, denote by $N_{i\nu}$ ($\text{cm}^{-3}\text{Hz}^{-1}$) the density of those particles whose transition frequency has been shifted to ν from their original frequency ν_0 as a result of their random velocity; for instance, when the populations are distributed by the Doppler profile,

$N_{i\nu} = N_i\phi(\nu)$, where $\phi(\nu)$ is the Doppler line profile given by

$$\phi(\nu) = \frac{1}{\Delta\nu_D\sqrt{\pi}} e^{-x^2} \quad (2.5)$$

where $x = (\nu - \nu_0)/\Delta\nu_D$ and $\Delta\nu_D = \nu_0(\Delta\nu_D/c)$. In this case, the pump rates into the frequency interval $[\nu, \nu + d\nu]$ are $P_{i\nu} = P_i\phi(\nu)$. The rate equation for the upper level then becomes

$$\frac{\partial N_{2\nu}}{\partial t} = P_{2\nu} - \Gamma_2 N_{2\nu} - A_{21} N_{2\nu} - J_\nu (N_{2\nu} B_{21} - N_{1\nu} B_{12}) - (N_{2\nu} C_{21} - N_{1\nu} C_{12}) \quad (2.6)$$

where J_ν is the angle averaged maser intensity. A very similar equation can be written for $N_{1\nu}$.

Astronomical masers are stable over periods much longer than any time scale in the rate equations, so steady state can be assumed. The quantities relevant for maser gain are the populations per sub-level, $n_{i\nu} = N_{i\nu}/g_i$. To simplify the algebra, we will assume equal statistical weights and loss rates, i.e. $g_1 = g_2 \equiv g$ and that $\Gamma_1 = \Gamma_2 \equiv \Gamma$. With the aid of eq. (2) and (3), the steady state level population equations for the maser become

$$0 = p_{2\nu} - \Gamma n_{2\nu} - A_{21} n_{2\nu} - B_{21} J_\nu (n_{2\nu} - n_{1\nu}) - C_{21} (n_{2\nu} - n_{1\nu} e^{-\Delta E/kT}) \quad (2.7)$$

$$0 = p_{1\nu} - \Gamma n_{1\nu} + A_{21} n_{2\nu} + B_{21} J_\nu (n_{2\nu} - n_{1\nu}) + C_{21} (n_{2\nu} - n_{1\nu} e^{-\Delta E/kT}) \quad (2.8)$$

where $p_i = P_i/g_i$ are the pump rates per sub-level.

Adding the two equations above, the exchange terms between the two levels cancel out, and the overall population of the maser system is

$$n_\nu \equiv n_{1\nu} + n_{2\nu} = n\phi(\nu)$$

where

$$n = (p_1 + p_2)/\Gamma \quad (2.9)$$

The equation above tells us that the overall population is distributed according to the thermal profile, irrespective of the maser intensity.

2.2.2 Population Inversion

To solve for the population difference $\Delta n_\nu = n_{2\nu} - n_{1\nu}$, we will neglect the spontaneous decays and collisional exchange terms. It can be shown that the functional form of the derived population difference will be the same and that we are justified in neglecting the spontaneous decays and collisions as long as A_{21} and C_{21} are much less than Γ . With these simplifications, the population difference can be derived by subtracting eqs. (2.7) and (2.8).

$$\Delta n_\nu = \frac{\Delta n_0}{1 + J_\nu/J_s} \phi(\nu) \quad (2.10)$$

where

$$\Delta n_0 = \Delta p/\Gamma, \quad \Delta p = p_2 - p_1, \quad J_s = \Gamma/2B_{21}$$

Clearly, when the maser is so intense that $J_\nu \gg J_s$, the frequency dependence of Δn_ν can deviate from the profile shape of $\phi(\nu)$.

Thus population inversion requires that $p_2 > p_1$, namely the pump rate per sub-level of the upper rate must exceed that of the lower rate. The efficiency of the pump process is characterized by the parameter

$$\eta = \frac{p_2 - p_1}{p_2 + p_1} = \frac{\Delta n_0}{n} \quad (2.11)$$

One can derive an excitation temperature T_{x0} from Δn_0 , the population difference in the absence of maser emission ($J_\nu = 0$), which is negative for an inverted

population.

$$\begin{aligned} e^{-h\nu/kT_{x0}} &= \frac{n_{2\nu}}{n_{1\nu}} = \frac{p_2}{p_1} \\ \Rightarrow |T_{x0}| &= \frac{h\nu}{k} \frac{1-\eta}{2\eta} \end{aligned} \quad (2.12)$$

The excitation temperature is independent of the pumping rate and is exclusively determined by the inversion efficiency, η . Note that the more efficient the inversion efficiency ($\eta \rightarrow 1$), the smaller $|T_{x0}|$ becomes. Hence, strong inversion corresponds to small $|T_{x0}|$.

The absorption coefficient depends on the population difference and is given by

$$\alpha_\nu = (n_1 - n_2)g_2B_{21}h\nu\phi(\nu)/4\pi \quad (2.13)$$

Hence, we can write the absorption coefficient for the maser¹ as

$$\alpha_\nu = \frac{\alpha_{0\nu}}{1 + J_\nu/J_s}, \quad \alpha_{0\nu} = \Delta n_0 g_2 B_{21} h\nu \phi(\nu)/4\pi \quad (2.14)$$

As in the case of the population difference, the frequency dependence of the opacity ($\rho\kappa_\nu = \alpha_\nu$) can deviate from the profile of $\phi(\nu)$ when the intensity is so high that $J_\nu \gg J_s$.

2.2.3 Unsaturated masers

The parameter J_s sets a scale for the radiative intensity to begin to affect the population difference. When $J_\nu \ll J_s$, then Δn_ν is independent of the maser radiation field and $\alpha_\nu = \alpha_{0\nu}$. Such a maser is called *unsaturated*. The unsaturated level populations can be used to construct an emission coefficient $\epsilon_\nu (= \rho j_\nu)$ and a

¹As there is population inversion, the absorption coefficient is negative and α_ν must be written as $|\alpha_\nu|$. However, for convenience, the absolute signs will be dropped from all expressions of α and T_x .

radiation dependent source function S_0 as

$$\epsilon_\nu = \frac{2h\nu^3}{c^2} B_{21} \frac{p_2}{\Gamma} \frac{h\nu}{4\pi} \phi(\nu) \quad (2.15)$$

$$S_0 = \frac{\epsilon_\nu}{\alpha_{0\nu}} = \frac{2h\nu^3}{c^2} \frac{1+\eta}{2\eta} \quad (2.16)$$

As with the excitation temperature T_{x0} , the source function S_0 depends only on the inversion efficiency and not on the rate of pumping.

The equation of radiative transfer can now be solved for any geometry, yielding

$$I_\nu = (S_0 + I_e) e^{\alpha_{0\nu} l} - S_0 \quad (2.17)$$

where I_e is the intensity of an external background source which may illuminate the maser. One can express the intensities in terms of their equivalent temperatures. Assuming that all the temperatures are in the Rayleigh-Jeans regime, the brightness temperature becomes

$$T_b = (T_{x0} + T_e) e^{\alpha_{0\nu} l} - T_{x0} \quad (2.18)$$

There are two potential sources of seed photons (which start the stimulated emission): internal, due to spontaneous decays from the upper level, and external, the radiation of a background source that may illuminate the maser. The relative importance of these sources is determined by the relative magnitudes of T_e and T_{x0} . However, due to exponential growth, the maser intensity exceeds the seed intensity within a few gain units. Since the seed photons can be neglected, the volume emission rate of maser radiation is the net excess of stimulated emission over absorption, which is given by $g_2 B_{21} J_\nu \Delta n_\nu$. From eq. (2.10), this can be written as

$$g B_{21} J_\nu \Delta n_\nu = \Phi_\nu e_\nu \quad (2.19)$$

where Φ_ν and e_ν are given by

$$\Phi_\nu = g_2 B_{21} J_s \Delta n_0 \phi(\nu) = \frac{1}{2} \Delta P \phi(\nu) \quad (2.20)$$

$$e_\nu = \frac{J_\nu}{J_\nu + J_s} \quad (2.21)$$

Thus, the production rate of maser photons is the product of two terms. The first term Φ_ν is the *production rate* of inverted population. It is determined by the pumping scheme and is independent of the intensity or the distance traveled in the source. The second term is a *conversion efficiency* factor and corresponds to the fraction of inverted particles that are converted to maser photons. The conversion efficiency increases with maser intensity since the higher the intensity, the higher the probability that a particle will interact with the radiation field and cause a maser photon.

In an unsaturated maser, the amplification is uniform, determined by parameters inherent to the pumping scheme. This is because the propagating radiation is too weak to affect the level populations. Since the gain is proportional to the pump rates, the maser responds exponentially to variations in pumping conditions. Such a maser can be expected to display erratic time variability.

2.2.4 Saturated masers

The exponential growth of unsaturated maser intensity cannot continue forever because it would eventually lead to infinite energy density for sufficiently long masers. From eq. (2.21), it is evident that once J_ν exceeds J_s , the conversion efficiency of inversions to maser photons approaches unity and the maser saturates. Under saturation, the masing operation is reaching its maximum efficiency. Saturation starts at the line center where the intensity is maximum and then spreads to the

wings with further increase in intensity.

From eq. (2.20), the expression for Φ_ν can be written as

$$\Phi_\nu = \frac{1}{2} \eta (P_2 + P_1) \phi(\nu) \quad (2.22)$$

As the conversion efficiency $e_\nu = 1$, every pumping event produces a maser photon with an efficiency that depends only on the details of the pumping scheme as shown in eq. (2.22). Hence, we can determine the specific luminosity, L_ν of a saturated maser without solving the equation of radiative transfer:

$$L_\nu = h\nu \int \Phi_\nu dV$$

If V is the volume of the saturated region, and P is the average pump rate, then

$$L_\nu = \eta h\nu P V \phi(\nu) = 4\pi\alpha_{0\nu} J_s V \quad (2.23)$$

where we used eq. (2.14) for the second equality. As $L_\nu = \int F_\nu dA$, where A is the area, one can write the above equation in differential form (using Gauss's theorem) as

$$\nabla \cdot \mathbf{F}_\nu = h\nu \Phi_\nu \quad (2.24)$$

This shows that the maser flux increases linearly with overall dimension.

The scale of maser intensity is set by J_s in the saturated domain and by the source function S_0 in the unsaturated region. The ratio of these is denoted as γ and is a measure of the amount of amplification the intensity has to undergo before the intensity saturates.

$$\gamma = J_s/S_0 \simeq \eta\Gamma/A_{21} \quad (2.25)$$

Typically, $\gamma \sim 10^7\eta - 10^8\eta$ for astronomical masers. If the inversion efficiency η is a few percent, then $\gamma \gtrsim 10^5$ so that masers saturate when their gains exceed $\ln \gamma \simeq 11$.

2.2.5 Radiative transfer in masers

We now wish to derive a general equation of radiative transfer applicable for any maser. The equation of radiative transfer is

$$\begin{aligned} \frac{dI_\nu}{dl} &= \alpha_\nu I_\nu + \epsilon_\nu \\ \Rightarrow \frac{dI_\nu}{\alpha_{0\nu} dl} &= \frac{I_\nu}{1 + J_\nu/J_s} + S_m \end{aligned} \quad (2.26)$$

where $S_m = \epsilon_\nu/\alpha_{0\nu}$ is the maser source function and is different from the conventional definition of the source function since the intensity dependence of the absorption coefficient is explicitly removed. From eqs. (2.9), (2.10) and (2.14), we can derive the expression for the maser source function as

$$S_m = S_0 \frac{1 + \eta/(1 + J_\nu/J_s)}{1 + \eta} \quad (2.27)$$

where S_0 is the source function in the unsaturated limit. We see that the source function shows only a slight variation from S_0 in the unsaturated maser to $S_0/(1+\eta)$ in the strongly saturated limit (normally, $\eta \ll 1$). Hence, this small variation will be ignored in subsequent discussion and eq. (2.26) with S_m replaced by S_0 will be used as the equation of radiative transfer that governs the maser behavior².

Consider a point in the maser where the source term is negligible. Once the source term is neglected, the radiative transfer becomes

$$\frac{dI_\nu}{dl} = \alpha_\nu I_\nu \quad (2.28)$$

Now, consider two streams of radiation propagating in opposite directions on a given ray. The stream in the positive direction is denoted by $I_{\nu+}$ and the stream

²It is easy to show that the transformation $S' = S_0/(1 + \eta)$ and $I'_\nu = I_\nu + \eta S'$ leads to an exact equation with the same mathematical form. Hence, the intensity variation of the source function can be easily incorporated if desired.

in the negative direction is denoted by $I_{\nu-}$. Then if both streams obey eq. (2.28),

$$\frac{dI_{\nu+}}{dl} = \alpha_{\nu} I_{\nu+} \quad \frac{dI_{\nu-}}{-dl} = \alpha_{\nu} I_{\nu-}$$

From these equations, it immediately follows that in the region of their applicability,

$$I_{\nu+} I_{\nu-} = \text{const}$$

i.e., the growing maser intensity increases at the expense of the oppositely moving stream. The stronger (the growing) stream is called the *dominant stream* and the oppositely moving (the weaker) stream is called the *subordinate stream*. An exact relation for the product of the intensities valid at every point in the maser can be obtained from the full equation of radiative transfer eq. (2.26) for the two streams. It can be easily shown that

$$\frac{dI_{\nu+} dI_{\nu-}}{\alpha_{0\nu} dl} = S_0 (I_{\nu-} - I_{\nu+}) \quad (2.29)$$

$$\Rightarrow I_{\nu+} I_{\nu-} = \int (I_{\nu-} - I_{\nu+}) S_0 \alpha_{0\nu} dl \quad (2.30)$$

2.3 Effects of Geometry: Beaming

Radiation beaming is an integral part of maser properties and crucial for its understanding in any geometry. Maser radiation is highly beamed in any source having appreciable gain, irrespective of its shape. Unlike in other disciplines within astronomy, beaming in a maser does not necessarily refer to directionality of maser radiation. Beaming in a maser refers to the exponential decline of the maser gain (and hence intensity of radiation) as a function of angular deviations from the direction of peak gain (with respect to a given direction on the sky). The reason for this is that the intensity always increases with distance traveled in the source,

and it is impossible to devise a geometry where all the path lengths are of equal length. This is true even in a sphere, the ultimate isotropic structure at any point other than its center. In a spherical geometry, the beaming effect does not result in the source being “missed” by an observer because of his/her orientation with respect to the source, but causes it to be perceived as significantly smaller in angular extent compared to its true size.

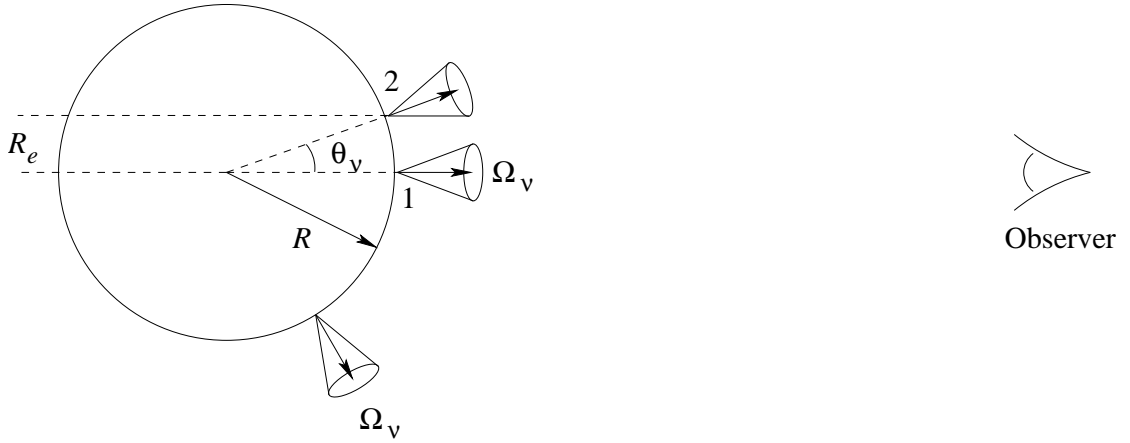


Figure 2.1 An illustration of the beaming effect due to geometry in a spherical maser. The radiation in any direction is beamed with a solid angle Ω_v . This results in the observer perceiving a source size that is much smaller than its true size.

For example, Figure 2.1 shows the “beaming” effect in a spherical geometry. The radiation in any direction from the source has an effective solid angle given by Ω_v . The apparent size of the source as seen by the observer is thus dictated by the location where the radiation cone surface is parallel to the observer (marked “2” in Figure 2.1), and is related to the size of the sphere, R as $R_e = R \sin \theta_y$.

2.3.1 Beaming in Unsaturated Masers

In an unsaturated maser, gain and path length are proportional to each other. Let l_0 denote the longest path through the source in direction θ_0 . For sufficiently long paths and well-behaved geometries, the path length along rays inclined at a small angle θ to the direction θ_0 can be shown to be

$$l(\theta) = l_0 \left[1 - \frac{1}{2} \left(\frac{l_0}{r_c} - 1 \right) \theta^2 \right] \quad (2.31)$$

where r_c is the local radius of curvature. For the particular ray length to be a maximum, the radius of curvature r_c must be less than l_0 , so that surfaces that are too flat are excluded. Using eq. (2.31) and assuming that $\alpha_{0\nu} l_0 \gg 1$, the angular dependence of intensity is given by

$$I_\nu(\theta) = I_\nu(\theta_0) e^{-(\theta/\theta_\nu)^2} \quad (2.32)$$

where θ_ν , the beaming angle is given by

$$\theta_\nu^2 = \frac{2}{\left(\frac{l_0}{r_c} - 1 \right) \alpha_{0\nu} l_0} \quad (2.33)$$

This shows that the angular distribution of intensity is sharply peaked and the maser radiation is strongly beamed outward along the longest chord through the source. Further, longer the ray path, the more pronounced the beaming.

For radiation that is highly beamed, the angle averaged intensity becomes

$$J_\nu = \frac{\Omega_\nu}{4\pi} I_\nu(\theta_0) \quad (2.34)$$

where $\Omega_\nu = \pi\theta_\nu^2$ is the solid angle of the beaming cone. The flux vector \mathbf{F}_ν points in the direction θ_0 and its magnitude is given by

$$F_\nu = \Omega_\nu I_\nu(\theta_0) = 4\pi J_\nu \quad (2.35)$$

2.3.2 Beaming in Saturated Masers

Beaming arises from the competition between rays moving in different directions for induced emission events. Hence the beaming of maser radiation persists into the saturated region even though the intensity does not vary exponentially with path length anymore. When the maser saturates, the flux vector can be obtained from the flux divergence relation eq. (2.24). Using this result with the beaming relation eq. (2.35) and noting from eqs. (2.14) and (2.20) that $h\nu\Phi_\nu = 4\pi\alpha_{0\nu}J_s$, we get

$$\nabla \cdot (J_\nu \mathbf{f}) = \alpha_{0\nu} J_s \quad (2.36)$$

where \mathbf{f} is the unit vector along the local dominant ray pointing in the direction of \mathbf{F}_ν . In sources where the trajectories of the flux vectors are straight lines, there is a point of symmetry from which the local flux vectors diverge. In these cases, the ray divergence center can be chosen as the origin of a spherical coordinate system. If l is the distance from that origin, the flux divergence relation in the local region where symmetry holds becomes

$$\frac{1}{l^2} \frac{d}{dl} (l^2 J_\nu) = \alpha_{0\nu} J_s \quad (2.37)$$

Now, the equation of radiative transfer for the dominant ray can also be written as an equation for the angle averaged intensity using eq. (2.34) as

$$\Omega_\nu \frac{d}{dl} (\Omega^{-1} J_\nu) = \alpha_{0\nu} J_s \quad (2.38)$$

Comparing eq. (2.37) and (2.38), we conclude that

$$l^2 \Omega_\nu = \text{const.} \quad (2.39)$$

Thus, the beaming actually becomes tighter following saturation (in those geometries for which the above analysis is valid) with the solid angle of the beaming cone

varying as l^{-2} instead of l^{-1} in unsaturated regions.

2.4 Pumping Mechanisms

One of the primary requirements for masing action is population inversion, which requires some pumping mechanism. In the absence of any exciting mechanisms, system particles tend to occupy the ground state. The particles are excited into higher states by either collisions or radiation from an external source. Hence, the pumping mechanism is called *radiative* or *collisional* according to the nature of the process that dominates these excitations.

In radiative pumps, the main mechanism that causes the population inversion is radiation from an external source. Consider a source that is illuminated by external radiation with a dilution factor $W = \Delta\Omega/4\pi$ and whose photon occupation number in the frequency ν_{ij} of the transition $i \rightarrow j$ is $\mathcal{N}_{ij} = 1/(e^{h\nu_{ij}/kT_{bij}} - 1)$. Considering rate equations with detailed balance and ignoring collisions, it can be shown that under steady state, the level populations are distributed by

$$\frac{n_i}{n_j} = \frac{W}{\exp(h\nu_{ij}/kT_{bij}) - (1 - W)} \quad (2.40)$$

Clearly, for the radiation to cause population inversion which is a significant deviation from local thermodynamic equilibrium, the radiation field must deviate from a blackbody. It suffices for the deviation from blackbody to be as minor as a simple geometric dilution ($W < 1$). Optically thin dust provides one of the ways for the radiation field to deviate significantly from a blackbody and so provides one of the important radiative pump mechanisms for masers.

In collisional pumps, the particles are excited to high energy states by collisions followed by radiative decays to lower levels. Usually, the energy separation of

the masing transition is much smaller than the typical energy separation in the molecule so that the Einstein A coefficient for radiative decay across the masing transition is very small. This causes a cascade of particles to the upper masing level which causes population inversion. Note that if the collisional rate is high, levels tend to thermalize and population inversion would disappear.

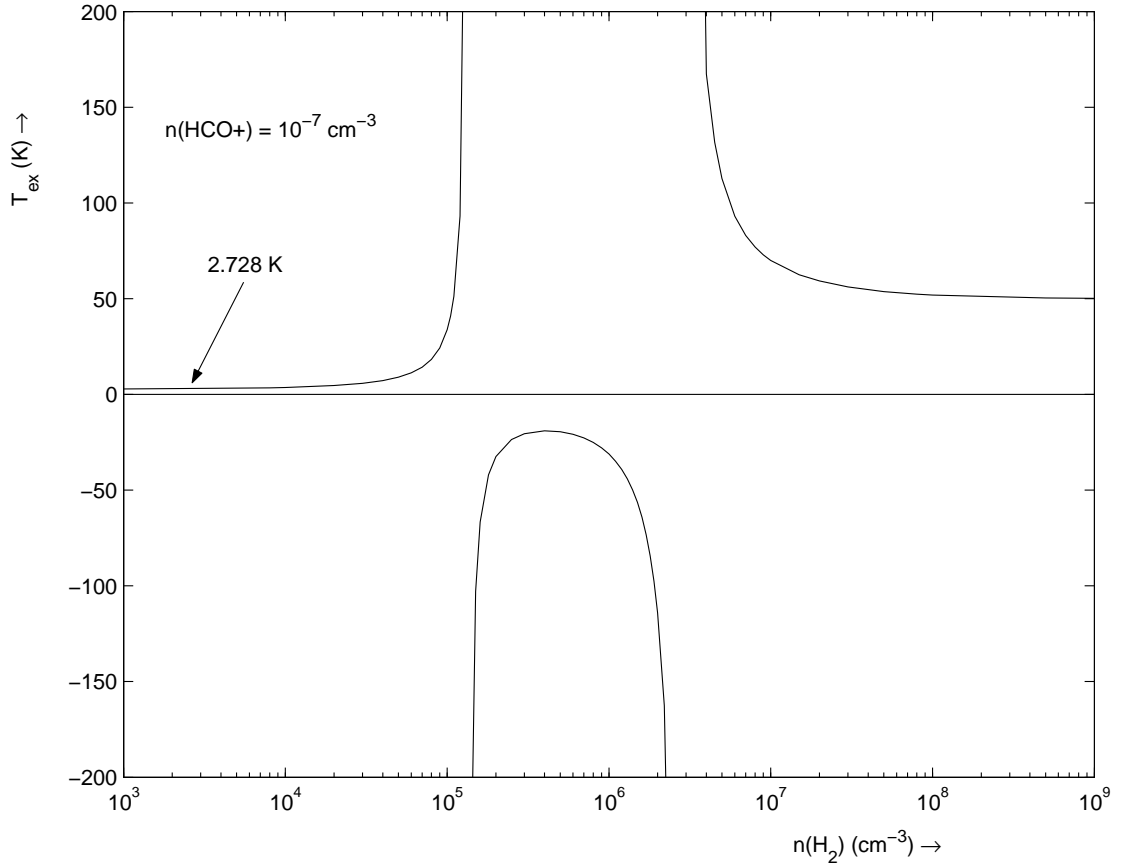


Figure 2.2 Excitation temperature of the HCO^+ molecule ($J = 1 \rightarrow 0$) as a function of number density of H_2 for a simple model of a gas cloud with kinetic temperature $T_K = 50$ K. A weak population inversion (characterized by negative excitation temperatures) is seen for a small range of densities.

For instance, Figure 2.2 shows the result of a calculation of the excitation temperature of the $J = 1 \rightarrow 0$ transition of HCO^+ in a uniform density gas cloud using the radiative transfer code RATRAN (Hogerheijde & van der Tak 2000).

The cloud was modeled with kinetic temperature $T_K = 50$ K and is permeated by the Cosmic Microwave Background (CMB) radiation field. Several models were run with increasing number density of H_2 keeping the number density of HCO^+ fixed at 10^{-7} cm^{-3} . One can see that the excitation temperature equals that of the CMB radiation field for low collisional rate, and thermalizes for high collisional rate. However, population inversion occurs over a small range of densities where the rate of collisions are “just right” to promote the cascading process indicated above. This example does not correspond to any physically observed maser and is quoted merely to illustrate the working of the collisional pump.

2.5 Conclusions

The basic theory behind maser emission has been presented. Population inversion, which is created by collisional or radiative processes causes exponential amplification of the intensity of seed radiation in an unsaturated maser. When the intensity of the radiation reaches a critical value, the maser becomes saturated, causing further amplification to be a linear rather than exponential function of the path length. Since the total gain is a sensitive function of the path length, maser radiation is “beamed”. Observations at very high angular resolution can help probe the microphysics of astronomical masers.

Chapter 3

The Energy Structure of the Methanol

Molecule

Methanol, CH_3OH , is an asymmetric rotor capable of internal rotation by the OH bond about the axis of the tetrahedron defined by the CH_3 group (Figure 3.1), but this rotation (also called torsion) is hindered by mutual interaction. The CH_3 group induces a three-fold barrier potential in the torsional motion of methanol. The combination of the asymmetry and the hindered motion gives a complex energy spectrum.

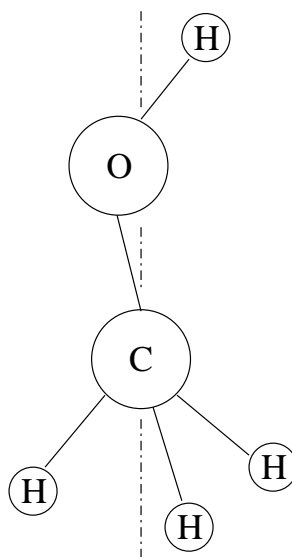


Figure 3.1 Schematic structure of the methanol molecule. The symmetry axis of the CH_3 group is shown in dot-dashed line. The CO bond is tilted with respect to the symmetry axis by $\sim 3^\circ$ and is exaggerated in the figure for illustration. The COH, and the HCH angles are $\sim 108^\circ$ each (data from Lees & Baker 1968).

It is useful to understand simpler molecular structures before exploring the complex structure of methanol. In the following sections, the symmetric rotor,

asymmetric rotor and a symmetric rotor with hindered motion are considered. A combination of these ideas can be used to understand the energy spectrum of methanol. The overview is taken from Townes & Schawlow (1975) unless otherwise stated.

3.1 The Symmetric Rotor

The rotational energy of a molecule is given by

$$W = \frac{1}{2}I_x^2\omega_x^2 + \frac{1}{2}I_y^2\omega_y^2 + \frac{1}{2}I_z^2\omega_z^2 \quad (3.1)$$

where x , y and z are directions along the principal axes of inertia, z being the symmetry axis of the molecule. Since the molecule is a symmetric top, I_x and I_y are equal, and by convention (in molecular spectroscopy) is called I_B . I_z by convention is designated as I_A or I_C depending on whether it is smaller or larger than I_B . As an example, let us designate I_z as I_C .

Then, the Hamiltonian of the symmetric rotor can be written as

$$H = \frac{1}{2I_B}(P_x^2 + P_y^2) + \frac{1}{2I_C}P_z^2 \quad (3.2)$$

$$= \frac{P^2}{2I_B} + P_z^2 \left(\frac{1}{2I_C} - \frac{1}{2I_B} \right) \quad (3.3)$$

where P_x , P_y and P_z are the components of the total angular momentum, P , along the x , y and z axes respectively. Since P^2 and P_z are good quantum numbers, the energy levels of the symmetric rotor are given by

$$\frac{W}{h} = BJ(J+1) + (C-B)K^2 \quad (3.4)$$

where the rotational constants B and C are defined as

$$B = \frac{h}{8\pi^2 I_B} \quad C = \frac{h}{8\pi^2 I_C} \quad (3.5)$$

From eq. (3.4), a couple of points can be noted. Since the energy levels depend on K^2 where K ranges from $-J$ to $+J$, all energy states save the $K = 0$ state are doubly degenerate¹. A prolate top has $I_C < I_B$, and hence energy levels are higher with increasing K for a fixed J . The opposite is true for an oblate top which has $I_C > I_B$, and energy levels lower with increasing K for a fixed J .

To describe the wave functions of the symmetric rotor, the coordinate system shown in Figure 3.2 is used. The X , Y and Z axes are fixed in space, while the x , y and z axes are fixed in the molecule. The z axis is along the symmetry axis of the molecule. θ and ϕ are equivalent to the polar angles between the axis fixed in space and the axis fixed in the molecule. χ is the angle of rotation around the axis fixed in the molecule.

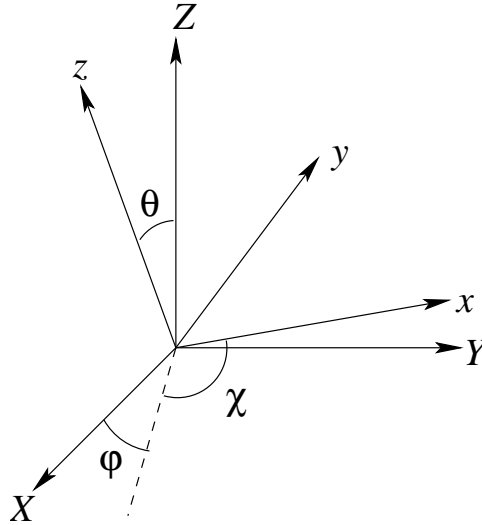


Figure 3.2 The coordinate system used to solve the wave functions of the symmetric rotor. The dashed line is the intersection of the xy and XY planes.

¹By convention, the capital letter K is used to designate the unsigned quantum number, and the small letter k is used to designate the signed quantum number.

The wave function can be shown (Kemble 1937) to be written as

$$\begin{aligned} \frac{1}{\sin \theta} \frac{\partial}{\partial \theta} \left(\sin \theta \frac{\partial \psi}{\partial \theta} \right) + \frac{1}{\sin^2 \theta} \frac{\partial^2 \psi}{\partial \phi^2} + \left(\frac{\cos^2 \theta}{\sin^2 \theta} + \frac{C}{B} \right) \frac{\partial^2 \psi}{\partial \chi^2} \\ - \frac{2 \cos \theta}{\sin^2 \theta} \frac{\partial^2 \psi}{\partial \psi \partial \phi} + \frac{W}{hB} \psi = 0 \end{aligned} \quad (3.6)$$

The solutions to above are written in the form

$$\psi = \Theta(\theta) e^{iM\phi} e^{iK\chi} \quad (3.7)$$

where M and K are integers. The function $\Theta(\theta)$ satisfies the equation

$$\begin{aligned} \frac{1}{\sin \theta} \frac{d}{d\theta} \left(\sin \theta \frac{d\Theta}{d\theta} \right) - \left[\frac{M^2}{\sin^2 \theta} + \left(\frac{\cos^2 \theta}{\sin^2 \theta} + \frac{C}{B} \right) K^2 \right. \\ \left. - 2 \frac{\cos \theta}{\sin^2 \theta} K M - \frac{W}{hB} \right] \Theta = 0 \end{aligned} \quad (3.8)$$

The total angular momentum quantum number J can be shown to be

$$J = \frac{1}{2}(|K + M| + |K - M|) \quad (3.9)$$

The quantum number K is the projection of J on the molecular symmetry axis, and M is the projection of J on the fixed space polar axis.

Examples of symmetric top molecules are NH_3 , PH_3 , CH_3CN and CH_3CF_3 .

3.2 The Asymmetric Rotor

In the case of an asymmetric rotor, the moments of inertia I_x , I_y and I_z are all different. If two moments of inertia are nearly equal, then the molecule is called a slightly asymmetric top. The molecular constants A , B and C can be defined in a manner analogous to eq. (3.5) from I_x , I_y and I_z , such that $A > B > C$. Then, a prolate symmetric top corresponds to $B = C$, and an oblate symmetric top corresponds to $A = B$.

The degree of asymmetry in an asymmetric rotor is typically characterized by Ray's asymmetry parameter, κ , which is given by

$$\kappa = \frac{2B - A - C}{A - C} \quad (3.10)$$

κ becomes -1 for a prolate symmetric top and $+1$ for an oblate symmetric top, and varies in between these two values for asymmetric tops.

For an asymmetric rotor, the total angular momentum J , and its projection on a fixed space axis M are constants of motion, and are thus good quantum numbers that can be used to specify the energy state of the rotor. However, no component of the angular momentum along any direction in the rotating molecule is constant. This implies that the quantum number K is not a good quantum number and cannot be used to specify the rotational state.

Recall that in the case of a symmetric rotor, for a fixed J , the energy levels increase with increasing K in the case of a prolate top, and decrease with increasing K in the case of an oblate top. Moreover, each energy level, except for the $K = 0$ state is doubly degenerate. In the case of an asymmetric rotor, the asymmetry breaks this degeneracy of energy levels, and this is called *K-doubling*. It can be shown that as the asymmetry parameter κ is changed from -1 to $+1$, a doubly degenerate level J_K (for $\kappa = -1$) splits into two levels, with one level merging with J_{J-K} , while the other level merges with J_{J-K-1} , where the latter two energy states are for $\kappa = 1$. Thus, one of the conventional techniques used to designate energy levels for an asymmetric rotor is to specify the value of J , and the value of K_{-1} for the limiting prolate and the value of K_1 for the limiting oblate symmetric rotor. For example, an energy state $J_{K_{-1}K_1}$ designates an energy level that has a total angular momentum J , and a K that in the case of a limiting prolate equals K_{-1} , and in the case of a limiting oblate equals K_1 .

For a more detailed discussion on asymmetric rotors, one is referred to Townes & Schawlow (1975) and the references therein. Examples of asymmetric rotors are H_2O , CH_2O , SO_2 and O_3 .

3.3 Hindered Torsional Motions in Symmetric Rotors

A common type of hindered motion is the rotation of one part of a molecule with respect to another. An example is the CH_3CF_3 molecule, where the CH_3 group rotates with respect to the CF_3 group about the C–C axis. One of the two symmetric groups is designated as the framework, and the other group is designated the internal rotor. The barrier potential depends on the degree of interaction between the two parts of the molecule. The extreme limiting cases of hindered motions are (a) where the mutual interaction is very strong so that the internal rotation is reduced to small torsional motions and (b) where the interaction is weak so that the two parts of the molecule can freely rotate with respect to each other.

Let the two parts of the molecule, 1 and 2 have moments of inertia about the symmetry axis as I_{z1} and I_{z2} respectively. The total moment of inertia about the symmetry axis is $I_z = I_{z1} + I_{z2}$. Further, let χ_1 and χ_2 be the angular positions of the two parts with respect to the symmetry axis. The difference in angular position is given by $\alpha = \chi_1 - \chi_2$.

Let us first consider the case of strong mutual interaction. The reduced moment of inertia for the two parts of the molecule twisting with respect to each other is

$$I_r = \frac{I_{z1}I_{z2}}{I_z} \quad (3.11)$$

The frequency of torsional oscillation is then given by

$$\nu = \frac{1}{2\pi} \sqrt{\frac{kI_z}{I_{z1}I_{z2}}} \quad (3.12)$$

where k is the torque constant. The total energy is then given by

$$\frac{W}{h} = BJ(J+1) + (C-B)K^2 + \nu(v_t + \frac{1}{2}) \quad (3.13)$$

where B and C are the molecular constants defined in eq. (3.5) and v_t is the torsional quantum number. If the barrier potential is due to a CH_3 group, each torsional level is triply degenerate, since there are three equivalent positions where the torsional motion can occur.

In case (b) where free rotation can occur, the angular momentum for the two parts of the molecule about the symmetry axis can be characterized by quantum numbers m_1 and m_2 where $m_1 + m_2 = K$. The rotational energy is then given by

$$W = hB[J(J+1) - K^2] + \frac{(m_1\hbar)^2}{2I_{z1}} + \frac{(m_2\hbar)^2}{2I_{z2}} \quad (3.14)$$

which can be reduced to

$$W = hBJ(J+1) + h(C-B)K^2 + \frac{I_z\hbar^2}{2I_{z1}I_{z2}} \left(m_1 - \frac{KI_{z1}}{I_z} \right)^2 \quad (3.15)$$

Let us consider the more general case of an intermediate amount of interaction between the two parts of the molecule. Since we are interested in hindered rotation about the CH_3 group, the barrier potential can be written as

$$V(\alpha) = \frac{1}{2}V_0(1 - \cos 3\alpha) \quad (3.16)$$

The total kinetic energy due to rotation is given by

$$2T = I_x\omega_x^2 + I_y\omega_y^2 + I_{z1}\dot{\chi}_1^2 + I_{z2}\dot{\chi}_2^2 \quad (3.17)$$

where I_x and I_y are the moments of inertia perpendicular to the symmetry axis. The Hamiltonian computed from eq. (3.17) will contain terms coupling the angular momentum about the symmetry axis and the angular momentum of internal rotation. To get rid of these terms, the following change of variables is applied.

$$\chi = \frac{I_{z1}\chi_1 + I_{z2}\chi_2}{I_z} \quad \alpha = \chi_1 - \chi_2 \quad (3.18)$$

Using this change of variables, the kinetic energy becomes

$$2T = I_x\omega_x^2 + I_y\omega_y^2 + I_z\dot{\chi}^2 + \frac{I_{z1}I_{z2}}{I_z}\dot{\alpha}^2 \quad (3.19)$$

From the equation above, the Hamiltonian is

$$H = \frac{P_x^2}{2I_x} + \frac{P_y^2}{2I_y} + \frac{P_z^2}{2I_z} + \frac{I_z}{2I_{z1}I_{z2}}P_\alpha^2 + \frac{1}{2}V_0(1 - \cos 3\alpha) \quad (3.20)$$

where $P_\alpha = \partial T / \partial \dot{\alpha}$ is the canonical momentum associated with the coordinate α . The change of variables in eq. (3.18) moves the coordinate system to a frame that is rotating with respect to the framework at an angular velocity of $(I_{z2}/I_z)\dot{\alpha}$ about the axis of symmetry of the molecule. The coordinate axes in this frame is called the “internal rotation axes” (Lin & Swalen 1959). To an observer in this frame, both the rotor and the framework appear to be rotating; however, the angular momentum from internal rotation is zero in this frame. The angular momentum operators P_x , P_y and P_z are related to the quantities in a fixed frame XYZ (where Z is parallel to the symmetry axis) through

$$\begin{aligned} P_x &= \cos(\rho\alpha)P_X - \sin(\rho\alpha)P_Y \\ P_y &= \sin(\rho\alpha)P_X + \cos(\rho\alpha)P_Y \\ P_z &= P_Z \end{aligned} \quad (3.21)$$

where

$$\rho = \frac{I_{z2}}{I_z} \quad (3.22)$$

The first three terms in the Hamiltonian in eq. (3.20) have the same form as in eq. (3.2). Since P_α commutes with P_x , P_y and P_z , the wave function of the system can be written as the product of the rotational and torsional wave functions (Nielsen 1932; Koehler & Dennison 1940)

$$\psi = \frac{1}{2\pi} e^{iK\chi} e^{iM\phi} \Theta_{JKM}(\theta) M(\alpha) \quad (3.23)$$

where the first three terms above are identical to eq. (3.7), and M satisfies

$$\left[-\frac{I_z \hbar^2}{I_{z1} I_{z2}} \frac{d^2}{d\alpha^2} + V(\alpha) \right] M(\alpha) = W_\alpha M(\alpha) \quad (3.24)$$

which is a form equivalent to the Mathieu equation. According to Floquet's theorem, a particular solution of the Mathieu equation can be written as

$$M(\alpha) = e^{i\alpha f} P(\alpha) \quad (3.25)$$

Since the wave function must be finite everywhere, the constant f must be real. Additional boundary conditions are imposed by the fact that the wave function must remain unchanged when either part of the molecule is rotated by a finite number of complete rotations, i.e.

$$\psi(\theta, \phi, \chi_1, \chi_2) = \psi(\theta, \phi, \chi_1 + 2\pi n_1, \chi_2 + 2\pi n_2) \quad (3.26)$$

Substituting these constraints into eqs. (3.23) and (3.25),

$$e^{iK\chi} e^{iM\phi} \Theta(\theta) e^{i\alpha f} M(\alpha) = e^{iK\chi} e^{2\pi i K(n_1 I_{z1} + n_2 I_{z2})/I_z} e^{iM\phi} \Theta(\theta) e^{i\alpha f} e^{2\pi i f(n_1 - n_2)} \quad (3.27)$$

Hence,

$$\frac{K(n_1 I_{z1} + n_2 I_{z2})}{I_z} + f(n_1 - n_2) = n \quad (3.28)$$

where n is an integer. This can be satisfied by setting f to be either ρK (adopted by Lin & Swalen 1959; Lees & Baker 1968) or $(\rho - 1)K$ (adopted by Koehler &

Dennison 1940), where ρ is defined in eq. (3.22). Since it is more convenient to take $f = \rho K$ in most cases (Lin & Swalen 1959), we will adopt this, and the torsional wave function is then

$$M(\alpha) = e^{i\rho K\alpha} P(\alpha) \quad (3.29)$$

Substituting this equation into eq. (3.24), the function P must satisfy

$$-\frac{I_z \hbar^2}{I_{z1} I_{z2}} \frac{d^2 P}{d\alpha^2} - 2iK \frac{\hbar^2}{I_{z1}} \frac{dP}{d\alpha} + \left[K^2 \frac{I_{z2} \hbar^2}{I_z I_{z1}} + V(\alpha) \right] P = W_\alpha P \quad (3.30)$$

The solutions to eq. (3.30) are different for different K . Hence, K should be included in the labeling index for the energy levels of the torsional Hamiltonian. Since the only explicit dependence of the above equation on α is through a $\cos 3\alpha$ term of $V(\alpha)$, the eigenfunction $M(\alpha)$ can be classified into three groups corresponding to an index $\sigma = 0, \pm 1$. It can be easily shown that the solutions for a given value of σ are equivalent to the solutions for $\sigma' = \sigma + 3k$ where k is an integer. The eigenfunctions M can be written as

$$M_{Kv_t\sigma} = e^{i\rho K\alpha} \sum_k a_{K,v_t,3k+\sigma} e^{i(3k+\sigma)\alpha} \quad (3.31)$$

The solutions to the coefficients a and the function P can be obtained by the method of continued fractions (Lin & Swalen 1959).

The total energy is given by

$$W = W_R + W_\alpha = hBJ(J+1) + h(B-C)K^2 + W_{K,v_t,\sigma} \quad (3.32)$$

Note that if $P_{K,v_t,\sigma}(\alpha)$ is a solution of eq. (3.30), then $P^*(\alpha)$ is a solution of its complex conjugate, which is the same equation with K replaced with $-K$. Hence, we have

$$M_{K,v_t,\sigma}(\alpha) = M_{-K,v_t,-\sigma}^*(\alpha) \quad (3.33)$$

This gives rise to the degeneracies

$$W_{K,v_t,1} = W_{-K,v_t,-1} \quad (3.34)$$

$$W_{K,v_t,0} = W_{-K,v_t,0} \quad (3.35)$$

Since the rotational energy levels W_R are degenerate between $\pm K$, all energy levels except the $K = 0, \sigma = 0$ level are doubly degenerate.

3.4 Hindered Torsional Motions in Asymmetric Rotors

We are now interested in the case where one of the two parts of the molecule undergoing hindered rotation with respect to each other is asymmetric. We will only consider the special case where the asymmetric rotor has a plane of symmetry which includes the axis of the symmetric rotor. Molecules which satisfy this condition include CH_3OH and CH_3NO_2 . The primary difference between this case and the case of hindered rotation in symmetric rotors is the introduction of cross terms in the moment of inertia tensor.

The coordinate system is chosen such that the z axis is parallel to the axis of rotation. The x axis is perpendicular to the plane of symmetry and the y axis lies in the plane of symmetry. The origin of the coordinate system is chosen to be the center of mass of the molecule. Then, the moment of inertia tensor assumes the form

$$\mathbf{I} = \begin{bmatrix} I_x & 0 & 0 \\ 0 & I_y & -I_{yz} \\ 0 & -I_{yz} & I_z \end{bmatrix} \quad (3.36)$$

The kinetic energy of rotation in this molecule is

$$2T = I_x \omega_x^2 + I_y \omega_y^2 + I_z \dot{\chi}_1^2 + I_z \dot{\chi}_2^2 - 2I_{yz} \omega_y \dot{\chi}_1 \quad (3.37)$$

where χ_1 is the angle of rotation of the asymmetric part about the axis and χ_2 is the angle for the symmetric part.

It can be shown through a transformation of variables that the Hamiltonian for hindered rotation in the asymmetric rotor can be reduced to a form similar to that for a symmetric case (eq. 3.20) with more complex coefficients and some perturbation terms. A more detailed description of the subject can be found in Lin & Swalen (1959); Townes & Schawlow (1975).

3.5 Application to Methanol

As mentioned previously, methanol is an asymmetric rotor capable of hindered rotation. Most of the material presented below is taken from Koehler & Dennison (1940); Burkhard & Dennison (1951); Ivash & Dennison (1953); Kirtman (1962) and Lees & Baker (1968).

The coordinate system chosen is similar to the one in §3.3, and is fixed in the molecule with its origin at the center of mass. The z axis is chosen parallel to the axis of internal rotation, which is assumed to be the axis of the methyl top. The x axis is chosen perpendicular to the COH plane, and the y axis is perpendicular to the x and z axes (and thus lies in the COH plane). I_{z2} is the moment of inertia of the methyl top about its axis, and I_{z1} is given by $I_{z1} + I_{z2} = I_z$. The values of various moments of inertia are tabulated in Table 3.1 (data taken from Lees & Baker 1968). The data show that the asymmetry in methanol is quite small.

As explained in §3.3, the preferred method of approaching the problem of hindered rotation in rotors is to remove the coupling between torsion and rotation to zeroth order by transforming to an internal axis system in which the methyl top and the framework have equal and opposite angular momentum. The zeroth order

Table 3.1 Moments of inertia for the methanol molecule. The data is taken from Lees & Baker (1968), and all measurements are given in $\text{amu}\cdot\text{\AA}^2$.

Moment of Inertia	Value ($\text{amu}\cdot\text{\AA}^2$)
I_x	21.2679 ± 0.0017
I_y	20.4834 ± 0.0015
I_{z1}	0.74956 ± 0.00003
I_{z2}	3.21321 ± 0.00003
I_{yz}	-0.0649 ± 0.0042

Hamiltonian, which is obtained by starting with operators derived from eq. (3.37), and applying transformations similar to eq. (3.18), can be written as

$$H^0 = H_{\text{Rsym}}^0 + H_{\text{Rasym}}^0 + H_{\text{T}}^0 \quad (3.38)$$

where H_{Rsym}^0 , H_{Rasym}^0 and H_{T}^0 refer to the parts of the Hamiltonian with a form associated with that of symmetric rotors, asymmetric rotors and hindered rotation respectively. The individual terms can be given as (Lees & Baker 1968)

$$H_{\text{Rsym}}^0 = \frac{1}{4} \left(\frac{I_y}{I_y^2 + I_{yz}^2} + \frac{1}{I_x} \right) (P_x^2 + P_y^2) + \frac{1}{2} \left(\frac{I_y + I_z}{I_y I_z - I_{yz}^2} - \frac{I_y}{I_y^2 + I_{yz}^2} \right) P_z^2 \quad (3.39)$$

$$H_{\text{Rasym}}^0 = \frac{1}{4} \left(\frac{I_y}{I_y^2 + I_{yz}^2} - \frac{1}{I_x} \right) (P_y^2 - P_x^2) + \frac{1}{2} \frac{I_{yz}}{I_y^2 + I_{yz}^2} (P_y P_z + P_z P_y) \quad (3.40)$$

$$H_{\text{T}}^0 = \frac{1}{2} \frac{I_y I_z - I_{yz}^2}{I_{z2}(I_{z1} I_y - I_{yz}^2)} P_\alpha^2 + \frac{1}{2} V_0 (1 - \cos 3\alpha) \quad (3.41)$$

The barrier potential V_0 for methanol is 375.6 cm^{-1} (Lees & Baker 1968).

The basis functions for H^0 are usually taken as eigenfunctions $|JKm\rangle$ of a symmetric rotor with free internal rotation. The quantum numbers J , K and m are the total angular momentum, its component along the molecular symmetry axis and the angular momentum of the methyl top along the symmetry axis respectively. From the discussion in §3.3, the eigenfunction $|JKm\rangle$ is the product of the symmetric rotor eigenfunction $|JK\rangle$ (eq. (3.7)) and $|Km\rangle$ (eq. (3.29)).

$$|Km\rangle = \frac{1}{2\pi} e^{i\rho K\alpha} e^{im\alpha} \quad (3.42)$$

where ρ in the asymmetric case is more complicated in the symmetric rotor case (eq. (3.22)) and is given by

$$\rho = \frac{I_{z2} \sqrt{I_y^2 - I_{yz}^2}}{I_y I_z - I_{yz}^2} \quad (3.43)$$

As explained in §3.3, the quantum mechanical tunneling breaks the degeneracy of the triply degenerate torsional energy states, which are characterized by $\sigma = 0, \pm 1$. From eq. (3.31), the eigenfunctions of H_T^0 are

$$|Kv_t\sigma\rangle = \sum_{m=3s+\sigma} a_{Kv_tm\sigma} |Km\rangle \quad (3.44)$$

Since the methyl top has no dipole moment perpendicular to its axis, its axial angular momentum cannot change in a transition. Thus, $\Delta m = 0$ for any transition, giving the selection rule $\Delta\sigma = 0$. Following Lin & Swalen (1959), Lees & Baker (1968) classify the $|Kv_t\sigma\rangle$ by the symmetry species of the C_3 group as A , E_1 or E_2 for $\sigma = 0, +1$ or -1 respectively.

Without considering the asymmetry, all the A energy levels are doubly degenerate, except for $K = 0$, and all $\pm K$ E_1 levels are degenerate with the $\mp K$ E_2 levels. For the E_1 ($\sigma = +1$) and E_2 ($\sigma = -1$) species, the K and $-K$ energy levels are widely separated by torsion. The asymmetry of the molecule produces only small shifts to these energy levels, and can be calculated by perturbation theory.

However, since the asymmetry terms of the Hamiltonian are diagonal in σ , the $\sigma = 1$, K level and the $\sigma = -1$, $-K$ level are not mixed under any high-order interaction, and hence these levels remain degenerate, as in the symmetric rotor case.

In the case of the A levels ($\sigma = 0$), the $\pm K$ torsional degeneracy is broken by the asymmetry of the molecule. This is called *K-doubling* after the similar effect seen in asymmetric rigid rotors (§3.2). Since the torsional symmetry alone is insufficient to distinguish between members of a doublet, an additional label based on the overall symmetry is required. To do this, Lees & Baker (1968) switch to a new basis set given by $(1/\sqrt{2})(|J, K, v_t, \sigma = 0\rangle \pm |J, -K, v_t, \sigma = 0\rangle)$, which are labeled as $E\pm$ and $O\pm$ for even and odd K respectively (except for $k = 0$). The $\langle K|K \pm 1\rangle$ elements of H_{Rasym}^0 mix the $E\pm$ functions with $O\mp$ functions, giving rise to $|(E+) + (O-)\rangle$ and $|(E-) + (O+)\rangle$ functions. These are labeled as $+$ and $-$ respectively by Ivash & Dennison (1953), and are used to distinguish the doublet energy levels. The selection rules for transitions between energy levels in the A species are

$$\begin{aligned} \Delta v_t &= \text{even} \\ \pm &\leftrightarrow \pm \quad |\Delta J| = 1 \quad |\Delta K| = 0, 1 \\ \pm &\leftrightarrow \mp \quad |\Delta J| = 0 \quad |\Delta K| = 0, 1 \end{aligned} \tag{3.45}$$

$$\begin{aligned} \Delta v_t &= \text{odd} \\ \pm &\leftrightarrow \pm \quad |\Delta J| = 0 \quad |\Delta K| = 0, 1 \\ \pm &\leftrightarrow \mp \quad |\Delta J| = 1 \quad |\Delta K| = 0, 1 \end{aligned} \tag{3.46}$$

It is to be noted that while the torsional energy levels are classified as E_1 and

E_2 for $\sigma = \pm 1$, both levels fall under the E symmetry species, and are indistinguishable when all allowed values (positive and negative) for the K quantum number are considered (Lees 1973). Moreover, there are two ways in which a molecule can transfer between the E_1 and E_2 energy levels. The first is through the $K = 0$ level, which is identical and thus indistinguishable for the E_1 and E_2 species (dipole selection rules allow $\Delta k = 0, \pm 1$). The second $E_1 \leftrightarrow E_2$ mode arises from the asymmetry of methanol, which mixes the $|JK\rangle$ states with the $|JK \pm 1\rangle$ and $|JK \pm 2\rangle$ states (Ivash & Dennison 1953; Lees & Baker 1968), and thus allows transitions with $|\Delta K| > 1$. Hence, Lees (1973) re-classify the E_1 and E_2 species as a single E species, with the signed quantum number k being used to specify energy levels.

Figures 3.3 and 3.4 show the low order rotational energy levels for A and E methanol respectively. Methanol was first detected in the interstellar medium by Ball et al. (1970). The first line discovered was the K -doubling line at 834 MHz towards Sagittarius (Sgr A and Sgr B2). Since then, over 700 rotational lines of methanol have been discovered in various surveys (Lovas 2004).

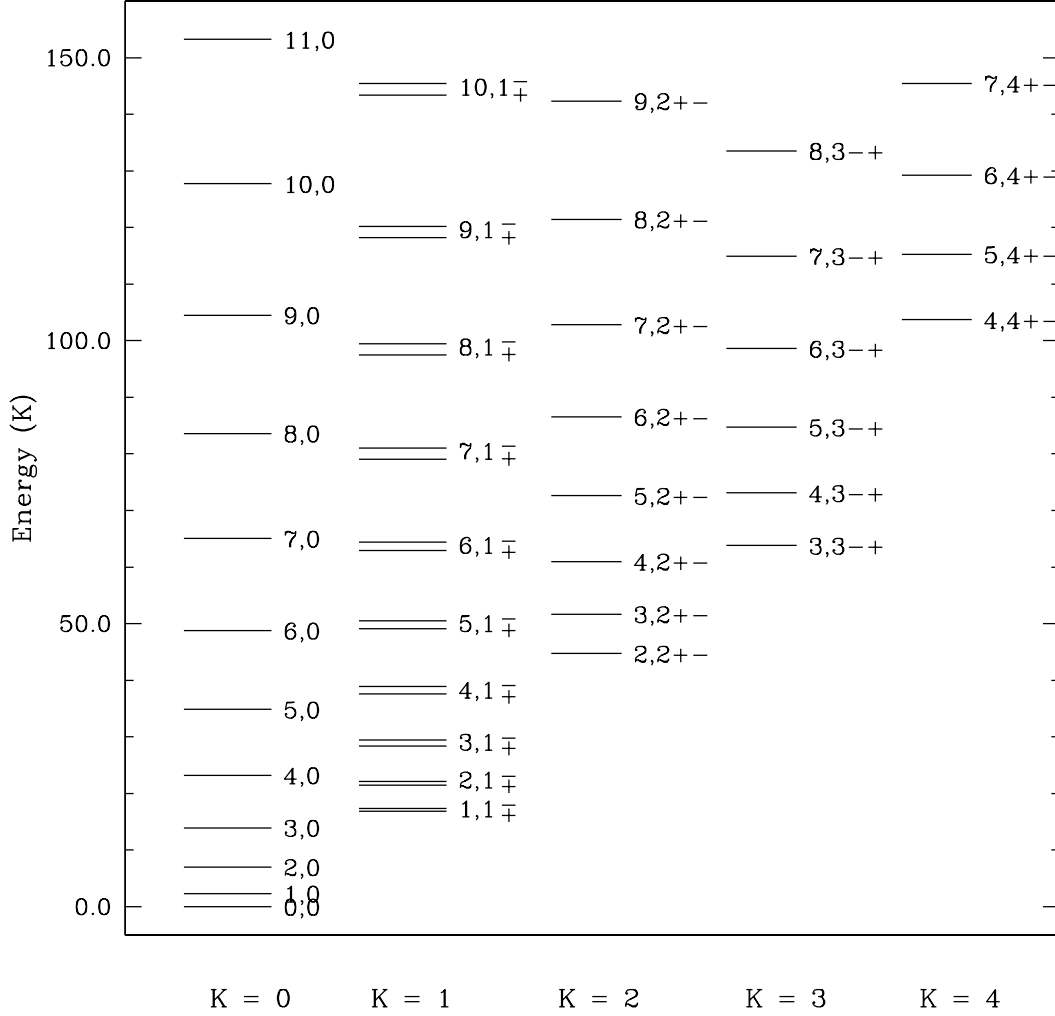


Figure 3.3 Partial energy level diagram for the *A* species of methanol. Energy levels are labeled as J, K ($v_t = 0$) followed by the $+/-$ label (where applicable). All energy levels are given with respect to the $J, K = 0, 0$ state, which is at 127.8 cm^{-1} above the bottom of the barriers of internal rotation (Pei et al. 1988). The *K*-doubling is shown only for $K = 1$, and is greatly exaggerated for illustration. For the other *K* ladders, the first label after the *K* quantum number indicates the higher energy level.

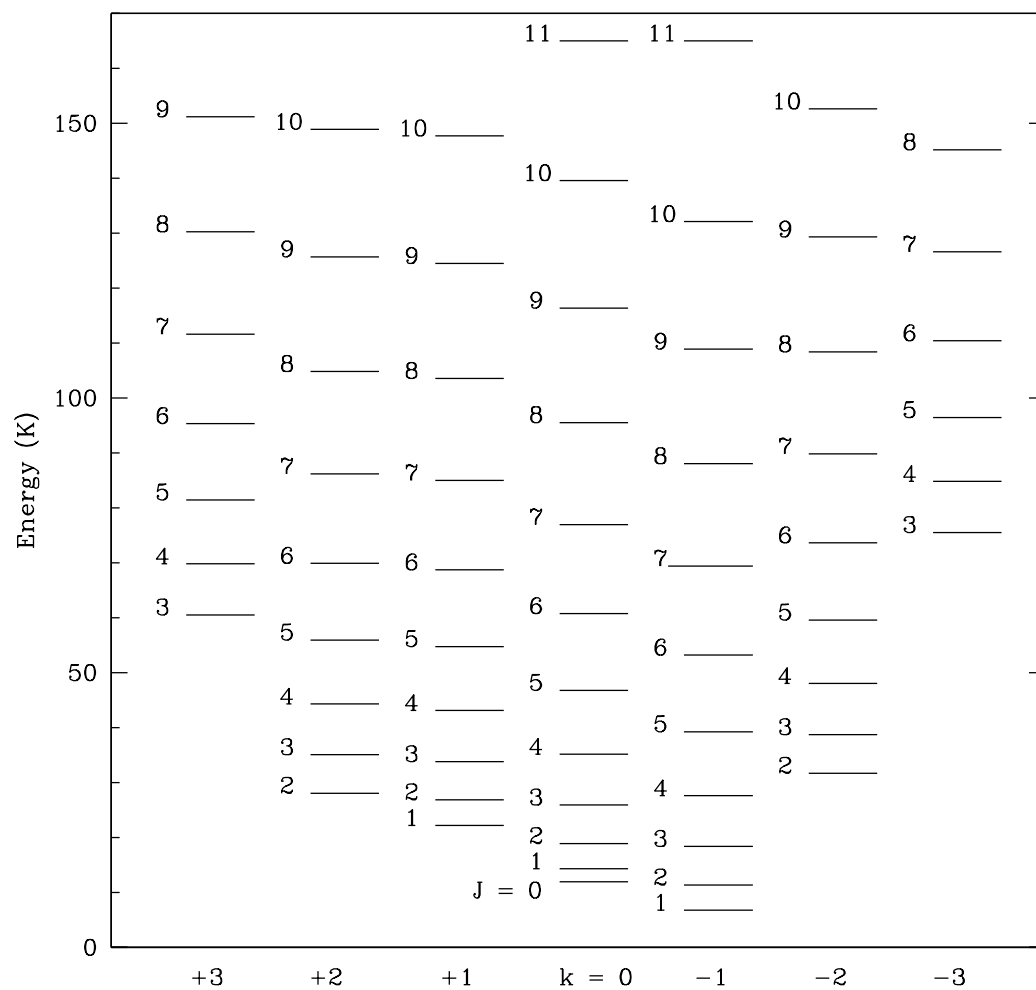


Figure 3.4 Partial energy level diagram for the E species of methanol. The energy levels for the $k = 0, \pm 1, \pm 2, \pm 3$ ladders are shown.

Chapter 4

Methanol Masers

4.1 An Overview of Methanol Masers

The richness of the methanol spectrum and the large number of lines detected in the interstellar medium make the task of organization and classification a difficult one. The maser transitions of methanol are classified into two groups: Class I and Class II.

Class I masers are found in a variety of galactic molecular clouds where they are generally separated from compact HII regions, strong IR sources and OH or H₂O masers (Menten et al. 1986b; Plambeck & Wright 1988; Bachiller et al. 1990; Plambeck & Menten 1990). Class II masers are observed towards star forming regions where they are associated with ultracompact HII regions (extremely compact HII regions around young massive stars with sizes $\lesssim 0.1$ pc and emission measures $\gtrsim 10^7$ pc cm⁻⁶) and OH/H₂O masers, but not OH/IR stars (Norris et al. 1987; Kemball et al. 1988; Koo et al. 1988; Menten et al. 1988b,a; Norris et al. 1988). Initial studies showed that Class I methanol maser sources do not emit Class II maser lines and vice versa. Further, Class I sources show enhanced absorption at frequencies of Class II transitions at 6.7 and 12.2 GHz, while Class II masers show emission at the same frequencies with absorption in Class I maser lines such as at 25 GHz (Menten et al. 1986a).

These observations were explained qualitatively through statistical equilibrium calculations of Cragg et al. (1992) based on large velocity gradients, which indicate that Class I masers result from collisional excitation followed by spontaneous radiative decay, while Class II masers appear when there is a source of continuum

radiation warmer than the gas kinetic temperature. According to this model, the temperature of the continuum radiation relative to the gas kinetic temperature is decisive in the switch from Class I to II behavior, which causes masing lines of one class to appear as absorption lines in the other. The work of Cragg et al. (1992) is limited to the case where radiative transitions to torsionally excited states are not important.

However, later studies show that Class I and Class II maser transitions are not mutually exclusive in a given region of the sky. For example, Ellingsen (2005) detected 95 GHz Class I methanol masers towards half of a sample of 6.7 GHz Class II methanol masers. Theoretical modeling of Voronkov et al. (2005) also predicts that in some conditions, the 6.7 GHz (Class II) transition can be weakly inverted simultaneously with strong inversion in the 25 GHz (Class I) transition, as observed in the Orion KL region. The analysis of Ellingsen (2005) does seem to confirm the hypothesis that while both Class I and Class II transitions can be seen in emission from a star forming region, the objects responsible for producing the Class I methanol masers are different from the ones that produce main line OH and Class II methanol masers. Additional extensive interferometer observations, and supportive theoretical modeling are required to determine the relation between Class I and Class II methanol masers. Examples of different Class I and Class II masing transitions in both E and A species are shown below in Table 4.1.

4.2 6.7 GHz Methanol Masers

The $5_1 - 6_0$ A^+ line of methanol at 6668.5192 MHz (the frequency was measured accurately by Breckenridge & Kukolich 1995), discovered by Menten (1991b) is the brightest of Class II methanol masers, and the second brightest maser transition

Table 4.1. A sample of masing transitions in methanol masers.

Class I			Class II		
Transition	ν (GHz)	Ref.	Transition	ν (GHz)	Ref.
$9_{-1} - 8_{-2} E$	9.9	a,b	$5_1 - 6_0 A^+$	6.7	k
$J_2 - J_1 E$	25	c,d	$2_0 - 3_{-1} E$	12.2	l
$4_0 - 3_1 E$	28.3	e	$2_1 - 3_0 E$	19.9	m
$4_{-1} - 3_0 E$	36.2	f	$9_2 - 10_1 A^+$	23.1	n
$7_0 - 6_1 A^+$	44.1	g	$7_{-2} - 8_{-1} E$	37.7	o
$5_{-1} - 4_0 E$	84.5	h,i	$6_2 - 5_3 A^-$	38.3	o
$8_0 - 7_1 A^+$	95.2	j	$6_2 - 5_3 A^+$	38.5	o
$9_0 - 8_1 A^+$	146.6	a	$3_1 - 4_0 A^+$	107.0	p

Note. — The references listed above (which do not necessarily refer to the discovery of the transition) are: (a) Menten (1991a) (b) Slysh et al. (1993) (c) Barrett et al. (1971) (d) Menten et al. (1988b) (e) Slysh et al. (1992) (f) Haschick & Baan (1989) (g) Haschick et al. (1990) (h) Nagai et al. (1979) (i) Batrla & Menten (1988) (j) Plambeck & Wright (1988) (k) Menten (1991b) (l) Batrla et al. (1987) (m) Wilson et al. (1985) (n) Wilson et al. (1984) (o) Haschick et al. (1989) (p) Val'tts et al. (1995)

ever observed. For instance, the brightness temperature of several maser spots in a prototypical source W3(OH) is 3×10^{12} K and greater (Menten et al. 1992). These masers are almost always found in regions of recent massive star formation. The 6.7 GHz masers are often accompanied by the 12.178597 GHz $2_0 - 3_{-1}$ E line, which is the second strongest Class II methanol maser, and the main line OH maser.

4.2.1 Pumping of 6.7 and 12.2 GHz Methanol Masers

The population inversion for both 6.7 and 12.2 GHz lines is caused by radiative processes. Radiative transfer calculations of Zeng (1992); Cragg et al. (1992); Peng & Whiteoak (1993) show that Class II methanol masers appear when the brightness temperature of external radiation is greater than the kinetic temperature in the source.

Sobolev & Deguchi (1994) use radiative transfer in the large velocity gradient (LVG) approximation to model the high intensities of the 12.2 GHz masers by including methanol levels to the second torsionally excited state. As all masers are strongly beamed (section 2.3), a beaming factor characterized by $\epsilon^{-1} = d \ln v / d \ln r$ is introduced by the authors in their models. The kinetic temperature of the gas is assumed to be 20–50 K, while exciting radiation is produced by a layer of warm dust at 100–200 K. Such a layer is an attribute of models of cometary ultracompact HII regions, and can be heated by a shock wave (created by highly supersonic motion of the massive star through the parent molecular cloud) or by emission of the central star (Mac Low et al. 1991; Churchwell et al. 1990; Wilson et al. 1991). The geometrical dilution factor of dust emission is assumed to be 0.5.

Based on the models above, Sobolev & Deguchi (1994) are able to conclude the

general characteristics of strong ($T_b > 10^{10}$ K) 12.2 GHz masers as follows:

- The hydrogen number densities should exceed $3 \times 10^6 \text{ cm}^{-3}$.
- Methanol abundance (relative to H_2) must exceed 7×10^{-7} , which is high as typical the abundance of methanol in star forming regions is between 10^{-10} and 10^{-7} (Kalenskii et al. 1997). However, the high abundances are found to be consistent with observations of masing regions.
- The kinetic temperature should be less than 50 K.
- The masers should be beamed with beaming factor $\epsilon^{-1} > 3$.

They further find that the second torsionally excited state plays a crucial role in the pump cycle and that collisions act as a cooling agent in the pump.

As mentioned before, 6.7 GHz masers usually accompany 12.2 GHz masers and the brightness temperature of the 6.7 GHz line is usually stronger than the 12.2 GHz line. The fact that the two masers occur simultaneously is curious as they result from two different species of methanol. Sobolev et al. (1997) apply the model described above for the *A* species of methanol and find that torsional pumping can account for the simultaneous occurrence of 6.7 and 12.2 GHz masers. Further they find that

- Sources where the 6.7 GHz line is stronger than the 12.2 GHz line by a factor of more than 10 define a narrow column density regime where the 6.7 GHz maser turns on first and where possibly the abundance of the *A* species is enhanced following evaporation of cold methanol from grains.
- Typical maser sources, where the ratio of intensities of 6.7 and 12.2 GHz lines is about 3.2 are likely to be greatly influenced by effects of saturation.

- In sources where the 12.2 GHz line is stronger than the 6.7 GHz line, the maser geometry involved less beaming and hydrogen density greater than 10^7 cm^{-3} . The 6.7 GHz masers are collisionally quenched for hydrogen densities greater than $\sim 10^8 \text{ cm}^{-3}$.

However, better collision rate coefficients, and the inclusion of additional energy levels (up to $v_t = 3$, $J = 18$) by Cragg et al. (2005) show that quenching does not occur until higher densities $n \gtrsim 10^9 \text{ cm}^{-3}$. At gas temperatures greater than 100 K, the better collision rate coefficients are equivalent to reducing the collisional cross section, and thus are equivalent to models of Sobolev et al. (1997) at lower densities. Since the other features of the new models match well with that of the old models, there is reasonable confidence that the theory behind the 6.7 GHz maser pump is well understood.

4.3 6.7 GHz Methanol Masers and Massive Star Formation

The physical conditions required for pumping 6.7 GHz methanol masers are commonly found in high-mass star forming regions. The UV radiation from a massive young stellar object (MYSO) can heat dust grains around it giving rise to the far-infrared radiation required for radiatively exciting methanol. The dust temperatures must exceed 125 K to produce maser emission with brightness temperatures exceeding 10^{10} K. The high methanol abundance can be realized through shock heating of dust grains, or sputtering through grain-grain collisions. Thus, from theoretical modeling, one would expect 6.7 GHz methanol masers to be associated with massive star formation.

The association between massive star formation and 6.7 GHz methanol masers was bolstered by the discovery of a number of methanol masers in surveys targeted

towards ultracompact HII regions (selected through their IRAS colors) and OH masers (Menten 1991b; MacLeod & Gaylard 1992; MacLeod et al. 1992; Gaylard & MacLeod 1993; Schutte et al. 1993; Caswell et al. 1995; van der Walt et al. 1995, 1996; Walsh et al. 1997; Slysh et al. 1999; Szymczak et al. 2000). Synthesis images of 6.7 GHz methanol masers obtained by Norris et al. (1993) showed masing spots distributed along lines or arcs, with some sources displaying clear velocity gradients along the line. This was suggested to arise from methanol masers being located in edge-on disks around the young massive stars. One of the predictions of this model is that the masers should be approximately coincident with the peak of the continuum emission from the central object.

However, a number of studies have shown that a significant fraction of methanol masers do not have associated radio continuum (Ellingsen et al. 1996a; Caswell 1996, 1997; Phillips et al. 1998). An upper limit of ~ 0.5 mJy beam $^{-1}$ was established in the survey of Phillips et al. (1998). The lack of radio continuum could be due to two reasons: (1) The methanol maser might be associated with an earlier phase of massive star formation. This would imply that a HII region either does not exist due to rapid accretion, or is too compact and optically thick to have measurable radio continuum at centimeter wavelengths (e.g. hypercompact HII regions have sizes $\lesssim 0.03$ pc and emission measures $\gtrsim 10^{10}$ pc cm $^{-6}$, which makes the free-free emission optically thick at millimeter wavelengths). (2) The methanol masers might be associated with lower mass stars whose UV flux might be too small to create a HII region. The latter explanation was favored by Phillips et al. (1998) who concluded from the detection statistics of their survey that the masers might be associated with stars down to spectral type B5.

Walsh et al. (2003) mapped the submillimeter wave continuum at 450 μ m and

850 μm towards 84 methanol masers. They found that 81 out of 84 masers were within $10''$ of a submillimeter peak. All but one of the maser sites exhibit submillimeter continuum emission from dust. This confirms that the methanol maser emission arises from deeply embedded objects. Bolometric luminosities were derived for sources for which distance estimates were available. The luminosity estimates were between $5 \times 10^3 L_{\odot}$ and $10^5 L_{\odot}$ indicating that the objects are associated with massive star formation. The results of Walsh et al. (2003) made it unlikely that 6.7 GHz methanol masers are associated with low to intermediate mass young stellar objects (YSOs) as hypothesized by Phillips et al. (1998).

The question of whether 6.7 GHz methanol masers are associated with stars that do not produce HII regions can be addressed through a search targeted towards low and intermediate mass YSOs in various stages of evolution. Minier et al. (2003) carried out a search for methanol masers towards 13 class 0 protostars, 44 class I young stellar objects, 3 protoplanetary disks (proplyds), and 65 (pre)protostellar condensations. In addition, 34 class II, 7 class III and 8 unclassified YSOs were observed serendipitously as they happened to lie in the field of view as the observations. Methanol maser emission was detected towards only one source, NGC 2024:FIR4, which was argued to be a massive young stellar object. An upper limit of 3×10^6 K was derived for the brightness temperature of any methanol maser associated with the low and intermediate mass YSOs. This argues firmly for 6.7 GHz methanol masers being associated only with massive star formation.

Thus, the lack of radio continuum associated with 6.7 GHz methanol masers points towards the masers being associated with phases of massive star formation preceding ultracompact HII regions. This is bolstered by high-resolution observa-

tions (e.g. van der Walt et al. 2003) which show that the maser emission is often offset from the location of the radio continuum (when it is detected). A study of the large scale (0.5–5 pc) environment around five radio quiet methanol masers was undertaken by Minier et al. (2005). Multi-wavelength continuum and spectral line observations were used to derive the mass, density and temperature of gas, luminosity, virial mass and dust temperature. The derived parameters ($L_{\text{tot}} > 10^4 L_{\odot}$, $M_{\text{gas}} \sim 100 - 1000 M_{\odot}$, $n_{H_2} = 10^4 - 10^5 \text{ cm}^{-3}$, extinction $A_V \sim 40 - 240 \text{ mag}$) are consistent with young deeply embedded clusters of MYSOs. Thus, 6.7 GHz methanol masers seem to originate in the environment of massive star formation although the direct association of masers with MYSOs is not yet established.

As indicated previously, linear distributions of masing spots with a velocity gradients along the line, discovered in high-resolution studies of methanol masers, were interpreted to trace circumstellar disks around the MYSOs by Norris et al. (1993). However, the mass enclosed within the disk was estimated by Minier et al. (2000) to be sub-solar for all the ten sources in their catalog that are consistent with the disk model. Further, the discovery of linear distribution of masing spots by De Buizer et al. (2005) in 38% of the water masers and 50% of OH masers showed that methanol masers are not special in this regard. Mid-infrared observations (e.g. De Buizer 2003; De Buizer & Minier 2005) show that in many cases, the linear methanol maser distribution is parallel to an outflow, which is not consistent with the disk hypothesis. These observations favor masing spots to occur along edges of outflows, rather than in circumstellar disks. Another model that can explain linear morphologies of methanol masers is where the masers arise in planar shocks that propagate nearly perpendicular to the line of sight through a dense molecular clump or a star forming core (Dodson et al. 2004). Thus, while some methanol

masers may indeed arise in circumstellar disks, there is evidence that they are more likely to be related to outflows and shock fronts around MYSOs.

To conclude, there is substantial evidence that 6.7 GHz methanol masers are associated with an early phase of massive star formation preceding the creation of an ultracompact HII region. The exact relation between a MYSO and methanol masers is however not established yet. The location of individual masing spots in the massive star forming complex is also not clear. High resolution multi-wavelength observations are required to understand the link between massive star formation and 6.7 GHz methanol maser emission.

Chapter 5

The 6–8 GHz C-Band High receiver at Arecibo

5.1 Introduction*

The science of radio astronomy involves detection of radio waves from astronomical objects in space. Astronomical objects emit radio waves by a variety of processes including thermal radiation from gas and dust in the interstellar medium, synchrotron emission from relativistic electrons spiraling around magnetic fields, free-free emission from electrons in ionized regions, and spectral line radiation from atomic and molecular transitions. Since the sources that radio astronomers observe are generally very distant, the intensity of radio waves from them is extremely low. This is compounded by the fact that the bandwidth of spectral lines is very small. For example, a cloud of atomic hydrogen with internal motions of 5 km/s emits only over a bandwidth of 25 kHz. A source at temperature T produces a maximum signal power $P = kTB$, where k is Boltzmann's constant (1.38×10^{-16} erg s⁻¹ K⁻¹ Hz⁻¹), and B is the bandwidth used to detect the signal. For a relatively warm interstellar cloud at 100 K, the signal power is no greater than 3.5×10^{-10} erg s⁻¹, a very weak signal indeed! Some signals are non-thermal, and can be stronger than this, but astronomers typically make maps of the radio sky, which requires point-

*This chapter is based on the accepted paper: Pandian et al. 2006 [Pandian, J. D., Baker, L., Cortes, G., Goldsmith, P. F., Deshpande, A. A., Ganesan, R., Hagen, J., Locke, L., Wadefalk, N., & Weinreb, S. 2006, IEEE Microwave Magazine, accepted; © 2006. IEEE. All rights reserved.] The paper is reproduced here with minor changes based on rights retained by the author along with additional sections to explain the design of the receiver.

ing the antenna successively in different directions. To cover a significant area of the sky with a small antenna beam width, thousands to many millions of separate pointings and integrations are needed. As a result, the time that can be spent analyzing the signal from any one direction is limited. A very sensitive system to detect and analyze radio astronomical signals is thus extremely desirable.

All radio telescope systems have three basic components: an antenna to collect the incident radiation, a receiver to detect this radiation, and a backend system which analyzes the signals. The functioning of the backend system depends on what type of signal is being observed – it may simply measure the total power in a broadband or continuum signal, or it may split the signal into several relatively narrow bands and measure the power in each, thereby producing a spectrum of the incident radiation. The most familiar type of radio telescope comprises of a parabolic dish that focuses radiation into the receiver with or without the aid of a secondary reflector. Dual reflector radio antenna systems can be of the Cassegrain or Gregorian type, similar to their counterparts at optical wavelengths. The overall sensitivity of the system is controlled primarily by the size and the efficiency of the antenna, and the sensitivity of the receiver.

The 305-m Arecibo telescope is the largest single dish radio telescope in the world (Figure 5.1). The projected area of the complete surface is just over 73,000 m², which is more than that of 17 football fields. Unlike most radio telescopes, the primary reflector at Arecibo is spherical rather than parabolic. Since a sphere focuses radiation into a line rather than a point, line feeds were used to detect the radiation from its initial operation in the early 1960's, until the late 1990's. A line feed is a very specialized traveling wave antenna, which combines the radiation collected by various portions of the spherical primary reflector with the proper

phase delays, thus correcting the substantial spherical aberration of the reflector (Figure 5.2). The value of the phase correcting characteristic of a line feeds is offset in part by their very narrow bandwidths (< 50 MHz) and lack of any tunability. Over the course of three decades, only a handful of line feeds were constructed, covering narrow portions of the frequency range extending to 2.4 GHz.



Figure 5.1 Aerial view of the Arecibo radio telescope after the Gregorian system was commissioned in 1997. The Gregorian dome and the line feed still used for 430 MHz move in elevation on the feed arm, the lower part of which is a curved track moving near the paraxial surface. The feed arm also rotates in azimuth. The moving parts are held by a triangular structure, which is itself suspended on steel cables running from three towers surrounding the primary reflector. The inward force of these cables on the towers is balanced by backstay cables extending radially from each of the towers.

The Arecibo telescope had a major upgrade in the mid 1990s (Goldsmith 1996). The major part of this project consisted of installing a pair of aspheric reflectors near the paraxial surface, where radiation from the primary is most tightly focused. These two reflectors were designed to compensate for the phase errors in the spherical primary reflector, but since they are reflective, the phase correction



Figure 5.2 A schematic showing the optics for the line feed and Gregorian systems at the Arecibo radio telescope. The line feed system collects radiation focused by the spherical primary, while the Gregorian system uses two additional reflectors to focus radiation to a point where the feed horn of the receiver is located.

is essentially independent of frequency. Thus, with the so-called Gregorian system, the Arecibo telescope focuses radiation essentially perfectly at frequencies as high as 10 GHz, and with bandwidths up to several GHz. This has resulted in a dramatic increase in the range of astronomical observations that can be carried out, and also has significantly improved the system's sensitivity due to better illumination of the primary reflector. As shown in Figure 5.2, the two Gregorian reflectors are enclosed by a protective dome. The radio signals enter through the circular aperture at the left hand bottom of the dome, and follow the paths indicated by the red lines, reflecting from the secondary, then the tertiary. With the Gregorian system, the Arecibo telescope focuses radiation to a point (as indicated in the Figure) or more accurately to a "spot" where it is collected by a fairly typical feed horn, which in this case is oriented downwards.

Thus, for the Arecibo Gregorian receivers, as for almost all radio astronomical

systems, the first component is the feed horn. The feed horn converts the incident free space TEM radiation into a waveguide TE or TM mode. In this sense, the angular width of the receiving power pattern of the feed horn must match the angular size of the cone of radiation coming from the antenna. Taking advantage of the reciprocity principle, we can also think of replacing the receiver by a transmitter, and thus the feed horn radiates a signal with an angular transmitting power pattern, which is the same as the receiving power pattern. This pattern of the feed horn determines the efficiency with which the antenna operates; in particular the aperture efficiency and antenna gain (relevant for point sources) and the main beam efficiency (relevant for extended sources). The feed horn also needs to have a very low reflection coefficient so that most of the signal is transmitted to the receiver. The output waveguide from the feed horn typically propagates both polarizations of the incoming signal.

Since most signals from space are unpolarized, or if partially polarized have a random polarization angle, a simple conversion of the electromagnetic signal from space into a guided wave in a single mode waveguide will result in the loss of approximately half the signal. To attain full efficiency as well as to measure the polarization state of the incident signal, it is necessary to have a device that separates the two orthogonal polarizations before they are each channeled into a single mode waveguide. This task is accomplished by the ortho-mode transducer (OMT). The OMT needs to have a return loss of 15 dB or better over the entire band of interest, in addition to having a low insertion loss. In order to carry out good polarimetry, the cross polarization introduced by the OMT should be less than that induced by the feed horn. The OMT is typically the most challenging part of a dual polarization broadband receiver design.

The outputs from the OMT are amplified using low noise amplifiers. The low noise amplifier and the stage following it are the primary contributors to the receiver noise temperature, since noise from successive components of the receiver are suppressed by the gain of the amplifier. To achieve very low noise, the amplifier and the OMT are typically cooled to temperatures which can be as low as 2 to 15 K. This requires the receiver components to be placed in an evacuated dewar. Moreover, since most designs keep the feed horn at room temperature (due to its relatively large size), there needs to be a device that thermally isolates the feed horn from the OMT while maintaining continuity for the RF signal. This device is called a thermal break, and typically uses choke grooves to minimize signal reflections.

The upgrade of the Arecibo telescope allowed operations up to a frequency of 10 GHz. Before 2004, the telescope had receivers for all frequencies between 1.1 and 10 GHz except for the 6 to 8 GHz frequency range of C-Band (4 to 8 GHz). The band includes the 6.668 GHz spectral line of methanol which emits stimulated radiation with very high brightness temperature ($> 10^{10}$ K) under conditions found around sites of massive star formation. Hitherto, all 6.7 GHz methanol maser studies have been carried out using Australian and European telescopes.

This paper reports on the 6 to 8 GHz receiver that was installed on the telescope in early 2004. With the installation of this instrument, Arecibo has continuous frequency coverage between 1.1 and 10 GHz. The following sections discuss the receiver design and present the measured performance in detail.

5.2 The Ortho-Mode Transducer

We adopted a finline design for the OMT from the work of Chattopadhyay & Carlstrom (1999) (Figure 5.3). A finline OMT consists of a thin metallic fin that is set inside a square or circular waveguide. The polarization mode which has electric field parallel to the fin is converted from a waveguide mode into a finline mode whose energy is confined to the space between the fin. This energy can then be brought out by curving the fin, and bringing it out of the wall of the waveguide, after which it is converted back into a waveguide mode by a gradual outward taper. The orthogonal polarization has electric field perpendicular to the fin and passes unperturbed if the fin is sufficiently thin. A resistive card suppresses any unwanted modes at the termination of the fin.

The design of Chattopadhyay & Carlstrom involved the removal of the finline mode through a 45° bend, which was found to give better cross polarization and isolation performance compared to a 90° bend. We took their prototype design for X-Band and scaled it to our band with some modifications. We replaced the multiple transitions between the finline and the normal waveguide after the bend with a single longer transition, as a traveling wave device is likely to give a better performance with a longer transition. Using the same reasoning, we also lengthened the initial transition in the finline from square waveguide to the narrow gap.

The rectangular waveguide used for 6 to 8 GHz is WR137 which has dimensions of 3.48 cm (1.372 inches) by 1.58 cm (0.622 inches). Hence, the square waveguide input for the OMT has an interior dimension of 3.48 cm (1.372 inches). This is tapered to 0.038 cm (0.015 inches) in the finline through two circular arcs over a length of 27.13 cm (10.68 inches). Following the 45° bend, the narrow gap is expanded to the standard dimension of 1.58 cm (0.622 inches) over a length of

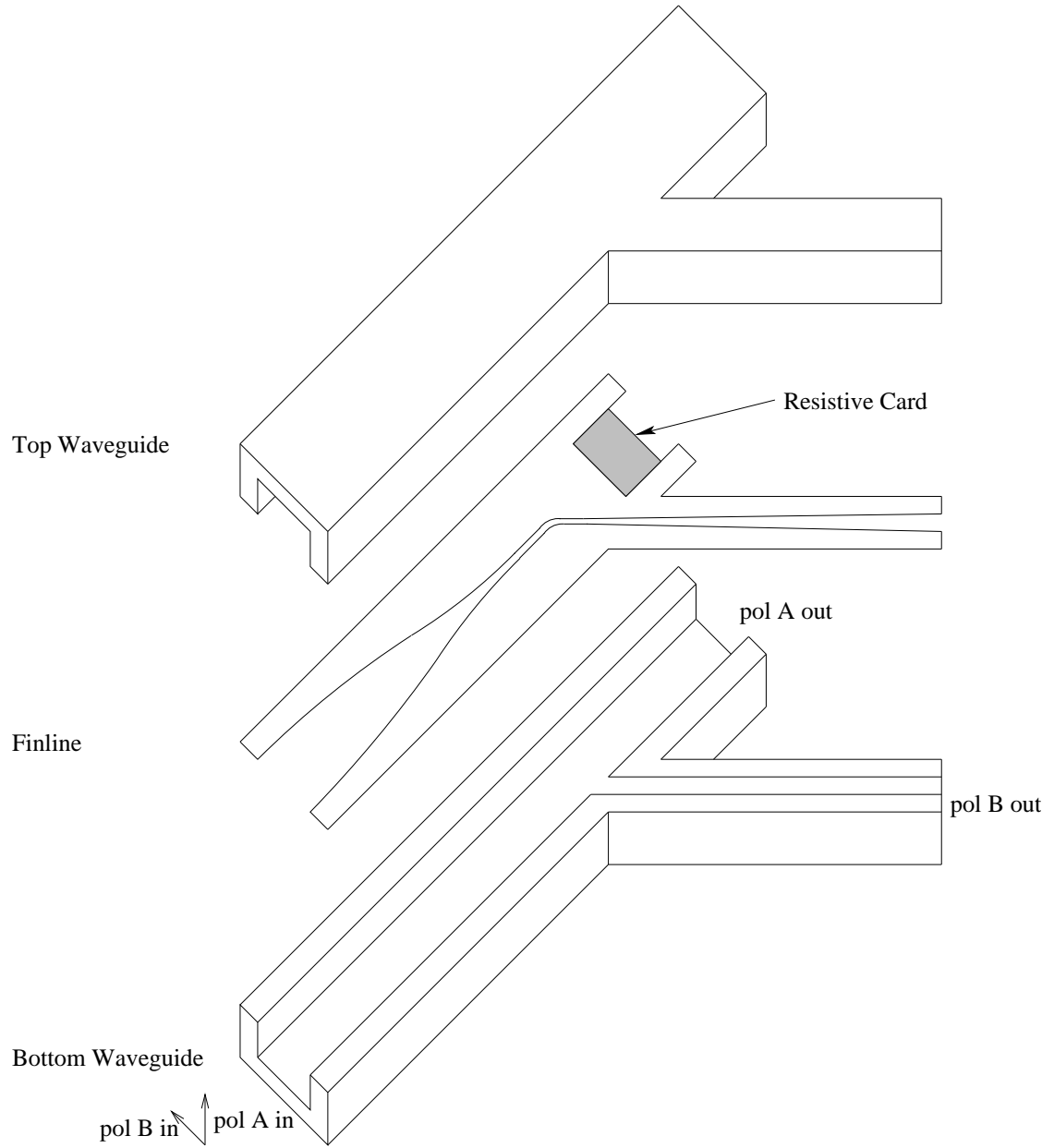


Figure 5.3 A schematic of the finline ortho-mode transducer (OMT) used to separate incoming fields into two orthogonal polarization components.

20.32 cm (8.0 inches). The fin is made out of a 0.13 cm (0.05 inch) thick aluminum sheet.

Figures 5.4 to 5.7 show the measured performance (at room temperature) of the OMT fabricated from the design above. The measurements were taken with

one port being terminated by a tapered ferrite rod, and the other two ports being connected to the network analyzer. The return loss conformed to our design goal save for a small portion in the band edge near 6 GHz. The isolation (coupling between the two output ports when the input is terminated) was 50 dB or better over the entire band, and the cross polarization isolation was better than 25 dB throughout. The insertion loss is primarily ohmic, and its contribution to the noise temperature would drop significantly when the device is cooled from room temperature to around 15 K.

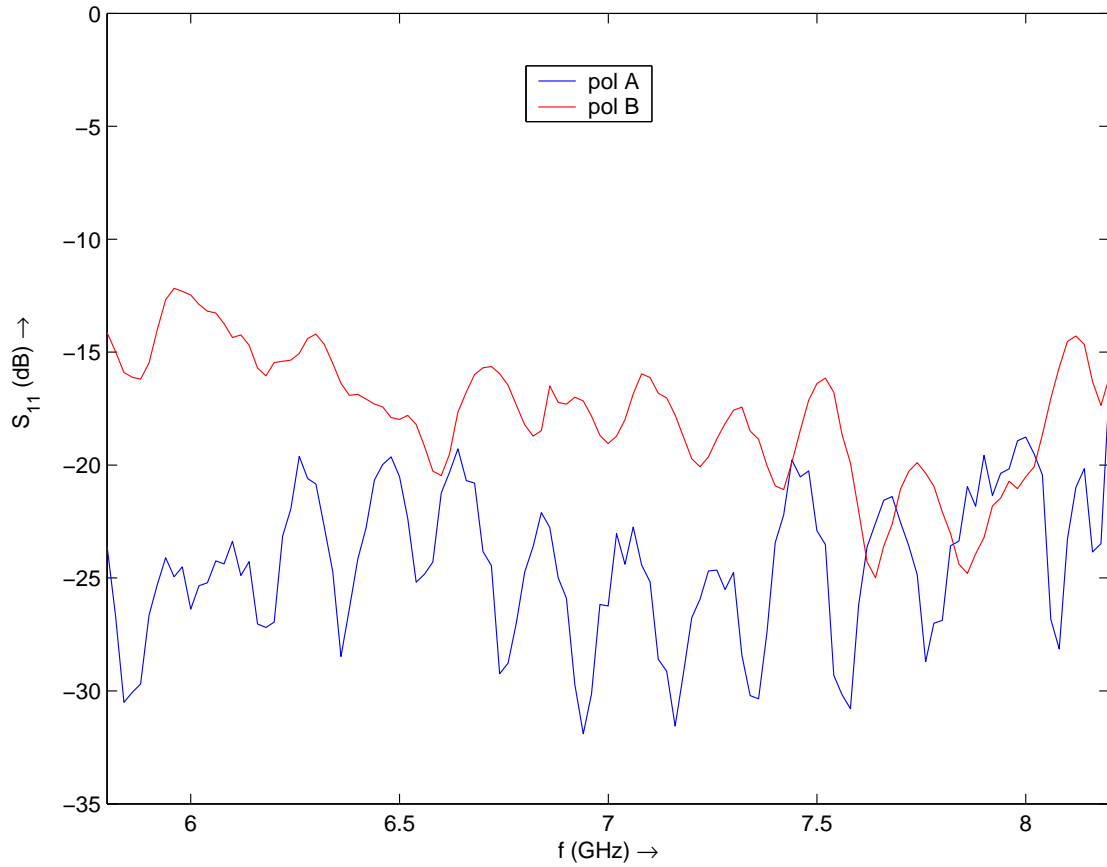


Figure 5.4 Measured return loss of the OMT. The blue curve is for polarization A which passes straight through, and the red curve is for polarization B which passes through the finline

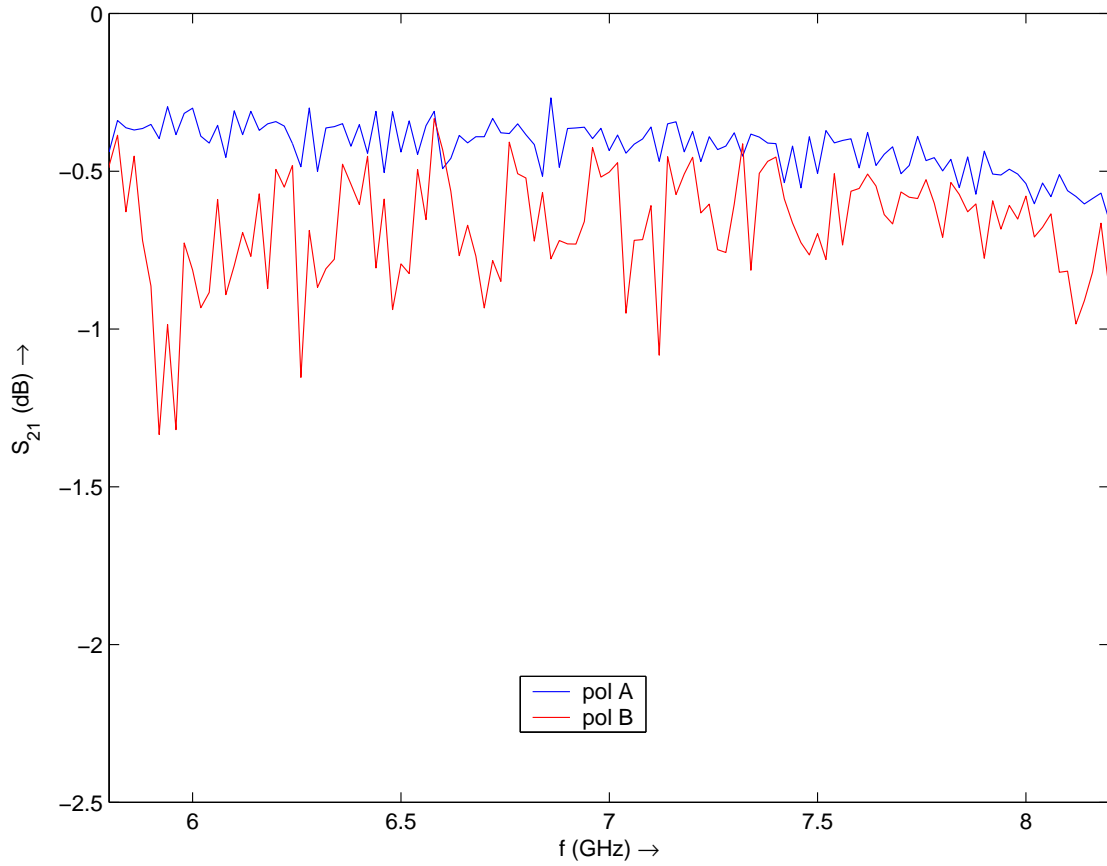


Figure 5.5 Measured insertion loss of the OMT. The blue curve is for polarization A which passes straight through, and the red curve is for polarization B which passes through the finline

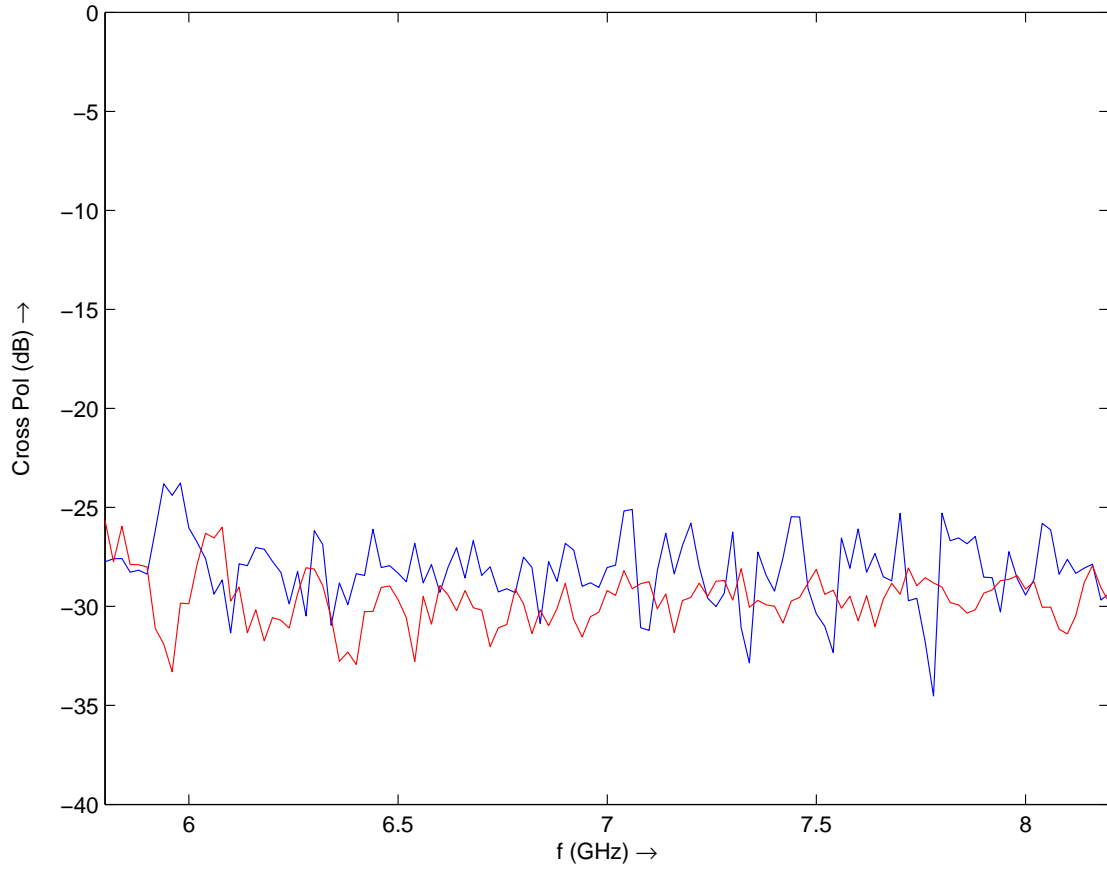


Figure 5.6 Measured cross-polarization isolation of the OMT. The blue line is for input polarization A when the output is measured at pol B, and the red curve is for polarization B input polarization when the output is measured at pol A. The third port is terminated appropriately during these measurements

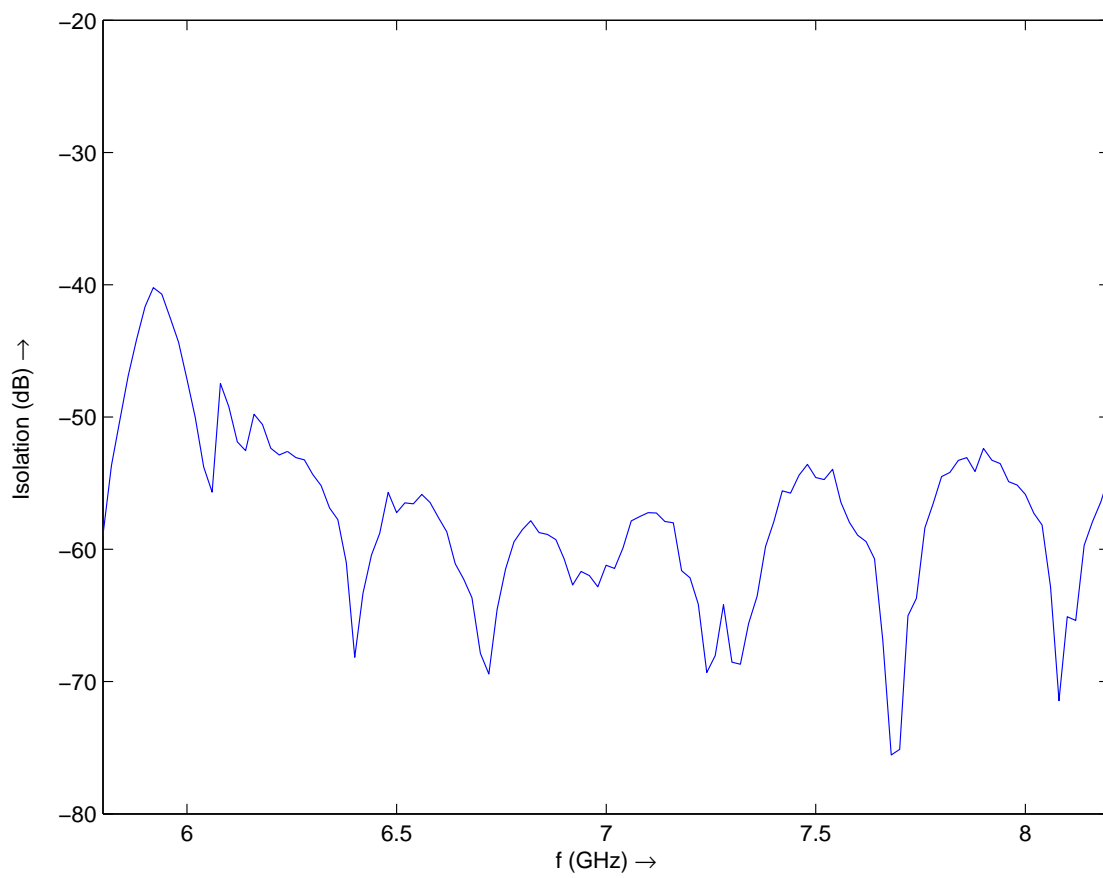


Figure 5.7 Measured isolation between the two output ports of the OMT.

5.3 The Feed Horn

The 6 to 8 GHz feed horn used in the receiver is a wide flare angle corrugated horn (Clarricoats & Oliver 1984). For the present design, we chose a 78° flare angle that provides an edge taper level of -15 dB at the edge of the tertiary Gregorian reflector (approximately 60° off axis) in the middle of the frequency band. In addition, we decided to have the corrugations running parallel to the horn axis for fabrication purposes.

The designed horn has an aperture diameter of 21.6 cm (8.5 in), and a circular waveguide input diameter of 4.95 cm (1.95 in). The horn design was verified using Ansoft HFSS and CST Microwave Studio. Figure 5.8 shows the calculated E_{VERT} field projected on a cross section of the corrugated horn at 7 GHz; notice the profile of the corrugations. The calculated input reflection coefficient (Figure 5.9) is better than 26 dB across the band.

We fabricated two horns (I and II) since the receiver will be upgraded to a dual beam receiver sometime in the near future. Only Horn-I has been installed in the receiver to date. We measured the radiation patterns of both horns with cuts at the E and H planes, and at 45° for θ between -90° and $+90^\circ$, with linear polarization excitation. A comparison of the measured data of Horn-I with the calculated field patterns is presented in Figures 5.10 to 5.12. In each, we show two Co-polar pattern cuts at 0° and 90° , and a Cross-polar pattern cut at 45° . We find a good correlation between calculated (continuous lines) and measured data (dots). The measured cross-polarization levels are below -24 dB except at 8 GHz, where they are -20 dB. The somewhat high peak values of the cross-polarization are acceptable for the Arecibo radio telescope since the Gregorian optics stretches the inner $\pm 30^\circ$ of the feed illumination to almost 90% of the aperture resulting in

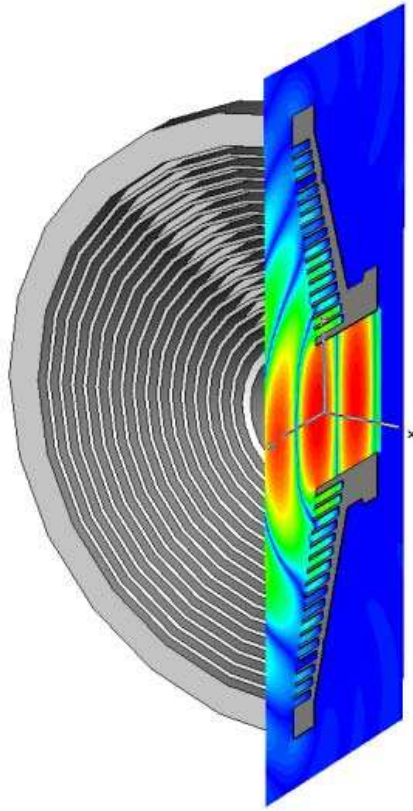


Figure 5.8 Calculated E_{VERT} projected on a cross section of the corrugated horn at 7 GHz

very low cross-polarization values over the antenna aperture to the order of -28 dB (see Table 5.1).

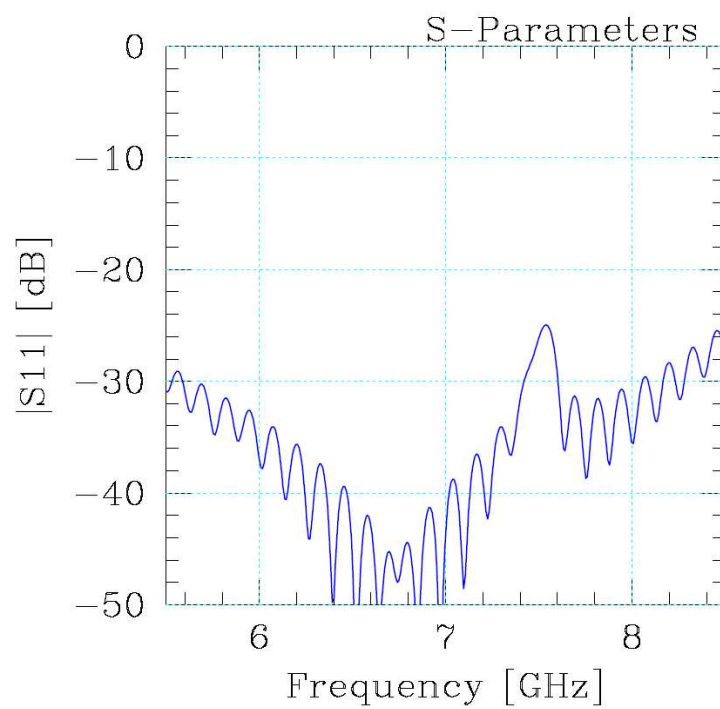


Figure 5.9 Calculated horn input reflection coefficient as a function of frequency

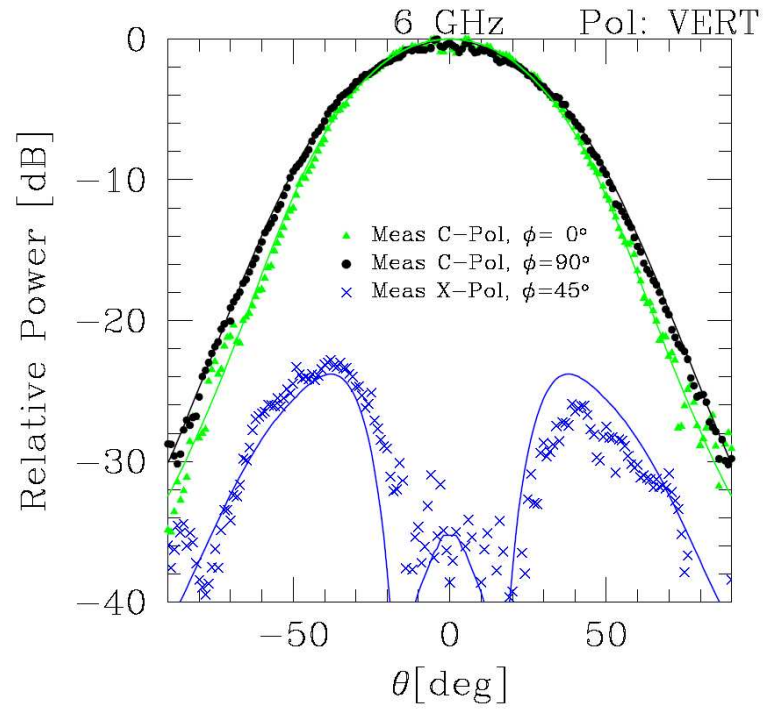


Figure 5.10 Calculated (continuous lines) and measured (dots) Co-polar radiation patterns cuts at 0° , 90° and Cross-polar at 45° (Horn-I at 6 GHz)

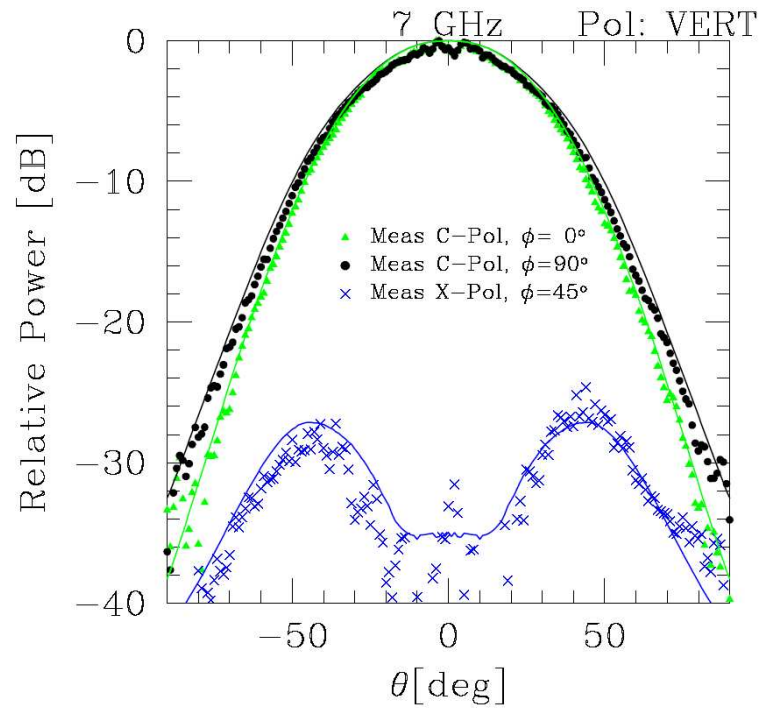


Figure 5.11 Calculated (continuous lines) and measured (dots) Co-polar radiation patterns cuts at 0° , 90° and Cross-polar at 45° (Horn-I at 7 GHz)

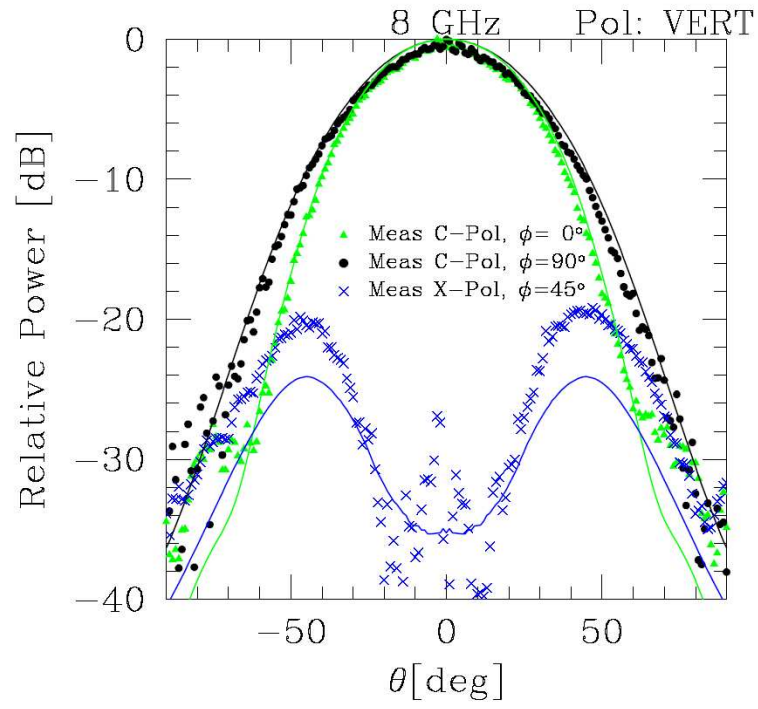


Figure 5.12 Calculated (continuous lines) and measured (dots) Co-polar radiation patterns cuts at 0° , 90° and Cross-polar at 45° (Horn-I at 8 GHz)

At 8 GHz (Figure 5.12), there is a decrease in the feed pattern edge taper at 60° due to an oversized OMT circular waveguide diameter. As a result, the antenna aperture illumination (η_{Illum}) decreases, reducing the overall effective aperture efficiency (η_{Aperture}) of the Arecibo radio telescope as shown in Table 5.1.

Table 5.1 Calculated overall Antenna Parameters at the input flange of the Arecibo radio telescope's feed horn: η_{Aperture} is the effective collecting area of the telescope divided by the illuminated area ($3.98 \times 10^4 \text{ m}^2$); η_{Illum} is the reduction in efficiency due to non-uniform illumination of the antenna; η_{Beam} is the fraction of total radiated power within -10 dB level of peak of power pattern; X-pol is the cross-polarization level in the antenna far field; T_A is the antenna temperature referred to the feed horn flange, and includes contributions from the cosmic microwave background (2.73 K), emission from the atmosphere, and also radiation from the dome and spillover radiation from the ground. Note that efficiency reduction due to surface errors is not included.

Frequency	η_{Aperture}	η_{Illum}	η_{Beam}	X-Pol	T_A
GHz	%	%	%	dB	K
6.0	82.2	93.6	80.2	-28.0	14.2
7.0	81.7	93.6	81.3	-29.0	13.0
8.0	78.5	90.1	81.8	-26.0	11.8

In order to analyze the antenna performance with this feed horn, we obtained a spherical wave expansion of the calculated full radiation pattern of the feed horn ($-180^\circ < \theta < +180^\circ$), and used an electromagnetic ray-tracing technique to obtain the fields at the Arecibo aperture and in the far field. From these, we calculated the antenna parameters from 6 to 8 GHz, some of which are presented in Table 5.1, which includes the aperture efficiency, η_{Aperture} (effective collecting area of the telescope divided by the illuminated area which is $3.98 \times 10^4 \text{ m}^2$), aperture illumination efficiency, η_{Illum} (reduction in efficiency due to non-uniform illumination

of the antenna), 10 dB beam efficiency, η_{Beam} (fraction of total radiated power within -10 dB of peak of power pattern), cross-polarization level in the antenna far field, X-Pol, and the antenna temperature, T_A (includes contributions from the 2.73 K cosmic microwave background radiation, emission from the atmosphere, and radiation from the dome and spillover radiation from the ground). All these values are calculated at the feed horn input flange. Reduction of efficiency due to surface errors is not included.

The calculated values of aperture efficiency include blockage losses, aperture phase efficiencies, and spillover efficiencies not shown individually in the table. Table 5.1 shows the decrease in aperture efficiency at 8 GHz due to the reduced illumination efficiency. The calculated cross-polarization values in the antenna far field are below -26 dB. The antenna noise temperature values decrease as a function of frequency due to the reduction of the size of the feed beam.

5.4 The Thermal Break

The feed horn and the dewar window are kept at room temperature (300 K) while the rest of the signal path starting with the OMT are cooled to 15 K. Hence, there needs to be a device that thermally isolates the 300 K stage from the 15 K stage. This is achieved using a thermal break. A thermal break comprises two waveguides that are separated from each other by a very small gap. A choke groove device is placed at the gap so that the impedance as seen at the wall of the waveguide is close to zero across most of the band. The design of this choke groove is described below.

The basic schematic of the choke groove is shown in Figure 5.13. The parameters to be determined are the location of the coaxial waveguide, R_c , and the height

of the groove (or length of the coaxial waveguide), which should be one-quarter of the guide wavelength in the coaxial waveguide, λ_g . This involves a knowledge of the electromagnetic wave propagation both radially outward along the gap, and axially along the coaxial waveguide.

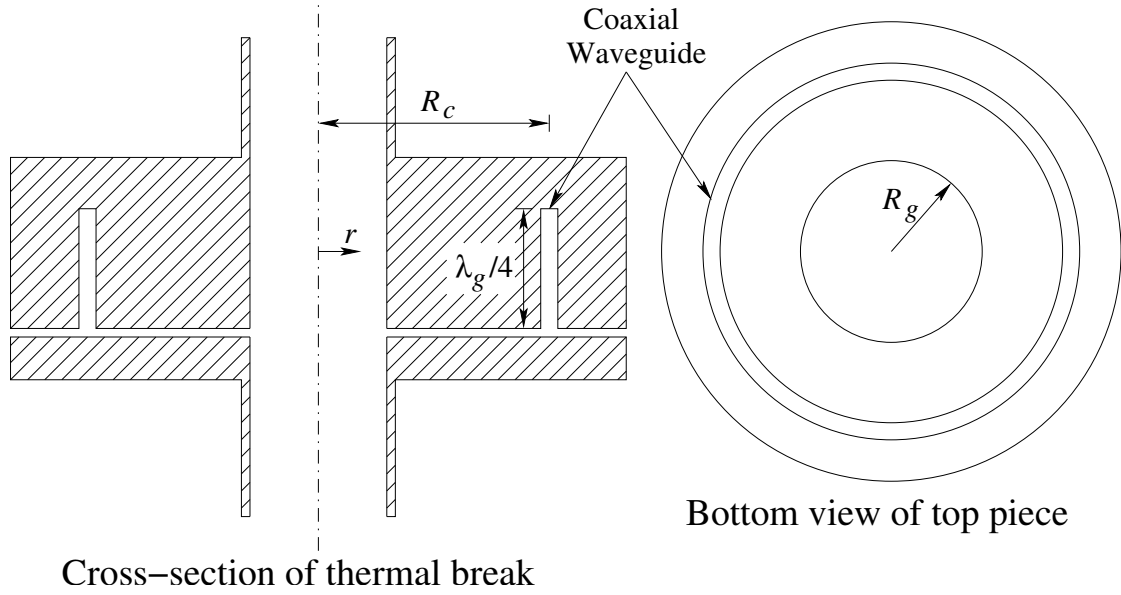


Figure 5.13 Schematic of a thermal break with a choke groove. The figure on the left shows a cross section of the device, and comprises of a top piece and a bottom piece that are thermally isolated through stand-offs made from a material like G10 fiberglass. The figure on the right shows the bottom view of the top piece. The inner radius of the circular waveguide is R_g and that of the choke groove is R_c

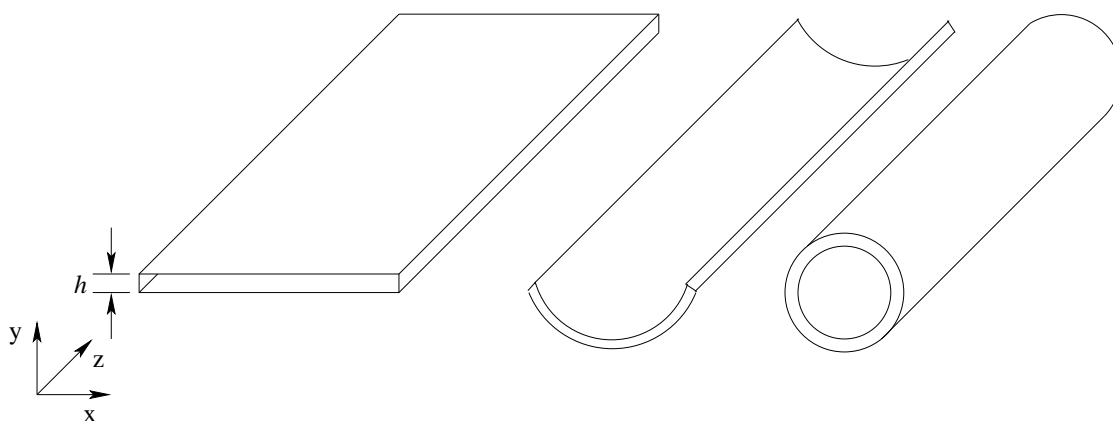


Figure 5.14 A coaxial waveguide can be treated as a rolled up thin rectangular waveguide.

Figure 5.14 shows a schematic of the coaxial waveguide which is treated as a rolled up thin rectangular waveguide. If the height h of the waveguide is small compared to its radius, we can analyze it as if it were not rolled up at all, except for the boundary condition that the field is periodic with period C , where $C = 2\pi R_c$ is the circumference of the waveguide. The direction of the E -field will be in the y direction. From Maxwell's equations, the wave propagation equation in the waveguide is

$$\frac{\partial^2 E}{\partial x^2} - (k_z^2 - k_0^2)E = 0 \quad (5.1)$$

where $k_0 = 2\pi/\lambda_0$ and λ_0 is the free space wavelength. Now, the boundary condition requires that the dependence of E on x be of the form $\cos(2\pi nx/C)$. Since the waveguide mode under consideration is TE_{11} , we have $n = 1$. Hence, we have

$$\frac{\partial^2 E}{\partial x^2} + \left(\frac{2\pi}{C}\right)^2 E = 0 \quad (5.2)$$

From the two equations above, we get

$$k_z = \sqrt{k_0^2 - \left(\frac{2\pi}{C}\right)^2} \quad (5.3)$$

The guide wavelength λ_g is given by $2\pi/k_z$ which becomes

$$\lambda_g = \frac{\lambda_0}{\sqrt{1 - \left(\frac{\lambda_0}{2\pi R_c}\right)^2}} \quad (5.4)$$

This gives the height of the choke groove, once R_c is determined (as described below).

In the radial waveguide (the section of the gap between the main circular waveguide and the coaxial waveguide), the electric field is a function of only r and θ , where (r, θ) refer to polar coordinates. The field cannot be a function of z as its divergence would then not be zero. From Maxwell's equations, we have

$$\nabla \times \nabla \times E - k_0^2 E = 0 \quad (5.5)$$

Taking the z component of above gives

$$(\nabla \times \nabla \times E)_z = \frac{1}{r} \frac{\partial}{\partial r} \left(r \frac{\partial E_z}{\partial r} \right) - \frac{1}{r} \frac{\partial}{\partial \theta} \left(\frac{1}{r} \frac{\partial E_z}{\partial \theta} \right) = k_0^2 E_z \quad (5.6)$$

The angular dependence of E_z must again be proportional to $\cos(n\theta)$, where for the same reason as before, $n = 1$. Thus, the above equation becomes

$$\frac{\partial^2 E_z}{\partial r^2} + \frac{1}{r} \frac{\partial E_z}{\partial r} + \left(k_0^2 - \frac{1}{r^2} E_z \right) = 0 \quad (5.7)$$

The solutions to this equation are the Bessel functions $J_1(k_0 r)$ and $Y_1(k_0 r)$, and the radial part of E_z is a linear combination of the two.

$$E_z(r) = J_1(k_0 r) + a Y_1(k_0 r) \quad (5.8)$$

The location of the groove (coaxial waveguide) can now be determined as follows. The purpose of the choke groove is to make the gap look like the wall of a normal waveguide, and hence the E -field in the gap is zero at $r = R_g$. Hence, the first task is to determine the linear combination of Bessel functions (the parameter a) that will give rise to a zero at $r = R_g$. Then, the location of the groove is given by the value of r that maximizes or minimizes this linear combination. Once R_c is determined, λ_g can be calculated which gives the height of the groove.

In our case, the circular waveguide had a radius $R_g = 2.48$ cm (0.975 inches). Doing the calculation described above, we determined R_c to be 3.51 cm (1.38 inches). The guide wavelength in the coaxial waveguide, λ_g turned out to be 4.42 cm (1.74 inches), and hence the groove height was set to 1.10 cm (0.435 inches). The gap in the waveguide is set to be as small as practical for better performance, and in our case turned out to be 0.018 cm (0.007 inches). We had two thermal breaks in the dewar, one for isolating the 70 K stage from the 300 K stage, and another for isolating the 15 K stage from the 70 K stage. This was done so as

to reduce the heat load on the second stage of the refrigerator (which nominally cools down to 15 K). Indeed, the use of two thermal breaks lowered the heat load to allow the second stage to cool down to around 10.5 K during actual operation, which in turn lowered ohmic contribution to the receiver noise temperature.

5.5 Low Noise Amplifiers

The low noise amplifiers used in the receiver utilize a monolithic-microwave integrated circuit (MMIC) which was designed at Caltech (Wadefalk & Weinreb 2005) and fabricated in the Northrop Grumman semiconductor foundry. The module is shown in Figure 5.15 with a closeup of the MMIC in Figure 5.16. The MMIC is the type WBA13 which utilizes 3 indium-phosphide high-electron-mobility transistors (HEMTs) with $0.1\mu\text{m}$ gate length. The amplifiers have extremely low noise (< 4 K) over a very wide bandwidth (4 to 12 GHz) as shown in Figure 5.17 when cooled to 12 K.

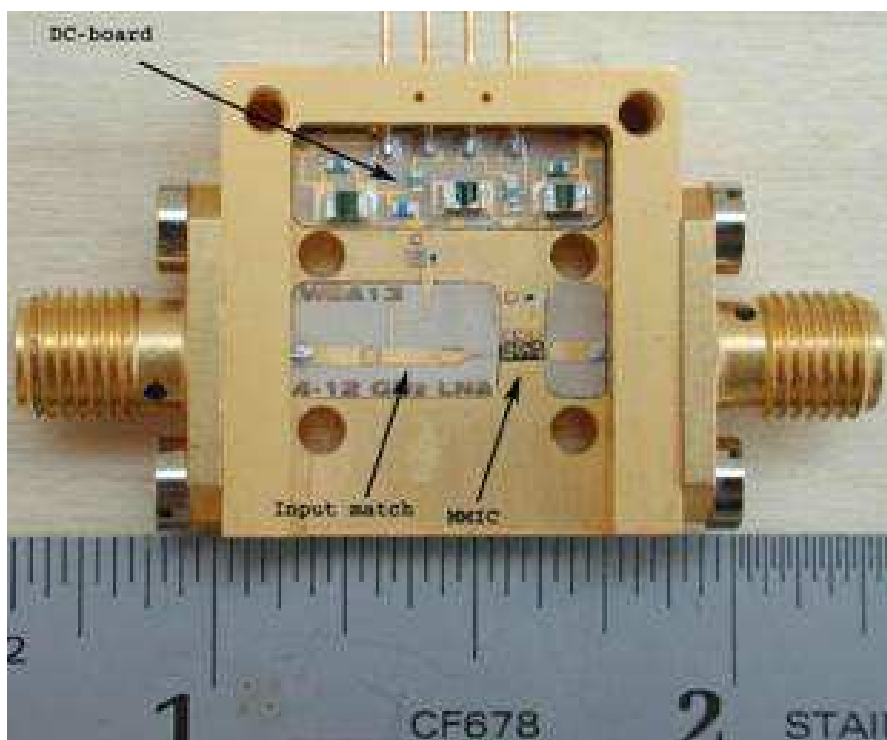


Figure 5.15 LNA module with covers removed. The module is comprised of input, output, and DC bias circuit boards and an InP MMIC 3-stage amplifier shown in Figure 5.16.

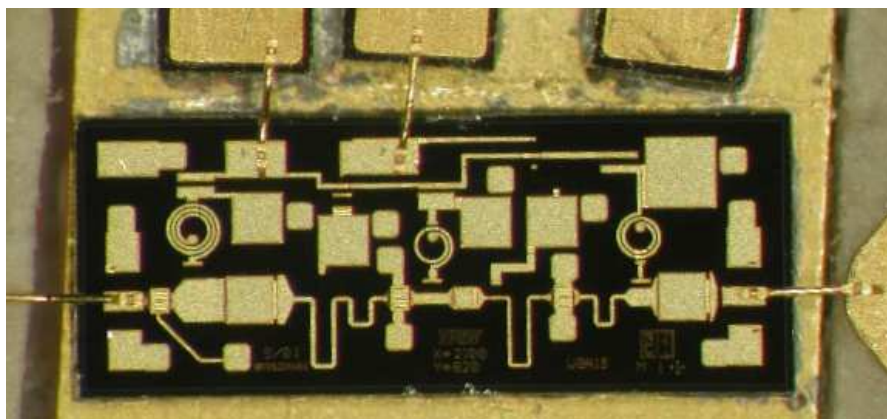


Figure 5.16 WBA13 MMIC used in the amplifier. The chip size is $2 \text{ mm} \times 0.73 \text{ mm}$. The bond wires are for input, output, gate, and drain voltage. In addition to the 3 transistors the chip contains thin-film resistors and capacitors and spiral inductors. Over 1000 amplifiers can be produced on one 3 inch wafer.

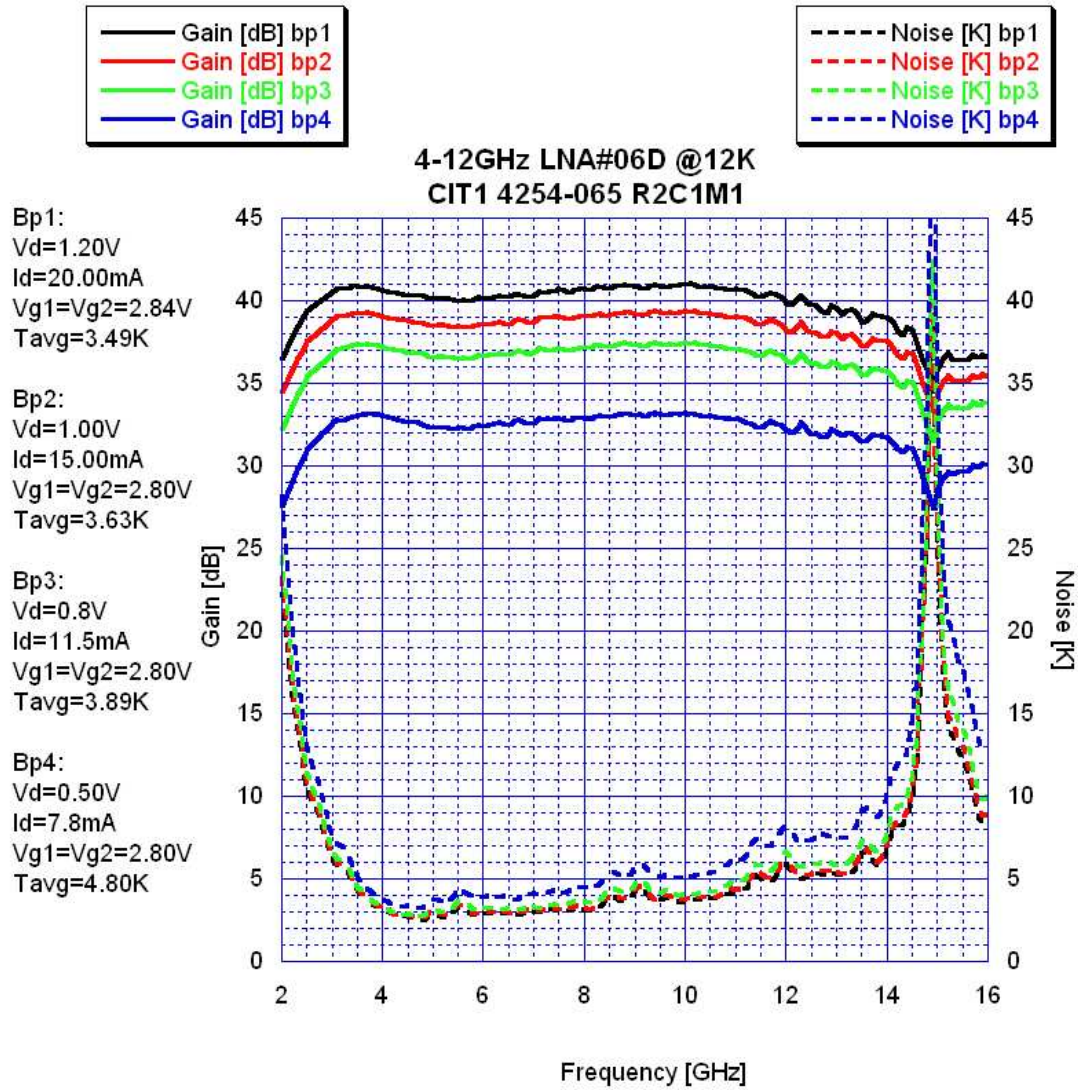


Figure 5.17 Measured gain and noise temperature at 12 K at 4 different bias settings for a typical LNA of the type used in the receiver. The highest bias power of 24 mW results in 41 dB gain and 3.5 K noise averaged from 4 to 12 GHz while a lower bias power of 3.9 mW still results in 33 dB gain and 4.8 K average noise. Over 50 of these amplifiers with very repeatable performance have been built at Caltech. At 300 K the noise temperature of the amplifier is approximately 50 K (0.7 dB noise figure).

5.6 Remainder of the Signal Path

The overall signal path in the receiver is shown in Figure 5.18. The low noise amplifier is preceded by an isolator and a directional coupler. The isolator was from Passive Microwave Technology and had specifications of 20 dB isolation with an input and output VSWR of 1.24, and an insertion loss of less than 0.38 dB (which was verified through actual measurements). The directional couplers are used for injecting power from a noise diode, and are used for calibration purposes during astronomical observations. The couplers were from MAC Tech., and had return loss of less than 25 dB, insertion loss of less than 0.15 dB, coupling of 30 ± 1.25 dB, and a directivity better than 30 dB which were well within specifications.

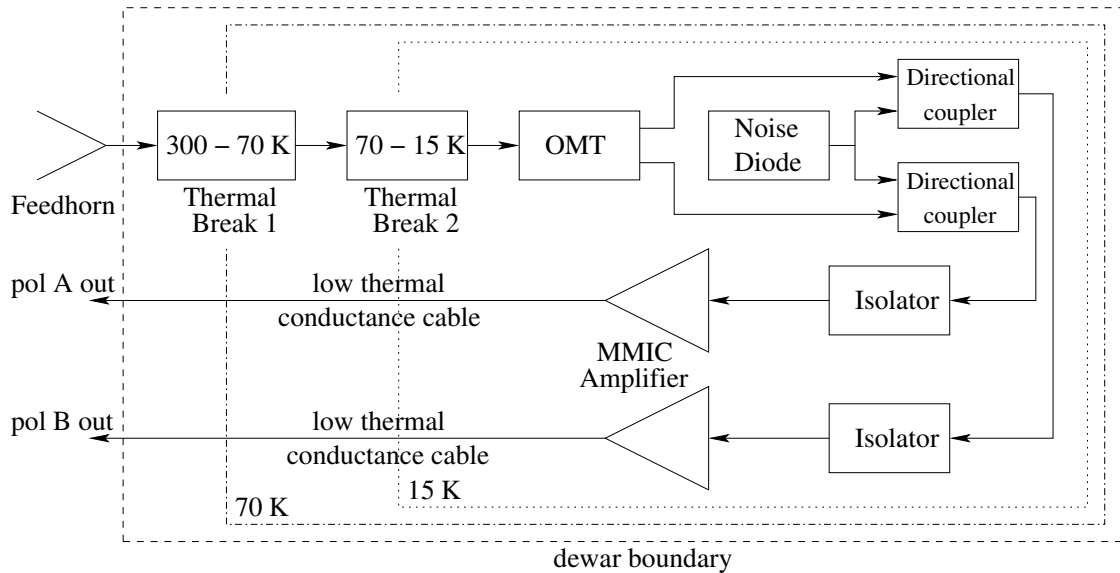


Figure 5.18 Schematic of the receiver showing the signal path from the feed horn to the exterior of the dewar.

The output from the low noise amplifier is then taken out of the dewar, and converted to a center frequency of 1.5 GHz. This is in turn transmitted over an optical fiber link to the signal processing area in a building adjacent to the

telescope. There, a digital autocorrelation spectrometer produces spectra.

5.7 Dewar Design

The cryogenic dewar is designed based on the guidelines outlined in Behrens et al. (1997). The refrigerator is a two stage device that operates on the Gifford-McMahon principle. The two stages cool to nominal temperatures of 70 K and 15 K respectively, the exact values depending on the heat load on each stage and the load curves of the refrigerator. There are two radiation shields connected to the two stages of the refrigerator. In the absence of radiation shields, the components at 15 K will be exposed to thermal radiation from the external dewar wall at 300 K. This will be a significant contribution to the heat load of the 15 K stage of the refrigerator. The radiation shield connected to the first (70 K) stage of the refrigerator captures the radiation from the dewar wall and reduces the loading of the 15 K stage. The 70 K stage of the refrigerator also has a higher cooling capacity compared to the 15 K stage, and is able to dissipate the radiation from the dewar wall.

The steps involved in the dewar design are outlined below:

- The receiver components including the refrigerator are first laid out with their proper dimensions in order to determine the dimensions of the radiation shields and the dewar.
- A heat load analysis is done to calculate the load on the two stages of the refrigerator. If the calculated heat loads are above the capacity of the selected refrigerator, a different model is selected, and the step above is repeated.
- Once the iteration between the two steps above is completed, the thickness of

the dewar wall, end plates, and other components are calculated to complete the dewar design.

The individual steps are outlined in more detail in the sections below.

5.7.1 Dewar Dimensions

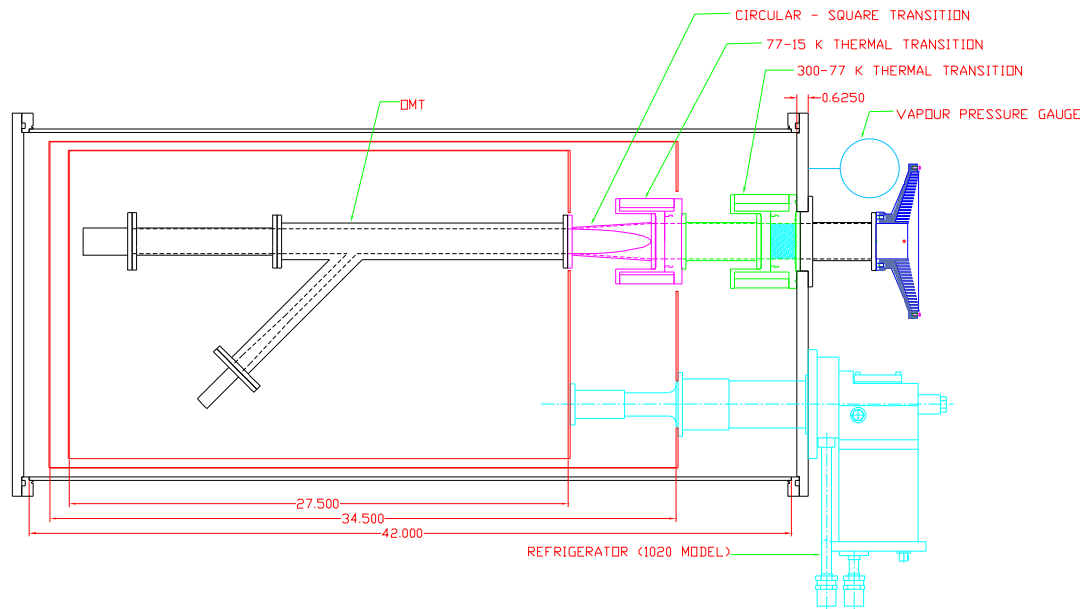


Figure 5.19 Layout of the major components of the receiver.

Figures 5.19 and 5.20 shows the layout of the major radio frequency components of the receiver. Only the components that are required to determine the dewar dimensions are shown. From these figures, the diameters of the 15 K shield, 70 K shield and dewar wall are 43.2 cm (17.0 inches), 45.7 cm (18.0 inches) and 48.3 cm (19.0 inches) respectively. The lengths of the 15 K shield, 70 K shield and the dewar are determined to be 69.9 cm (27.5 inches), 87.6 cm (34.5 inches) and 106.7 cm (42.0 inches) respectively.

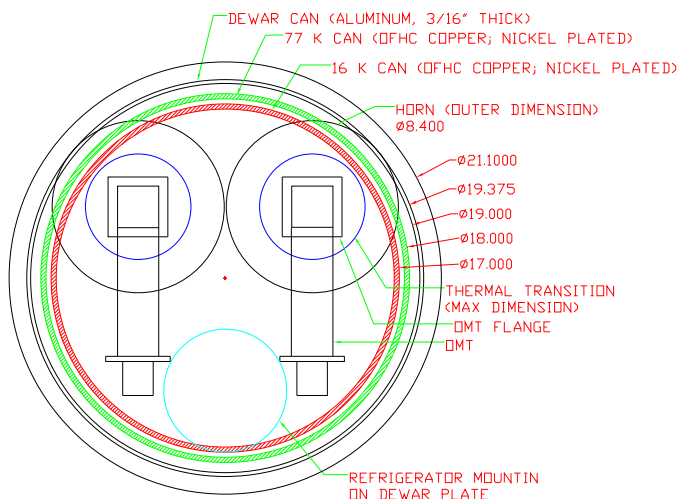


Figure 5.20 Top view of the dewar layout.

5.7.2 Heat Loads

The primary contribution to the heat loads on the refrigerator are due to radiative coupling between heat shields, and conduction through various components in the receiver. Convective heat loads are generally negligible as long as good vacuum is maintained in the dewar.

5.7.2.1 Radiative Heat Loads

The energy transfer between an object and perfectly absorptive surroundings is given by

$$Q = \sigma \epsilon (T_2^4 - T_1^4) \quad (5.9)$$

where σ is the Stefan-Boltzmann constant with a value of $\sigma = 5.67 \times 10^{-12}$ W cm⁻² K⁻⁴, ϵ is the emissivity of the object, and T_2 and T_1 are the temperatures of the object and surroundings respectively.

However, in most practical applications, the radiative coupling is between two surfaces of area A_1 and A_2 with emissivities ϵ_1 and ϵ_2 and temperatures T_1 and

T_2 ($T_2 > T_1$) respectively. The exact value of the exchange of radiant energy is dependent on the geometries of the two surfaces and is difficult to obtain. However, a rough estimate can be made using the following equation:

$$Q = \frac{\sigma A_1 (T_2^4 - T_1^4)}{\frac{1}{\epsilon_1} + \frac{A_1}{A_2} \left(\frac{1}{\epsilon_2} - 1 \right)} \quad (5.10)$$

The emissivities of common surfaces is given in Table 5.2. Clearly, polished surfaces reduce radiative heat loads and are thus preferred in dewar construction.

Table 5.2 Emissivities of surfaces used in dewar construction (data taken from White & Meeson 1968).

Material	ϵ
nickel plated copper	0.045
polished aluminum plate	0.03
highly oxidized aluminum	0.31

5.7.2.2 Conductive Heat Loads

The rate of heat conduction in a material between two points at temperatures T_1 and T_2 ($T_2 > T_1$) is given by

$$Q = k \frac{A}{l} (T_2 - T_1) \quad (5.11)$$

where k is the thermal conductivity of the material, A is the area of cross section and l is the length between the two points of interest. However, since the thermal conductivity of material is in general variable with temperature, we need to modify the above equation as

$$Q = \frac{A}{l} \int_{T_1}^{T_2} k \, dT \quad (5.12)$$

Figure 5.21 shows the variation of the thermal conductivity for 304 stainless steel as a function of temperature (data taken from Marquardt et al. 2002).

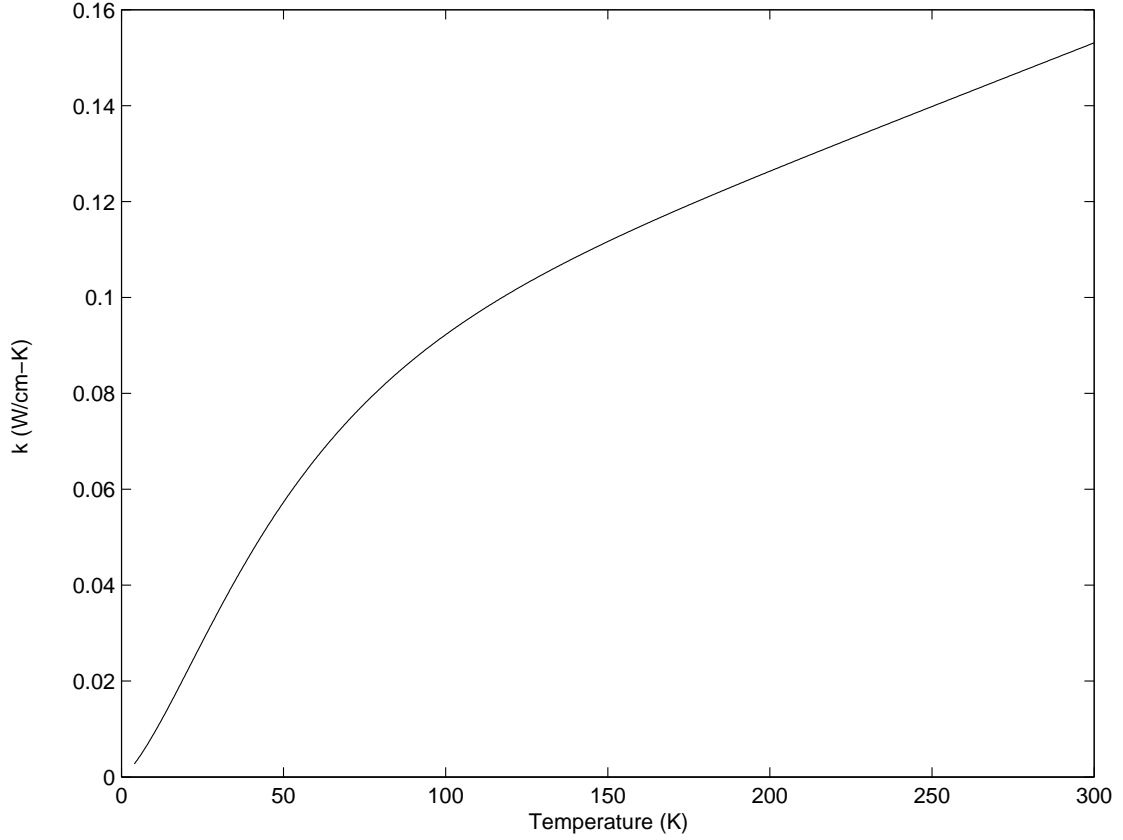


Figure 5.21 The thermal conductivity of 304 stainless steel as a function of temperature.

The values for the integral of thermal conductivity over temperature for different materials are shown in Table 5.3 (data from Behrens et al. 1997).

Conductive heat loads can be minimized by maximizing the length of materials, and minimizing their area.

5.7.2.3 Heat load on the 70 K stage

The 300 K dewar can is made of Aluminum, while the 70 K radiation shield is nickel plated oxygen free hard copper (OFHC). The heat load is examined for

Table 5.3 Thermal conductivity data for common materials used in dewar components.

Material	$\int_{15}^{70} k(T) dT$ (W/cm)	$\int_{70}^{300} k(T) dT$ (W/cm)
304 Stainless Steel	2.61	28.2
Beryllium Copper	12	138
G-10 Fiber glass	0.109	0.88

different finishing surfaces for the 300 K stage.

1. Radiative coupling between radiation shield cylinders:

The areas of the 70 K and 300 K cans are

$$A_{70} = 1951 \text{ in}^2 = 12,586.61 \text{ cm}^2$$

$$A_{300} = 2543 \text{ in}^2 = 16,405.16 \text{ cm}^2$$

The heat load is then given by equation (5.10)

$$\begin{aligned}
 Q_1 &= \frac{\sigma A_{70}(300^4 - 70^4)}{\frac{1}{\epsilon_{70}} + \frac{A_{70}}{A_{300}} \left(\frac{1}{\epsilon_{300}} - 1 \right)} \\
 &= 24.08 \text{ W assuming oxidized aluminum} \\
 &= 12.26 \text{ W assuming polished aluminum} \\
 &= 14.97 \text{ W assuming nickel plated aluminum}
 \end{aligned}$$

2. Radiative coupling in top plate:

The areas of the 70 K and 300 K top plates (where the feed horn is located) are

$$A_{70} = 197 \text{ in}^2 = 1273.10 \text{ cm}^2$$

$$A_{300} = 232 \text{ in}^2 = 1496.93 \text{ cm}^2$$

Applying the same equation as above, the heat load is

$$\begin{aligned}
 Q_2 &= 2.41 \text{ W assuming oxidized aluminum} \\
 &= 1.17 \text{ W assuming polished aluminum} \\
 &= 1.44 \text{ W assuming nickel plated aluminum}
 \end{aligned}$$

3. Radiative coupling in bottom plate:

The areas of the bottom plates of the 70 K and 300 K stages are

$$\begin{aligned}
 A_{70} &= 254 \text{ in}^2 = 1641.73 \text{ cm}^2 \\
 A_{300} &= 283 \text{ in}^2 = 1829.21 \text{ cm}^2
 \end{aligned}$$

The heat load can then be calculated as

$$\begin{aligned}
 Q_3 &= 3.10 \text{ W assuming oxidized aluminum} \\
 &= 1.47 \text{ W assuming polished aluminum} \\
 &= 1.82 \text{ W assuming nickel plated aluminum}
 \end{aligned}$$

4. Thermal conduction in the thermal break:

Thermal conduction in the thermal break occurs through the G-10 fiber glass that is used for standoffs. To minimize the conductive heat load, the standoffs have hollowed interiors. The outer and inner diameters of the standoffs are 0.4" and 0.25" respectively. The length of the standoffs is 3". Hence the heat load from the four standoffs in the thermal break can be calculated from

equation (5.12) as

$$\text{Length } l = 3 \text{ in} = 7.62 \text{ cm}$$

$$\text{Area } A = 0.076 \text{ in}^2 = 0.494 \text{ cm}^2$$

$$\begin{aligned} Q_4 &= 4 \times \frac{l}{A} \int_{70}^{300} k_{G10} dT \\ &= 0.228 \text{ W} \end{aligned}$$

5. Radiative coupling in the thermal break:

This occurs in the narrow gap between the 300 K and 70 K stages in the thermal break.

$$\text{Area } A = 17.8 \text{ in}^2 = 115.12 \text{ cm}^2$$

$$Q_5 = 0.967 \text{ W assuming both surfaces to be oxidized aluminum}$$

6. Conduction in RF cables (0.141" cable):

This cable has the outer conductor (outer diameter, OD = 0.141", inner diameter, ID = 0.1175") made of 304 stainless steel and beryllium copper inner conductor (OD = 0.0359"). Relatively long lengths of 10" are used for the cable to minimize the conductive heat load. There are 8 cables in the dewar for two beams.

$$l = 10 \text{ in} = 25.4 \text{ cm}$$

$$A_{outer} = 4.7 \times 10^{-3} \text{ in}^2 = 0.03078 \text{ cm}^2$$

$$A_{inner} = 10^{-3} \text{ in}^2 = 6.53 \times 10^{-3} \text{ cm}^2$$

$$\begin{aligned} Q_6 &= \frac{A_{outer}}{l} \int_{70}^{300} k_{SS} dT + \frac{A_{inner}}{l} \int_{70}^{300} k_{BC} dT \\ &= 69.65 \text{ mW/cable} \end{aligned}$$

7. Total heat load on the 70 K stage:

The approximate total heat load on the 70 K stage can now be calculated, keeping in mind that there will be two thermal breaks and 8 RF cables in the dual beam system. Thus, the total heat load is

$$\begin{aligned}
 Q &= Q_1 + Q_2 + Q_3 + 2(Q_4 + Q_5) + 8Q_6 \\
 &= 32.54 \text{ W assuming oxidized aluminum for dewar can and plates} \\
 &= 17.85 \text{ W assuming polished aluminum for dewar can and plates} \\
 &= 21.18 \text{ W assuming nickel plated aluminum for dewar can and plates}
 \end{aligned}$$

The major contributors to the heat load are Q_1 , Q_2 and Q_3 . The quantity Q_1 can be reduced significantly if one uses super-insulation. Super-insulation comprises of a highly reflective surface that is wrapped in several layers around the inner shield (the 70 K stage in this case). Successive layers are thermally insulated with respect to each other. The heat load on the 70 K shield is proportional to the fourth power of the temperature of the insulation closest to the shield, which will be less than 300 K when super-insulation is used. This reduces the heat load tremendously. For example, a single layer of super-insulation between the 300 K and 70 K stages will assume a temperature of approximately 250 K, which will reduce the heat load by a factor of 2 compared to the case where no super-insulation is used.

5.7.2.4 Heat load on the 15 K stage

The 70 K stage and the 15 K radiation shields are made of nickel plated oxygen free hard copper.

1. Radiative coupling between radiation shield cylinders:

The area of the two surfaces are

$$A_{15} = 1469 \text{ in}^2 = 9,475.43 \text{ cm}^2$$

$$A_{70} = 1951 \text{ in}^2 = 12,586.61 \text{ cm}^2$$

The radiative heat load between the two surfaces is given by equation (5.10)

$$\begin{aligned} Q_1 &= \frac{\sigma A_{15}(70^4 - 15^4)}{\frac{1}{\epsilon_{15}} + \frac{A_{15}}{A_{70}}\left(\frac{1}{\epsilon_{70}} - 1\right)} \\ &= 33.7 \text{ mW} \end{aligned}$$

2. Radiative coupling between top plates:

The area of the two top plates are

$$A_{15} = 203 \text{ in}^2 = 1306.6 \text{ cm}^2$$

$$A_{70} = 202 \text{ in}^2 = 1303.50 \text{ cm}^2$$

The heat load can then be calculated as

$$Q_2 = 4.08 \text{ mW}$$

3. Radiative coupling between bottom plates:

The area of the bottom plates are

$$A_{15} = 227 \text{ in}^2 = 1464.38 \text{ cm}^2$$

$$A_{70} = 254 \text{ in}^2 = 1641.73 \text{ cm}^2$$

The heat load between the two surfaces is then

$$Q_3 = 4.83 \text{ mW}$$

4. Thermal conduction in the thermal break:

The G-10 fiber glass standoffs in the 70 K–15 K thermal break are identical

to their counterparts in the 300 K–70 K transition. Thus the heat load due to 4 standoff can be calculated as

$$\begin{aligned} Q_4 &= 4 \times \frac{A}{l} \int_{15}^{70} k_{G10} dT \\ &= 28.27 \text{ mW} \end{aligned}$$

5. Radiative coupling in the thermal break:

This is very similar to the calculation in the 300 K–70 K thermal break.

$$\text{Area } A = 17.8 \text{ in}^2 = 115.12 \text{ cm}^2$$

$$Q_5 = 2.87 \text{ mW assuming both surfaces to be oxidized aluminum}$$

6. Radiation from vacuum window:

The signal from the astronomical source comes through a window in the dewar. To maintain vacuum in the dewar, the window is fitted with Eccofoam material which can be assumed to have an emissivity $\epsilon = 1$. Hence, 300 K radiation from the Eccofoam is impingent on some components in the 15 K stage (mostly oxidized aluminum in the OMT). The resulting heat load is computed as

$$\text{Area } A = 3 \text{ in}^2 = 19.27 \text{ cm}^2$$

$$\begin{aligned} Q_6 &= \frac{\sigma A}{\frac{1}{\epsilon_{foam}} + \frac{1}{\epsilon_{Al}} - 1} (300^4 - 15^4) \\ &= 274.35 \text{ mW} \end{aligned}$$

7. RF cables (0.141" cable):

The various parameters of this cable have been given already in the previous

section. The length of the cable is 8".

$$\begin{aligned}
 l &= 8 \text{ in} = 20.32 \text{ cm} \\
 A_{outer} &= 4.7 \times 10^{-3} \text{ in}^2 = 0.03078 \text{ cm}^2 \\
 A_{inner} &= 10^{-3} \text{ in}^2 = 6.53 \times 10^{-3} \text{ cm}^2 \\
 Q_7 &= \frac{A_{outer}}{l} \int_{15}^{70} k_{SS} dT + \frac{A_{inner}}{l} \int_{15}^{70} k_{BC} dT \\
 &= 7.81 \text{ mW/cable}
 \end{aligned}$$

8. Total heat load on 15 K stage:

The approximate total heat load on the 15 K stage can now be calculated keeping in mind that there are two thermal transitions, and 8 RF cables. Then, the total heat load is

$$\begin{aligned}
 Q &= Q_1 + Q_2 + Q_3 + 2(Q_4 + Q_5) + Q_6 + 8Q_7 \\
 &= 441.72 \text{ mW}
 \end{aligned}$$

5.7.2.5 Choice of Refrigerator

It should be noted that the heat load analysis presented in the previous section is approximate. The contribution of thermal conduction through the wires from the bias connectors have not been considered, although this is expected to be small due to the very small area of the wires. Thus, a conservative safety margin should be considered when choosing the refrigerator.

Some of the commonly used refrigerator models and their cooling capacities are shown in Table 5.4.

The inside wall of the dewar (which is the source of the heat loads on the refrigerator) is chosen to be nickel plated (since the longevity of a polished aluminum surface is limited). From the heat load analysis above, the CTI Model 1020 would

Table 5.4 Refrigeration capacity of refrigerator models commonly used in cryogenic dewars.

Refrigerator	Capacity at 70 K	Capacity at 15 K
CTI Model 22	6.5 W	0.8 W
CTI Model 350	16 W	2.5 W
CTI Model 1020	38 W	7 W
Leybold UCH-130	105 W	11 W

be required to satisfy the heat load requirements, and is thus chosen for installation in the dewar.

5.7.3 Mechanical design of the dewar

Since the dewar is evacuated, the thickness of the dewar walls and end plates should be sufficient to withstand a pressure of 1 atmosphere (~ 100 kPa or 15 pounds-force per square inch or psi). The relevant equations, taken from Behrens et al. (1997) for the mechanical design are given below.

The thickness of the dewar wall is determined from

$$P_a = \frac{K}{n} E \left(\frac{t}{D} \right)^3 \quad (5.13)$$

where P_a is the pressure, K is a correction factor found from Figure 5.22, n is a safety factor (typically around 4), E is the elasticity modulus, t is the thickness of the dewar wall and D is the dewar diameter.

In our case, $D = 19$ in, $L = 42$ in, $E = 1.05 \times 10^7$ in⁻² (for Aluminum which is chosen over steel due to weight considerations), and P_a is the atmospheric pressure, 15 psi. Since the diameter of the dewar is too large to be commercially available as

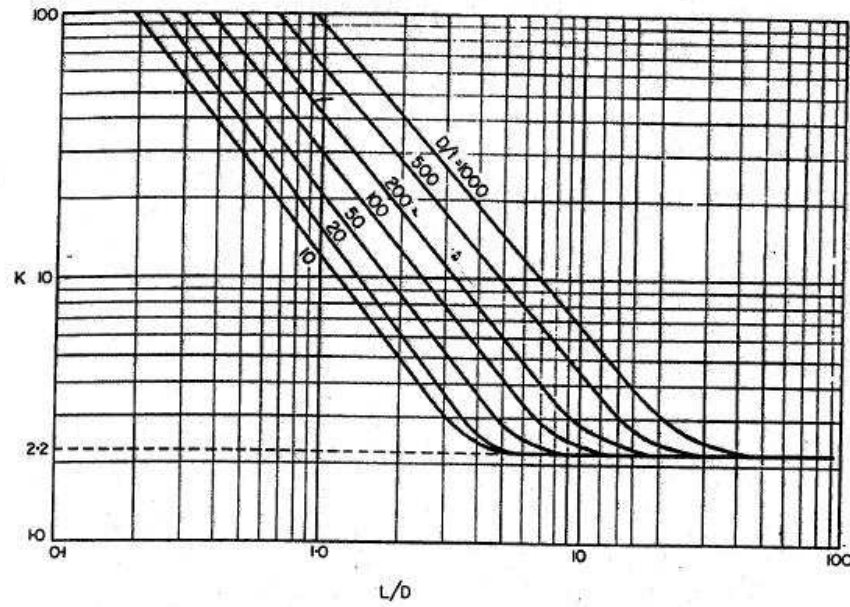


Figure 5.22 The correction factor K in equation (5.13). L , D and t are the length, diameter and the thickness of the dewar wall respectively.

a pipe, the dewar construction involves rolling a sheet of material into a cylinder followed by welding at the seams. The thickness of the dewar wall thus has to conform to a commercially available thickness of sheet (e.g. 1/8 in or 3/16 in).

Assuming a thickness of 3/16 in, (D/t) is around 100 and (L/D) is 2.2. From Figure 5.22, the correction factor K is around 10. From equation (5.13), n can be calculated to be around 7, which is sufficient. A similar calculation with a 1/8 inch thick wall yields n to be 2.4 which is inadequate. Hence, we chose the dewar wall thickness to be 0.1875 in.

The thickness of the end plates is determined from the following equation (also taken from Behrens et al. 1997):

$$P_a = \frac{256}{3(1 - M^2)} \frac{E \cdot \delta}{D} \left(\frac{t}{D} \right)^3 \quad (5.14)$$

where P_a is the atmospheric pressure in psi, E is the modulus of elasticity in in^{-2} , D is the diameter of the plate in inches, t is the thickness of the plate in inches,

δ is the deflection at the center of the plate in inches and M is a quantity that is 0.3 for metals. Using the dimensions outlined above, the thickness of the plate required for a deflection δ of 0.01 in is 0.58 in. The nearest thickness of a plate that is commercially available is 0.625 in, and is hence chosen for the plate thickness.

5.7.4 Additional Design Considerations

The additional design consideration that needs to be considered is the time taken to cool the dewar from room temperature to the operating temperature of 15 K. During the testing and commissioning phase, the receiver is expected to go through cool down and warm up cycles. It is thus desirable to keep the time taken to cool the receiver as short as possible. The dominant contribution to the cool down time is the time taken to cool the waveguide components (made from Aluminum) to 15 K.

The energy required to cool an object of mass m from temperature T_1 to T_2 is given by

$$H = m \int_{T_1}^{T_2} C_p dT \quad (5.15)$$

where C_p is the specific heat at constant pressure for the material. In our case, we used splines to extrapolate tabulated data (Corruccini & Gniewek 1960) on the specific heat of Aluminum (Figure 5.23). Using the data in Figure 5.23, we calculated the energy per unit mass to cool Aluminum from 290 K to 15 K to be

$$\int_{15}^{290} C_p dT = 162 \text{ J/g} \quad (5.16)$$

Since the weight of the two OMTs and other waveguide components is 6 kg, the energy required to cool the receiver to 15 K is at least 974 kJ. Since the cooling capacity of the second stage of the CTI-1020 refrigerator is 7 W at 15 K, the total

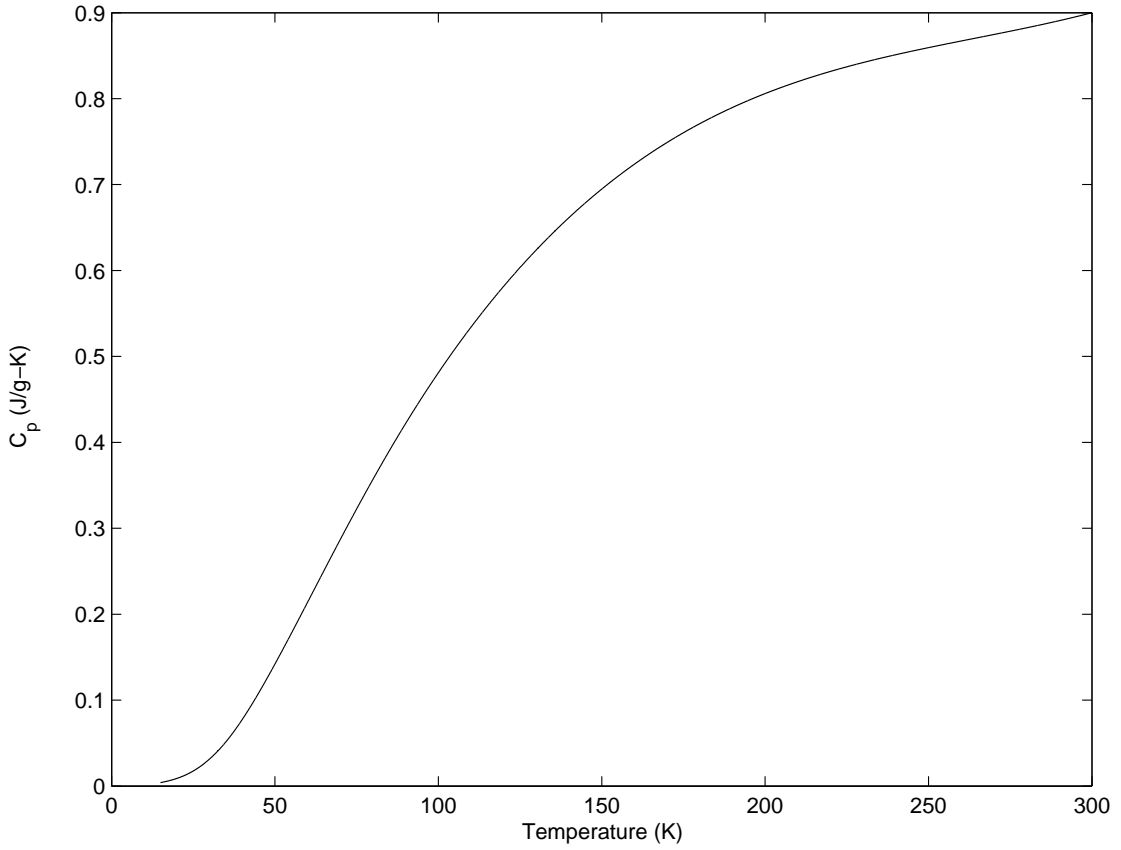


Figure 5.23 The specific heat of Aluminum as a function of temperature.

time required to cool the receiver to 15 K is at least 38.7 hours.

The cool down time can be reduced significantly if the components are pre-cooled using liquid nitrogen. The energy per unit mass required to cool Aluminum from 77 K to 15 K is

$$\int_{15}^{77} C_p dT = 8.3 \text{ J/g} \quad (5.17)$$

Thus, the time required for the receiver to cool down to 15 K after pre-cooling it to 77 K is only 2 hours. Hence, the receiver design incorporated a pre-cooling device, which comprised of input and return tubing for liquid nitrogen, connected to a block of copper connected to the 15 K stage.

5.8 Receiver Noise Temperature

We evaluated the overall noise temperature of the receiver using the Y-factor method. The receiver was mounted such that the feed horn was looking at the sky, which served as the cold load. Then, a piece of Eccosorb absorbing material was placed in front of the horn to serve as the hot load. By measuring the receiver power with the two loads, the noise temperature of the receiver, T_{rx} can be evaluated by

$$T_{rx} = \frac{T_{amb} - YT_{sky}}{Y - 1} \quad (5.18)$$

where T_{amb} is the ambient temperature, T_{sky} is the sky temperature, and $Y = P_{hot}/P_{cold}$ is the ratio of the power measured using hot and cold loads.

The sky temperature is the sum of the contribution of the Cosmic Microwave Background and the opacity and emission of the atmosphere, which depend on the amount of precipitable water vapor. The measurements were carried out in the early morning when the sky conditions were clear with relatively low water vapor content (for Arecibo) and we estimated the emission from the sky at zenith to be 6.5 K (Goldsmith 2001). We made measurements over the course of seven days, and averaged the resulting measurements together. The results are shown in Figure 5.24. Losses from the directional coupler, isolator and cables contribute to the receiver noise temperature in addition to the low noise amplifier. Due to the high gain of the low noise amplifier (~ 40 dB), the noise contribution from the post-amplifier stage is negligible.

The receiver noise temperature measurement was in turn used to calibrate the noise diodes that would be used for calibration during astronomical observations.

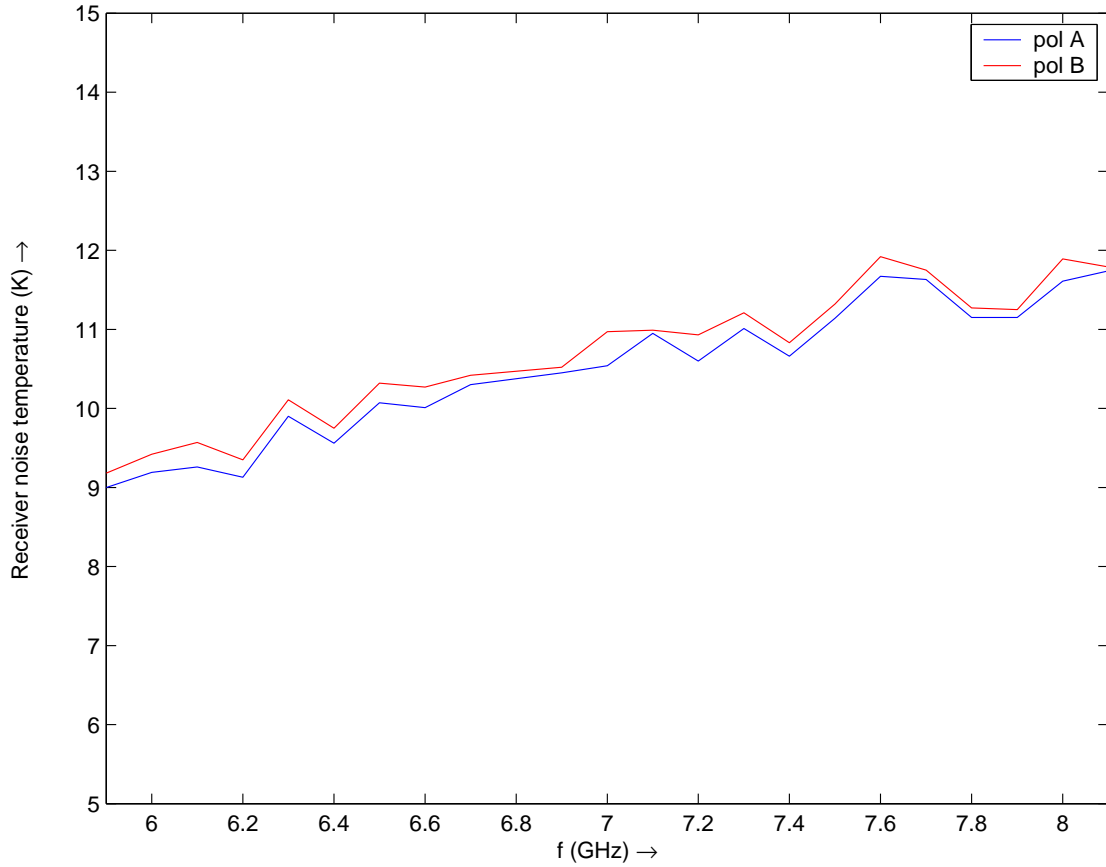


Figure 5.24 Measured receiver noise temperature. Note the higher noise temperature for pol B due to the higher insertion loss of the OMT for this polarization

5.9 Overall System Performance

The telescope itself makes a significant contribution to the overall system temperature due to spill-over and stray radiation. These effects are dependent on the azimuth and zenith angle of the telescope. Thus, the net system temperature ranges from 23–29 K in one polarization (designated pol A in Figures 5.4 and 5.5), and 28 – 34 K in the other polarization (designated pol B), with higher system temperatures occurring at larger zenith angles.

The beam response was measured by using a set of raster-scans in azimuth at uniformly and closely spaced zenith-angle offsets about the direction of an as-

tronomical source, B1040+123. The scans covering about 36 square arcminutes were obtained at a suitably fast rate to avoid large changes in the zenith angle, in order to minimize the possible uncertainties arising from any associated variations in the telescope performance. The data were recorded at 1 ms intervals with full polarization information, and gain calibrated using a local reference noise source switched at 25 Hz. Four bands of 100-MHz width each around 6.6 GHz were observed with 128 spectral channels per band, and the spectral data were combined later to obtain a band-averaged response. Suitable regridding and interpolation were performed to obtain a beam map with fine and uniform sampling in the azimuth and the zenith-angle offsets. The estimated response in Stokes I is shown in Figure 5.25. The elliptical beam pattern is a result of the final illumination aperture of diameter 213 m by 237 m (Kildal et al. 1994). The coma side-lobe is apparent around the main response whose angular widths in the two directions are consistent with the expectation. Figure 5.26 displays two orthogonal cuts sampled through, and normalized to, the peak response. The coma response is seen to be on the average below -12 dB of the main beam peak.

At present, the feed horn, isolators, directional couplers and low noise amplifiers for the second beam are not installed. Consequently, the receiver is working as a normal single beam instrument at present. It is expected to be upgraded to a full dual beam receiver by spring 2007.

5.10 Conclusions

The combination of the traveling wave OMT device and the ultra low noise MMIC amplifiers has allowed us to develop a broadband 6 to 8 GHz receiver with a noise temperature of around 10 K. The combination of receiver noise and the additional

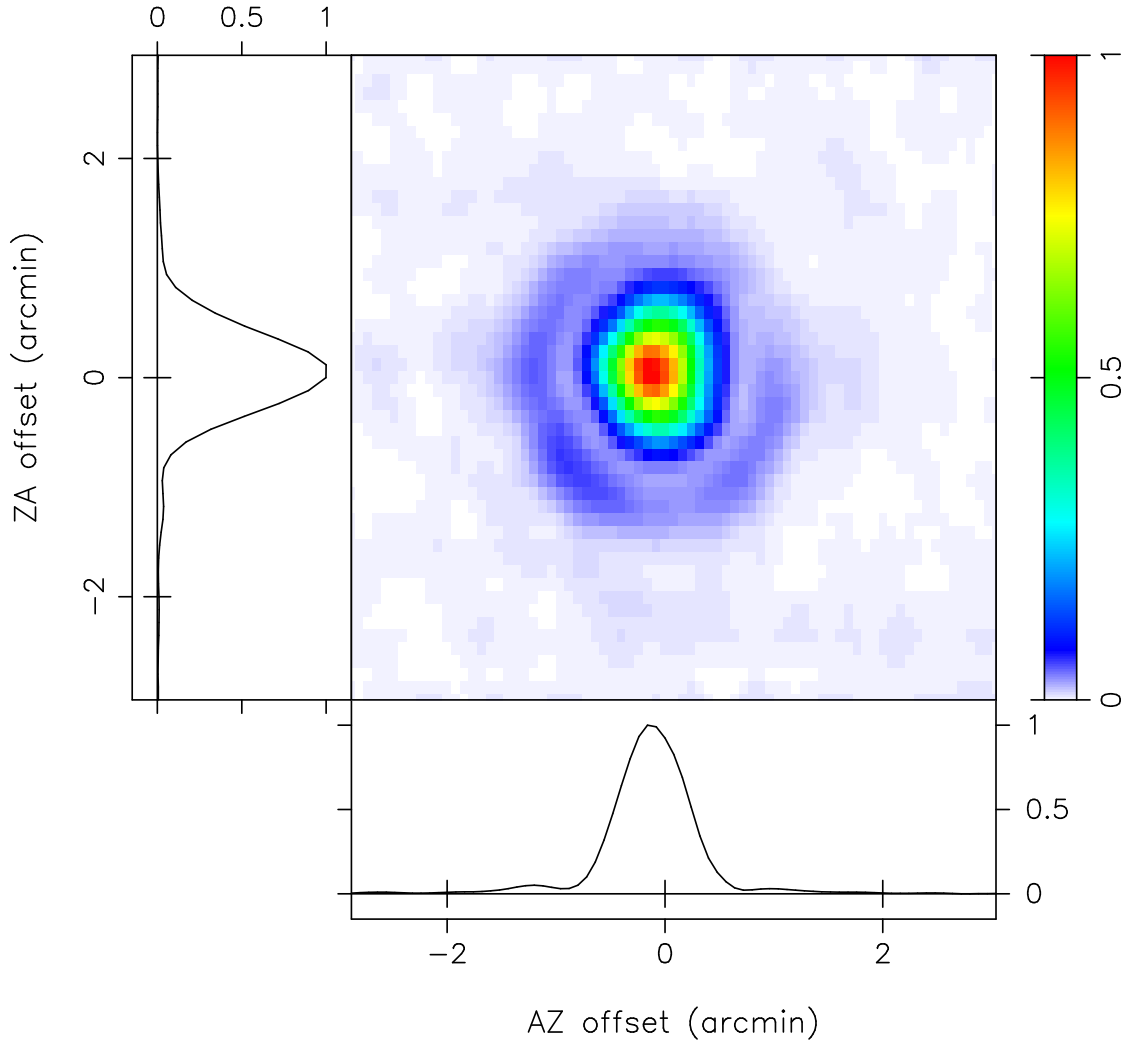


Figure 5.25 Normalized beam response mapped as a function of offsets in azimuth and zenith-angle, and estimated using full polarization measurements from a set of raster-scans on a continuum source B1040+123. The estimates shown here correspond to the response in the Stokes I parameter.

noise contributions by the telescope optics gives an overall receiver temperature of around 28 K and 34 K in the two polarizations, making this one of the best broadband receivers at Arecibo. The large collecting area of the telescope gives rise to a system equivalent flux density of around 4.5 Jy at 7 GHz making this the most sensitive instrument in the world for studies of 6.7 GHz methanol masers.

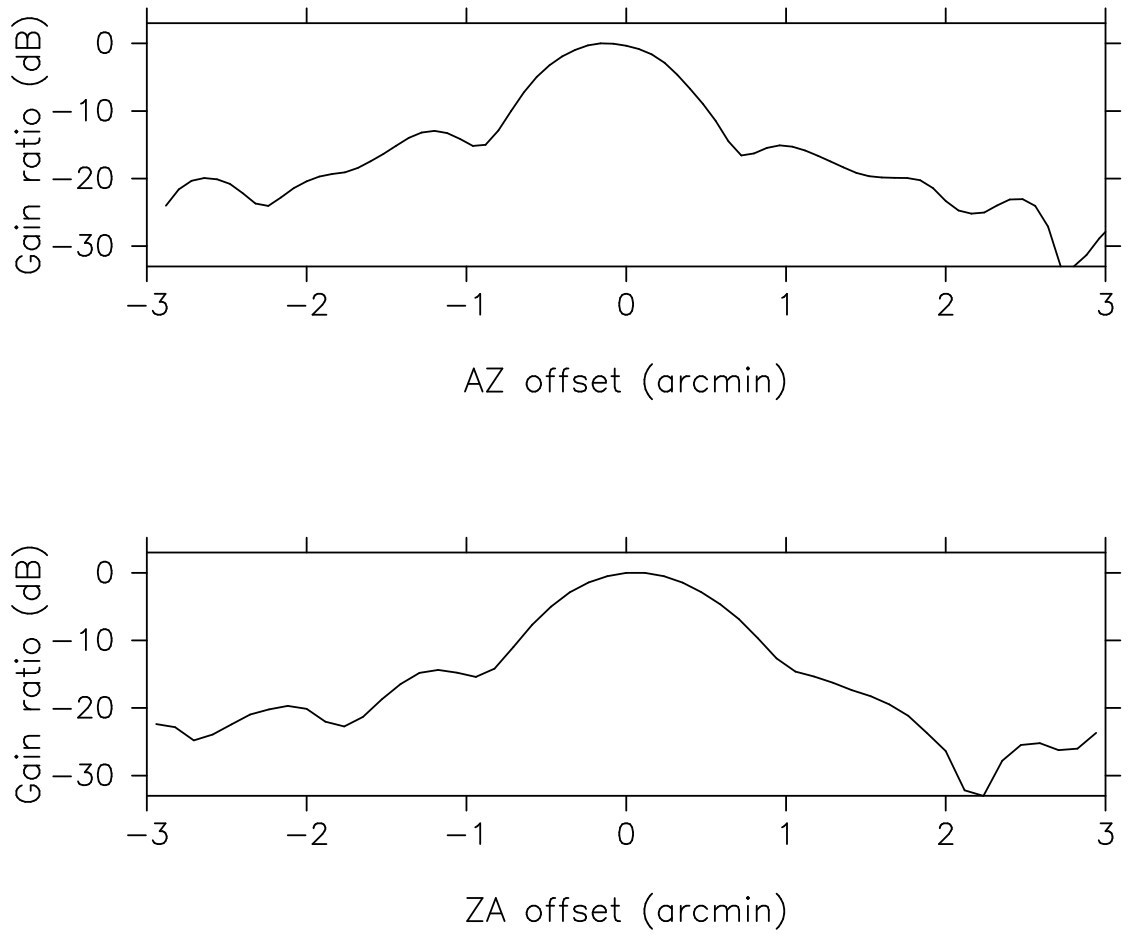


Figure 5.26 The beam profiles in azimuth and zenith angle respectively, sampled from the beam-map (shown in Figure 5.25) as cuts through its peak, are shown in dB scale with respect to the peak response.

Chapter 6

The Arecibo Methanol Maser Galactic Plane Survey—I: Data

6.1 Introduction*

It is widely recognized that molecular masers can be a powerful tool in the study of early stages of star formation. The 6.7 GHz methanol maser, discovered by Menten (1991b), is unique compared to its OH and H₂O counterparts in that it has been observed exclusively towards regions containing young, massive stars. Further, a number of recent studies suggest that 6.7 GHz methanol maser emission is associated with very early phases of massive star formation (Ellingsen 2006; Minier et al. 2005, 2001).

There have been approximately 519 methanol masers detected to date in various targeted and blind surveys (Pestalozzi et al. 2005). While many detections have been made by targeted surveys towards ultracompact H II regions selected based on their IRAS colors, blind surveys have shown that IRAS-based surveys underestimate the number of methanol masers by a factor of two (Ellingsen et al. 1996b; Szymczak et al. 2002). The total number of 6.7 GHz methanol masers in the Galaxy is thus estimated to be between 845 and 1200 (van der Walt 2005).

In this paper we present the results of a sensitive blind survey of a portion of the Galactic plane that is visible to the Arecibo radio telescope. The data from

*This chapter is based on the accepted paper: Pandian et al. 2007a [Pandian, J. D., Goldsmith, P. F., & Deshpande, A. A. 2007, *The Astrophysical Journal*, accepted; © 2007. The American Astronomical Society. All rights reserved.] It is reprinted here with minor changes, based on rights retained by the author.

such a survey can be productive for many purposes. Studies based on an unbiased sample of 6.7 GHz methanol masers are crucial for determining the link between methanol masers and massive star formation. It is of considerable interest to determine whether faint methanol masers discovered in a sensitive survey have different properties than those of bright masers; Szymczak & Kus (2000) discovered that methanol masers associated with IRAS sources that did not satisfy color criteria for ultracompact H II regions (Wood & Churchwell 1989; Hughes & MacLeod 1989) were relatively weak. Finally, if all 6.7 GHz methanol masers are indeed associated with early phases of massive star formation, they are potential tools for studying Galactic spiral structure, and thus it is of interest to carry out surveys that sample as large a range in Galactic longitude as possible.

6.2 Observations

The observations were made between June 2004 and March 2006 using the 6 – 8 GHz (C-Band High) receiver at the 305 m Arecibo radio telescope. The telescope has an rms pointing error of $7''$ and an average full width half maximum (FWHM) beamwidth of $40''$. The backend was the digital “interim” correlator which has four boards, each of which can be configured independently. The boards were configured into two pairs, each pair recording the autocorrelations of the two orthogonal linear polarizations with 9-level sampling, and 2048 channels per polarization to cover a bandwidth of 3.125 MHz. The two pairs of boards were staggered in frequency in order to provide a net velocity coverage of $+110$ to -70 km s $^{-1}$, with a velocity resolution of 0.14 km s $^{-1}$ after Hanning smoothing at the 6668.518 MHz rest frequency of the $5_1 - 6_0$ A $^+$ transition of methanol (Menten 1991b; a more accurate measurement of the rest frequency is presented by Breckenridge

& Kukolich 1995 as 6668.519 MHz; this results in a change in velocities by 0.04 km s⁻¹, which is less than the precision of the velocity of peak emission given in Table 1). The observations were centered on a frequency corresponding to the local standard of rest.

The nominal target region of the sky was $35^\circ \lesssim l \lesssim 55^\circ$, $|b| \lesssim 0.4^\circ$, which we divided into 100 sub-regions. Each sub-region was mapped in a rectangular grid (in right ascension and declination), the separation between grid points being 15'' in right ascension and 20'' in declination. Overall, we sampled approximately 780,000 sky positions. A noise diode with known noise temperature was fired every 250–270 sec in order to calibrate the antenna temperature scale of the data. The data were calibrated in terms of flux density by using the elevation-dependent gain curves (see Figure 6.1). Since the telescope gain drops at both high and low zenith angles, we planned the survey such that all observations would be carried out when the target region was between zenith angles of 5° and 18°. The residuals obtained from the fit to the telescope gain curves indicate that the flux calibration has an uncertainty of approximately 10%.

Part of the observations were done in “drift mode” where the telescope is fixed and the sky drifts through the beam. The integration time per grid point in this mode was 1 sec, which yielded an rms noise level of ~ 70 mJy in each spectral channel after Hanning smoothing averaging both polarizations. Between June and November 2004, the primary, secondary, and tertiary reflector surfaces were readjusted, resulting in improved telescope performance. Following this, we carried out the rest of the survey by driving the telescope at twice the sidereal rate and integrating for 0.5 sec on each sample of the sky. This resulted in an rms noise level of ~ 85 mJy in each spectral channel after Hanning smoothing and averaging both

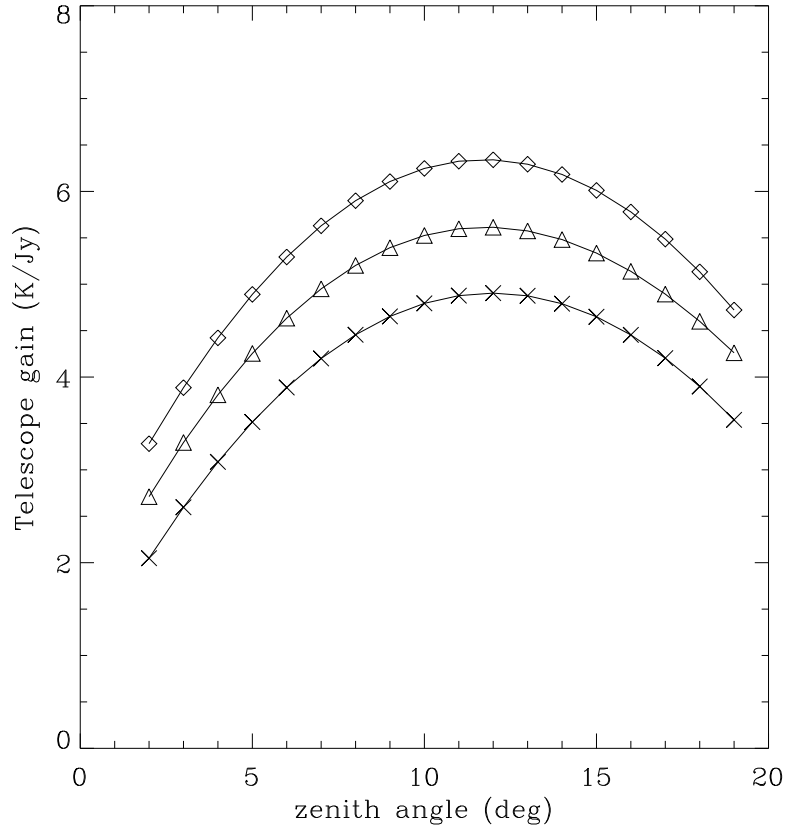


Figure 6.1 The Arecibo telescope gain in K/Jy as a function of zenith angle for three different frequencies. The gain curves at 6600 MHz, 7000 MHz, and 7400 MHz are indicated by diamonds (\diamond), triangles (\triangle), and crosses (\times) respectively.

polarizations. Positions observed during bad weather were typically re-observed so that the spatial noise distribution in a map would be as uniform as possible.

The data reduction was carried out in IDL using procedures maintained by the observatory. The data for each sub-region was reduced to give a data cube. We implemented an automated matched filter algorithm in three dimensions (two spatial dimensions and one frequency dimension) to extract candidate sources from the data cube. The data were first convolved in the frequency domain with a Gaussian of a given line width, since Gaussians are good models for describing

maser line profiles. Each spectral channel image was then output as a FITS file, from which point sources were extracted using SExtractor (Bertin & Arnouts 1996). A convolution filter was applied to the images within SExtractor before extracting the point sources. In our case, this filter was set to the point spread function of the telescope (Figure 5.25) since the masers are unresolved by single dish telescopes. The angular response of the telescope was approximated by a single Gaussian fitted to the two dimensional main lobe of the telescope beam. The procedure above was repeated for different Gaussian line widths in the frequency domain since maser line widths are variable. The convolving line widths varied from 0.05 km s^{-1} to 0.5 km s^{-1} . We tested the algorithm on simulated data cubes to determine the probability of detection for different signal to noise ratios. The results of the simulation are shown in Figure 6.2. The simulation shows that our source extraction algorithm achieves greater than 95% probability of detection for signals that have signal to noise ratio higher than 3.0, and since the noise in the data cubes is no greater than 0.09 Jy, we conclude that our source catalog is complete at the level of 0.27 Jy.

The candidate sources obtained above were re-observed using a one minute position switched observation. These observations were centered on the velocity of the source, and had one pair of boards with a velocity resolution of 0.14 km s^{-1} , and a second pair of boards with a velocity resolution of 0.03 km s^{-1} . These observations enabled us to distinguish real sources from statistical noise fluctuations, and in addition gave high velocity resolution, high signal to noise spectra for all sources. Sources weaker than $\sim 0.5 \text{ Jy}$ were typically observed with a two minutes on source to obtain a high signal to noise ratio. Since we average the two polarizations, our results are not affected by the small levels of linear polarization as observed by Ellingsen (2002).

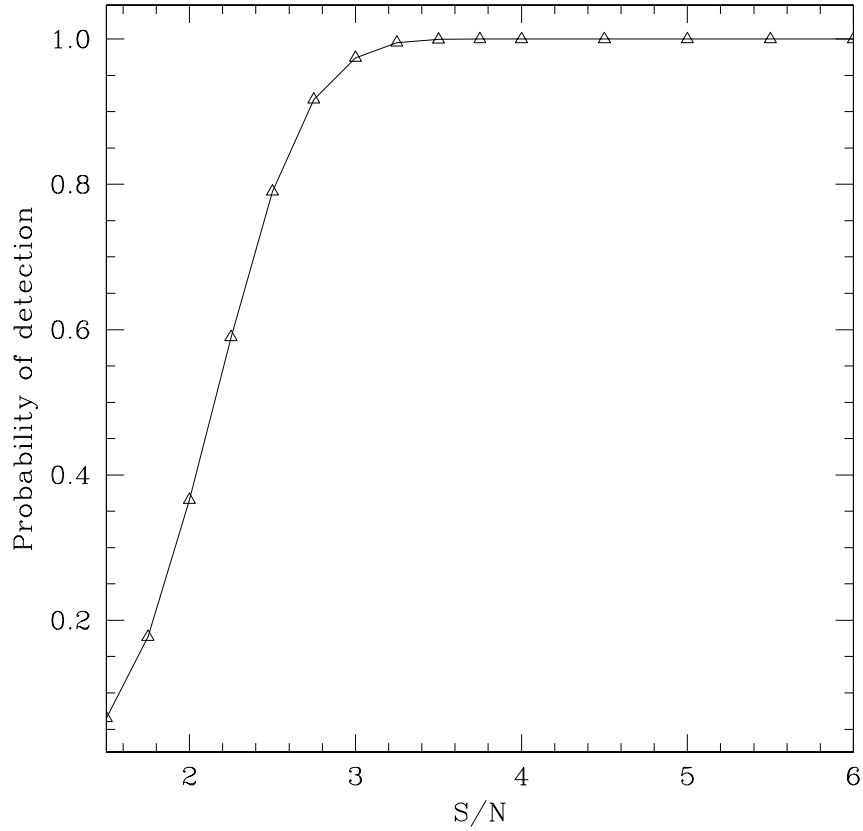


Figure 6.2 The probability of detection of a signal as a function of signal to noise ratio for our source extraction algorithm determined using simulated data cubes. The signal detection probability is greater than 95% for signal to noise ratio of 3.0. The detection threshold used results in a false alarm probability of less than 10^{-7} .

There were instances where emission was discovered at the edges of our data cubes. In these cases, we made additional observations around these positions to determine the spatial peak of emission before carrying out follow-up observations.

6.3 Results

We detected a total of 86 sources, 48 of which are new detections. The region $35.2^\circ \leq l \leq 53.7^\circ$, $|b| \leq 0.41^\circ$ was completely sampled, while a larger area of

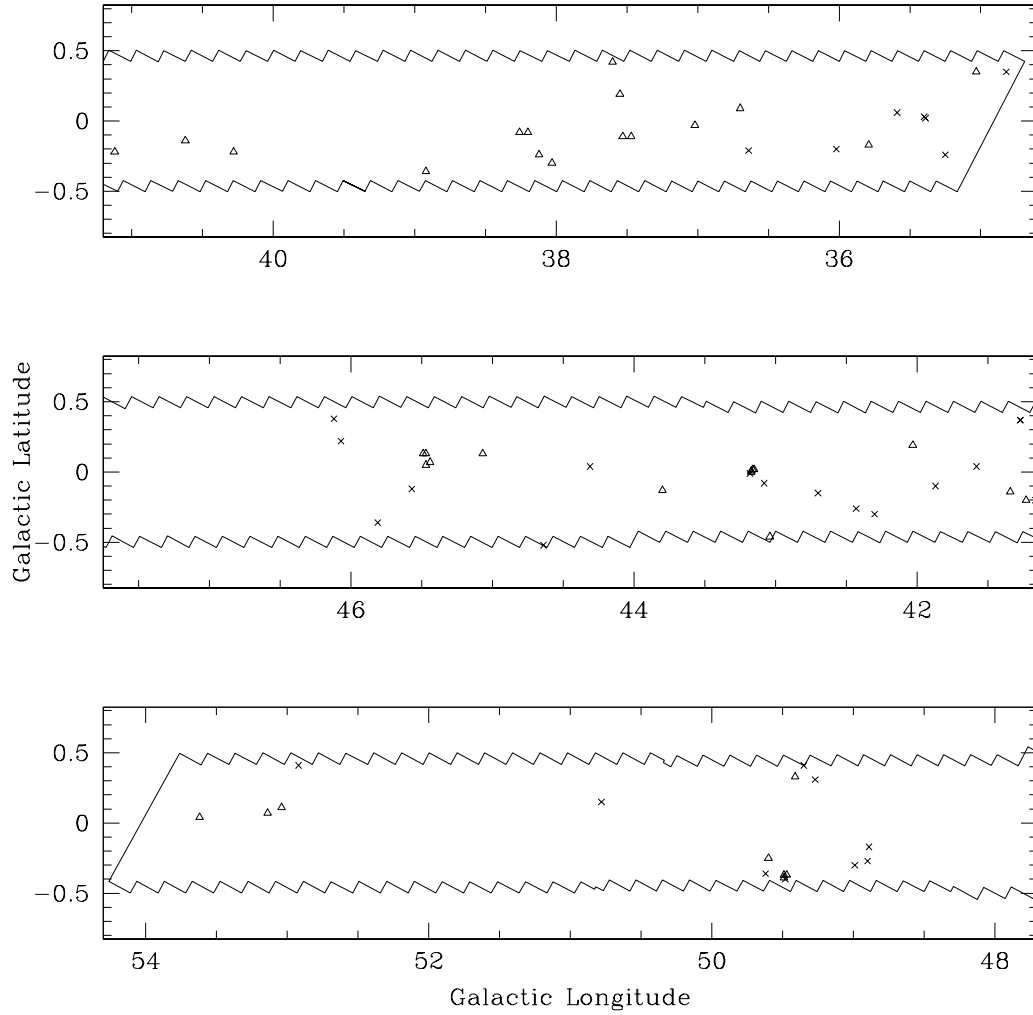


Figure 6.3 The region mapped in the Arecibo Methanol Maser Galactic Plane Survey shown in Galactic coordinates. New detections are denoted by crosses and prior detections are denoted by open triangles. The cluster of sources around $l = 43.2^\circ$ belongs to the W49 region, while the cluster around $l = 49.5^\circ$ belongs to the W51 region.

$34.7^\circ \leq l \leq 54.3^\circ$, $|b| \leq 0.54^\circ$ was incompletely sampled. The region surveyed is shown in Figure 6.3 along with the positions of the detected sources. The important parameters of the sources detected are shown in Table 6.1. In the table, each source is defined by its Galactic coordinates, and is followed by its equatorial coordinates;

Δv is the velocity range of emission, v_p is the velocity of peak emission, S_p is the peak flux density, and S_i is the integrated flux density. Epoch refers to the date of observation and the final column gives the reference for detection of each source.

Some sources in Table 6.1, indicated by the superscript “a”, are relabeled by different l, b coordinates compared to the ones in Pestalozzi et al. (2005) for reasons described later. The source 41.87–0.10 was detected at the edge of a data cube, and could not be detected in successive observations of the region. Hence, the actual coordinates of this source could be different from those quoted here. The source 42.03+0.19 was first detected in the Onsala Survey (which is not yet published in a refereed journal). The coordinates for this source, listed in Pestalozzi et al. (2005), are very different from our coordinates. We think that this could be due to a software problem, similar to the one giving rise to incorrect coordinates for IRAS sources published in Pestalozzi et al. (2005). Hence, we label this source with l, b determined from our coordinates.

Table 6.1: Methanol masers discovered in the Arecibo Methanol Maser Galactic Plane Survey (AMGPS). The columns show the source name, celestial coordinates, velocity range of emission, velocity of peak emission, peak flux density, integrated flux density, epoch of observation and the reference for discovery.

Source (l, b)	α (J2000)	δ (J2000)	Δv	v_p	S_p	S_i	Epoch	Ref.
			km s ⁻¹	km s ⁻¹	Jy	Jy km s ⁻¹		det.
34.82+0.35	18 53 37.4	01 50 32	58.5, 60.1	59.7	0.24	0.10	Oct. 2004	1
35.03+0.35	18 54 01.3	02 01 28	40.2, 47.4	44.4	30.77	27.41	Oct. 2004	2
35.25−0.24	18 56 30.9	01 57 11	56.0, 73.3	72.4	1.47	0.71	Oct. 2004	1
35.39+0.02	18 55 51.2	02 11 37	94.0, 97.2	96.9	0.19	0.11	Oct. 2004	1
35.40+0.03	18 55 51.1	02 12 25	88.8, 90.7	89.1	0.56	0.30	Oct. 2004	1
35.59+0.06	18 56 04.3	02 23 28	43.8, 51.8	45.9	0.82	0.96	Oct. 2004	1
35.79−0.17	18 57 17.5	02 28 04	56.6, 64.9	60.7	22.49	37.74	Oct. 2004	7
36.02−0.20	18 57 45.8	02 39 15	92.4, 93.5	93.0	0.16	0.08	Oct. 2004	1

Continued on next page

Table 6.1 (Continued)

Source (l, b)	α (J2000)	δ (J2000)	Δv	v_p	S_p	S_i	Epoch	Ref.
			km s ⁻¹	km s ⁻¹	Jy	Jy km s ⁻¹		det.
36.64−0.21	18 58 55.9	03 12 05	77.0, 79.3	77.3	1.64	0.52	Apr. 2005	1
36.70+0.09	18 57 59.3	03 24 05	52.2, 63.2	54.7	7.00	8.51	Apr. 2005	7
36.84−0.02	18 59 39.3	03 27 55	52.8, 64.2	61.7	1.66	4.65	Sep. 2005	1
36.90−0.41	19 00 08.6	03 20 35	83.1, 85.1	84.7	0.45	0.26	Apr. 2005	1
36.92+0.48	18 57 00.7	03 46 01	−36.3, −35.6	−35.9	1.52	0.51	Sep. 2005	1
37.02−0.03	18 59 05.1	03 37 47	77.5, 85.3	78.4	7.24	4.77	Sep. 2005	7
37.38−0.09	18 59 52.3	03 55 12	67.5, 70.9	70.6	0.19	0.13	Sep. 2005	1
37.47−0.11	19 00 08.1	03 59 49	53.6, 63.3	54.7	9.83	22.41	Sep. 2005	7
37.53−0.11	19 00 17.4	04 03 15	48.2, 56.6	50.0	4.48	5.77	Sep. 2005	5
37.55+0.19	18 59 11.4	04 12 14	78.1, 88.2	83.7	5.27	6.44	Sep. 2005	4
37.60+0.42	18 58 28.0	04 20 46	84.6, 94.7	85.8	17.30	25.29	Sep. 2005	7
37.74−0.12	19 00 38.0	04 13 18	49.9, 50.5	50.3	0.93	0.25	Sep. 2005	1

Continued on next page

Table 6.1 (Continued)

Source (l, b)	α (J2000)	δ (J2000)	Δv	v_p	S_p	S_i	Epoch	Ref.
			km s ⁻¹	km s ⁻¹	Jy	Jy km s ⁻¹		det.
37.76–0.19	19 00 56.5	04 12 08	54.9, 66.0	55.1	0.59	1.46	Sep. 2005	1
37.77–0.22	19 01 03.0	04 12 13	68.8, 70.3	69.6	0.82	0.37	Sep. 2005	1
38.03–0.30	19 01 51.4	04 24 16	54.6, 65.9	55.6	11.71	18.10	Sep. 2005	7
38.08–0.27	19 01 48.4	04 27 25	66.7, 67.8	67.5	0.59	0.18	Sep. 2005	1
38.12–0.24	19 01 45.2	04 30 32	66.5, 79.7	70.2	1.92	5.67	Sep. 2005	5
38.20–0.08	19 01 20.1	04 39 37	77.7, 88.5	79.6	11.09	16.26	Sep. 2005	7
38.26–0.08	19 01 27.2	04 42 09	6.1, 15.9	15.4	7.03	5.39	Sep. 2005	7
38.26–0.20	19 01 54.0	04 38 38	64.1, 73.5	70.2	0.72	1.28	Sep. 2005	1
38.56+0.15	19 01 10.3	05 04 26	23.1, 31.2	31.5	0.18	0.13	Sep. 2005	1
38.60–0.21	19 02 34.0	04 56 40	61.4, 69.5	62.6	0.57	0.59	Sep. 2005	1
38.66+0.08	19 01 36.7	05 07 42	–31.9, –30.7	–31.5	2.19	0.71	Sep. 2005	1
38.92–0.36 ^a	19 03 39.7	05 09 36	30.8, 33.5	31.9	1.26	1.29	Sep. 2005	5

Continued on next page

Table 6.1 (Continued)

Source (l, b)	α (J2000)	δ (J2000)	Δv	v_p	S_p	S_i	Epoch	Ref.
			km s ⁻¹	km s ⁻¹	Jy	Jy km s ⁻¹		det.
39.39–0.14	19 03 45.3	05 40 39	58.2, 75.5	60.4	1.14	0.77	Sep. 2005	1
39.54–0.38	19 04 53.5	05 41 59	47.4, 49.4	47.8	0.20	0.24	Sep. 2005	1
40.28–0.22 ^a	19 05 42.1	06 26 08	62.4, 85.7	73.9	24.47	68.03	Oct. 2005	5
40.62–0.14	19 06 02.3	06 46 37	29.7, 36.7	31.1	15.20	6.97	Oct. 2005	2
40.94–0.04	19 06 16.1	07 06 00	36.2, 43.2	36.6	2.35	1.50	Oct. 2005	1
41.08–0.13	19 06 49.3	07 11 01	57.2, 58.4	57.5	0.79	0.33	Oct. 2005	1
41.12–0.11	19 06 50.7	07 13 57	33.1, 37.4	36.6	1.14	0.63	Oct. 2005	1
41.12–0.22 ^a	19 07 15.4	07 10 54	55.0, 66.6	63.4	2.01	1.23	Oct. 2005	5
41.16–0.20	19 07 15.1	07 13 20	61.6, 63.8	63.6	0.27	0.20	Oct. 2005	1
41.23–0.20 ^a	19 07 21.9	07 17 06	54.0, 64.9	55.4	3.46	7.55	Oct. 2005	5
41.27+0.37	19 05 24.6	07 35 02	19.4, 20.6	20.3	0.26	0.16	Oct. 2005	1
41.34–0.14	19 07 22.8	07 25 17	6.6, 15.0	11.7	17.80	25.40	Oct. 2005	6

Continued on next page

Table 6.1 (Continued)

Source (l, b)	α (J2000)	δ (J2000)	Δv	v_p	S_p	S_i	Epoch	Ref.
			km s ⁻¹	km s ⁻¹	Jy	Jy km s ⁻¹		det.
41.58+0.04	19 07 09.4	07 42 19	10.4, 12.3	11.9	0.50	0.22	Oct. 2005	1
41.87−0.10	19 08 10.8	07 54 04	15.5, 23.7	15.8	0.22	0.10	Oct. 2005	1
42.03+0.19	19 07 29.0	08 10 39	6.8, 17.3	12.8	26.32	30.10	Oct. 2005	6
42.30−0.30	19 09 44.2	08 11 33	26.2, 34.7	28.1	6.33	5.07	Oct. 2005	1
42.43−0.26	19 09 50.2	08 19 32	65.8, 69.1	66.8	1.91	1.61	Oct. 2005	1
42.70−0.15	19 09 55.8	08 36 56	−47.1, −39.0	−42.9	3.25	4.03	Oct. 2005	1
43.04−0.46 ^a	19 11 39.7	08 46 32	54.1, 63.6	54.8	7.19	10.39	Oct. 2005	5
43.08−0.08	19 10 22.4	08 59 01	9.6, 14.9	10.2	9.20	4.11	Oct. 2005	1
43.15+0.02	19 10 11.9	09 05 24	12.3, 14.3	13.3	24.29	12.03	Oct. 2005	3
43.16+0.02	19 10 13.9	09 06 16	6.8, 22.1	9.3	27.77	50.54	Oct. 2005	3
43.17+0.01	19 10 16.1	09 06 16	18.1, 22.4	19.0	9.27	15.05	Oct. 2005	3
43.17−0.00	19 10 17.7	09 05 54	−1.7, 4.2	−1.2	2.68	1.44	Oct. 2005	3

Continued on next page

Table 6.1 (Continued)

Source (l, b)	α (J2000)	δ (J2000)	Δv	v_p	S_p	S_i	Epoch	Ref.
			km s ⁻¹	km s ⁻¹	Jy	Jy km s ⁻¹		det.
43.18–0.01	19 10 20.2	09 06 06	10.3, 11.6	11.1	0.88	0.63	Oct. 2005	1
43.80–0.13	19 11 54.8	09 35 48	38.4, 43.6	39.6	55.56	43.18	Mar. 2006	2
44.31+0.04	19 12 16.4	10 07 44	55.0, 56.6	55.7	0.66	0.43	Mar. 2006	1
44.64–0.52	19 14 54.6	10 10 02	48.8, 49.9	49.3	0.55	0.29	Mar. 2006	1
45.07+0.13	19 13 22.5	10 51 01	56.8, 60.0	57.8	48.27	22.26	Mar. 2006	2
45.44+0.07	19 14 19.0	11 09 07	49.1, 50.6	50.0	1.09	0.71	Mar. 2006	3
45.47+0.05	19 14 24.5	11 09 40	55.4, 59.8	56.0	5.69	9.40	Mar. 2006	2
45.47+0.13	19 14 08.2	11 12 24	57.0 73.5	65.7	5.49	4.88	Mar. 2006	2
45.49+0.13	19 14 11.8	11 13 13	56.7, 66.4	57.2	8.77	4.98	Mar. 2006	3
45.57–0.12	19 15 13.2	11 10 25	1.2, 9.8	1.6	0.40	0.30	Mar. 2006	1
45.81–0.36	19 16 31.9	11 16 22	54.7, 70.8	59.9	11.31	8.41	Mar. 2006	1
46.07+0.22	19 14 55.6	11 46 12	22.3, 25.1	23.3	1.23	1.20	Apr. 2006	1

Continued on next page

Table 6.1 (Continued)

Source (l, b)	α (J2000)	δ (J2000)	Δv	v_p	S_p	S_i	Epoch	Ref.
			km s ⁻¹	km s ⁻¹	Jy	Jy km s ⁻¹		det.
46.12+0.38	19 14 26.4	11 53 24	57.5, 62.9	59.0	1.13	1.05	Apr. 2006	1
48.89−0.17	19 21 47.5	14 04 58	57.2, 57.5	57.3	0.13	0.02	Oct. 2004	1
48.90−0.27	19 22 10.1	14 02 38	63.6, 72.5	72.0	0.83	0.57	Oct. 2004	1
48.99−0.30	19 22 26.3	14 06 37	62.5, 72.6	71.6	0.58	0.55	Oct. 2004	1
49.27+0.31	19 20 44.8	14 38 29	−6.8, 7.5	−3.2	8.12	13.71	Oct. 2004	1
49.35+0.41	19 20 33.2	14 45 48	66.1, 69.2	68.0	7.00	6.72	Apr. 2005	1
49.41+0.33 ^a	19 20 58.9	14 46 46	−27.0, −9.8	−12.1	9.25	23.18	Apr. 2005	5
49.47−0.37	19 23 38.3	14 29 58	55.6, 76.1	63.8	7.01	17.35	Oct. 2004	3
49.48−0.40	19 23 46.1	14 29 38	47.7, 65.3	51.4	8.06	14.90	Oct. 2004	1
49.49−0.37	19 23 40.0	14 31 04	54.4, 65.7	56.1	32.27	49.27	Oct. 2004	2
49.49−0.39	19 23 43.9	14 30 31	49.9, 65.0	59.3	738.4	574.7	Oct. 2004	3
49.60−0.25 ^a	19 23 26.7	14 40 19	59.9, 66.7	62.9	38.11	78.16	Oct. 2004	5

Continued on next page

Table 6.1 (Continued)

Source (l, b)	α (J2000)	δ (J2000)	Δv	v_p	S_p	S_i	Epoch	Ref.
			km s ⁻¹	km s ⁻¹	Jy	Jy km s ⁻¹		det.
49.62–0.36	19 23 52.8	14 38 10	48.8, 60.1	49.3	1.23	1.13	Oct. 2004	1
50.78+0.15	19 24 17.2	15 53 54	47.6, 50.9	49.1	5.26	2.79	Sep. 2005	1
52.92+0.41	19 27 35.2	17 54 26	38.8, 45.0	39.1	6.64	4.68	Mar. 2006	1
53.04+0.11 ^a	19 28 55.7	17 52 01	9.7, 10.5	10.1	1.66	0.69	Mar. 2006	5
53.14+0.07 ^a	19 29 17.5	17 56 24	23.4, 25.4	24.6	1.02	0.54	Mar. 2006	5
53.62+0.04 ^a	19 30 22.6	18 20 28	18.2, 19.5	19.0	18.94	7.16	Mar. 2006	5

References — (1) This paper; (2) Menten 1991b; (3) Caswell et al. 1995; (4) Slysh et al. 1999;
(5) Szymczak et al. 2000; (6) Pestalozzi et al. 2002; (7) Szymczak et al. 2002.

Individual spectra for all sources are shown in Figure 6.4. Spectra of previously detected sources are included in part because most have much higher signal to noise compared to previous observations, and in part for variability studies.

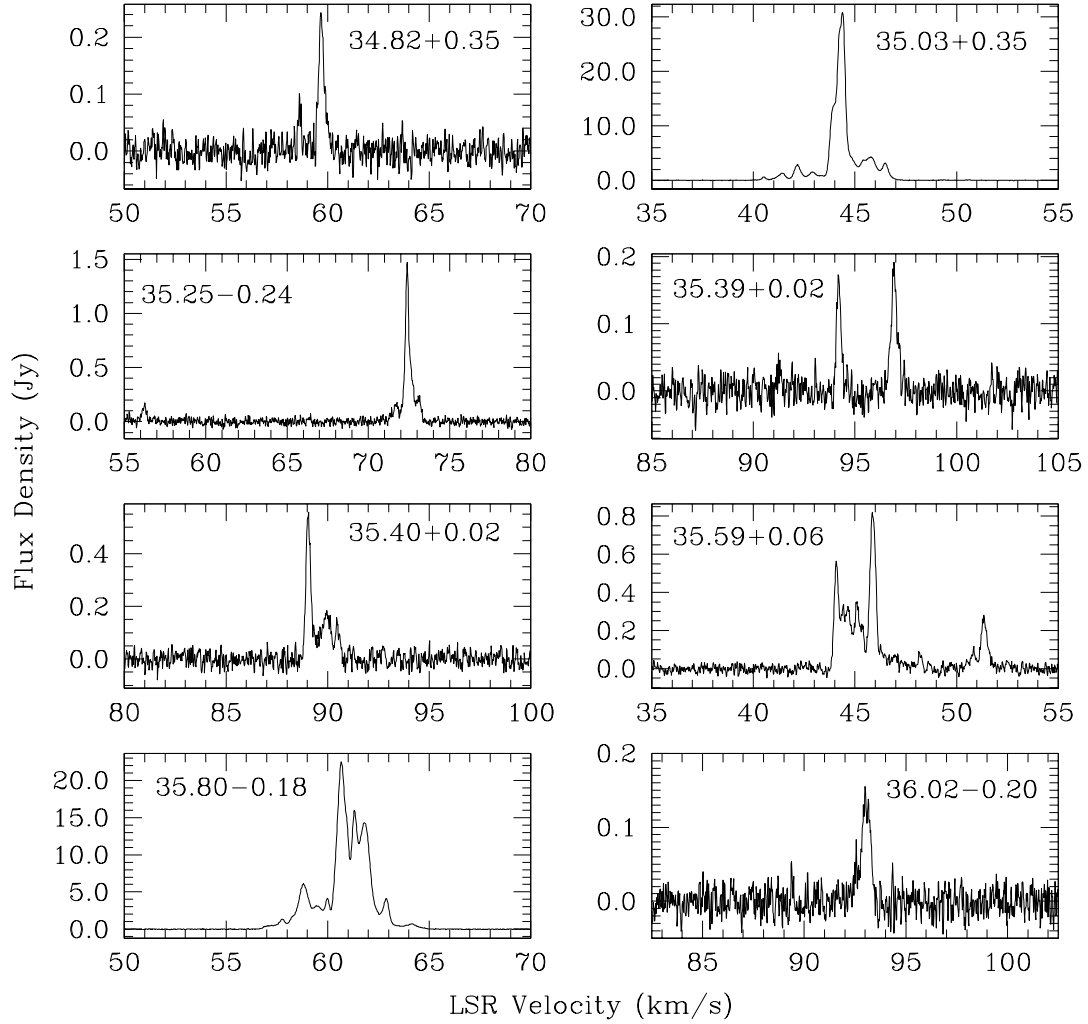


Figure 6.4 Spectra of 6.7 GHz methanol masers detected in the Arecibo Methanol Maser Galactic Plane Survey. The velocity resolution of all spectra is 0.03 km s⁻¹.

Figure 6.4 (Continued)

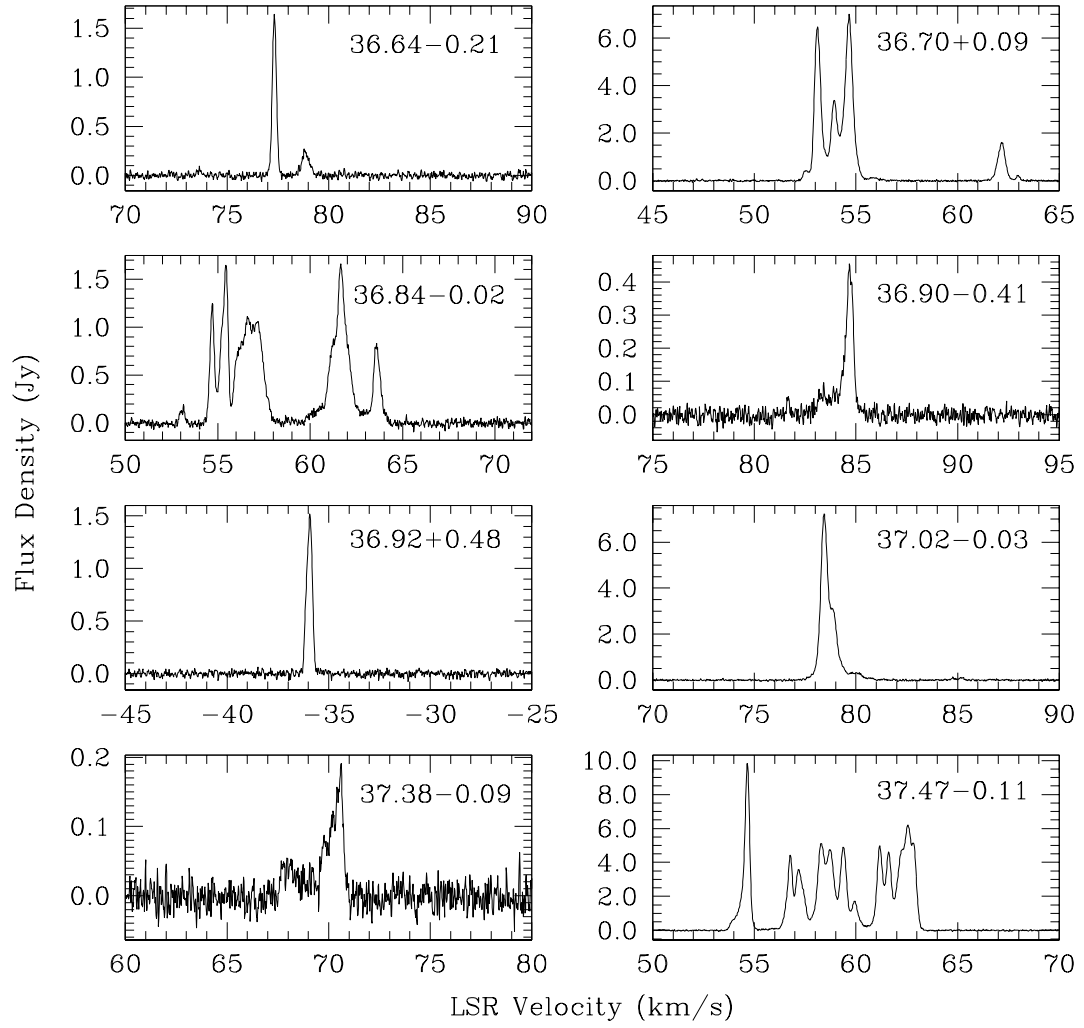


Figure 6.4 (Continued)

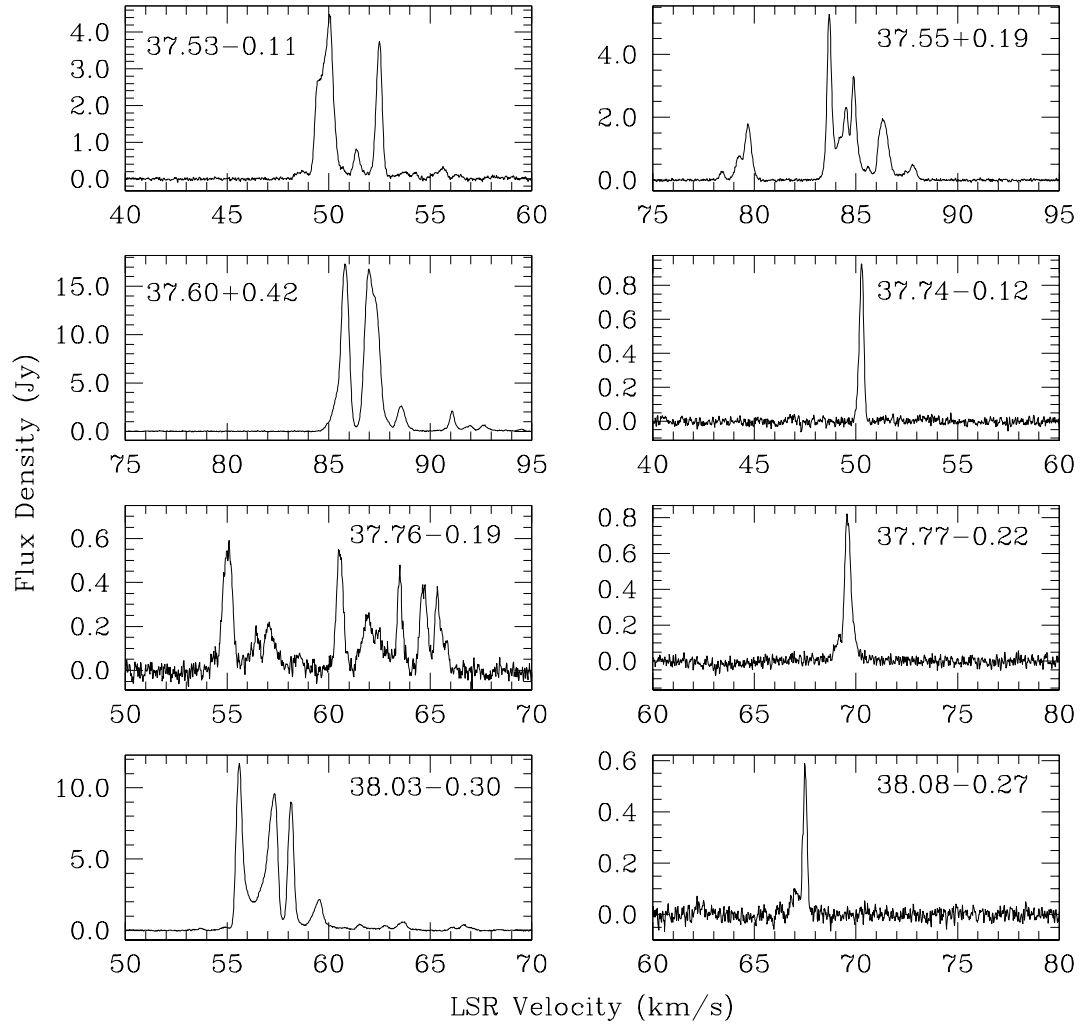


Figure 6.4 (Continued)

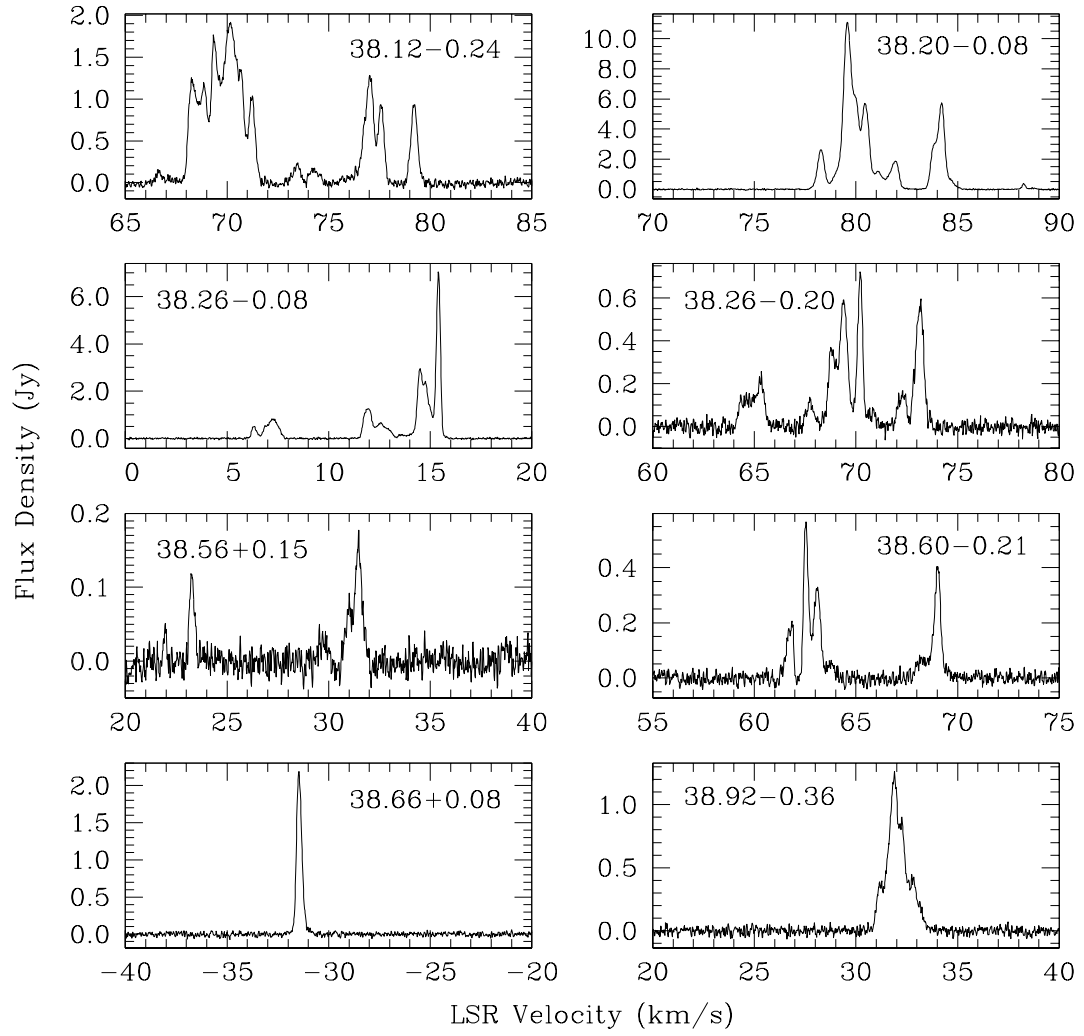


Figure 6.4 (Continued)

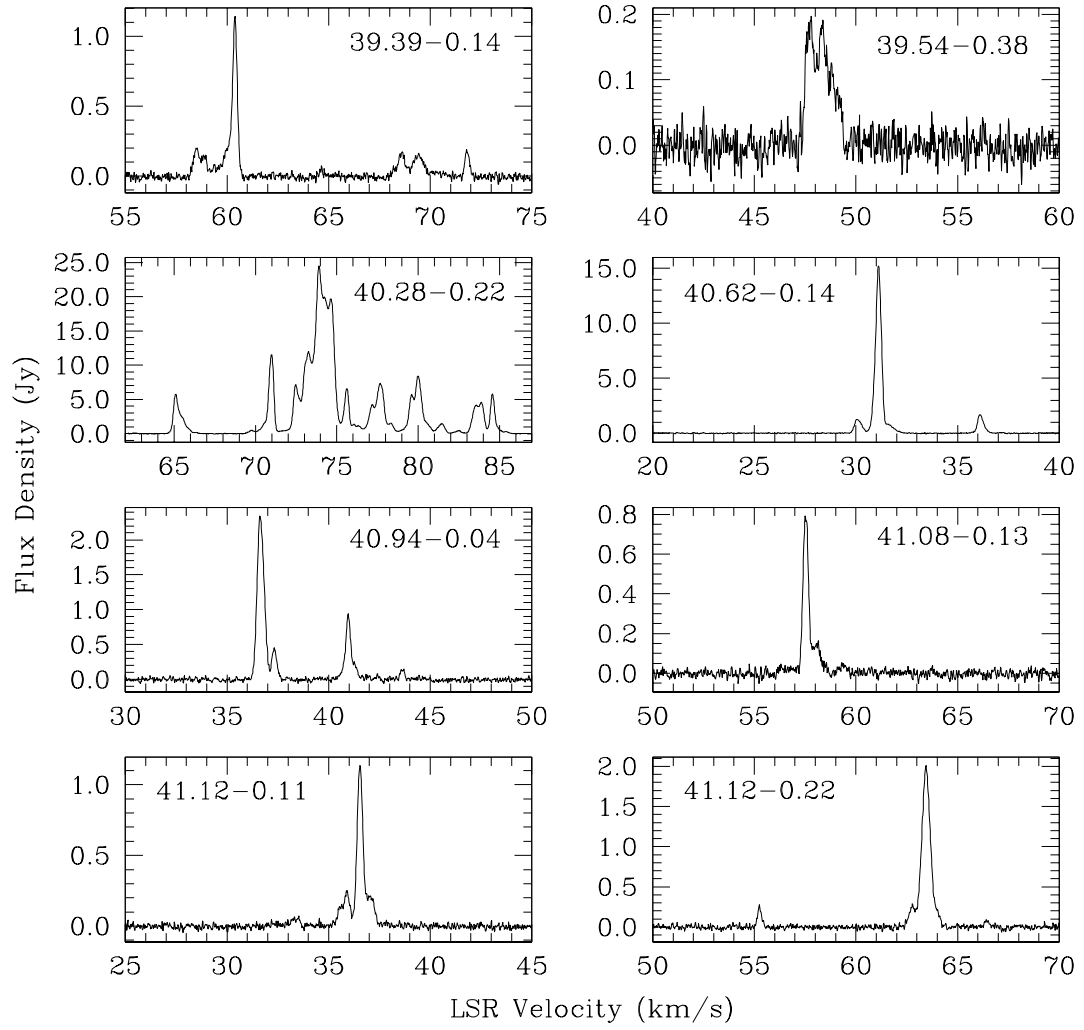


Figure 6.4 (Continued)

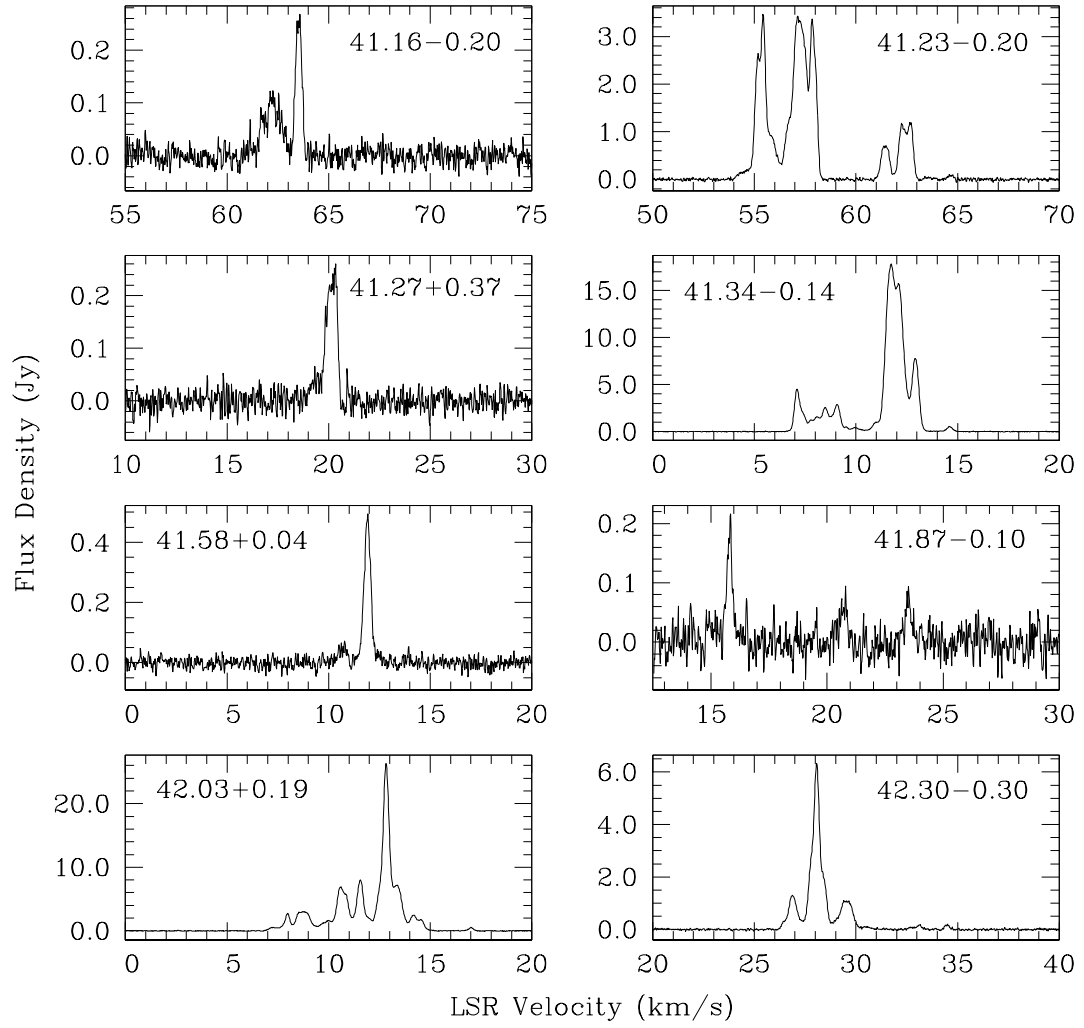


Figure 6.4 (Continued)

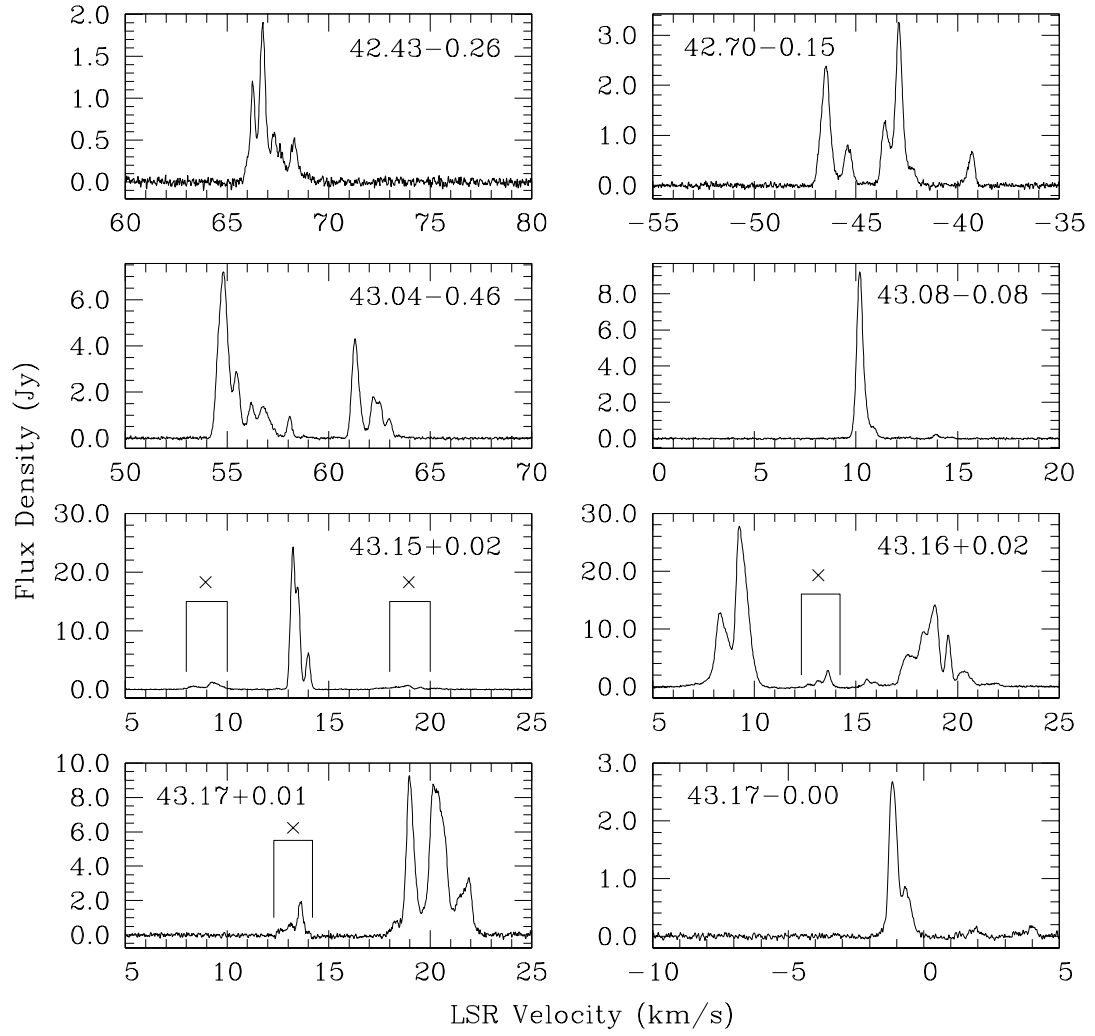


Figure 6.4 (Continued)

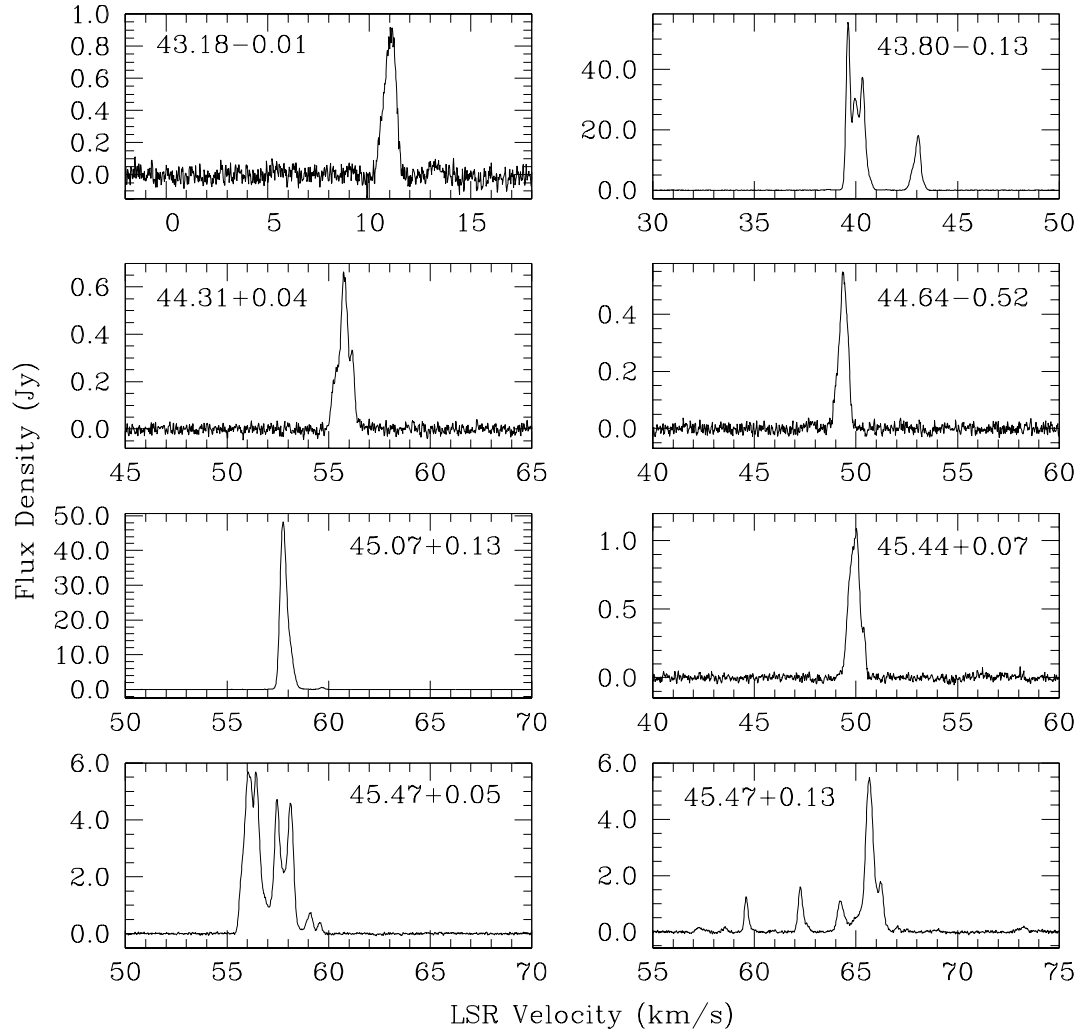


Figure 6.4 (Continued)

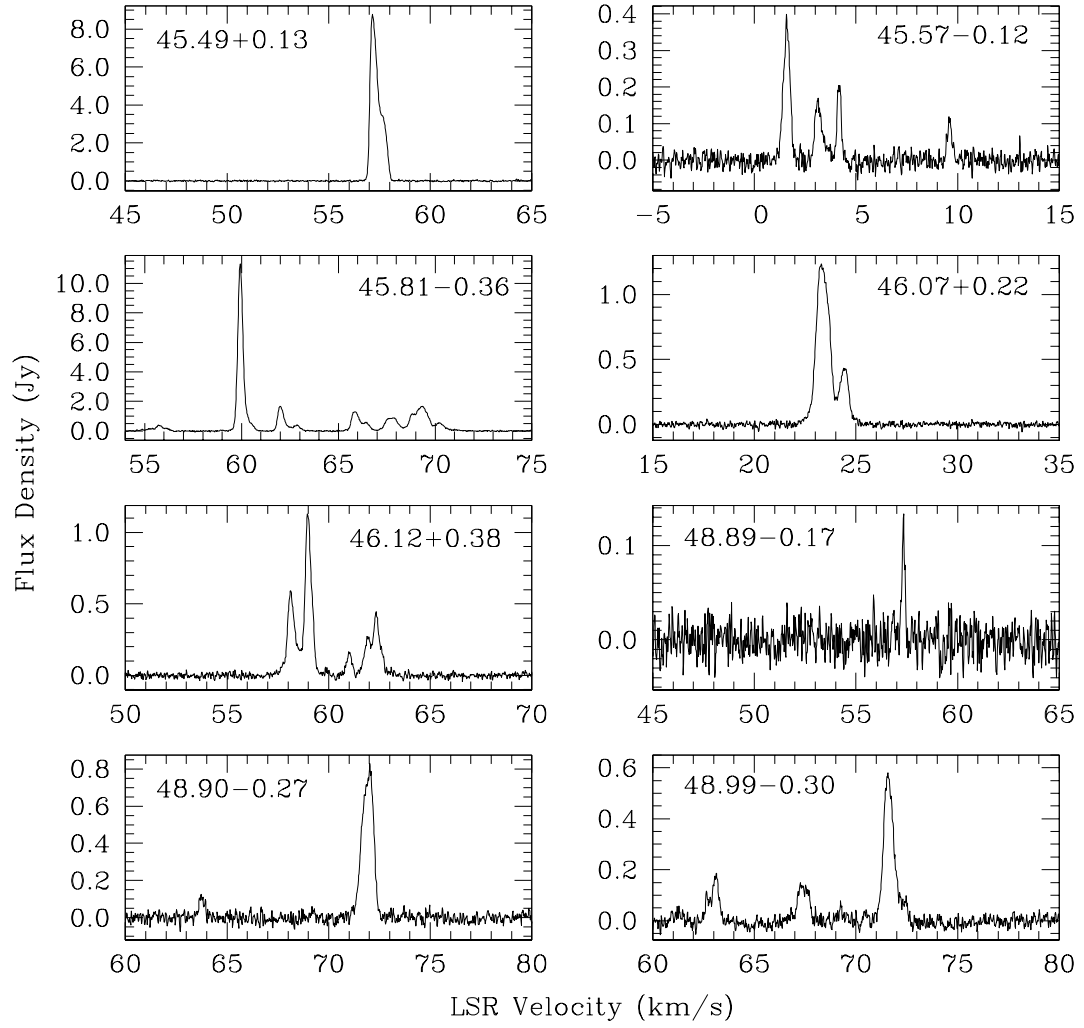


Figure 6.4 (Continued)

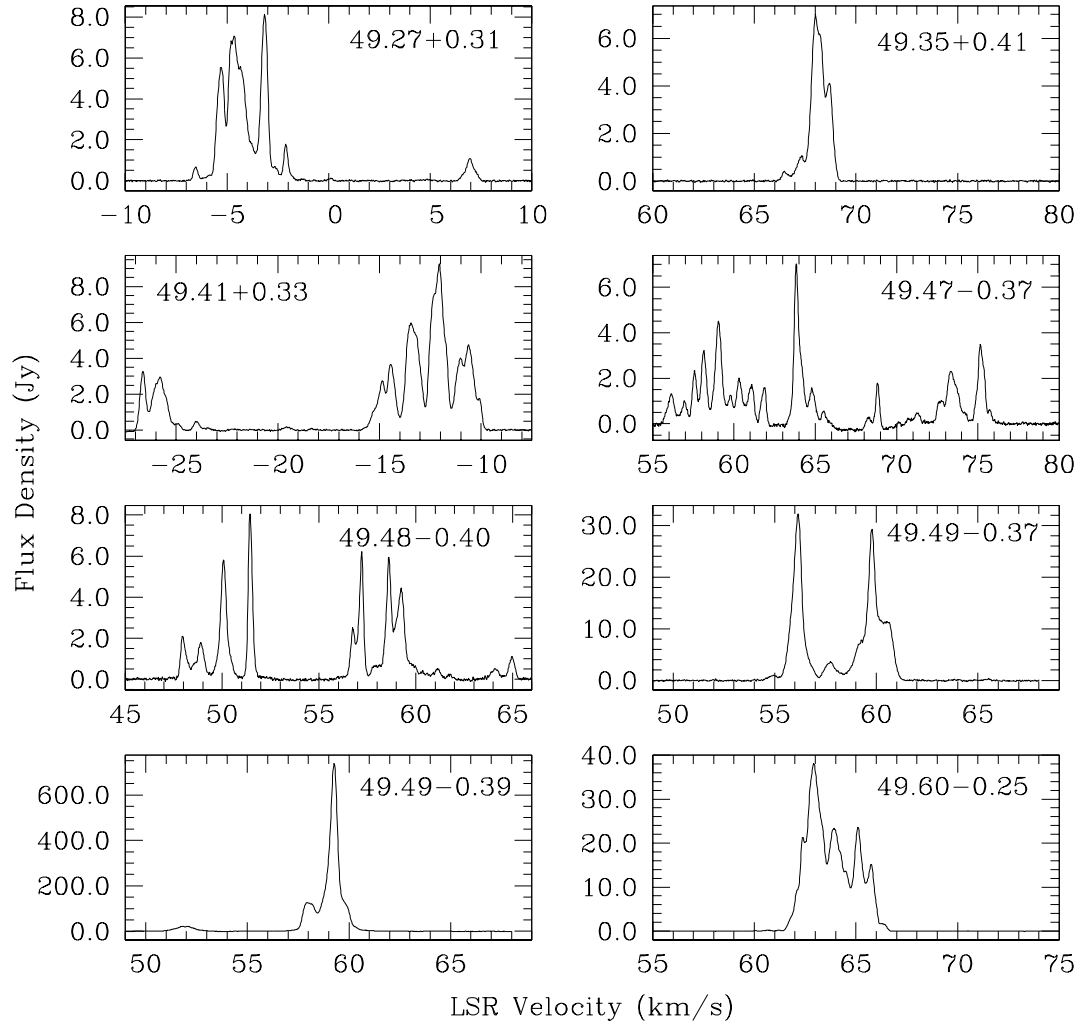
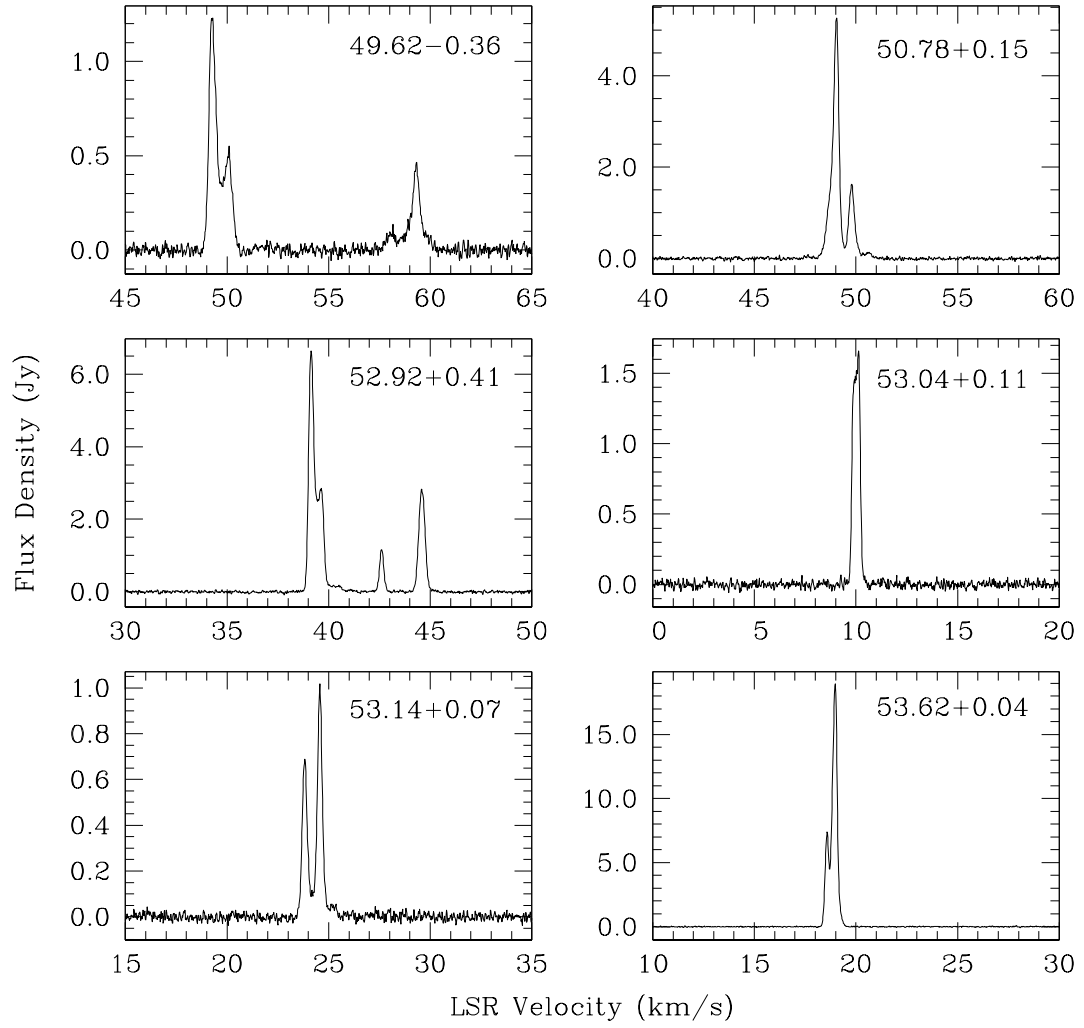


Figure 6.4 (Continued)



We note that the source 49.57–0.38 listed in the general catalog of 6.7 GHz methanol masers (Pestalozzi et al. 2005) is a sidelobe of source 49.49–0.39 (W51) as mentioned by Szymczak et al. (2000). We were also unable to detect the source 49.66–0.45 which was observed towards IRAS 19220+1431 by Slysh et al. (1999). While this could be due to source variability, the non-detection of this source by van der Walt et al. (1995), coincidence of the velocity of peak emission with that of the strong nearby source 49.49–0.39, and the difference between the velocity range of the maser and that of the CS (2–1) line (Bronfman et al. 1996) strongly suggest that this source is also a sidelobe of 49.49–0.39.

Previously published data on known detections is summarized in Table 6.2. In particular, we list the difference between the position determined from our data cubes and that published previously, $\Delta\theta$, peak flux density, S_p and epoch of the observation. We found that the positions of the IRAS sources surveyed by Szymczak et al. (2000), that are listed in the general catalog of methanol masers (Pestalozzi et al. 2005) are incorrect, often by $1'$. This in turn results in incorrect Galactic coordinates being calculated, with which the sources are named. Further, since the true position of the methanol maser is often offset from the position of the IRAS source, we choose to re-label the names of these sources with Galactic coordinates calculated from our survey. We also re-label a source in the general catalog that was detected in the unpublished Onsala Survey, whose coordinates differ from ours by $6'$. We retain the names of all other sources that were published elsewhere, even if their Galactic coordinates differ from that calculated from our positions, for the sake of consistency.

Table 6.2: Previously published data compared with our data for known detections.

Source	α	δ	$\Delta\theta$	Ref.	Epoch	S
	(J2000)	(J2000)	($''$)		(Jy)	
35.03+0.35	18 54 01.3	02 01 28	...	1	Oct. 2004	30.8
	18 54 00.6	02 00 50	39	7	2000	38.9
	18 54 00.6	02 01 15	17	3	1992	56
	18 54 01.8	02 01 19	12	2	Jun. 1991	50
35.79-0.17	18 57 17.5	02 28 04	...	1	Oct. 2004	22.5
	18 57 16.1	02 27 44	29	7	2000	24.5
36.70+0.09	18 57 59.3	03 24 05	...	1	Apr. 2005	7.0
	18 58 00.9	03 23 30	42	7	2000	8.6
37.02-0.03	18 59 05.1	03 37 47	...	1	Sep. 2005	7.2
	18 58 59.9	03 37 40	78	7	2000	7.1
37.47-0.11	19 00 08.1	03 59 49	...	1	Sep. 2005	9.8
	19 00 06.7	03 59 27	30	7	2000	12.5
37.53-0.11	19 00 17.4	04 03 15	...	1	Sep. 2005	4.5
	19 00 14.4	04 02 35	60	7	2000	5.8
	19 00 15.8	04 03 07	25	5	Jul. 1999	5.7
37.55+0.19	18 59 11.4	04 12 14	...	1	Sep. 2005	5.3
	18 59 11.6	04 12 08	7	7	2000	8.1
	18 59 09.9	04 12 14	22	5	Aug. 1999	6.6
	18 59 09.9	04 12 14	22	4	Mar./Apr. 1999	4

Continued on next page

Table 6.2 (Continued)

Source	α (J2000)	δ (J2000)	$\Delta\theta$ ($''$)	Ref.	Epoch (Jy)	S
37.60+0.42	18 58 28.0	04 20 46	...	1	Sep. 2005	17.3
	18 58 28.5	04 20 34	14	7	2000	24.3
38.03-0.30	19 01 51.4	04 24 16	...	1	Sep. 2005	11.7
	19 01 50.0	04 23 54	30	7	2000	18.6
38.12-0.24	19 01 45.2	04 30 32	...	1	Sep. 2005	1.9
	19 01 47.6	04 30 32	36	7	2000	4.2
	19 01 43.0	04 30 45	35	5	Jul. 1999	2.3
38.20-0.08	19 01 20.1	04 39 37	...	1	Sep. 2005	11.1
	19 01 22.8	04 39 10	49	7	2000	8.4
38.26-0.08	19 01 27.2	04 42 09	...	1	Sep. 2005	7.0
	19 01 28.7	04 42 02	23	7	2000	7.9
38.92-0.36	19 03 39.7	05 09 36	...	1	Sep. 2005	1.3
	19 03 43.5	05 09 49	58	5	Mar. 1999	5.4
40.28-0.22	19 05 42.1	06 26 08	...	1	Oct. 2005	24.5
	19 05 36.4	06 26 09	85	5	Aug. 1999	18
40.62-0.14	19 06 02.3	06 46 37	...	1	Oct. 2005	15.2
	19 06 00.8	06 46 37	22	3	1992	17
	19 06 01.1	06 46 35	18	2	Jun. 1991	14
41.12-0.22	19 07 15.4	07 10 54	...	1	Oct. 2005	2.0

Continued on next page

Table 6.2 (Continued)

Source	α (J2000)	δ (J2000)	$\Delta\theta$ ($''$)	Ref.	Epoch (Jy)	S
	19 07 16.9	07 10 02	57	5	Aug. 1999	3.7
41.23–0.20	19 07 21.9	07 17 06	...	1	Oct. 2005	3.5
	19 07 21.0	07 17 25	23	5	Aug. 1999	3.2
41.34–0.14	19 07 22.8	07 25 17	...	1	Oct. 2005	17.8
	19 07 21.870	07 25 17.34	14	6	?	51
42.03+0.19	19 07 29.0	08 10 39	...	1	Oct. 2005	26.3
	19 07 20.8	08 14 12	245	6	?	12
43.04–0.46	19 11 39.7	08 46 32	...	1	Oct. 2005	7.2
	19 11 37.4	08 46 30	34	5	Jun. 1999	10
43.15+0.02	19 10 11.9	09 05 24	...	1	Oct. 2005	24.3
	19 10 10.6	09 05 27	19	3	1992	26
43.16+0.02	19 10 13.9	09 06 16	...	1	Oct. 2005	27.8
	19 10 15.3	09 06 08	22	5	Jun. 1999	31
	19 10 11.9	09 06 15	30	3	1992	22
	19 10 13.5	09 06 11	8	2	Jun. 1991	28
43.17+0.01	19 10 16.1	09 06 16	...	1	Oct. 2005	9.4
	19 10 14.6	09 06 18	22	3	1992	12.8
43.17–0.00	19 10 17.7	09 05 54	...	1	Oct. 2005	2.7
	19 10 16.2	09 06 02	24	3	1992	3.4

Continued on next page

Table 6.2 (Continued)

Source	α (J2000)	δ (J2000)	$\Delta\theta$ ($''$)	Ref.	Epoch (Jy)	S
43.80–0.13	19 11 54.8	09 35 48	...	1	Mar. 2006	55.6
	19 11 53.3	09 35 46	22	5	Jun. 1999	79
	19 11 53.8	09 35 46	15	3	1992	144
	19 11 53.9	09 35 51	14	2	Jun. 1991	152
45.07+0.13	19 13 22.5	10 51 01	...	1	Mar. 2006	48.3
	19 13 22.0	10 50 52	12	5	Jul. 1999	45
	19 13 22.2	10 50 52	10	3	1992	33
	19 13 22.1	10 50 54	9	2	Jun. 1991	42
45.44+0.07	19 14 19.0	11 09 07	...	1	Mar. 2006	1.1
	19 14 21.7	11 09 14	40	5	May 1999	4.1
	19 14 17.9	11 08 58	19	3	1992	1.9
45.47+0.05	19 14 24.5	11 09 40	...	1	Mar. 2006	5.7
	19 14 25.7	11 09 26	23	2	Jun. 1991	3
45.47+0.13	19 14 08.2	11 12 24	...	1	Mar. 2006	5.5
	19 14 08.6	11 12 27	7	5	Jul. 1999	10
	19 14 07.5	11 12 17	12	3	1992	5.3
	19 14 08.8	11 12 28	10	2	Jun. 1991	15
45.49+0.13	19 14 11.8	11 13 13	...	1	Mar. 2006	8.8
	19 14 11.3	11 13 07	9	3	1992	13.4
49.41+0.33	19 20 58.9	14 46 46	...	1	Apr. 2005	9.3

Continued on next page

Table 6.2 (Continued)

Source	α (J2000)	δ (J2000)	$\Delta\theta$ ($''$)	Ref.	Epoch (Jy)	S
	19 20 57.0	14 46 40	28	5	Jul. 1999	13
49.47–0.37	19 23 38.3	14 28 58	...	1	Oct. 2004	7.0
	19 23 38.3	14 30 09	71	3	1992	12
49.49–0.37	19 23 40.0	14 31 04	...	1	Oct. 2004	32.3
	19 23 39.5	14 31 01	8	3	1992	33
49.49–0.39	19 23 43.9	14 30 31	...	1	Oct. 2004	738.4
	19 23 43.4	14 30 35	8	3	1992	850
	19 23 42.1	14 30 41	28	2	Jun. 1991	979
49.60–0.25	19 23 26.7	14 40 19	...	1	Oct. 2004	38.1
	19 23 27.9	14 38 11	129	5	Jul. 1999	29
53.04+0.11	19 28 55.7	17 52 01	...	1	Mar. 2006	1.7
	19 28 54.0	17 51 56	25	5	Jul. 1999	3.3
53.14+0.07	19 29 17.5	17 56 24	...	1	Mar. 2006	1.0
	19 29 17.7	17 56 20	5	5	Aug. 1999	1.1
53.62+0.04	19 30 22.6	18 20 28	...	1	Mar. 2006	18.9
	19 30 28.1	18 20 53	82	5	Jul. 1999	6.3

References — (1) This paper; (2) Menten 1991b; (3) Caswell et al. 1995;
(4) Slysh et al. 1999; (5) Szymczak et al. 2000; (6) Pestalozzi et al. 2002;
(7) Szymczak et al. 2002.

6.4 Notes on selected sources

38.92-0.36. This source was detected by Szymczak et al. (2000) towards IRAS 19012+0505 as a 5.4 Jy source, but was undetected by Szymczak et al. (2002). We measured a peak flux density of 1.26 Jy towards this source in Sep. 2005. Thus, peak flux density of this source has decreased by a factor of 4.3 in 6.5 years, and by at least a factor of 2 in one year given the detection limits of Szymczak et al. (2002).

41.87-0.10. This is a mysterious source. We detected this source at right ascension $19^h08^m10^s.8$, declination $07^\circ54'04''$ in the survey data taken on Oct. 1, 2005. The source had a peak flux density of 0.84 Jy at a velocity of 23.3 km s^{-1} (Figure 6.5). However, the follow-up data taken on Oct. 19, 2005 revealed a different spectrum with a peak flux density of 0.22 Jy at a velocity of 15.8 km s^{-1} , while the feature around 23.3 km s^{-1} had a peak flux density of only 0.09 Jy (Figure 6.5). Future attempts to detect this source were unsuccessful. The 3σ limits on the source are 0.27 Jy, 0.08 Jy and 0.07 Jy on Oct. 22, 2005, Nov. 15, 2005 and Mar. 23, 2006 respectively. Since there are no nearby strong sources at this velocity, it is unlikely that this source is a side-lobe detection. Since the source happened to lie at the edge of our map of the region, we are not sure about the accuracy of the source position.

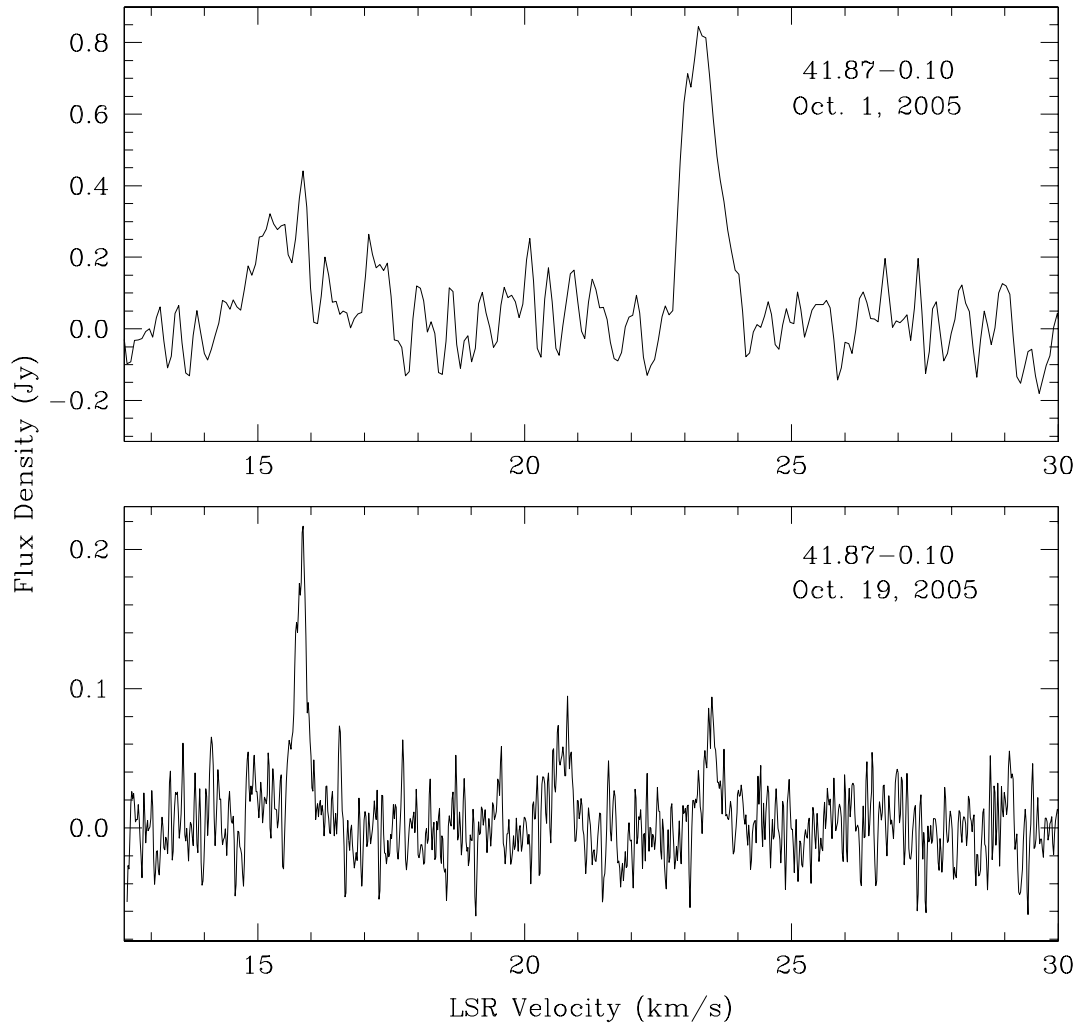


Figure 6.5 The top panel shows the spectrum of source 41.87–0.10 from the survey data obtained on Oct. 1, 2005. The bottom panel shows the spectrum of the same source obtained in follow-up observations on Oct. 19, 2005. The source was undetected in all subsequent observations.

W49N region. This is a complex region containing a cluster of methanol masers. In order to distinguish the different masing regions, we first identified the different spectral features at various locations in the region. Next, we identified the spatial peaks of each spectral feature. This enabled us to identify at least five distinct

regions with methanol emission. Four of these regions were also identified by Caswell et al. (1995).

The source 43.15+0.02 has a peak flux density of 24.3 Jy at 13.3 km s⁻¹. 43.16+0.02 has a main double peaked feature between 8 and 10 km s⁻¹, and other features between 15 and 22 km s⁻¹. The source 43.17+0.01 has features between 18 and 23 km s⁻¹, which are blended with 43.16+0.02. 43.17-0.00 has a 2.7 Jy peak around -1 km s⁻¹, while 43.18-0.01 has a 0.9 Jy peak around 11 km s⁻¹. In addition, there is an additional center that emits at 13.7 km s⁻¹, the position of which is not well determined from our data cubes, but is around R.A. 19^h10^m12^s.6, Dec. 09°06'11". Unfortunately, we do not have follow-up data at this position for verification, and consequently, we are not including this source in our source list. An image made from aperture synthesis will be required to define all the methanol emitting regions unambiguously.

Since the sources 43.16+0.02 and 43.17+0.01 have blended features, we carried out a simple deconvolution procedure to get the real spectra. If two sources, labeled 1 and 2 have spectra $S_1^a(\nu)$ and $S_2^a(\nu)$ respectively, the measured spectra $S_1^m(\nu)$ and $S_2^m(\nu)$ can be written as

$$S_1^m(\nu) = S_1^a(\nu) + \alpha S_2^a(\nu) \quad (6.1)$$

$$S_2^m(\nu) = S_2^a(\nu) + \alpha S_1^a(\nu) \quad (6.2)$$

Here, the parameter α determines the amount of blending, and can in theory be determined from the beam shape and the separation of the two sources. We assume a symmetric pattern for the main beam, so that the amount of contamination of source 1 onto source 2 is the same as the blending of source 2 onto source 1. The

equations above can be inverted easily to obtain

$$S_1^a(\nu) = \frac{S_1^m(\nu) - \alpha S_2^m(\nu)}{1 - \alpha^2} \quad (6.3)$$

$$S_2^a(\nu) = \frac{S_2^m(\nu) - \alpha S_1^m(\nu)}{1 - \alpha^2} \quad (6.4)$$

In the case of sources 43.16+0.02 and 43.17+0.01, the spectral features between 8 and 10 km s⁻¹ are associated only with 43.16+0.02. We used this fact to determine the parameter α to be 0.15. The deconvolution explained above was used to obtain the spectra shown in Figure 6.4.

W51 region. W51 is another complex region that has a cluster of methanol masers. One of the masers in this complex is very strong (> 700 Jy), which makes the data analysis for this region unusually difficult due to very relative ease with which this source can be detected in sidelobes of the antenna response pattern. We identified four distinct sites of methanol emission using techniques explained in the W49N section above. We also observed that sources 49.49-0.39 and 49.49-0.37 were blended between 57 and 60 km s⁻¹. We deconvolved these two sources using the technique explained above. The parameter α in the equations above was determined to be 0.023 using the feature at 52 km s⁻¹, which is associated only with the source 49.49-0.39. The deconvolved spectra are shown in Figure 6.4.

6.5 Discussion

This paper presents the basic results of the Arecibo Methanol Maser Galactic Plane Survey (AMGPS). An analysis of the distribution of sources, association with massive star formation and implications for Galactic structure will be given in a separate paper (Pandian et al. 2007b).

A part of our target region ($l \leq 40^\circ$) was covered by the blind survey of Szym-

czak et al. (2002) which had a 1σ sensitivity of 0.4 to 0.7 Jy. We detected 21 new sources in this region. The histogram of flux densities of the sources detected in our survey is shown in Figure 6.6. From the figure, it is clear that a significant fraction of new detections have flux densities less than or equal to 2 Jy. This highlights the importance of high sensitivity in carrying out unbiased surveys of this type.

It is also evident from Figure 6.6 that there are some new detections that are reasonably strong, with one source having a peak flux density of 11.3 Jy. These sources are in regions that have not been covered by unbiased surveys. Since they have not been detected in previous targeted surveys, it is very likely that they do not have infrared counterparts in the IRAS catalog, nor do they have previously detected OH maser emission associated with them. The latter is probably a consequence of the fact that OH maser emission is typically a factor of 7 weaker than that of the 6.7 GHz methanol emission (Caswell et al. 1995).

It can be seen from Table 6.1 and Figure 6.3 that there are very few sources at $l > 49.5^\circ$, which corresponds to the tangent point of the Carina-Sagittarius spiral arm. Since the number density of methanol masers as a function of Galactic longitude drops significantly beyond the tangent point of a spiral arm, surveys towards the inner regions of the Galaxy ($l \lesssim 35^\circ$) are likely to yield many more sources than surveys towards other regions. Another feature that is evident from Figure 6.3 is the dearth of sources between Galactic longitudes of 46° and 49° . A similar patchiness in the maser distribution was found in the earlier blind survey of Ellingsen et al. (1996b), as exemplified by the region $325^\circ \leq l \leq 326.4^\circ$. Our result is perhaps more dramatic, especially considering the higher sensitivity of AGMPS. We do not have at this time any explanation for this patchy distribution.

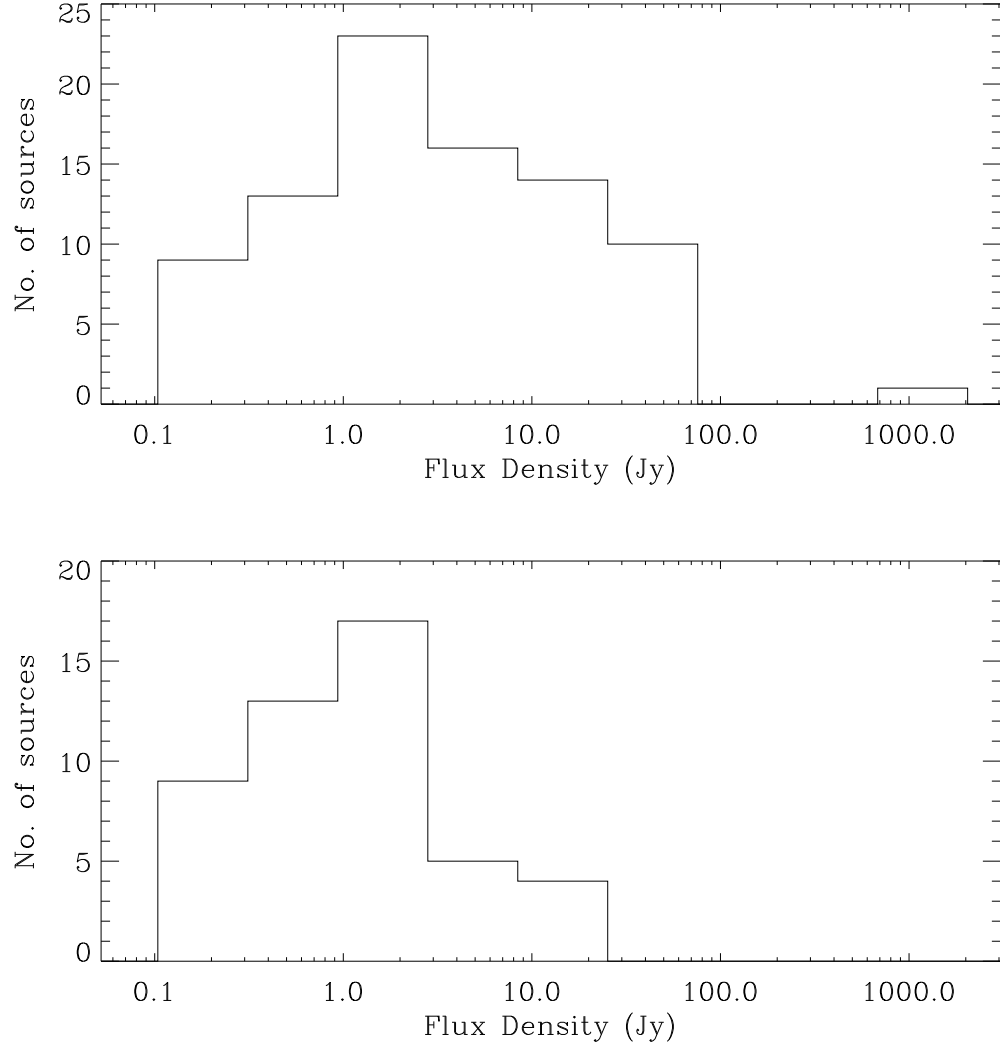


Figure 6.6 The distribution of flux densities of methanol masers discovered in the AMGPs. The top panel shows the histogram for all sources detected in the survey, while the bottom panel shows the histogram for new detections. Note that the lowest bin will be affected by incompleteness.

Further, it is apparent from Table 6.1 that many methanol masers occur in clusters. Notable examples other than the W49N and W51 regions are the groups around $(l, b) = (37.7\text{--}38.2, -0.2)$ (there seem to be two groups of masers in this region), $(41.1, -0.2)$ and $(45.5, 0.10)$. There are several other pairs of masers that

are located close to each other both spatially and in velocity. We take this to reflect the clustered nature of massive star formation.

The data in Table 6.2 can be used to estimate variability in methanol masers. Since this is not a systematic study of variability like the work of Goedhart et al. (2004), we cannot estimate any quantitative measure for variability. Qualitatively, we can determine variability for a maser if the change in its measured peak flux density exceeds the combined measurement errors. To do this, we first determined the errors in the flux densities for each survey by combining the accuracy of the flux calibration with the error resulting from antenna pointing errors. A pair of measurements differing by more than their error estimates is interpreted to be suggestive of variability. This does not take into account variability or lack of it among individual velocity features of the masers. Using this metric, we found that 28 out of the 38 masers listed in Table 6.2 are likely to be variable. These peak flux densities of these sources have typically changed by over 25%. The fraction of the maser population that is variable is comparable to that determined by Caswell et al. (1995) (sources marked as “v” and “sv” in Table 1 of Caswell et al. 1995).

6.6 Conclusions

We have carried out a very sensitive blind survey for 6.7 GHz methanol masers in the Galactic plane that is visible from the Arecibo radio telescope. The survey has resulted in the detections of 48 new methanol masers along with 38 previously known masers. The clustered nature of massive star formation seems to be reflected on the distribution of methanol masers in the sky. There is evidence that a significant fraction (about 74% in our survey) of methanol masers are variable.

Chapter 7

The Arecibo Methanol Maser Galactic Plane Survey–II: Statistical and Multi-wavelength Counterpart Analysis

7.1 The Sample

The methanol maser sample comes from the AMGPS which is discussed in detail in §6. The sample has 86 methanol masers, 77 of which have peak flux densities above the completeness limit of 0.27 Jy. The follow up observations in AMGPS collected high and low velocity resolution (0.04 km s^{-1} and 0.14 km s^{-1} respectively after Hanning smoothing) data for each methanol maser simultaneously. As explained in §6.2, sources weaker than $\sim 0.5 \text{ Jy}$ were observed for two minutes on source, while the stronger sources were observed for one minute on source. The rms noise in the spectra are typically 17 mJy and 8 mJy for the high and low velocity resolutions respectively for the two minute observation, and 24 mJy and 12 mJy respectively for the one minute observation.

7.2 Distribution in the Galaxy

It is to be noted that AMGPS is fully sampled only for $35.2^\circ \leq l \leq 53.7^\circ$ and $|b| \leq 0.41^\circ$. Hence, to consider the distribution of methanol masers in the Galaxy, all sources that lie outside these coordinates must be excluded along with the sources that lie below the completeness limit. This gives a sample of 72 methanol masers.

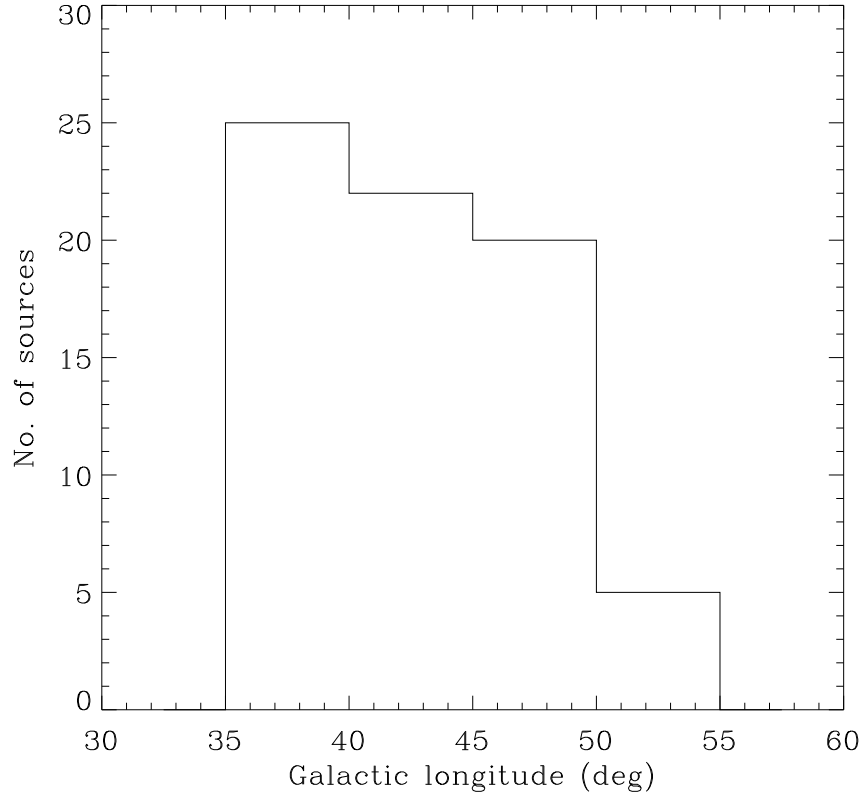


Figure 7.1 Distribution of methanol masers as a function of Galactic longitude. Note the 35° – 40° bin and the 50° – 55° bin will be slightly affected by lack of coverage.

Figure 7.1 shows the distribution of methanol masers as a function of Galactic longitude. Note the sharp decline in the number of methanol masers beyond a longitude of 50° . This is due to the tangent point of the Carina–Sagittarius spiral arm being crossed at $l \sim 49.6^{\circ}$. The increase in the number of methanol masers at lower Galactic longitudes is most likely due to the molecular ring in the Galaxy.

The distribution of methanol masers as a function of Galactic latitude is shown in Figure 7.2. A Gaussian fit to the distribution has a mean at a latitude of -0.09° and a full width at half maximum of 0.49° . The width of the distribution is comparable to that of embedded massive stars determined from the IRAS point source

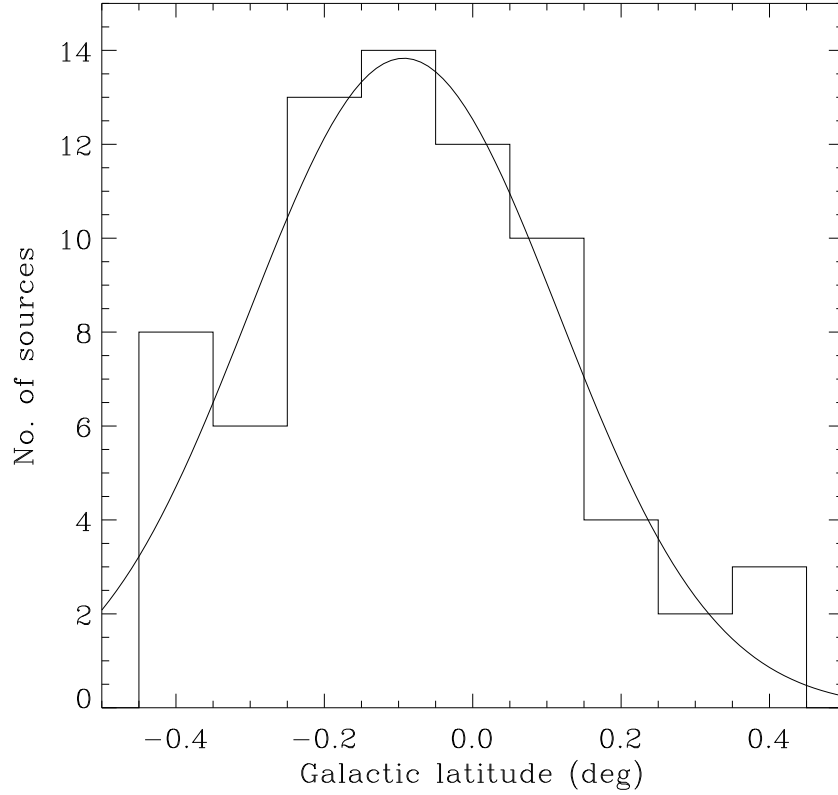


Figure 7.2 Distribution of methanol masers as a function of Galactic latitude. A Gaussian fit to the distribution is overlaid. The Gaussian fit has a mean at -0.09° and a full width to half maximum of 0.49° .

catalog (Wood & Churchwell 1989). The fit parameters to the distribution are very similar to those obtained by Pestalozzi et al. (2005) for the general catalog of methanol masers (which contains over 500 sources). Over half of the sources in the general catalog were detected in targeted surveys towards tracers of massive star formation such as ultracompact HII regions and OH masers. Thus, the close agreement of the distribution of the AMGPS sources (which come from a blind survey) with that of Pestalozzi et al. (2005) gives further evidence for the association of 6.7 GHz methanol masers with massive star formation.

The equatorial plane of the Galaxy was defined by the International Astronomi-

cal Union (IAU) based on primarily neutral hydrogen measurements of the Galaxy (Blaauw et al. 1959). The measurement of the mid-plane of the distribution of massive stars at a Galactic latitude of -0.09° could be due to an uncertainty in the definition of the Galactic plane from the HI observations, or a difference in the plane defined by HI and young massive stars.

7.3 Implications for Galactic Structure

Since massive stars form preferentially along spiral density waves which compress molecular gas to high densities, 6.7 GHz methanol masers are potential probes of the spiral structure of the Galaxy. Unfortunately, distances to methanol masers are not known precisely, except for a few regions (e.g. the distance to W3OH was measured through parallax by Xu et al. 2006). Distances are mostly calculated kinematically by assuming that the observed radial velocity of the source arises from its rotation around the Galaxy. Then, using a model for the rotation curve of the Galaxy (e.g. Clemens 1985; Brand & Blitz 1993), one can derive an estimate for the distance to the source. The uncertainty in the distance is large since the source is usually not in perfect circular rotation, deviations from which arise due to random motions, spiral shocks, expansion such as at edges of HII regions and supernova explosions, etc. To compound these difficulties, the distance to the source from the Sun is double valued for certain radial velocities in the inner regions of the Galaxy (positive radial velocities for $0^\circ \leq l \leq 90^\circ$, negative radial velocities for $270^\circ \leq l \leq 360^\circ$).

Although there are techniques to distinguish between the two values of the kinematic distance (called near and far distance), we do not at present have the data required to resolve the distance ambiguity for our methanol maser sample.

Hence, we use an $l - v$ diagram to see what information methanol masers provide regarding the structure of our Galaxy. Two constructs of the $l - v$ diagram are shown in Figures 7.3 and 7.4 respectively. The observed radial velocities are assumed to have deviations from the values observed from pure circular rotation by up to $\pm 10 \text{ km s}^{-1}$ due to the various phenomena described above. Figure 7.3 shows the loci of various spiral arms in the model of Vallee (1995). Figure 7.4 shows the spiral arm loci for the NE2001 model of Cordes & Lazio (2002). The spiral arm loci are calculated using the rotation curve of Clemens (1985).

The clumping of sources around $l \sim 49.6^\circ$ seems to arise from the tangent point of the Carina–Sagittarius spiral arm. The model of Vallee (1995) fits this feature reasonably well, while the tangent point in the model of Cordes & Lazio (2002) occurs at approximately 1° lower Galactic longitude which does not fit our data. It is to be noted that the spiral arm model of Cordes & Lazio (2002) is derived from ionized gas, which is likely to be offset from the location of young massive stellar objects in a spiral arm. As the molecular gas orbiting the Galaxy encounters a spiral density wave, it gets compressed thereby initiating star formation. Since massive stars form on a relatively short timescale, the region sprouts HII regions by the time it exits the density wave. Thus, for trailing spiral arms, deeply embedded massive young stellar objects are more likely to be found at the inner (concave) edge of the spiral arm, while ionized gas is more likely to be found along the outer (convex) edge of the spiral arm. Thus, one would expect the tangent point of a spiral arm to be located at larger Galactic longitudes as seen in ionized gas, compared to early tracers of massive star formation such as 6.7 GHz methanol masers. This makes the discrepancy between the tangent point of the Carina–Sagittarius spiral arm as seen from our data, and the NE2001 model especially

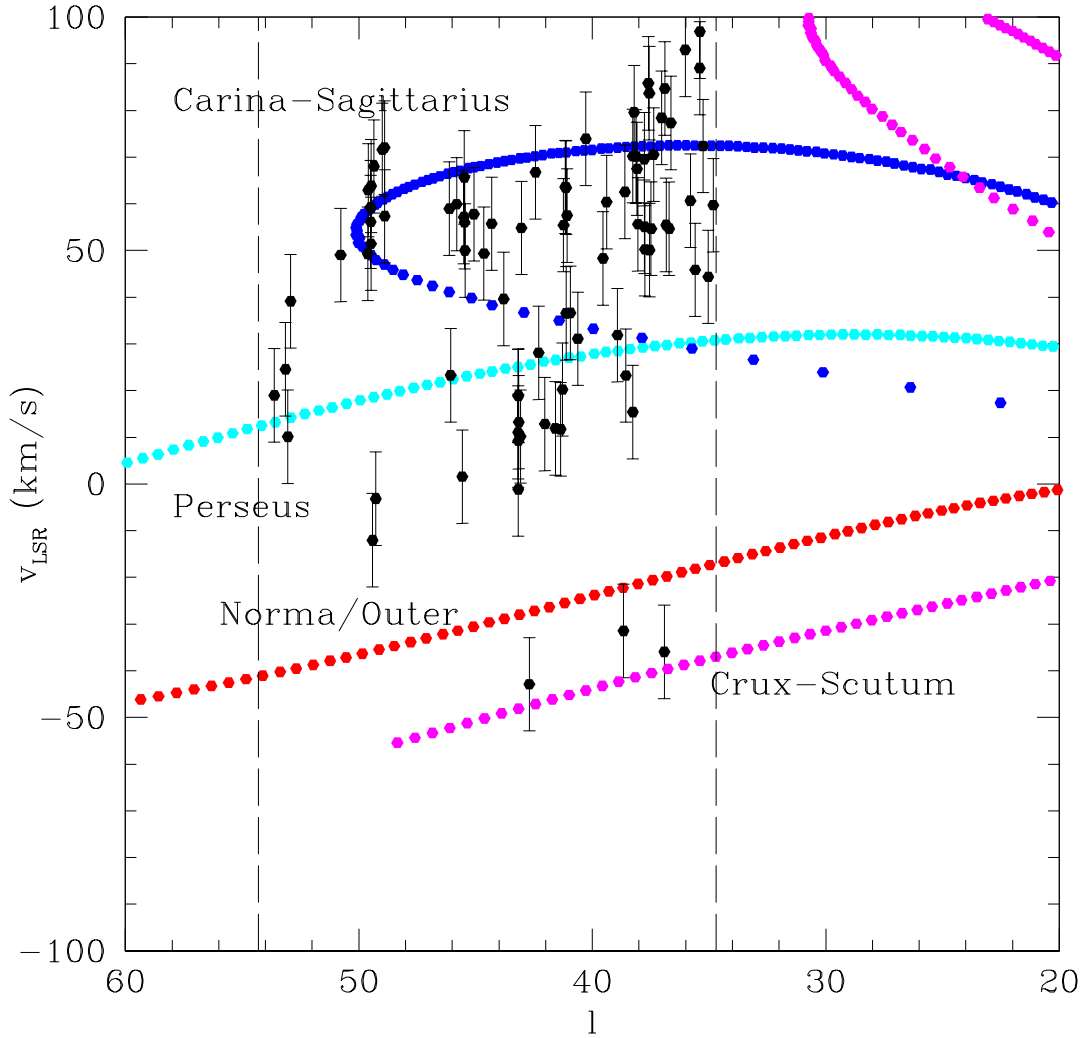


Figure 7.3 The methanol maser sample of AMGPS on an $l - v$ diagram. The loci of spiral arms from the model of Vallee (1995) are overplotted. The dashed lines show the Galactic longitude limits of AMGPS.

puzzling.

The other interesting feature is the observation of three sources at radial velocities lower than -30 km s^{-1} (with respect to the local standard of rest). At least two points fit the spiral arm beyond the Outer arm, which is the extension of the Crux-Scutum arm (which can also be seen to the upper right in Figures 7.3 and

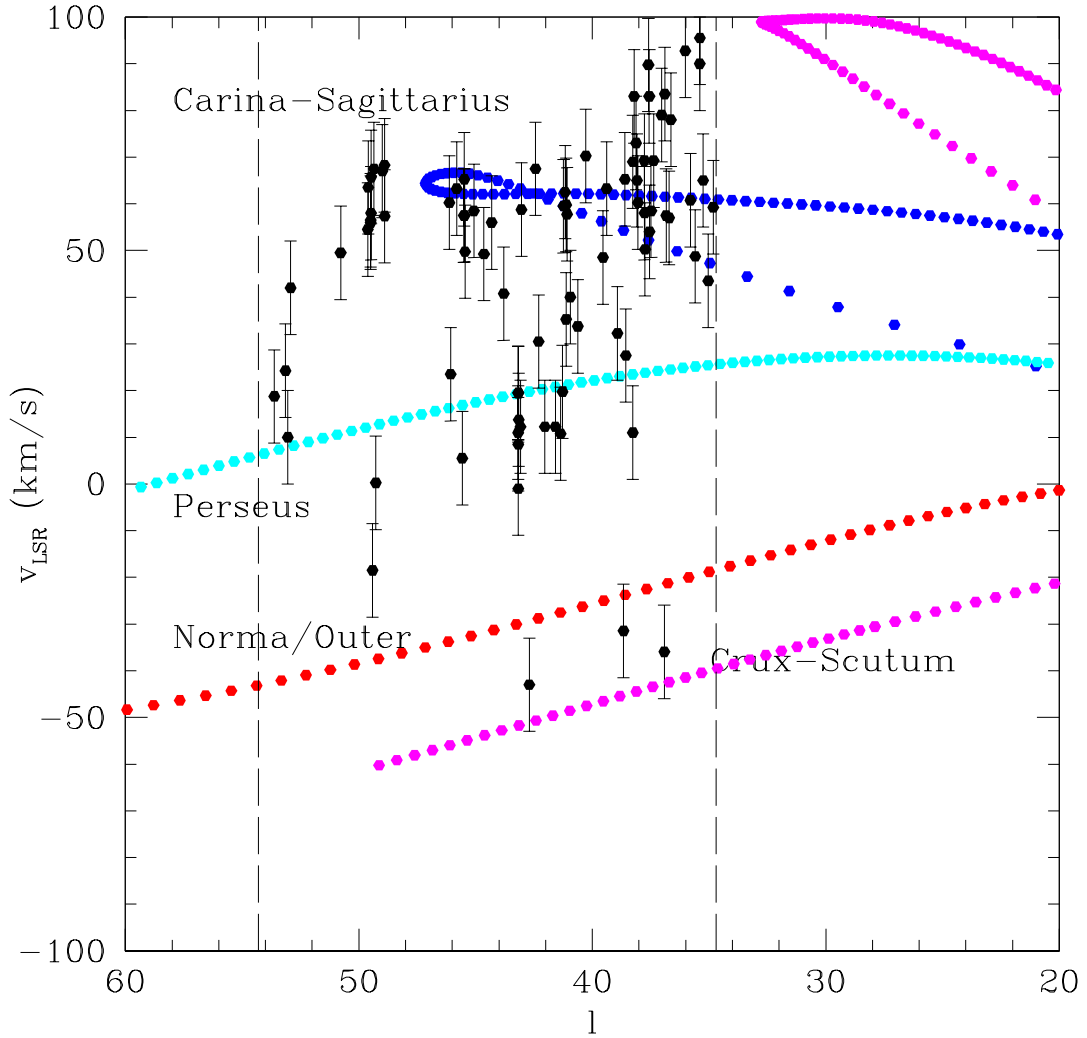


Figure 7.4 The methanol maser sample of AMGPS on an $l - v$ diagram. The loci of spiral arms from the NE2001 model of Cordes & Lazio (2002) are overplotted. The dashed lines show the Galactic longitude limits of AMGPS.

7.4). The distances to these sources is over 17 kpc from the Sun, which is among the farthest known distance to a methanol maser. Thus, sensitive surveys for 6.7 GHz methanol masers can trace structures beyond those detected by other tracers of massive star formation.

7.4 The Number of Methanol Masers in the Galaxy

The number of 6.7 GHz methanol masers in the Galaxy has been estimated by van der Walt (2005). The procedure followed is to estimate the number of stars in the mass range (m_1, m_2) born in a time interval Δt between distances R_1 and R_2 from the center of the Galaxy. This number, $N(m_1, m_2)$ can be estimated in terms of the star formation law $\psi(r)$ (the gas consumption rate per unit surface area), and the initial mass function (IMF) $\phi(m)$ as

$$N(m_1, m_2) = 2\pi\Delta t \int_{R_1}^{R_2} \psi(r) r dr \int_{m_1}^{m_2} \phi(m) dm \quad (7.1)$$

where the IMF is normalized such that

$$\int_{m_l}^{m_u} \phi(m) m dm = 1 \quad (7.2)$$

where m_l and m_u are the lower and upper limits for which the IMF is known. Then, a spiral arm model of the Galaxy is used to model the distribution of young massive star forming regions as a function of Galactic longitude as seen from the Sun. This distribution is then scaled such that the number of masers in a chosen longitude bin coincides with the number of masers detected in a blind survey. Since all surveys are flux limited, a minimum number of methanol masers can be derived by summing over all longitude bins.

It is to be noted that since the distribution is scaled using the statistics from a survey, the resulting estimate for the number of methanol masers in the Galaxy is independent of the star formation rate and the IMF assumed. Two star formation laws, $\psi_1(r) \propto \Sigma_{H_2}(r)$ where Σ_{H_2} is the surface density of molecular gas, and $\psi_2(r) \propto \Sigma_G^{1.5}(r) (R_s/r)$ where Σ_G is the total gas surface density and $R_s = 8$ kpc, and the spiral arm model of Vallee (1995) was used by van der Walt (2005) to determine the minimum number of methanol masers to be 845. This was obtained by

scaling the longitude distribution to the observations between Galactic longitudes of 330° and 340° , which includes a blind survey by Ellingsen et al. (1996b).

Since our survey is an order of magnitude more sensitive more than that of Ellingsen et al. (1996b), our observations can be used to revise the minimum number of methanol masers in the Galaxy. The AMGPS detected 44 methanol masers brighter than 0.27 Jy between longitudes of 40° and 50° . Using this number as the normalization for the longitude distribution of van der Walt (2005), the number of methanol masers in the Galaxy, brighter than 0.27 Jy, is at least 1125. Note that the region $|b| > 0.41^\circ$ is incompletely sampled by AMGPS, and hence the number quoted above should be taken as a lower limit.

The total number of methanol masers in the Galaxy is also estimated through Monte Carlo simulations of van der Walt (2005). The simulations assigned luminosities to a simulated population of methanol masers at positions calculated using the star formation laws and spiral structure indicated above. The luminosities assigned were calculated from the current sample of methanol masers detected to date, which are assumed to be representative of the entire population of methanol masers. The distances to the masers were calculated kinematically using the rotation curve of the Galaxy and hence often suffered from an ambiguity between near and far distances. Hence, the luminosities for both near and far distances were calculated, and individual masers in the simulated sample were assigned the near distance luminosity with probability P_{near} , and the far distance luminosity with probability $(1 - P_{\text{near}})$. Once luminosities were assigned for the simulated population, the fraction of masers that would be detected at a given threshold flux density was calculated, which was used to determine the completeness of a blind survey as a function of the detection limit for different P_{near} . The total number of

methanol masers can then be derived by dividing the number estimated from the statistics of a blind survey with the completeness limit for that survey.

Using this technique, the total number of methanol masers in the Galaxy was estimated to be 1200 ± 84 . We find that the statistics from our survey are consistent with the calculations of van der Walt (2005). From the Monte Carlo simulations of van der Walt (2005), a survey with a detection limit of 0.27 Jy will have a completeness of $\sim 0.89 - 0.94$ for $P_{\text{near}} = 0.5 - 0.9$. This translates to a total number of methanol masers of 1197–1264, which is well within the limits quoted above.

In light of this discussion, it is interesting to note the turn-over in the distribution of methanol masers as a function of flux density (Figure 6.6). Note that only the first bin in this plot is affected by incompleteness. The plot shows that the peak of the distribution occurs for flux densities between ~ 0.9 and 3 Jy. This indicates that the rate of detection of a survey that is much deeper than AMGPS will not be much higher than the detection rate of AMGPS itself. This information will be useful for planning future methanol maser surveys.

7.5 Line Properties: Gaussian Analysis

The spectra of 6.7 GHz methanol masers are in general, very complex with several velocity components blended together. This makes Gaussian component analysis a daunting task. We used a modified version of the interactive IDL routine “xgauss-fit” available from the FUSE IDL Tools website¹ for our Gaussian analysis. We modified the routine so that it could fit up to 25 Gaussians simultaneously (as opposed to 8 Gaussians in the original version), and also incorporated the χ^2 metric

¹http://fuse.pha.jhu.edu/analysis/fuse_idl_tools.html

into the interactive widget to determine the quality of a given fit.

We found it extremely difficult to get a “good” fit to complex spectra. Moreover, we found that fits obtained using generic fitting routines are not unique. This is primarily because there are no *a priori* constraints on the number of Gaussian components in the spectrum. This translates to an uncertainty in the statistics of the component linewidths. Even if we restrict the number of Gaussians from χ^2 arguments, there are many arrangements of the different components to achieve a similar fit. Due to the difficulty in obtaining good fits to complex sources, we restrict our analysis to relatively simple sources, and have at present carried out the Gaussian component analysis for 49 out of the 86 sources detected in the AMGPs. An example of a complex spectrum, and an attempted fit is shown in Figure 7.5.

One of the techniques to get over the problem of closely spaced blended components is to do a partial deconvolution of the spectrum. This works as follows: Consider two Gaussian signals, x and y with variances σ_x^2 and σ_y^2 respectively. Let z denote the signal arising from the convolution of x and y . The Fourier transform of z , designated by Z , is the product of the Fourier transforms of x and y , which are designated as X and Y respectively. Note that the Fourier transform of a Gaussian is also a Gaussian, the variance of the Gaussian in the Fourier domain being equal to the inverse of the variance of the original Gaussian. Hence, the signal z is also a Gaussian, and its width, σ_z is related to the widths of σ_x and σ_y as

$$\sigma_z^2 = \sigma_x^2 + \sigma_y^2 \quad (7.3)$$

Thus, if we take the Fourier transform of the spectrum of a source, and divide the amplitude by the Fourier transform of a synthetic Gaussian, the inverse transform will give us a signal which has been deconvolved by an amount that can be deter-

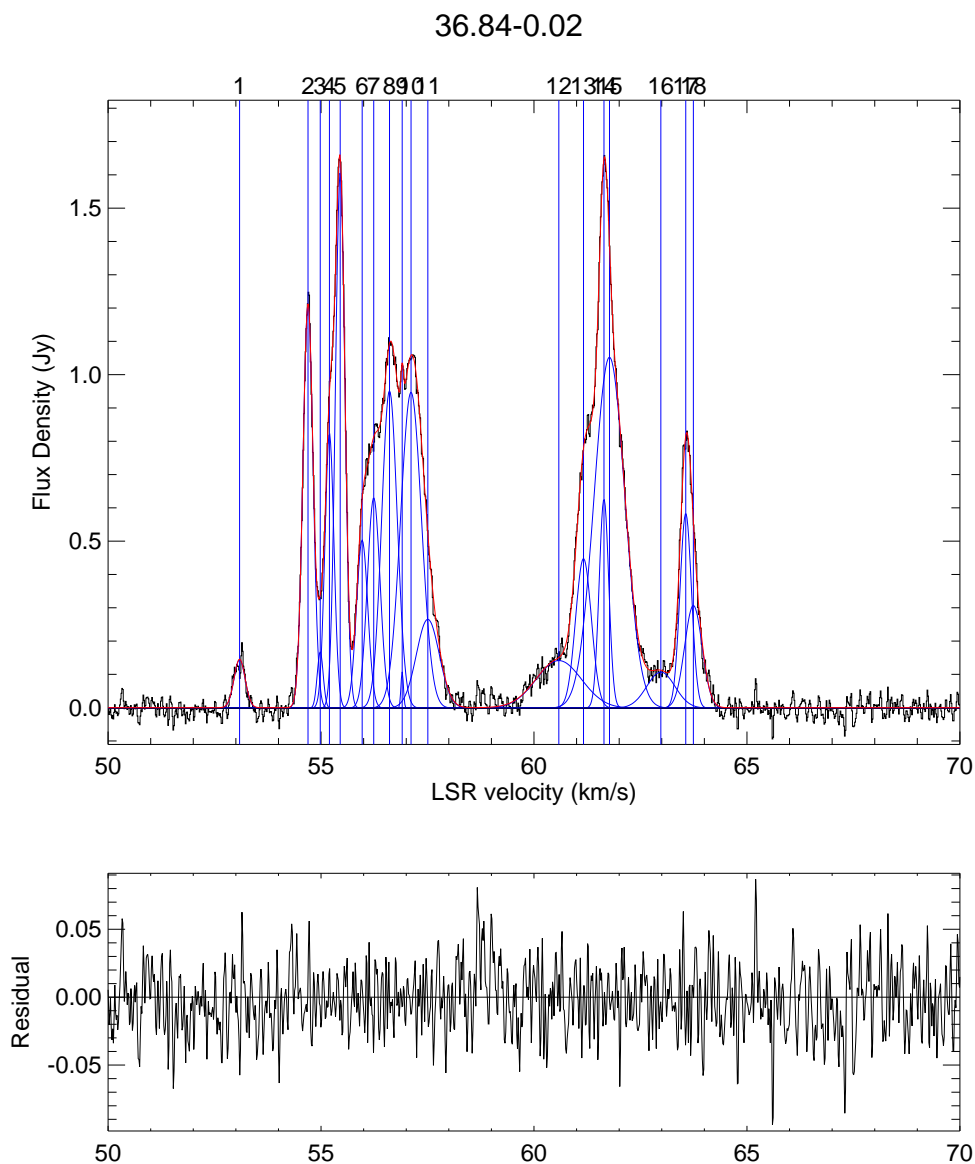


Figure 7.5 An example of a complex spectrum, and an attempted Gaussian component analysis. The blue lines show the locations of the Gaussians, and the individual Gaussians, and the red line shows the overall fit. A similar fit can be achieved by using slightly fewer or more components, and by different placement of components.

mined from eq. (7.3). The information on the position of components is encoded in the phase of the Fourier transform, and is thus not lost as long as the phase is left intact. Care must be taken that the width of the deconvolving Gaussian is not larger than the width of any component in the original spectrum.

This technique can potentially be used to determine the number of components and their positions in a complex spectrum. It is to be noted that since the amplitude of the Fourier transform of a Gaussian falls with frequency, the division of the Fourier transform of a noisy signal with that of a deconvolving Gaussian will increase the noise in the resulting signal. Thus, some truncation and interpolation must be used in the Fourier domain to limit the deterioration of the signal to noise ratio of the deconvolved spectrum. For this reason, this technique is probably applicable only for strong signals. Fortunately, strong sources tend to display more complex spectra, which to some extent may be an effect of sensitivity. This technique will be implemented in future, and at present, we restrict ourselves to signals that have less than ~ 10 components blended together. Our fits for these sources are not likely to be unique; however, our goal is to derive the statistics on the linewidths of the components.

As mentioned previously, we have carried out the Gaussian component analysis for 49 sources in our catalog. This yielded a total of 275 components. Individual fits, and fit parameters for each source are tabulated in Appendix B. The distribution of FWHM linewidths binned into 0.05 km s^{-1} bins is shown in Figure 7.6. The mean linewidth is found to be 0.38 km s^{-1} , and the median value is 0.33 km s^{-1} .

The prior work of Szymczak & Kus (2000) determined the mean full width at half maximum (FWHM) of Gaussian components to be 0.17 km s^{-1} , and the

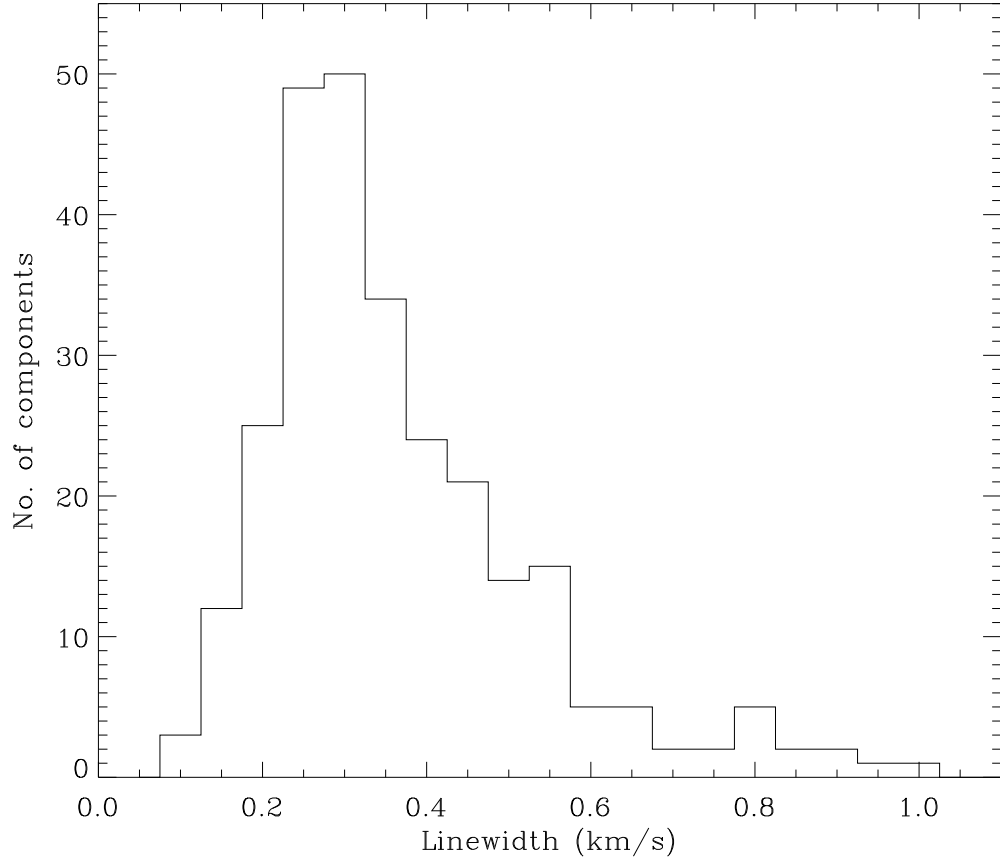


Figure 7.6 The distribution of FWHM linewidths. There are three components that have linewidths greater than 1 km s^{-1} , that are not shown in the figure.

median to be 0.14 km s^{-1} . These values are a factor of two lower than the values that we determine from our analysis. Unlike the claim of Szymczak & Kus (2000), we find no evidence for faint sources to have narrow linewidths. To make sure that our results are not biased by our excluding complex sources, we obtained sample fits for a few complex sources. While these fits are not likely to be unique, it is unlikely that the number of components used in the fit are off by more than 20% based on the χ^2 of the fit. The distribution of these components was found to be similar to that of Figure 7.6, and the values of mean and median linewidths

were similar to those quoted above. We note that our result is consistent with the measurements of Menten (1991b) and Caswell et al. (1995). It is also curious that our histogram has the same shape as that of Szymczak & Kus (2000), the primary difference being the scaling of the linewidth axis by a factor of two.

7.6 Counterparts at Other Wavelengths

An multi-wavelength analysis of the astronomical sources responsible for pumping 6.7 GHz methanol masers is required to understand the relation between the maser emission and its environment, which is surmised to be high-mass star formation. Hence, it is of interest to search for counterparts to the masers in catalogs published in the literature, as well as undertake new observations at wavelengths where data is not available. The catalogs of interest at present are 2MASS (J , H and K bands), GLIMPSE (3.6, 4.5, 5.8 and 8.0 μm), MSX (8.28, 12.13, 14.65 and 21.3 μm), IRAS (12, 25, 60 and 100 μm) and NVSS (1.4 GHz continuum).

A question that must be addressed in this regard is the search radius for a counterpart, keeping in mind that a large search radius may preclude a direct association between the source and the maser. Since the metric governing association of two sources is the physical separation between them, the angle of separation on the sky will be a function of the distance to the source. This is however, not practical since the distances to most methanol masers are not known. Considering a fiducial distance to a massive star forming region as ~ 3 kpc, an angular separation of $5''$ translates to a physical separation of 15,000 AU. Since warm dust heated by the central star is required for the maser pump, a search radius of $5''$ can be taken as a conservative upper limit for possible association.

It is also important to consider the uncertainty in the position of the methanol

maser itself. This is primarily related to the pointing error of the telescope. The root mean square (rms) pointing error of the Arecibo radio telescope is $\sim 5''$ in both azimuth and zenith angle. This has been verified by both our measurements of pointing using continuum sources, and independent measurements by the observatory staff. Hence, the overall rms pointing error in right ascension and declination can be taken to be $\sim 7''$. Although the pointing error is to some extent dependent on the azimuth angle and zenith angle, the overall statistical distribution of pointing errors is a Gaussian to good approximation. Hence, the error circle, the uncertainty in the position of any methanol maser, defined at the 95% confidence level, is $\sim 18''$. Hence, the search radius for counterparts is taken to be $23''$.

The large search radius, resulting from the pointing error precludes a counterpart analysis with the 2MASS and GLIMPSE catalogs. The relatively high angular resolution of these surveys coupled with their sensitivity and the numerous stars visible in near infrared wavelengths imply that a large number of point sources (50 sources is not uncommon) from these catalogs will lie within any methanol maser. Thus, these two catalogs are excluded from our analysis until the methanol maser positions are refined to sub-arcsecond accuracy.

The counterparts to the methanol maser sample from AMGPS in IRAS, MSX and NVSS catalogs are summarized in Table 7.1. Sources in the well known star forming regions W49N and W51 are excluded since the density of methanol masers in these regions is high enough that a given IRAS, MSX or NVSS source will lie within the search radius of more than one maser. The source 41.87–0.10 is also excluded due to the uncertainty in its position.

While sources that are farther than $23''$ from the methanol maser are unlikely to be directly associated with the maser emission, it is of interest to note whether

there are any IRAS, MSX, NVSS sources, or other tracers of star formation (e.g. OH, H₂O masers, NH₃ emission) are detected within 1' of the maser. A search radius of 1' is chosen in part to conform with previous studies of the subject (e.g. Pestalozzi et al. 2005), and in part to ensure that any star formation tracers detected would be associated with the same complex that contains the massive young stellar object responsible for the methanol maser emission. The results for the larger search radius are summarized for all sources in Table 7.2.

Table 7.1: Possible counterparts to the methanol maser sample of AMGPs in IRAS, MSX and NVSS catalogs. The columns after the methanol maser show the IRAS, MSX and NVSS sources that are within $23''$ of the maser and their angular separation from the maser in arcseconds.

Methanol Maser	IRAS source	sep (")	MSX source	sep (")	NVSS source	sep (")
34.82+0.35	18511+0146	12.1	G034.8211+00.3519	7.9		
35.03+0.35			G035.0252+00.3502	12.2		
35.25-0.24	18539+0153	17.2				
35.39+0.02					185550+021153	16.75
35.40+0.03	18533+0208	7.3	G035.3988+00.0237	4.2		
35.79-0.17	18547+0223	6.9	G035.8012-00.1779	22.7		
36.70+0.09	18554+0319	11.5				
36.84-0.02	18561+0323	12.9				
36.92+0.48			G036.9194+00.4825	12.4		

Continued on next page

Table 7.1 (Continued)

Methanol Maser	IRAS source	sep (")	MSX source	sep (")	NVSS source	sep (")
37.38–0.09			G037.3815-00.0816	13.9		
37.53–0.11			G037.5450-00.1118	22.0	190016+040307	19.34
37.55+0.19	18566+0408	22.8	G037.5536+00.2008	21.6		
37.60+0.42	18559+0416	13.4				
37.74–0.12			G037.7391-00.1156	10.4		
37.76–0.19			G037.7527-00.1933	6.0		
37.77–0.22			G037.7625-00.2181	19.5		
			G037.7631-00.2140	20.3		
38.03–0.30	18593+0419	6.3				
38.08–0.27			G038.0757-00.2652	18.8		
38.26–0.08	18589+0437	15.6	G038.2577-00.0733	17.7		
38.26–0.20	18594+0434	6.3	G038.2537-00.1996	18.3		
38.66+0.08					190135+050739	20.83

Continued on next page

Table 7.1 (Continued)

Methanol Maser	IRAS source	sep (")	MSX source	sep (")	NVSS source	sep (")
39.39–0.14	19012+0536	2.7	G039.3880-00.1421	6.4		
40.28–0.22			G040.2816-00.2190	15.2		
40.62–0.14	19035+0641	17.9	G040.6225-00.1377	11.4		
41.08–0.13			G041.0723-00.1256	7.9		
41.12–0.11	19044+0709	9.8	G041.1207-00.1062	9.8		
41.12–0.22			G041.1195-00.2216	11.1		
41.23–0.20			G041.2282-00.1966	11.5		
41.27+0.37			G041.2676+00.3732	18.5		
41.34–0.14			G041.3477-00.1414	7.9		
42.03+0.19	19050+0806	17.0	G042.0341+00.1905	19.8		
42.43–0.26	19074+0814	7.8	G042.4343-00.2597	14.6	190950+081927	4.31
42.70–0.15	19075+0832	5.5				
43.80–0.13	19095+0930	22.6	G043.7955-00.1275	11.0		

Continued on next page

Table 7.1 (Continued)

Methanol Maser	IRAS source	sep (")	MSX source	sep (")	NVSS source	sep (")
44.31+0.04			G044.3103+00.0416	15.8		
45.07+0.13	19110+1045	11.6	G045.0711+00.1325	10.4		
45.47+0.05			G045.4658+00.0457	20.9		
45.47+0.13	19117+1107	6.0	G045.4782+00.1323	7.8	191408+111229	6.07
45.57-0.12			G045.5664-00.1193	14.8		
45.81-0.36	19141+1110	8.4	G045.8059-00.3521	20.6		
46.07+0.22			G046.0599+00.2240	19.6	191455+114601	11.26
48.99-0.30	19201+1400	4.4	G048.9897-00.2992	1.6	192225+140633	7.24
49.27+0.31	19184+1432	15.5				
49.35+0.41			G049.3496+00.4150	17.8		
49.60-0.25	19211+1434	11.4	G049.5993-00.2488	3.4		
50.78+0.15			G050.7796+00.1520	11.4		
52.92+0.41	19253+1748	12.6	G052.9217+00.4142	13.3		

Continued on next page

Table 7.1 (Continued)

Methanol Maser	IRAS source	sep (")	MSX source	sep (")	NVSS source	sep (")
53.04+0.11			G053.0366+00.1110	3.2		
53.14+0.07	19270+1750	4.8	G053.1417+00.0705	1.5		
53.62+0.04			G053.6185+00.0376	4.3		

Table 7.2: This table lists whether there are (a) IRAS, MSX and NVSS counterparts within $23''$, and (b) IRAS, MSX and NVSS sources, water masers, OH masers, other methanol masers, or other tracers of star formation such as CO, CS or NH_3 detected within $1'$ of each methanol maser in the AMGPS sample (excluding W49N, W51 regions and source 41.87–0.10).

Methanol Maser	IRAS source?		MSX source?		NVSS source?		H ₂ O	OH	other methanol	other SF
	23''	60''	23''	60''	23''	60''	maser?	maser?	masers?	tracers?
34.82+0.35	y	y	y	y	n	n	n	n	y	y
35.03+0.35	n	y	y	y	n	y	y	y	y	y
35.25–0.24	y	y	n	y	n	n	n	n	n	n
35.39+0.02	n	y	n	y	y	y	n	n	n	n
35.40+0.03	y	y	y	y	n	y	n	n	n	n
35.59+0.06	n	n	n	y	n	y	n	n	n	y
35.79–0.17	y	y	y	y	n	n	n	y	n	n

Continued on next page

Table 7.2 (Continued)

Methanol Maser	IRAS source?		MSX source?		NVSS source?		H ₂ O	OH	other methanol	other SF
	23''	60''	23''	60''	23''	60''	maser?	maser?	masers?	tracers?
36.02–0.20	n	n	n	n	n	n	n	n	n	n
36.64–0.21	n	y	n	n	n	n	n	n	n	n
36.70+0.09	y	y	n	y	n	n	n	y	n	y
36.84–0.02	y	y	n	y	n	n	n	n	n	n
36.90–0.41	n	n	n	y	n	n	n	n	n	n
36.92+0.48	n	y	y	y	n	y	n	n	n	y
37.02–0.03	n	n	n	y	n	y	n	n	n	n
37.38–0.09	n	n	y	y	n	n	n	n	n	n
37.47–0.11	n	n	y	y	n	n	y	n	n	y
37.53–0.11	n	y	y	y	y	y	y	n	n	y
37.55+0.19	y	y	y	y	n	n	y	y	n	y
37.60+0.42	y	y	n	n	n	n	y	n	n	n

Continued on next page

Table 7.2 (Continued)

Methanol Maser	IRAS source?		MSX source?		NVSS source?		H ₂ O	OH	other methanol	other SF
	23''	60''	23''	60''	23''	60''	maser?	maser?	masers?	tracers?
37.74–0.12	n	n	y	y	n	n	y	n	n	y
37.76–0.19	n	y	y	y	n	n	n	n	n	y
37.77–0.22	n	y	y	y	n	y	y	n	n	y
38.03–0.30	y	y	n	y	n	y	n	y	n	n
38.08–0.27	n	y	y	y	n	n	n	n	n	n
38.12–0.24	n	y	n	y	n	y	n	n	n	y
38.20–0.08	n	n	n	y	n	n	n	n	n	n
38.26–0.08	y	y	y	y	n	n	n	n	n	n
38.26–0.20	y	y	y	y	n	n	n	n	n	n
38.56+0.15	n	y	n	y	n	y	n	n	n	n
38.60–0.21	n	n	n	y	n	n	n	n	n	y
38.66+0.08	n	y	n	y	y	y	n	n	n	n

Continued on next page

Table 7.2 (Continued)

Methanol Maser	IRAS source?		MSX source?		NVSS source?		H ₂ O	OH	other methanol	other SF
	23''	60''	23''	60''	23''	60''	maser?	maser?	masers?	tracers?
38.92–0.36	n	y	y	y	n	n	y	n	n	y
39.39–0.14	y	y	y	y	n	n	n	n	n	y
39.54–0.38	n	n	n	n	n	n	n	n	n	n
40.28–0.22	n	n	y	y	n	n	n	n	n	n
40.62–0.14	y	y	y	y	n	n	y	y	n	y
40.94–0.04	n	n	n	n	n	n	n	n	n	n
41.08–0.13	n	n	y	y	n	n	n	n	n	n
41.12–0.11	y	y	y	y	n	n	n	n	n	n
41.12–0.22	n	y	y	y	n	n	y	n	n	n
41.16–0.20	n	n	n	y	n	n	n	n	n	y
41.23–0.20	n	y	y	y	n	n	n	n	n	n
41.27+0.37	n	n	y	y	n	n	n	n	n	n

Continued on next page

Table 7.2 (Continued)

Methanol Maser	IRAS source?		MSX source?		NVSS source?		H ₂ O	OH	other methanol	other SF
	23''	60''	23''	60''	23''	60''	maser?	maser?	masers?	tracers?
41.34–0.14	n	y	y	y	n	n	n	n	n	n
41.58+0.04	n	n	n	y	n	n	n	n	n	n
42.03+0.19	y	y	y	y	n	n	n	n	n	n
42.30–0.30	n	y	n	n	n	n	n	n	n	n
42.43–0.26	y	y	y	y	y	y	y	n	n	y
42.70–0.15	y	y	n	n	n	n	n	n	n	n
43.04–0.46	n	y	n	y	n	n	y	y	y	y
43.08–0.08	n	n	n	n	n	n	n	n	n	n
43.80–0.13	y	y	y	y	n	y	y	y	n	y
44.31+0.04	n	y	y	y	n	n	n	n	n	n
44.64–0.52	n	n	n	y	n	n	n	n	n	n
45.07+0.13	y	y	y	y	n	y	y	y	y	y

Continued on next page

Table 7.2 (Continued)

Methanol Maser	IRAS source?		MSX source?		NVSS source?		H ₂ O	OH	other methanol	other SF
	23''	60''	23''	60''	23''	60''	maser?	maser?	masers?	tracers?
45.44+0.07	n	y	n	y	n	y	y	y	n	y
45.47+0.05	n	y	y	y	n	y	y	y	y	y
45.47+0.13	y	y	y	y	y	y	y	y	n	y
45.49+0.13	n	n	n	y	n	n	y	n	n	y
45.57−0.12	n	y	y	y	n	n	n	n	n	n
45.81−0.36	y	y	y	y	n	n	n	n	n	n
46.07+0.22	n	n	y	y	y	y	n	n	n	n
46.12+0.38	n	n	n	y	n	n	n	n	n	n
48.89−0.17	n	y	n	y	n	n	n	n	n	n
48.90−0.27	n	y	n	y	n	n	n	n	n	n
48.99−0.30	y	y	y	y	y	y	y	n	n	n
49.27+0.31	y	y	n	y	n	n	n	n	n	n

Continued on next page

Table 7.2 (Continued)

Methanol Maser	IRAS source?		MSX source?		NVSS source?		H ₂ O	OH	other methanol	other SF
	23''	60''	23''	60''	23''	60''	maser?	maser?	masers?	tracers?
49.35+0.41	n	n	y	y	n	n	n	n	n	n
49.41+0.33	n	y	n	y	n	y	n	n	y	n
49.60−0.25	y	y	n	y	n	y	n	n	n	y
49.62−0.36	n	n	n	y	n	n	n	n	n	n
50.78+0.15	n	y	n	y	n	n	n	n	n	n
52.92+0.41	y	y	y	y	n	n	n	n	n	n
53.04+0.11	n	y	y	y	n	n	n	n	n	y
53.14+0.07	y	y	y	y	n	n	n	n	n	n
53.62+0.04	n	n	y	y	n	n	n	n	n	y

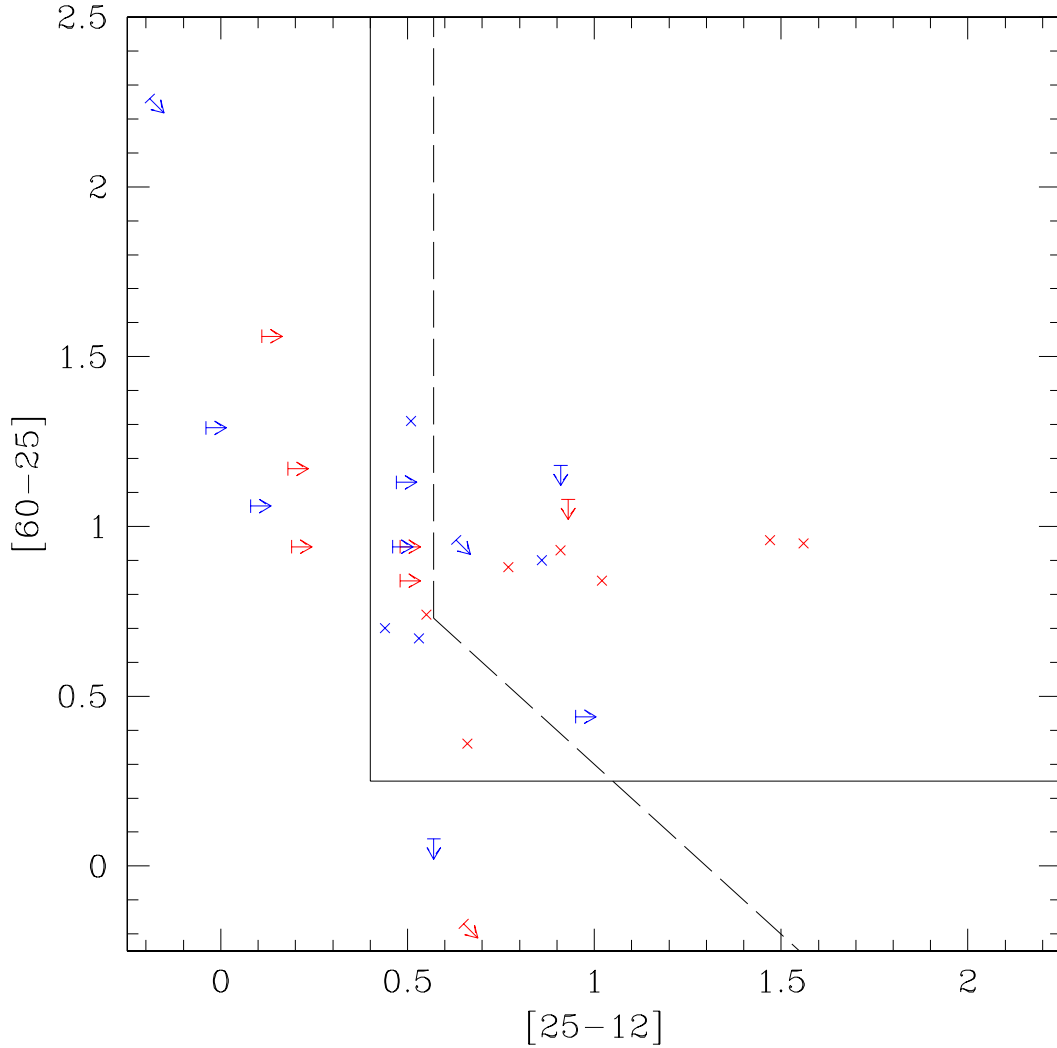


Figure 7.7 The color-color diagram for possible IRAS counterparts of 6.7 GHz methanol masers discovered in AMGPS. The colors for previous detections are shown in red, while those of new detections are shown in blue. Color limits pointing at 45° indicate upper limits in both $[25-12]$ color and $[60-25]$ colors. Sources to the right of the dashed lines satisfy WC89 colors for ultracompact HII regions, while sources to the right of the bold lines satisfy HM89 criteria for the same.

From Table 7.1, it is clear that only 26 out of 76 sources have possible IRAS counterparts. The color-color diagram of these IRAS sources (the one associated with W49 region included) is shown in Figure 7.7. The colors for previous de-

tections are shown in red, while those of new detections are shown in blue. The two sets of criteria usually used to identify embedded massive stars (primarily ultracompact HII regions) are those of Wood & Churchwell (1989) and Hughes & MacLeod (1989). These criteria will be abbreviated as WC89 and HM89 respectively. In Figure 7.7, sources to the right of the dashed lines satisfy WC89, while sources to the right of the solid lines satisfy HM89. HM89 imposes an additional constraint on the $100\ \mu\text{m}$ flux of the source, which is not shown in the figure.

Only six sources satisfy WC89 criteria, which exclude sources with poorly determined colors (lower or upper limits on any color). A larger number of sources satisfy HM89 criteria, although the requirements on the $100\ \mu\text{m}$ flux eliminates some of the sources that lie on the right of the solid lines. This shows that targeted searches for methanol masers towards IRAS color selected sources will miss an outstanding population of masers in the Galaxy. One of the reasons for the poor correspondence between methanol masers and IRAS sources could be source confusion in crowded fields of the Galactic plane, which resulted in many sources being not included in the point source catalog. It can also be seen in Figure 7.7 that a few sources do not satisfy WC89 or HM89 criteria at all. It is not clear whether these are due to projection effects, or whether a small population of methanol masers are associated with IRAS sources which do not satisfy colors for embedded massive stars.

One of the results of Szymczak & Kus (2000) is that most of the IRAS sources in the upper left part Figure 7.7 are relatively weak masers. Ten of the new detections in the Figure 7.7 (marked in blue) are weaker than 5 Jy. Most of the red points in the diagram are stronger than 5 Jy. Since there is no segregation between the red and blue points, we do not see the result of Szymczak & Kus (2000) in our data.

Only 41 out of 76 methanol masers have possible MSX point source counterparts. Visually inspecting MSX image fields, four sources are clearly associated with MSX dark clouds, while the association with dark clouds is more uncertain for an additional four sources. The lack of point source counterparts for a majority of sources is a bit surprising, especially because there are no obvious dark clouds at the sites of a majority of masers lacking point source counterparts.

Seven out of 76 sources have NVSS point sources within $23''$. The emission at 1.4 GHz is thought to come from thermal bremsstrahlung (or free-free emission) in the ionized regions surrounding the massive star. The optical depth of a plasma due to free-free emission, under the Altenhoff et al. (1960) approximation is

$$\tau_\nu \sim \frac{0.08235}{\nu^{2.1} T_e^{1.35}} \int n_e^2 dl \quad (7.4)$$

where the frequency, ν is in GHz, T_e is the electron temperature and $\int n_e^2 dl$ is the emission measure in $\text{cm}^{-6} \text{ pc}$. If the HII region is optically thick, the emission scales as the square of the frequency. Thus, the intensity of radiation at low frequencies can be a small fraction of the intensity at a frequency corresponding to an optical depth of unity. This, compounded by the compactness of the source makes it undetectable at low frequencies. The emission measure of a HII region decreases with age (as it expands), and hence younger HII regions are optically thick at higher frequencies. Thus, the lack of NVSS counterparts for a majority of methanol masers strongly suggests that the masers are primarily associated with phases of massive star formation prior to an ultracompact HII region.

It is apparent from Table 7.2 that a few sources have no tracers of star formation associated with them within $1'$. The nature of these “isolated” methanol masers is a mystery at this moment. One possibility is that they are one of the earliest signposts of massive star formation, that have counterparts primarily in millimeter

and submillimeter wavelengths. Observations at these wavelengths are required to understand the isolated methanol masers.

Chapter 8

Ongoing and Future Work

In addition to the work presented in §6 and §7, we have ongoing work, and work planned for future regarding 6.7 GHz methanol masers and their relation to high-mass star formation and Galactic structure. A brief summary of these projects is presented below.

8.1 Probing Galactic Structure Using 6.7 GHz Methanol Masers

A discussion of the use of 6.7 GHz methanol masers to probe Galactic structure, and difficulties faced in this regard has been presented in §7.3. In this section, we describe an ongoing project to determine kinematic distances to a sample of ~ 60 methanol masers using data from the Green Bank Telescope (GBT) and the Very Large Array (VLA).

8.1.1 The Kinematic Distance Ambiguity

As discussed in §7.3, one of the primary challenges in the use of tracers of massive star formation to probe the spiral structure of the Galaxy is the ambiguity between near and far distances (called kinematic distance ambiguity or KDA) towards the inner Galaxy. The kinematic distance ambiguity is illustrated in Figure 8.1 by calculating the observed radial velocity of a source at a fixed Galactic longitude (assumed here as 30°) as a function of the distance of the source from the Sun. From the figure, it is clear that all radial velocities above zero correspond to two

distances, the smaller value being called the near distance, and the other value being called the far distance. Once the source is beyond the solar circle (as seen from the center of the Galaxy), the distance becomes single valued. The point corresponding to the peak radial velocity is called the tangent point. From Figure 8.1, it can be seen that the change in radial velocity with respect to change in distance is much more gradual near the tangent point compared to other points. Thus the errors in the calculated distance (due to non-circular motions) are larger near the tangent point compared to other points.

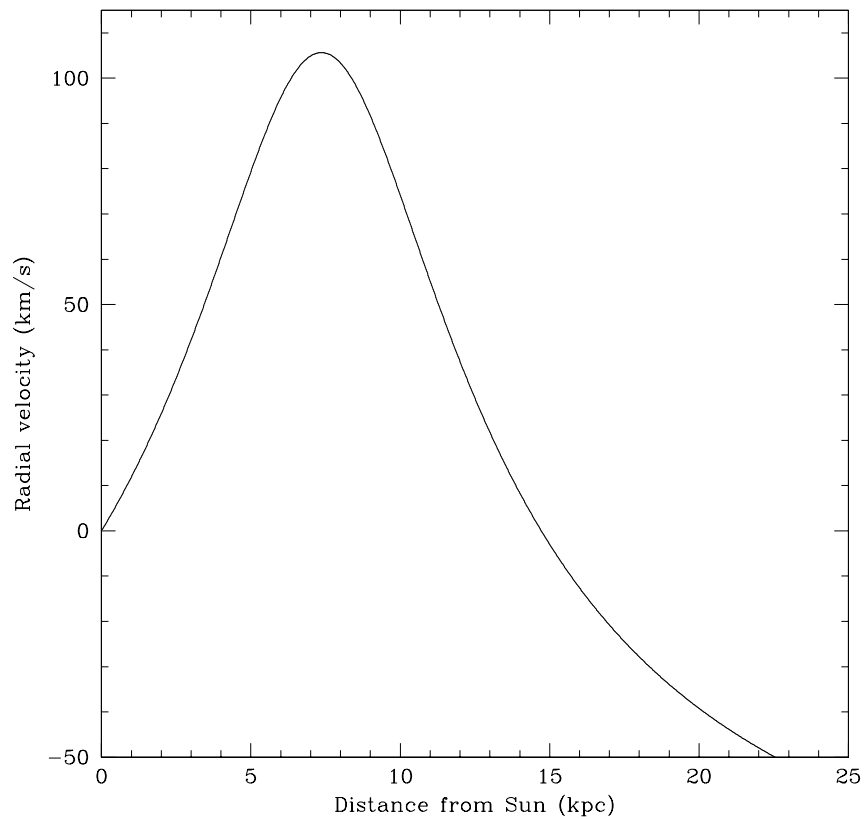


Figure 8.1 The radial velocity of a source at fixed Galactic longitude (30° in this case) as a function of distance from the Sun. The Brand & Blitz (1993) rotation curve has been used to calculate radial velocities.

8.1.2 Resolving the Kinematic Distance Ambiguity—I

A technique to resolve the kinematic distance ambiguity is to measure an absorption spectrum of some selected species towards the source of interest, and compare the velocities at which absorption is detected with the velocity of the source itself. The method will work only if the source of interest is the cause of the continuum emission against which absorption lines are detected. The absorption lines arise from interstellar clouds that lie between the source and the observer, which absorb the emission from the source at frequencies corresponding to atomic and molecular transitions of the various species in the cloud. These absorption lines are Doppler shifted to the radial velocity of the absorbing cloud. If the source is at the near kinematic distance (closer than the tangent point), then there cannot be any absorption lines between the radial velocity of the source and the tangent point velocity, since these velocities are characteristic of the material behind the source (refer Figure 8.1). Hence, if absorption lines are seen between the tangent point velocity and the radial velocity of the source, one can conclude that the source lies at the far kinematic distance. An illustration of this concept is shown in Figure 8.2, which is taken from Kolpak et al. (2003).

The tracer used to measure the absorption spectrum must be relatively abundant in interstellar clouds. Otherwise, one can get spurious results from a lack of absorption lines arising from there being not enough material present in a cloud (that is in the line of sight) to produce absorption. Two tracers that have been used successfully for this purpose are neutral hydrogen (e.g. Kolpak et al. 2003) and the 4.8 GHz transition of formaldehyde (e.g. Watson et al. 2003). Using HI as a tracer has advantages over formaldehyde, as HI is more abundant, and will not be absorbed against the Cosmic Microwave Background (CMB) unlike the 4.8 GHz

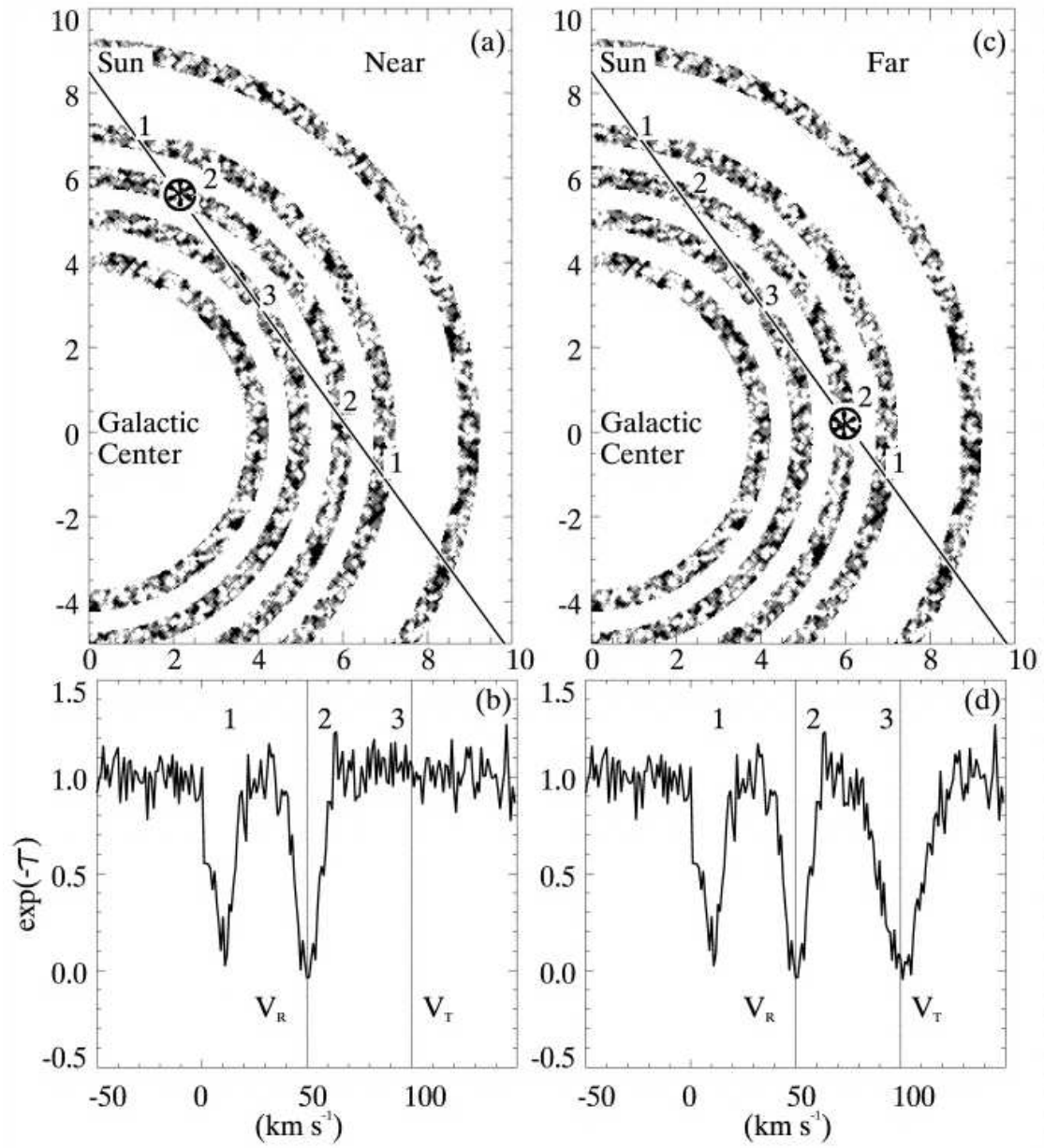


Figure 8.2 An illustration of using absorption lines to distinguish between near and far kinematic distance. Panels (a) and (c) show the cases where the source is at the near and far distance respectively, while panels (b) and (d) show the absorption spectrum that would be measured for these two cases. A comparison between the velocity of the source, V_R , the tangent point velocity V_T , and the maximum velocity at which absorption is measured can thus be used to distinguish between cases (a) and (c). The figure is taken from Kolpak et al. (2003)

transition of formaldehyde. However, it is very difficult to obtain an HI absorption spectrum using a single dish telescope since the large beam of the telescope will cover a solid angle much larger than that of the source, causing emission from the foreground gas to swamp the absorption signal from the source of interest. This can be circumvented using an interferometer to directly determine an absorption spectrum (without subtracting an “off” spectrum). A more formidable disadvantage of using HI compared to using formaldehyde arises from the fact that young HII regions are more likely to have detectable continuum at 4.8 GHz compared to 1.4 GHz (see discussion in §7.6).

8.1.3 Application to 6.7 GHz Methanol Masers

The results in §7.6 show that it is unlikely for a 6.7 GHz methanol maser to have associated continuum at 1.4 GHz. However, since massive stars form in clusters, it is likely that one or more of the stars in the cluster containing the massive young stellar object (MYSO) that excites the methanol maser emission is in a later stage of evolution, so that there is 1.4 GHz continuum from the star forming complex containing the methanol maser. Thus a sample of targets can be chosen for HI absorption line studies by looking for compact 1.4 GHz continuum sources within a $90''$ radius of the methanol maser.

It is important to establish the association of a compact 1.4 GHz source with the methanol maser itself before embarking on any absorption line studies. This is done by measuring radio recombination lines towards the continuum source. A close correspondence (to within, say 10 km s^{-1}) between the velocity of the recombination line and that of the methanol maser emission will be strong evidence for association of the continuum source with the star forming complex containing

the methanol maser. If no recombination lines are observed, then the source is not likely to be in a star forming region, and is probably just projected against the methanol maser in the sky.

We used the NVSS catalog to identify methanol masers, taken from the general catalog of Pestalozzi et al. (2005), that are coincident or closely associated with 1.4 GHz point sources. A flux limit of ~ 30 mJy on the continuum flux density was imposed due to constraints of telescope time required to obtain absorption spectra. Some sources had prior measurements of recombination lines in the catalog of Lockman (1989). We observed 45 sources that did not have prior recombination line measurements using the GBT. Using the powerful GBT spectrometer, we observed 8 recombination line transitions ($H103\alpha$ to $H110\alpha$) simultaneously in both polarizations (a total of 16 IFs). Frequency switching was used to get an additional square root of two gain in the signal to noise ratio compared to position switched observations. The data for all recombination lines were combined to be able to detect weak recombination lines. An example of the gain in signal to noise by combining multiple recombination lines is shown in Figure 8.3.

We were able to detect recombination lines towards 44 out of 45 sources. This work gave us a list of ~ 60 methanol masers towards which we could measure HI absorption spectra. We used the VLA in the C-configuration (CnB configuration for sources at very low declination to avoid a very elliptical restoring beam) to measure the absorption spectra. The observations were completed by the end of October 2005, and the data reduction is ongoing at present.

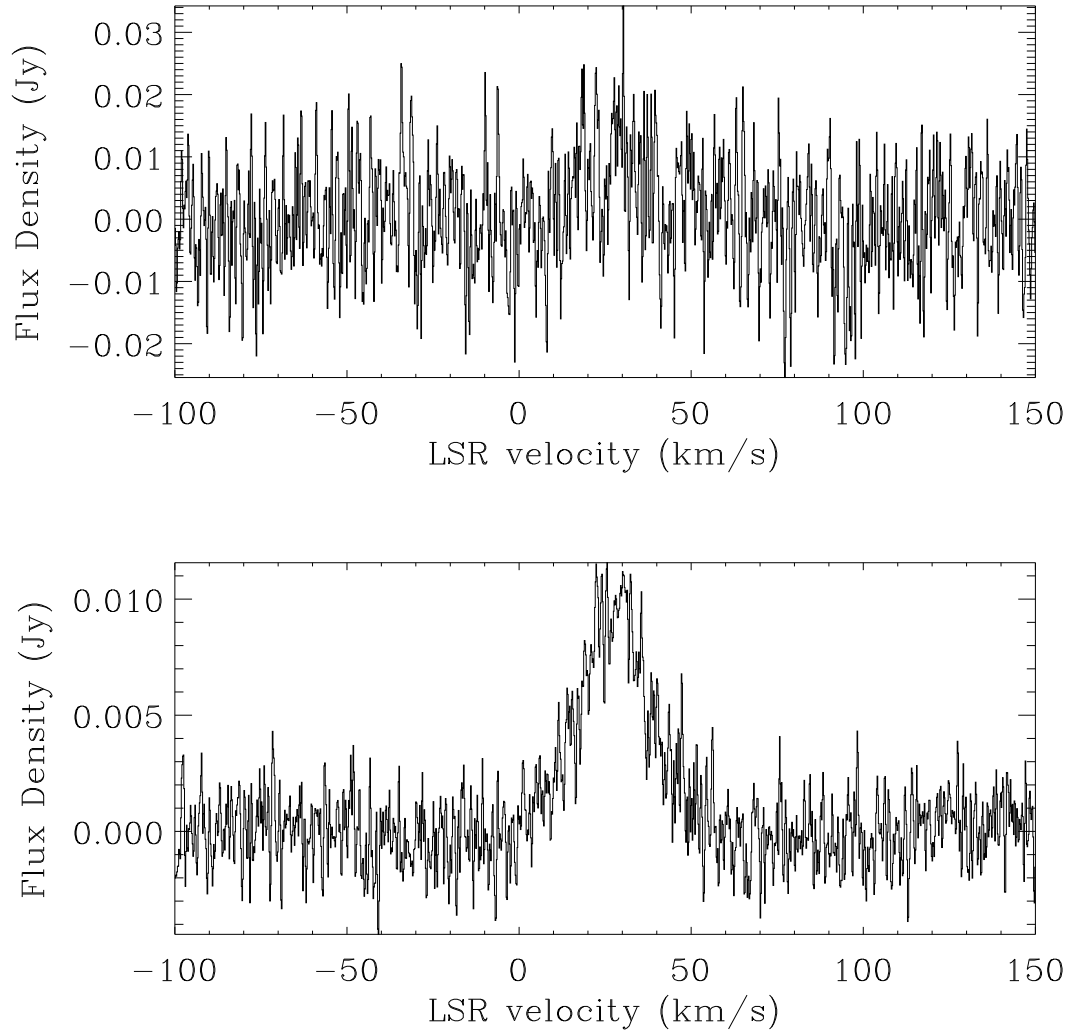


Figure 8.3 GBT recombination line data for source 58.75+0.65. The top panel shows the data at a single frequency without folding the frequency switched data. The signal to noise ratio in this spectrum is equivalent to that of a position switched observation. The bottom panel shows the result of combining 7 recombination lines (one recombination line had to be discarded due to spectrometer issues), and folding the frequency switched data which results in an additional gain in signal to noise ratio by $\sqrt{2}$.

8.1.4 Resolving the Kinematic Distance Ambiguity–II

The technique presented in §8.1.2 to resolve the KDA requires the source of interest to have associated continuum emission. The absence of directly associated or

nearby (within $90''$) radio continuum for a majority of 6.7 GHz methanol masers implies that other techniques should be investigated to resolve the KDA for methanol masers.

One technique that is relevant to MYSOs is the correlation of HI self-absorption features with molecular emission features. The use of HI self-absorption was hypothesized to be a robust method to resolve the KDA for molecular clouds by Liszt et al. (1981). The method relies on all molecular clouds retaining cold HI with sufficient opacity, which though has not been proved observationally, has been found to be true in the models of Flynn et al. (2004). If the molecular cloud is at the near distance, the cold HI in the cloud will absorb the warmer background emission giving rise to self-absorption at the velocity of the cloud. On the other hand, a cloud at the far distance will not exhibit any HI self-absorption, since there is no background emission at the velocity of the cloud to absorb.

This technique was used by Busfield et al. (2006) to resolve the distance ambiguity towards 66 out of 94 young massive stellar objects. We intend to utilize this technique to try to resolve the KDA towards the AMGPS methanol maser sample. Our proposal to obtain $^{13}\text{CO } J = 1 - 0$ spectra towards the methanol maser sample at the Arizona Submillimeter Heinrich Hertz Telescope has been approved, and we expect to collect data in December 2006. The VLA Galactic Plane Survey (VGPS; Stil et al. 2006) will be used for the HI data.

The completion of these projects will enable us to compare the results of Galactic structure inferred from methanol masers, which that determined from other tracers of massive star formation such as ultracompact HII regions. Moreover, once distances have been estimated to methanol masers, we can compute their luminosities. This will enable us to use the AMGPS data to calculate the methanol

maser luminosity function, which will be invaluable for refining theoretical models of methanol masers.

8.2 6.7 GHz Methanol Masers in M33

As indicated in §4.2, 6.7 GHz methanol masers are the second brightest maser transition ever observed, and are typically much brighter than OH masers. However, 6.7 GHz methanol masers have not been discovered in galaxies beyond the Magellanic clouds. In particular, surveys have shown that there is no analog to OH megamasers at 6.7 GHz (Phillips et al. 1998; Darling et al. 2003). The properties of methanol masers in the Magellanic clouds (Sinclair et al. 1992; Beasley et al. 1996) are consistent with those of our Galaxy, given appropriate consideration for different galactic properties such as metallicity. It would be of interest to detect methanol masers in a Milky Way like galaxy. If the number of sources detected were large, one could derive the methanol maser luminosity function since all sources would be at the same distance. Further, one could look for correlations of methanol masers with giant molecular cloud masses, other types of masers, etc. The nearest spiral galaxy that can be observed using the Arecibo radio telescope is M33.

It is difficult to develop an optimal strategy to search for extragalactic methanol masers since the luminosity function of methanol masers in our Galaxy is unknown. This is mostly due to difficulties in determining distances to methanol masers, which is compounded by the kinematic distance ambiguity. Hence, we used the following approach: We selected sources in the general catalog that have flux densities greater than 100 Jy. These sources are more likely to be at the near distance, since the far distance would imply an unreasonably large luminosity for

the maser. We then scaled the source flux density to the distance of M33, which we take to be 840 kpc (averaging the results of Lee et al. 2002 and Freedman et al. 1991 which gives a result consistent with the distance determined by Kim et al. 2002). We repeated this procedure for methanol masers that do not have any distance ambiguity. We thereby obtained an estimate for the distribution of flux density of methanol masers in M33, which of course must be regarded with considerable skepticism, as the original Galactic sample has significant biases, not to mention the unknown differences in the properties of massive star formation in M33 and the Milky Way.

With these caveats, we found a “high flux density tail” for our hypothetical methanol maser population in M33 that extends from 50 mJy down to 10 mJy, with a majority of sources in this interval having flux densities weaker than 15 mJy. The number of maser sources becomes large only at the 10 mJy level, and consequently, we adopted this as the target sensitivity for our search. A position switched observation with a total integration time of 1 hour (30 minutes on source, 30 minutes off source) at Arecibo would achieve a 5σ sensitivity better than 10 mJy when the data is smoothed to a velocity resolution of 0.30 km s^{-1} .

Since massive star formation occurs mostly in giant molecular clouds (GMCs), we chose our target list from the basic catalog of GMCs in M33 (Engargiola et al. 2003). We observed a total of 14 GMCs with the strongest associated CO emission in July 2005. The observations were centered on the velocity of CO emission for each GMC. There were no detections of methanol masers which is surprising. For an individual GMC, a 3σ upper limit on the flux density of a methanol maser in M33 is around 4.5 mJy.

Assuming that all the GMCs do exhibit methanol maser emission at a weak

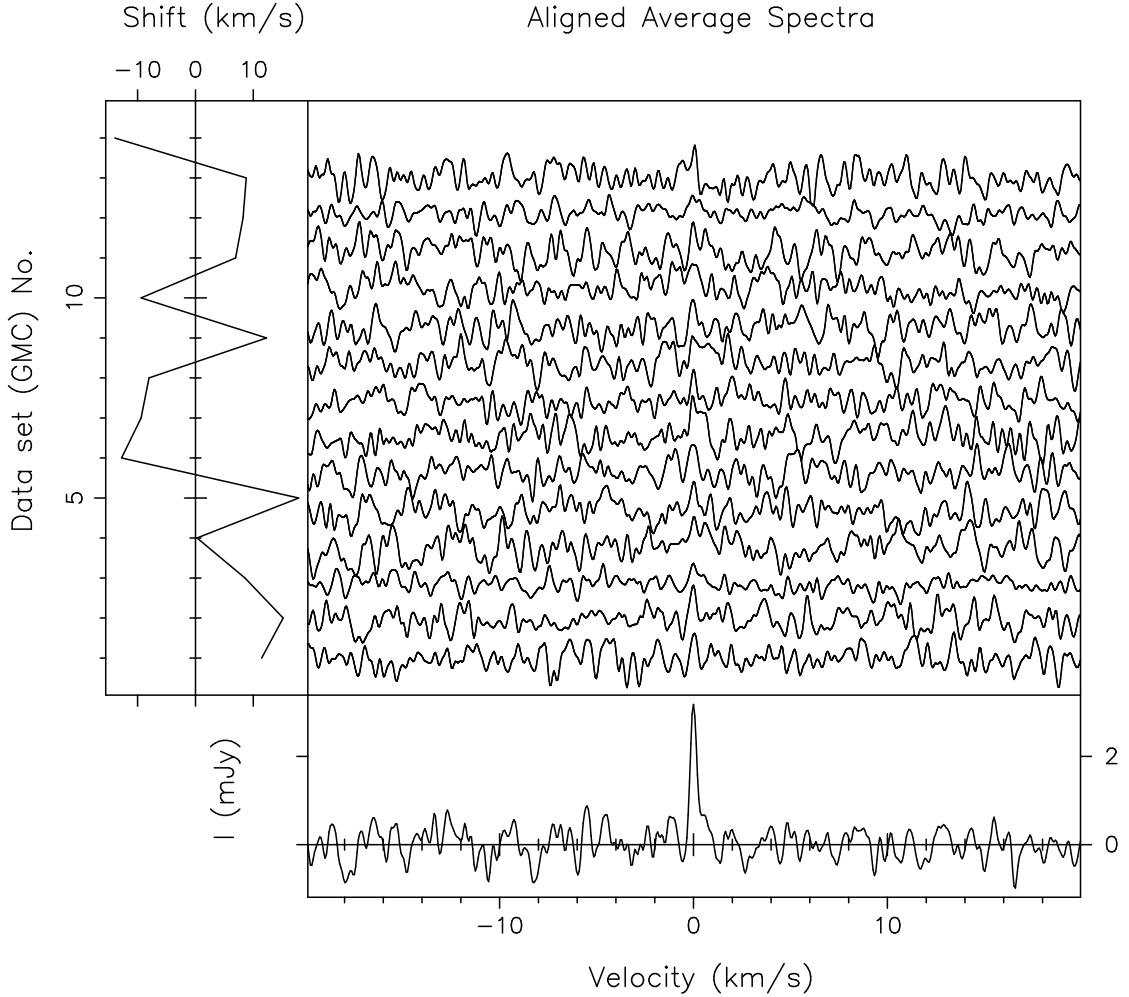


Figure 8.4 The bottom panel shows the result of adding the spectra of 14 GMCs that have been shifted in velocity to the velocity of peak cross-correlation with a Gaussian template. This spectrum is labeled as spectrum A. The x-axis of the plot shows the velocity offset from that of the CO emission line. The top panel shows the shifted individual GMC spectra, each of which is smoothed to a linewidth of 0.25 km s^{-1} . The side panel shows the amount of velocity shift applied for each spectrum.

level, one can add the data for all GMCs to get a better upper limit on the emission. This assumes that the emission occurs at the same velocity offset with respect to the velocity of the central channel in any given spectrum, which is not necessarily true. To allow for different velocity offsets for the location of emission in different GMCs, we follow the following procedure. We first select a section of the spectrum

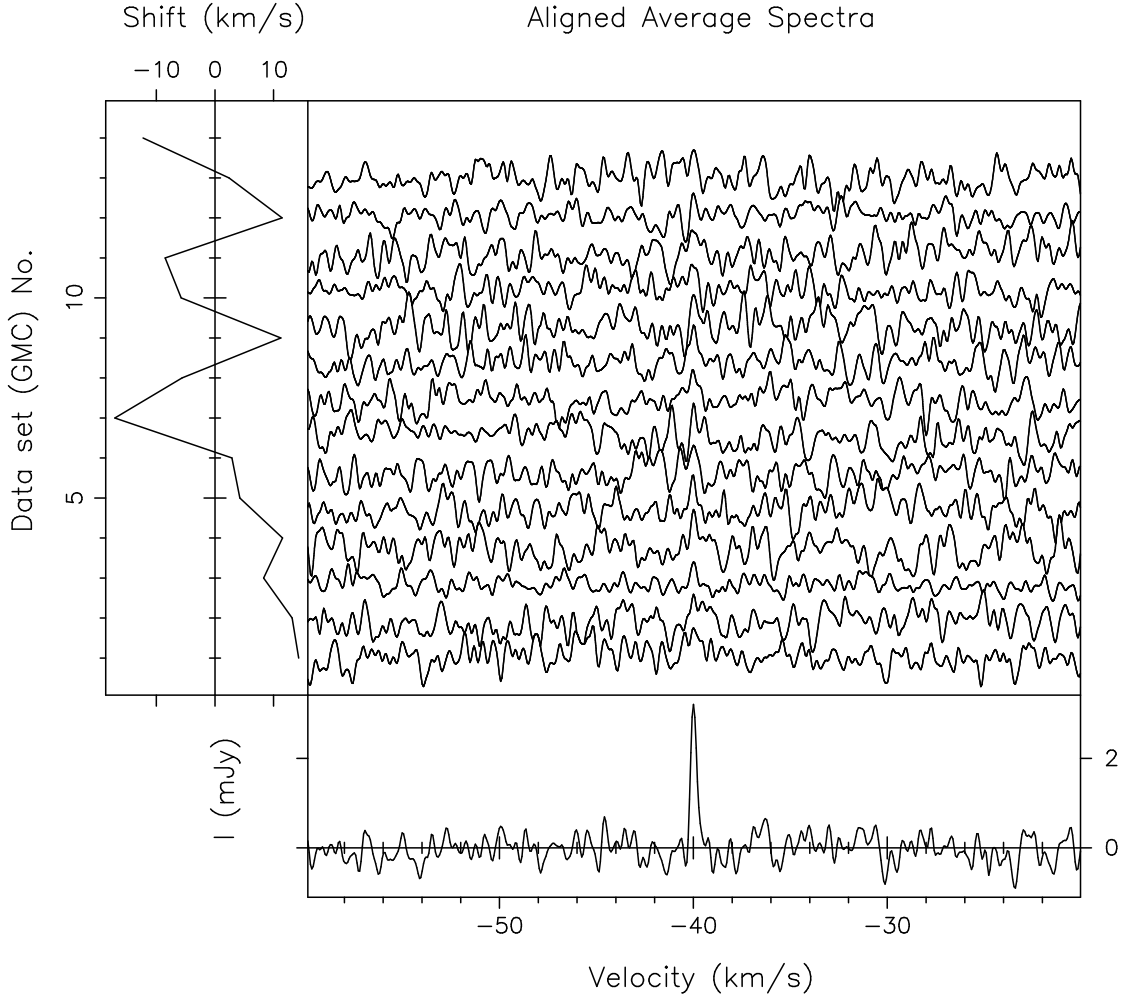


Figure 8.5 The bottom panel shows the result of adding the spectra of 14 GMCs that have been shifted in velocity to the velocity of peak cross-correlation with a Gaussian template. This analysis has been done over a portion of the spectrum where no methanol maser emission is expected and the result is labeled as spectrum B. The x-axis of the plot shows the velocity offset from that of the CO emission line. The top panel shows the shifted individual GMC spectra, each of which is smoothed to a linewidth of 0.25 km s^{-1} . The side panel shows the amount of velocity shift applied for each spectrum.

around the velocity of CO emission for each GMC ($\sim \pm 40 \text{ km s}^{-1}$), which includes the largest offset one would expect between the methanol maser and the molecular line emission (expected to be less than 15 km s^{-1}). Each sub-spectrum is then cross-correlated with a Gaussian whose width represents the expected linewidth of

the maser emission ($\sim 0.30 \text{ km s}^{-1}$ from §7.5). Each sub-spectrum is then shifted by the offset between the central channel and the channel of peak cross-correlation. Following this procedure, the shifted data for all GMCs are added together. We label the resulting spectrum as “A”, and is shown in Figure 8.4.

It is to be noted that the above procedure will create a line feature resembling the correlation template (a Gaussian signal in this case) from the constructive alignment of purely random noise. Hence, the procedure is repeated for a different portion of the spectrum, where one does not expect to see any methanol maser emission, and the resulting spectrum is labeled “B” (Figure 8.5). We then compare the A and B spectra. If there were to be a weak but detectable average emission signature, the peak in the spectrum A will be higher than the peak in spectrum B by a statistically significant amount. Since this is not the case as can be seen from Figures 8.4 and 8.5, we conclude that there is no detectable methanol maser emission in the data. The resultant 3σ upper limit on the average emission is $\sim 1 \text{ mJy}$.

This is a full order of magnitude below the flux density that we would expect to be common in M33 from the extrapolation of our admittedly uncertain results in the Milky Way. This difference, if real, would certainly suggest some large-scale difference in the molecular clouds or massive young stars in M33 compared to the Milky Way. A much more meaningful result could be obtained if we had better knowledge of the methanol maser luminosity function in our Galaxy. We expect to publish our results in the near future.

8.3 Obtaining Accurate Positions for 6.7 GHz Methanol Masers

One of the limiting factors in using the AMGPS methanol maser sample to understand the link between 6.7 GHz methanol masers and massive star formation is the large uncertainty in the methanol maser positions. As seen in §7.6, it is at present not possible to use GLIMPSE or 2MASS data to determine mid and near infrared counterparts to the methanol masers discovered in AMGPS.

We have proposed to obtain MERLIN observations of the AMGPS methanol maser sample to determine positions accurate to a fraction of an arcsecond. The accurate positions will also allow us to embark on Very Long Baseline Interferometry (VLBI) experiments, to study both kinematics of star forming regions using the milli-arcsecond structure of the numerous masing spots in any given maser, and Galactic structure by determining parallax to the strong masers similar to the work of Xu et al. (2006) which led to a revision of the distance to the Perseus spiral arm.

8.4 Linking 6.7 GHz Methanol Masers and Massive Star Formation

While 6.7 GHz methanol masers seem to probe *an* early phase of massive star formation, it is still not entirely clear with *which* phase(s) it is associated. Multi-wavelength observations on a methanol maser sample derived from a blind survey are required to solve this problem. A subset of the AMGPS methanol maser sample is an excellent starting point for this problem since AMGPS is the most sensitive blind survey carried out to date for 6.7 GHz methanol masers.

The first task in this process is to establish the nature of the source responsible for pumping a given methanol maser. A combination of continuum and line observations are required for this purpose. The continuum observations are required to determine the spectral energy distribution (SED) of the sources. Since data at resolution of $1''$ or better is already available for wavelengths shorter than $\sim 20\mu\text{m}$, new observations are only required between centimeter and submillimeter wavelengths. SED modeling can distinguish between different evolutionary stages of MYSOs. For instance, fitting a combination of free-free and dust emission templates to the SED between radio and submillimeter wavelengths can distinguish between ultracompact HII regions, hypercompact HII regions and hot molecular cores.

Line observations are required to determine bulk properties, and probe the kinematics of the sources. Masses of the sources associated with methanol masers can be estimated through submillimeter observations of dust, and observations of multiple transitions of optically thin tracers of gas such as C^{18}O . The temperatures of the regions can be estimated through observations of different J and K ladders of CH_3CN , and kinematics can be probed through observations of tracers like CO and NH_3 .

Since statistical arguments are required to determine the turn-on and turn-off points of methanol masers, the work above needs to be carried out for a number of methanol masers. Since massive star formation takes place in crowded environments, high resolution observations through interferometers are required to avoid confusion between closely spaced multiple sources, although single dish observations can be a good starting point. The advent of a number of new millimeter and submillimeter interferometers such as CARMA, SMA and ALMA makes this an

excellent time to undertake this work. This is a long term project requiring efforts from many collaborators since a lot of telescope time is required from a number of telescopes. We have at present proposed to obtain VLA Q-Band (7 mm) continuum observations in the D-configuration for a small sample of methanol masers as a pilot project.

Appendix A

Waveguide Calibration

A.1 S-parameters

In general, to characterize a network, one needs to have a knowledge of the components that comprise the network. However, linear networks or non-linear networks working in the small signal regime can be completely characterized by parameters measured at the ports of the network without any knowledge of its components. The number of parameters required depends on the number of ports in the network. Once these parameters are determined, the behavior of the network in various environments can be described even though we do not know the contents of the network.

As an example, consider the two port network as shown in Figure A.1 (the network is assumed to be linear). The four variables we here associate with this network are the voltages V_1 and V_2 , and currents I_1 and I_2 . These variables can be related using the Z -parameters by

$$V_1 = Z_{11}I_1 + Z_{12}I_2 \quad (\text{A.1})$$

$$V_2 = Z_{21}I_1 + Z_{22}I_2 \quad (\text{A.2})$$

The Z -parameters can be measured at the ports of the network by terminating one port appropriately and exciting the other port. For example, Z_{11} can be measured by open-circuiting port 2, exciting port 1 by a current I_1 and measuring the resulting voltage V_1 .

$$Z_{11} = \left. \frac{V_1}{I_1} \right|_{I_2=0} \quad (\text{A.3})$$

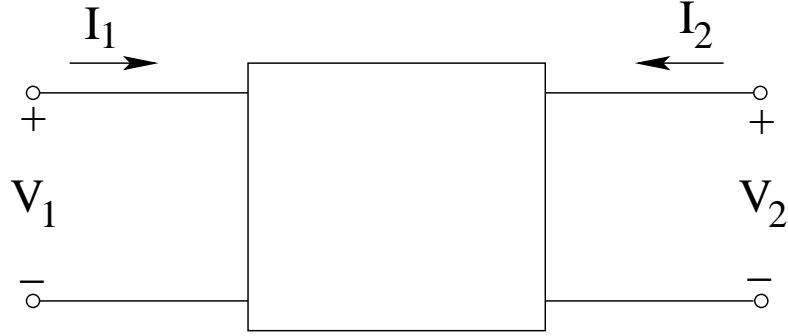


Figure A.1 Schematic of a two-port network.

In microwave circuits at high frequencies, it is difficult to short-circuit or open-circuit the network and hence it is cumbersome to measure parameters involving voltages and currents. Instead, it is much easier to deal with traveling waves. The scattering parameters or S-parameters refer to how traveling waves are reflected and transmitted when a n-port network is inserted into a transmission line.

The generalized S-parameters are defined by Kurokawa (1965). These parameters refer to the relationship between the complex voltage waves incident and reflected from each port of the network. For the i -th port, the incident and reflected voltage waves are defined as

$$a_i = \frac{V_i + Z_i I_i}{2\sqrt{|\operatorname{Re}\{Z_i\}|}} \quad (\text{A.4})$$

$$b_i = \frac{V_i - Z_i^* I_i}{2\sqrt{|\operatorname{Re}\{Z_i\}|}} \quad (\text{A.5})$$

where Z_i is an arbitrary reference impedance. For most measurements, the reference impedance is the characteristic impedance of the transmission line Z_0 which is a real quantity. Then, for a two-port network (refer Figure A.2), the voltage

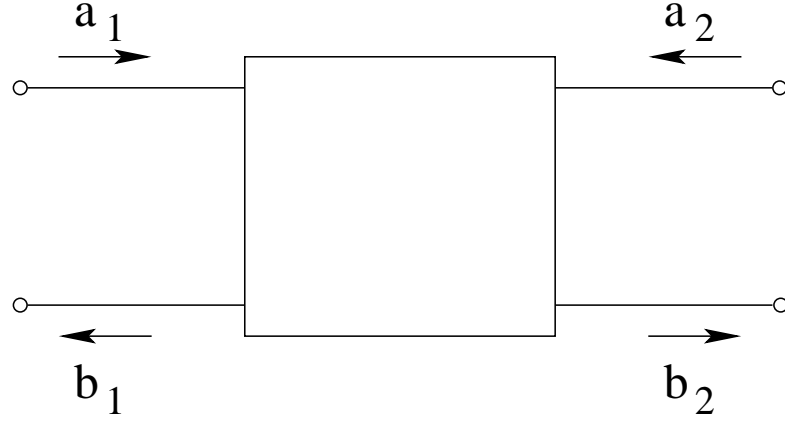


Figure A.2 Voltage waves in a two-port network

waves are given by

$$a_1 = \frac{V_1 + Z_0 I_1}{2\sqrt{Z_0}} = \frac{V_{i1}}{\sqrt{Z_0}} \quad (\text{A.6})$$

$$b_1 = \frac{V_1 - Z_0 I_1}{2\sqrt{Z_0}} = \frac{V_{r1}}{\sqrt{Z_0}} \quad (\text{A.7})$$

$$a_2 = \frac{V_2 + Z_0 I_2}{2\sqrt{Z_0}} = \frac{V_{i2}}{\sqrt{Z_0}} \quad (\text{A.8})$$

$$b_2 = \frac{V_2 - Z_0 I_2}{2\sqrt{Z_0}} = \frac{V_{r2}}{\sqrt{Z_0}} \quad (\text{A.9})$$

where V_{i1} , V_{i2} , V_{r1} and V_{r2} are the incident and reflected waves in ports 1 and 2 respectively.

Then, in the case of a linear two-port network, the S-parameters are related to the voltage waves through

$$b_1 = S_{11}a_1 + S_{12}a_2 \quad (\text{A.10})$$

$$b_2 = S_{21}a_1 + S_{22}a_2 \quad (\text{A.11})$$

The physical meaning of the S-parameters are as follows: S_{11} refers to the ratio of the amplitude of the voltage wave coming out of port 1 when port 2 is terminated by a matched load (which sets $a_2 = 0$) to the amplitude of the incident wave. S_{22}

is similar to S_{11} except that the measurement is done on port 2 while port 1 is terminated by a matched load. $|S_{11}|^2$ and $|S_{22}|^2$ refer to the ratio of the reflected power to the incident power at ports 1 and 2 respectively while the other port is terminated by a matched load. They are a measure of the mismatch of the network to the input signal.

S_{21} is the ratio of the voltage wave output from port 2 in response to the input wave at port 1 with the measurement taken by terminating port 2 by a matched load. Similarly S_{12} is the ratio of the voltage wave output from port 1 in response to the input wave at port 2 with the measurement taken by terminating port 1 by a matched load. $|S_{21}|^2$ and $|S_{12}|^2$ are the power gains of the system in the forward and reverse directions respectively. In the case of a reciprocal two-port network, $|S_{11}|^2 = |S_{22}|^2$ and $|S_{21}|^2 = |S_{12}|^2$.

A.2 Measurement of S-parameters

S-parameters are usually measured using vector network analyzers. Network analyzers measure the reflection and transmission characteristics of devices and networks by applying a known signal and measuring the response of the test device. To cover a frequency range of interest, the incident signal is generated by sweeping an RF source. The incident signal and the signal transmitted through the device or reflected from its input are applied to a receiver for measurement, signal processing and display. Details of the source, signal separation device and receiver are usually given in the manual pages of network analyzers.

An ideal measurement system would have infinite dynamic range, isolation and directivity characteristics, no impedance mismatches in any part of the test setup, and a flat frequency response. In reality, in any high frequency measurement, there

are measurement errors associated with the system that contribute to uncertainty in the results. While random and drift errors cannot be corrected, systematic errors (which are the most significant source of measurement uncertainty in high frequency measurements) can be corrected for by appropriate calibration. Most of the theory presented in the next two sections is taken from Hewlett-Packard (1989).

A.3 One-port Error Model

The one-port error model is shown in Figure A.3. The reflection coefficient is measured by separating the incident signal from the reflected signal (using a directional bridge or coupler) and then taking the ratio of the two values. Ideally, the reflected signal consists only of the signal reflected by the device under test.

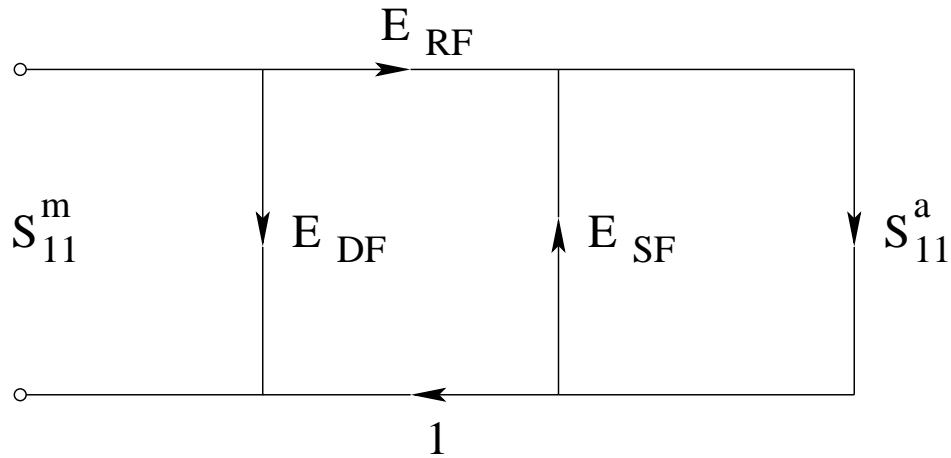


Figure A.3 One-port error model.

However, part of the incident signal appears at the coupled port (where the reflected signal is measured) due to leakage through the test set or due to reflections in the adapters between signal separation and the measurement plane. The vector sum of the leakage and miscellaneous reflections appearing at the analyzer receiver

is called **directivity**, E_{DF} . The greater is the directivity, the better is the signal separation. The error caused by directivity usually produces the major ambiguity in measurements of low reflection devices.

Further, as the impedance of the test port is never exactly the characteristic impedance (leading to source mismatch), part of the reflected signal coming from the device under test will be bounced off of the test port, adding to the original incident signal. This re-reflection effect and the resultant incident power variation is characterized by E_{SF} . **Source match** is a major source of uncertainty in measurements if there is a large impedance mismatch at the measurement plane. Typical sources of large impedance mismatch are the interface between coaxial lines and waveguides, and connections between the analyzer port and coaxial cables.

In addition, the magnitude and phase response of the system is not flat with respect to frequency. This can be taken into account easily if the frequency response is the same for both the incident and reflected signals. However, imperfectly matched samplers and differences in length and loss between incident and test signal paths lead to variations in the frequency response between the incident and reflected signals. This leads to a frequency response error E_{RF} .

Based on the model, one can derive the mathematical relation between the three error quantities, the actual data S_{11}^a and the measured data S_{11}^m . Let a^m and b^m be the voltage waves incident on and reflected from the measurement plane, while a^a and b^a be the quantities at the device under test. Then, from the flow

diagram in Figure A.3,

$$a^a = a^m E_{RF} + b^a E_{SF} \quad (\text{A.12})$$

$$\Rightarrow a^m = \frac{a^a - b^a E_{SF}}{E_{RF}}$$

$$b^m = a^m E_{DF} + b^a \quad (\text{A.13})$$

$$\Rightarrow \frac{b^m}{a^m} = S_{11}^m = E_{DF} + \frac{b^a E_{RF}}{a^a - b^a E_{SF}} \quad (\text{A.14})$$

Since $S_{11}^a = b^a/a^a$, eq. (A.14) becomes

$$S_{11}^m = E_{DF} + \frac{S_{11}^a E_{RF}}{1 - E_{SF} S_{11}^a} \quad (\text{A.15})$$

If the value of the three error terms are known, then one can derive the actual data from the measured response of the test device. As the errors are functions of frequency, they must be known at all frequencies of interest. The values of the three error terms are found using three independent standards whose S_{11}^a is known at all frequencies.

Three most commonly used standards are a short circuit, an open circuit and a perfect load for which $S_{11}^a = -1$, 1 and 0 respectively. By measuring S_{11}^m for each of these standards, the three error terms can be computed, which can be used to calculate S_{11}^a from the measured value S_{11}^m in an actual setup as

$$S_{11}^a = \frac{S_{11}^m - E_{DF}}{E_{SF}(S_{11}^m - E_{DF}) + E_{RF}} \quad (\text{A.16})$$

While specially designed shielded standards are available commercially for coaxial lines, the problem is more complicated if the measurement plane is a waveguide port. The dimensions of the waveguide used depends on the frequency of interest, and the bandwidth for which the waveguide can be used in single mode, is limited to around 30 – 40%. Hence, standards for waveguides have to be custom designed for each waveguide. Usually the standards chosen are three waveguide shorts with

the total phase delay of the shorts being 0° , 120° and 240° respectively. Then, S_{11}^a for the three standards will be $-1\angle 0^\circ$, $-1\angle 120^\circ$ and $-1\angle 240^\circ$ respectively.

Most network analyzers can do the calculations for the one-port calibration using the standards for coaxial lines (the open circuit, short circuit and perfect load) internally. However, not all analyzers are equipped to do the calculations for a more general choice of standards as is the case for waveguide calibration. In this case, it may be necessary to do the calculations using the raw measurements externally. From eq. (A.15), one can derive equations for the error quantities from measurements S_{11}^{m1} , S_{11}^{m2} and S_{11}^{m3} of three general standards with S-parameters S_{11}^{a1} , S_{11}^{a2} and S_{11}^{a3} respectively as

$$E_{RF}(\nu) = -\frac{A(\nu)}{D^2(\nu)} \quad (\text{A.17})$$

$$E_{DF}(\nu) = \frac{B(\nu)}{D(\nu)} \quad (\text{A.18})$$

$$E_{SF}(\nu) = \frac{C(\nu)}{D(\nu)} \quad (\text{A.19})$$

where $A(\nu)$, $B(\nu)$, $C(\nu)$ and $D(\nu)$ are given by

$$A(\nu) = (S_{11}^{a1} - S_{11}^{a2})(S_{11}^{a2} - S_{11}^{a3})(S_{11}^{a3} - S_{11}^{a1}) \quad (\text{A.20})$$

$$(S_{11}^{m1} - S_{11}^{m2})(S_{11}^{m2} - S_{11}^{m3})(S_{11}^{m3} - S_{11}^{m1})$$

$$B(\nu) = S_{11}^{a1}S_{11}^{a2}(S_{11}^{m1} - S_{11}^{m2})S_{11}^{m3} + S_{11}^{a2}S_{11}^{a3}(S_{11}^{m2} - S_{11}^{m3})S_{11}^{m1} \quad (\text{A.21})$$

$$+ S_{11}^{a3}S_{11}^{a1}(S_{11}^{m3} - S_{11}^{m1})S_{11}^{m2}$$

$$C(\nu) = S_{11}^{a1}(S_{11}^{m3} - S_{11}^{m2}) + S_{11}^{a2}(S_{11}^{m1} - S_{11}^{m3}) + S_{11}^{a3}(S_{11}^{m2} - S_{11}^{m1}) \quad (\text{A.22})$$

$$D(\nu) = S_{11}^{a1}S_{11}^{a2}(S_{11}^{m1} - S_{11}^{m2}) + S_{11}^{a2}S_{11}^{a3}(S_{11}^{m2} - S_{11}^{m3}) + S_{11}^{a3}S_{11}^{a1}(S_{11}^{m3} - S_{11}^{m1}) \quad (\text{A.23})$$

Once the error terms are calculated, one can use eq. (A.16) to calculate S_{11}^a from the measured value S_{11}^m in any test setup.

A.4 Two-port Error Model

In a two-port measurement, in addition to directivity, source match and reflection tracking, one has to deal with load match, transmission tracking and isolation.

Errors from **load match** result from the impedance of the transmission return port not being matched exactly to the characteristic impedance of the system. This results in some of the transmitted signal being reflected from test port 2, and from other mismatches between the output of the test device and the receiver input. A portion of this signal may be re-reflected at ports 1 and 2 affecting S_{21}^m , or transmitted at port 1 affecting S_{11}^m . This error term, E_{LF} , causes the magnitude and phase of the transmitted signal to vary as a function of S_{22}^a .

Transmission tracking, E_{TF} , refers to the frequency response of the system to the transmitted signal. It is measured by connecting a through section between ports 1 and 2, and correcting the data for source and load match errors.

Isolation, E_{XF} represents the part of the incident signal that appears at the receiver without actually passing through the test device. Isolation is measured with the test set in transmission configuration and with terminations installed at the points where the test device will be connected. For most measurements, the isolation of the network analyzer is adequate and E_{XF} can be ignored.

To summarize, the full two-port model consists of two sets of error terms, forward and reverse, with each set consisting of six error terms,

- Directivity, E_{DF} and E_{DR}
- Isolation, E_{XF} and E_{XR}
- Source match, E_{SF} and E_{SR}
- Load match, E_{LF} and E_{LR}

- Reflection tracking, E_{RF} and E_{RR} , and
- Transmission tracking, E_{TF} and E_{TR} .

The flow diagram for the full two-port error model is shown in Figure A.4.

From the flow diagram, the full two-port error model equations can be derived to

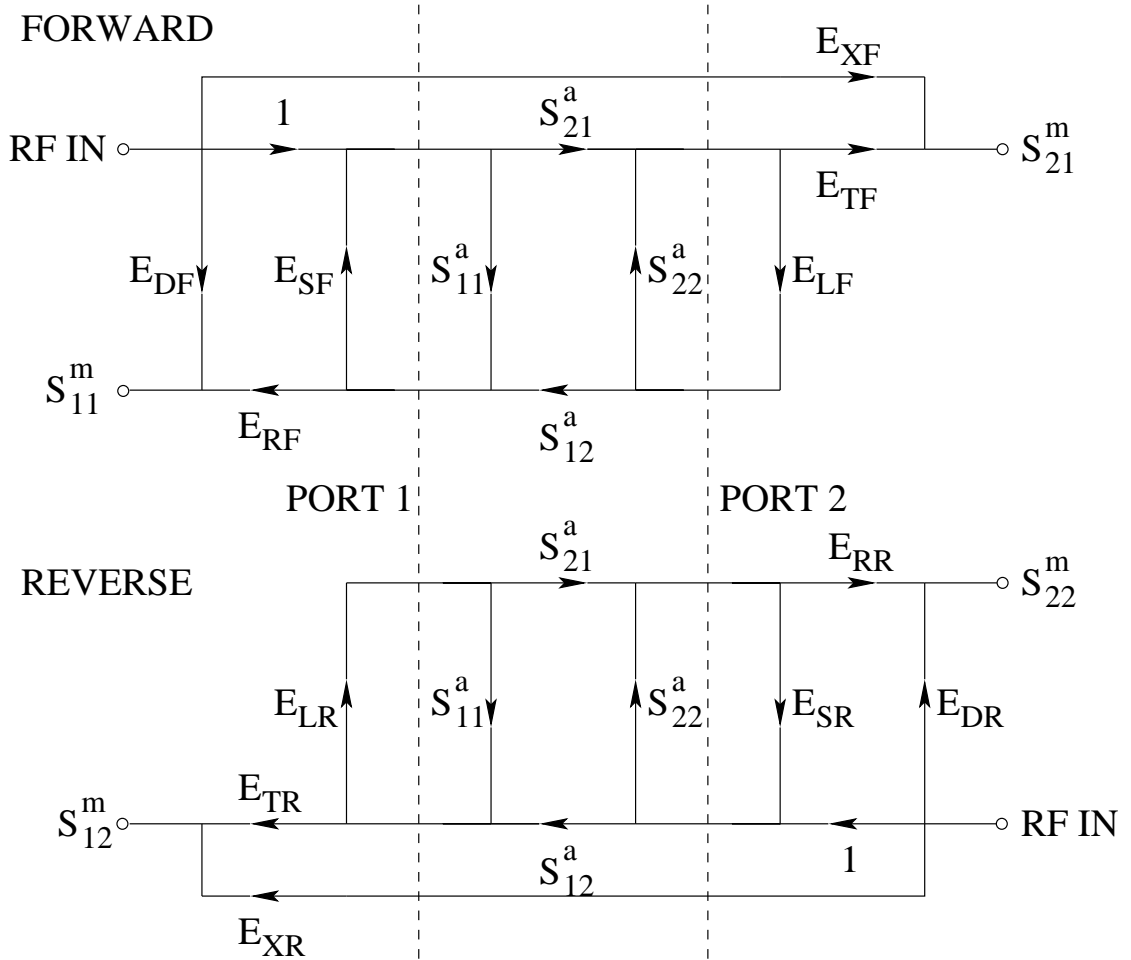


Figure A.4 Two-port error model.

be

$$S_{11}^a = \frac{N_{11}(\nu)}{DN(\nu)} \quad (\text{A.24})$$

$$S_{21}^a = \frac{N_{21}(\nu)}{DN(\nu)} \quad (\text{A.25})$$

$$S_{12}^a = \frac{N_{12}(\nu)}{DN(\nu)} \quad (\text{A.26})$$

$$S_{22}^a = \frac{N_{22}(\nu)}{DN(\nu)} \quad (\text{A.27})$$

where $N_{11}(\nu)$, $N_{21}(\nu)$, $N_{12}(\nu)$ and $N_{22}(\nu)$ are given by

$$N_{11}(\nu) = \left(\frac{S_{11}^m - E_{DF}}{E_{RF}} \right) \left[1 + \left(\frac{S_{22}^m - E_{DR}}{E_{RR}} \right) E_{SR} \right] - \left[\left(\frac{S_{21}^m - E_{XF}}{E_{TF}} \right) \left(\frac{S_{12}^m - E_{XR}}{E_{TR}} \right) E_{LF} \right] \quad (\text{A.28})$$

$$N_{21}(\nu) = \left[1 + \left(\frac{S_{22}^m - E_{DR}}{E_{RR}} \right) (E_{SR} - E_{LF}) \right] \left(\frac{S_{21}^m - E_{XF}}{E_{TF}} \right) \quad (\text{A.29})$$

$$N_{12}(\nu) = \left[1 + \left(\frac{S_{11}^m - E_{DF}}{E_{RF}} \right) (E_{SF} - E_{LR}) \right] \left(\frac{S_{12}^m - E_{XR}}{E_{TR}} \right) \quad (\text{A.30})$$

$$N_{22}(\nu) = \left(\frac{S_{22}^m - E_{DR}}{E_{RR}} \right) \left[1 + \left(\frac{S_{11}^m - E_{DF}}{E_{RF}} \right) E_{SF} \right] - \left[\left(\frac{S_{21}^m - E_{XF}}{E_{TF}} \right) \left(\frac{S_{12}^m - E_{XR}}{E_{TR}} \right) E_{LR} \right] \quad (\text{A.31})$$

$$DN(\nu) = \left[1 + \left(\frac{S_{11}^m - E_{DF}}{E_{RF}} \right) E_{SF} \right] \left[1 + \left(\frac{S_{22}^m - E_{DR}}{E_{RR}} \right) E_{SR} \right] - \left[\left(\frac{S_{21}^m - E_{XF}}{E_{TF}} \right) \left(\frac{S_{12}^m - E_{XR}}{E_{TR}} \right) E_{LF} E_{LR} \right] \quad (\text{A.32})$$

A.4.1 Two-port waveguide calibration

The first step in the full two-port waveguide calibration is to determine the one-port reflection error terms using the methodology indicated in the previous section.

By applying the waveguide shorts to ports 1 and 2, the reflection error terms

E_{DF} , E_{SF} , E_{RF} , E_{DR} , E_{SR} and E_{RR} can be determined.

After taking the one-port measurements, a through waveguide is connected between ports 1 and 2 and a two-port measurement is taken. The through waveguide should have $S_{11}^a = S_{22}^a = 0$ and unity transmission with some propagation delay. The propagation delay can be used as a reference delay when measuring a device, and in this situation, $S_{21}^a = S_{12}^a = 1$.

As indicated before, in most measurements, the isolation of the analyzer is adequate and hence, the terms E_{XF} and E_{XR} can be ignored. Denoting the S-parameters measured with the through waveguide as S_{ij}^{mt} , $i, j = \{1, 2\}$, one can now solve for the load match and transmission tracking error terms as

$$E_{LF} = \frac{E_{DF} - S_{11}^{mt}}{E_{DF}E_{SF} - E_{SF}S_{11}^{mt} - E_{RF}} \quad (\text{A.33})$$

$$E_{LR} = \frac{E_{DR} - S_{22}^{mt}}{E_{DR}E_{SR} - E_{SR}S_{22}^{mt} - E_{RR}} \quad (\text{A.34})$$

$$E_{TF} = \frac{E_{RF}S_{21}^{mt}}{E_{RF} - E_{DF}E_{SF} + E_{SF}S_{11}^{mt}} \quad (\text{A.35})$$

$$E_{TR} = \frac{E_{RR}S_{12}^{mt}}{E_{RR} - E_{DR}E_{SR} + E_{SR}S_{22}^{mt}} \quad (\text{A.36})$$

One can now compute the calibrated S-parameters of the test device S_{ij}^a from the measured values S_{ij}^m in an actual test setup from equations (A.24)–(A.27).

A.5 Experimental Demonstration of Waveguide Calibration

To demonstrate the technique of waveguide calibration, we tested an S-Band feed horn that had been designed to have an input match better than 25 dB across a 100 MHz band centered around 2.38 GHz (the feed horn was designed for use in the radar system at Arecibo). The feed horn was coupled to a waveguide to coaxial line adapter, which was connected to the vector network analyzer using 7mm test

cables. An array of Eccosorb absorbers were placed at the end of the feed horn to create a good termination.

The waveguide to coaxial line adapter was deliberately mistuned to introduce a large error in the measured S_{11} scattering parameter. The raw data measured with this set up is shown in Figure A.5. The effect of the mistuned waveguide to coaxial adapter can be seen from the measured S_{11} , which is much higher than the value expected from the feed horn design.

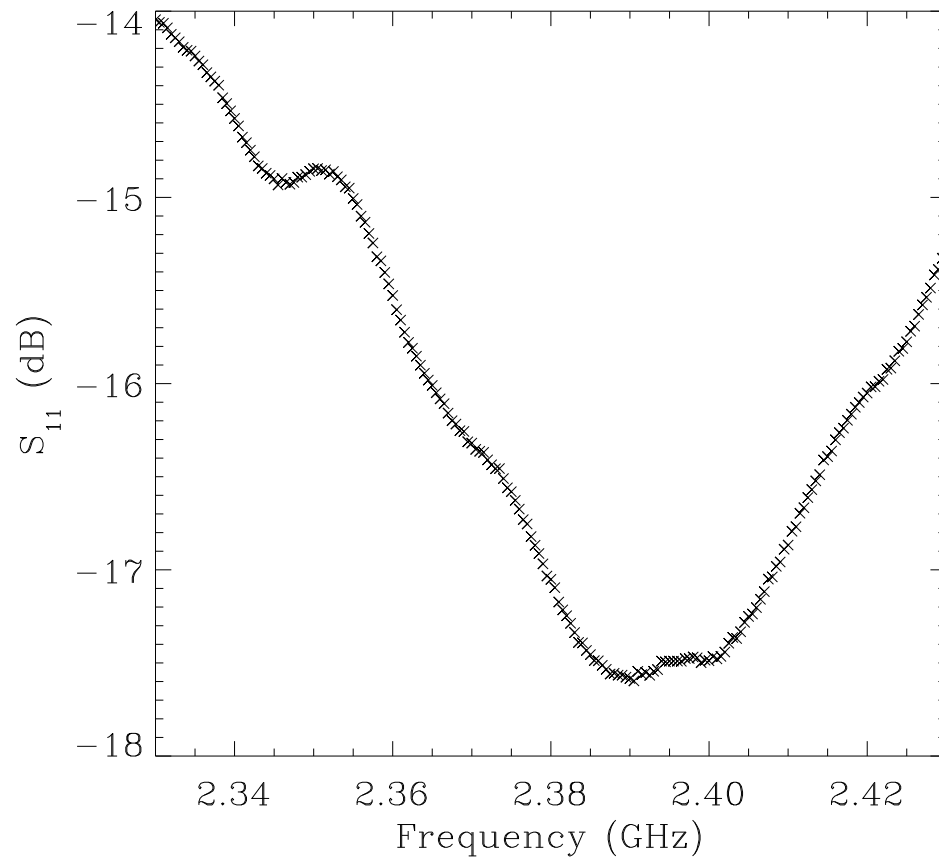


Figure A.5 S-Band feed horn response with mistuned waveguide to coaxial line adapter. The reflections of the incident wave on the mistuned wave to coaxial line adapter cause the measured S_{11} to be significantly higher than the value expected from the feed horn, which is the device under test.

To measure the true response of the feed horn, we need to calibrate out the response of the waveguide to coaxial line adapter. We thus measured the response of the waveguide to coaxial line adapter when terminated by three waveguide shorts. The three shorts introduced a net phase delay of 0° , 120° and 240° respectively. We then carried out the waveguide calibration using the equations in §A.3, the result of which is shown in Figure A.6. One can see that the calibrated S_{11} is consistent with the design parameters.

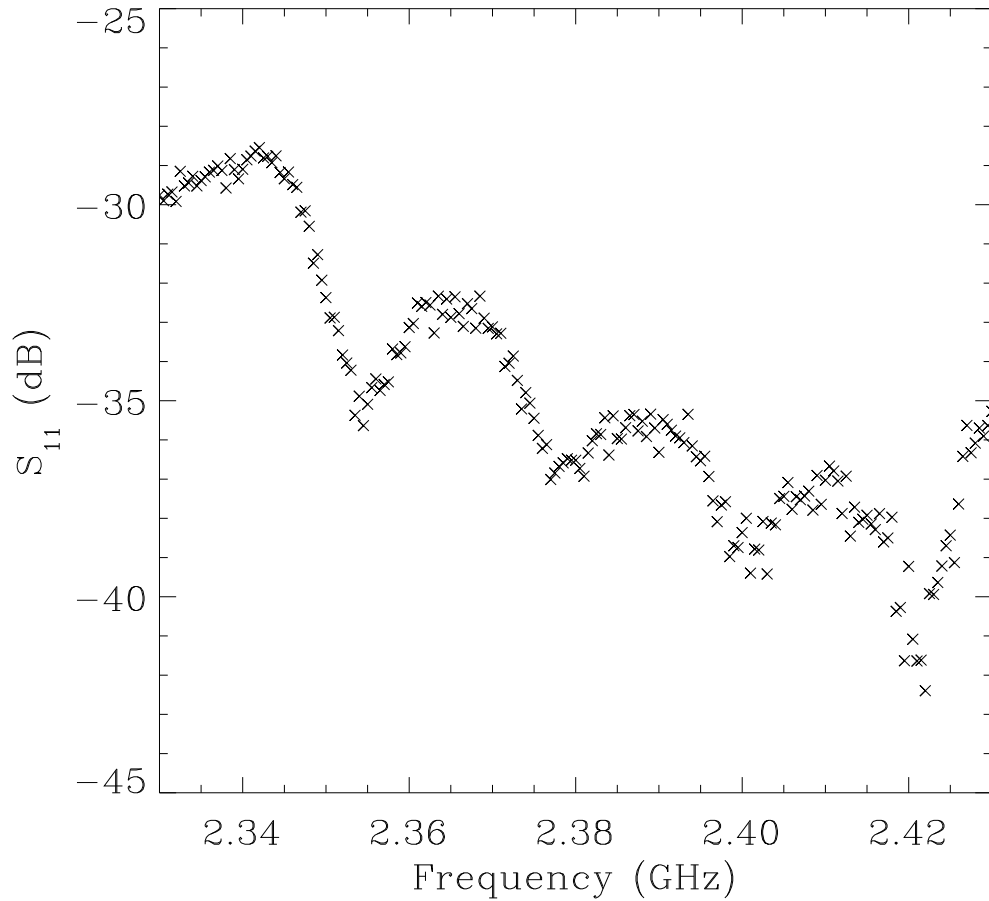


Figure A.6 S-Band feed horn data with waveguide calibration applied. This calibrates out the response of the waveguide to coaxial line adapter, thereby giving the response from the device under test.

The network analyzer we used for this purpose had the capability to carry out waveguide calibration internally. This offered a chance to test our waveguide calibration procedure by comparing our results above with the data calibrated inside the analyzer itself. Hence, we loaded the data on the calibration shorts into the network analyzer, repeated the measurements above, and applied the calibration internally. The resulting S_{11} is shown in Figure A.7. The close correspondence between the two figures as seen in Figures A.8 verifies our calibration procedure.

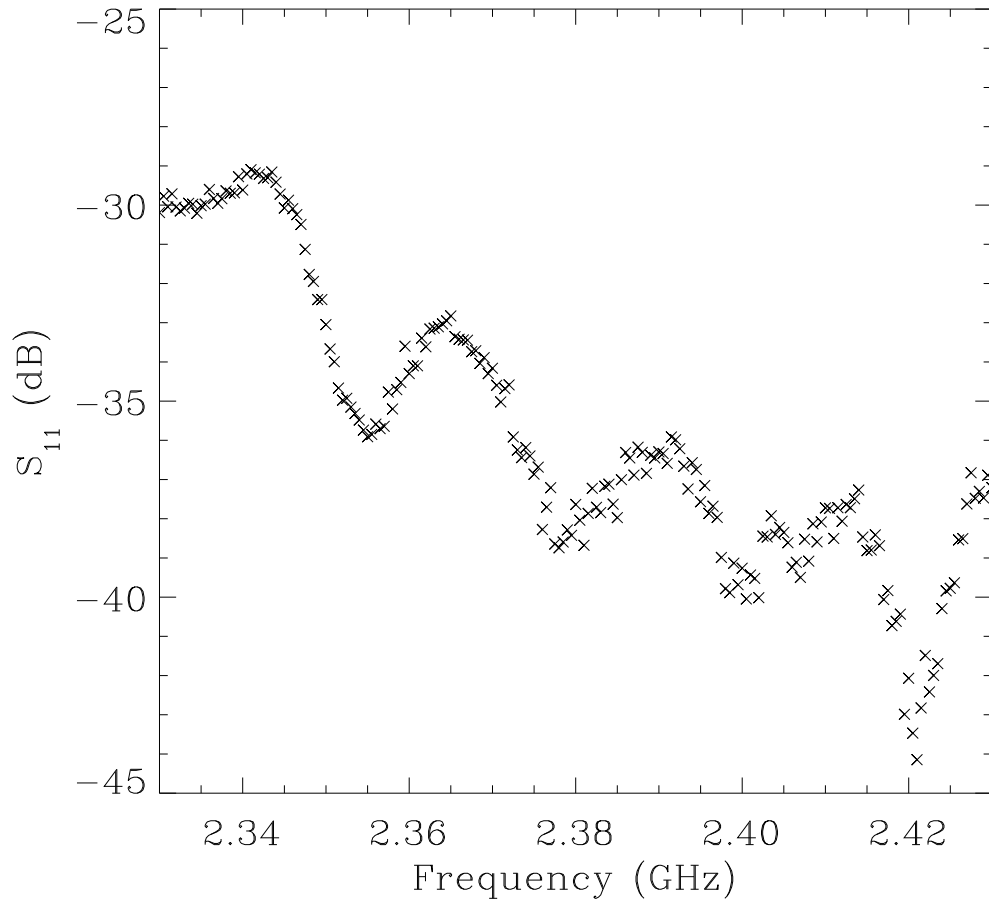


Figure A.7 S-Band feed horn data calibrated internally in the vector network analyzer. This serves as a check on the calibration procedure that is performed external to the network analyzer (Figure A.6), as the two results must be similar.

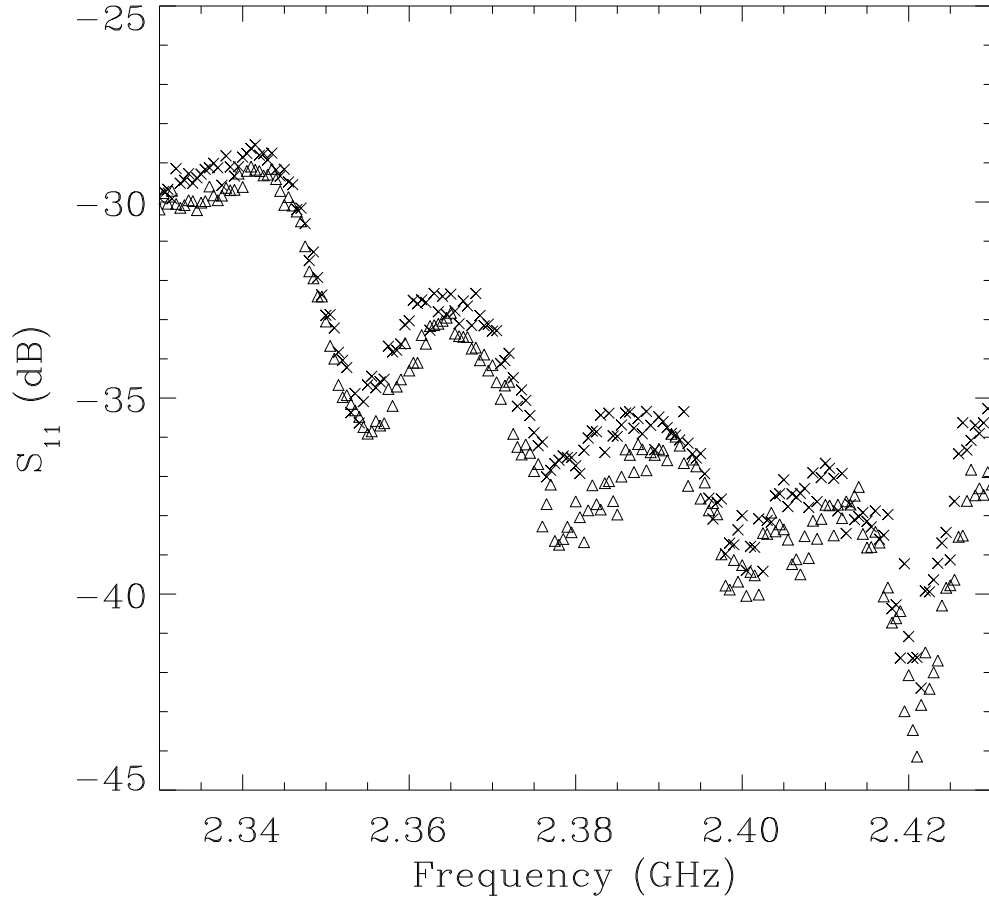


Figure A.8 The S-Band feed horn data calibrated externally is shown in crosses (\times). Overlaid in triangles (Δ) is the data obtained by performing the calibration internally in the network analyzer. The agreement of the two results verifies our calibration procedure.

The network analyzer used to measure the response of test equipment for the C-Band High receiver (§5) did not have the capability to do internal waveguide calibration. We thus applied the procedures outlined in §A.3 and §A.4.1 to measure the true response of various waveguide components, and verify that they satisfied design specifications.

Appendix B

Gaussian Component Analysis

In this chapter, we show the results of the Gaussian component analysis for each of the 49 sources for which we carried out the work. The selection criteria for the sources are given in §7.5.

During our follow up observations, we obtained spectra at both high and low velocity resolutions (0.04 and 0.14 km s⁻¹ respectively after Hanning smoothing) simultaneously. The low velocity resolution spectra have higher signal to noise, and occasionally reveal features that are only slightly above the noise threshold in the high resolution spectra. In these cases, information from the low resolution spectra is used to fit features close to the noise threshold in the high resolution data. In the absence of this information, it will not be possible to distinguish very weak emission features from occasional baseline ripples. Several such features are visible in the figures in this chapter, and no formal mention of the fitting procedure will be made in the figure captions.

There are some sources which have two groups of emission features that are well separated in velocity. In these cases, the two emission features are fitted separately to minimize the number of signal free channels during the fitting procedure. The reduced χ^2 for individual fits range from 1.1 to 2.0 depending on the baseline characteristics and the source complexity.

Table B.1 Gaussian Components of source 34.82+0.35. The columns show the amplitude, S in Jy, center, v_c in km s⁻¹ and the FWHM Δv_{FWHM} in km s⁻¹ for each component.

No.	S (Jy)	v_c (km s ⁻¹)	Δv_{FWHM} (km s ⁻¹)
1	0.08	58.62	0.16
2	0.23	59.67	0.28
3	0.05	59.95	0.28

Table B.2 Gaussian Components of source 35.25–0.24. The columns show the amplitude, S in Jy, center, v_c in km s⁻¹ and the FWHM Δv_{FWHM} in km s⁻¹ for each component.

No.	S (Jy)	v_c (km s ⁻¹)	Δv_{FWHM} (km s ⁻¹)
1	0.14	56.21	0.30
2	0.07	71.38	0.18
3	0.16	71.71	0.30
4	0.31	72.25	0.36
5	1.24	72.39	0.21
6	0.25	72.59	0.12
7	0.35	72.71	0.24
8	0.22	73.08	0.33

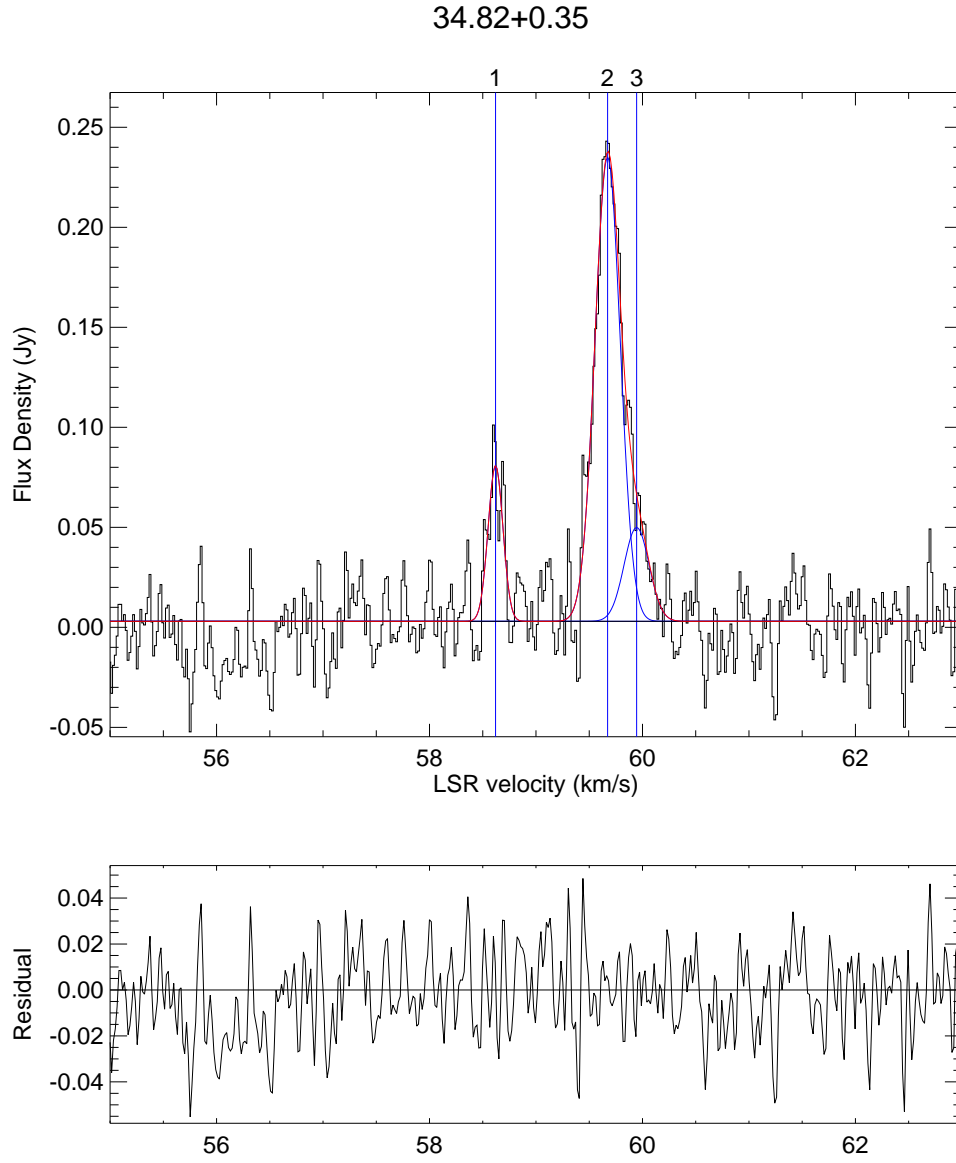


Figure B.1 Gaussian component fit to source 34.82+0.35. The top panel shows the spectrum, and overlays of each Gaussian and its position in blue, and the fit in red. The bottom panel shows the residual. The Gaussians are numbered in the same order as in the corresponding Table.

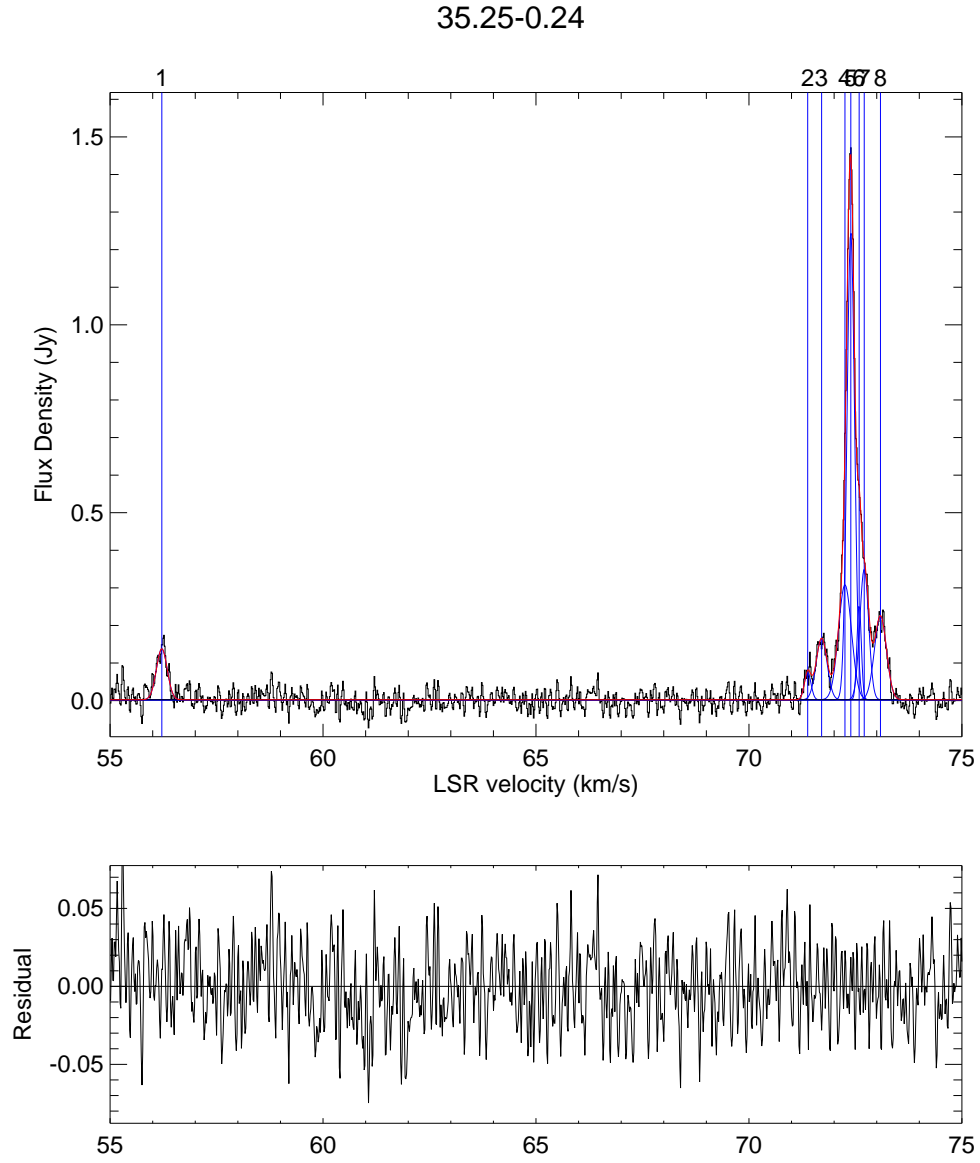


Figure B.2 Gaussian component fit to source 35.25–0.24. The top panel shows the spectrum, and overlays of each Gaussian and its position in blue, and the fit in red. The bottom panel shows the residual. The Gaussians are numbered in the same order as in the corresponding Table.

Table B.3 Gaussian Components of source 35.39+0.02. The columns show the amplitude, S in Jy, center, v_c in km s⁻¹ and the FWHM Δv_{FWHM} in km s⁻¹ for each component.

No.	S (Jy)	v_c (km s ⁻¹)	Δv_{FWHM} (km s ⁻¹)
1	0.03	91.27	0.25
2	0.17	94.20	0.25
3	0.17	96.92	0.38

Table B.4 Gaussian Components of source 35.40+0.03. The columns show the amplitude, S in Jy, center, v_c in km s⁻¹ and the FWHM Δv_{FWHM} in km s⁻¹ for each component.

No.	S (Jy)	v_c (km s ⁻¹)	Δv_{FWHM} (km s ⁻¹)
1	0.53	89.03	0.26
2	0.08	89.39	0.54
3	0.17	89.96	0.46
4	0.13	90.49	0.25

Table B.5 Gaussian Components of source 36.02-0.20. The columns show the amplitude, S in Jy, center, v_c in km s⁻¹ and the FWHM Δv_{FWHM} in km s⁻¹ for each component.

No.	S (Jy)	v_c (km s ⁻¹)	Δv_{FWHM} (km s ⁻¹)
1	0.05	92.55	0.23
2	0.13	92.96	0.31
3	0.09	93.22	0.26

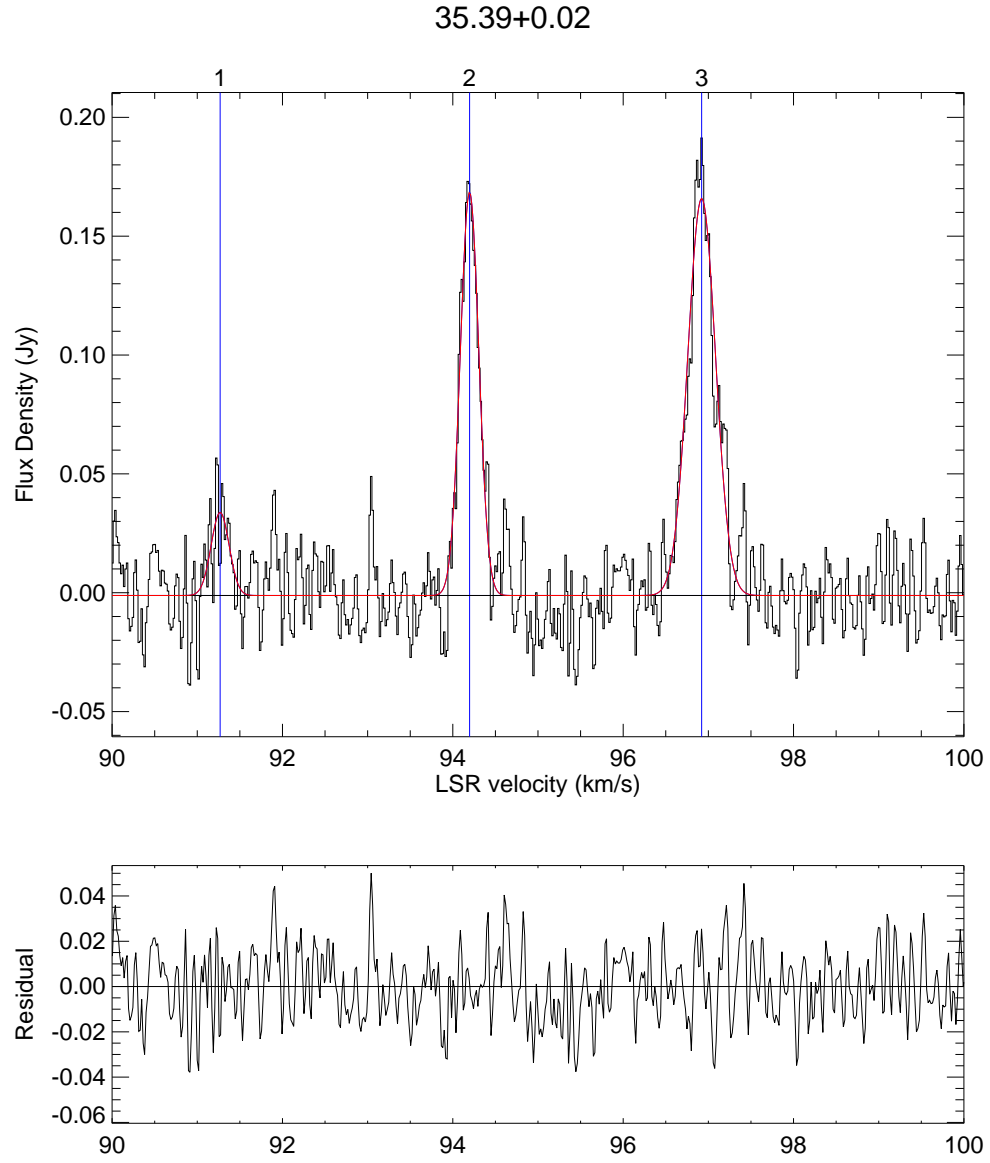


Figure B.3 Gaussian component fit to source $35.39+0.02$. The top panel shows the spectrum, and overlays of each Gaussian and its position in blue, and the fit in red. The bottom panel shows the residual. The Gaussians are numbered in the same order as in the corresponding Table.

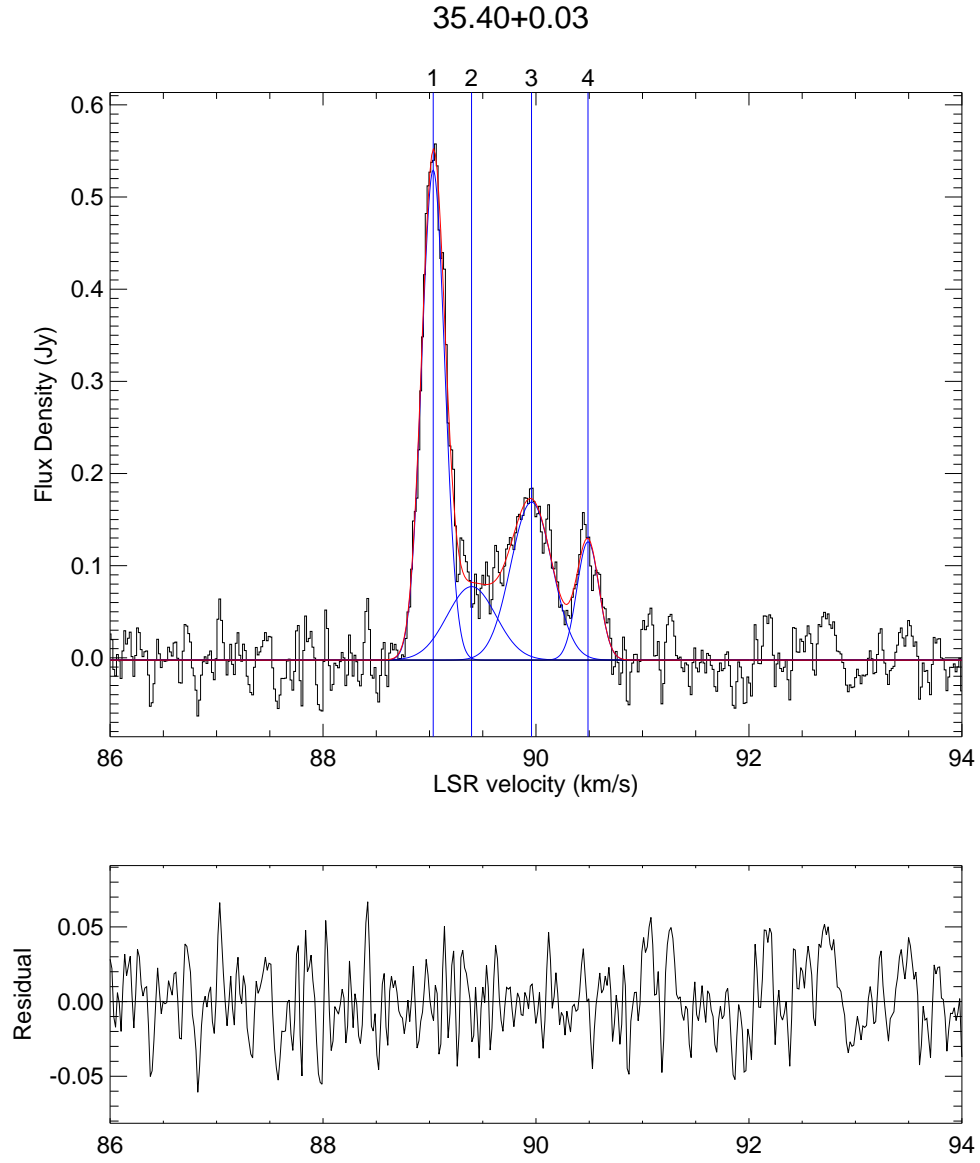


Figure B.4 Gaussian component fit to source 35.40+0.03. The top panel shows the spectrum, and overlays of each Gaussian and its position in blue, and the fit in red. The bottom panel shows the residual. The Gaussians are numbered in the same order as in the corresponding Table.

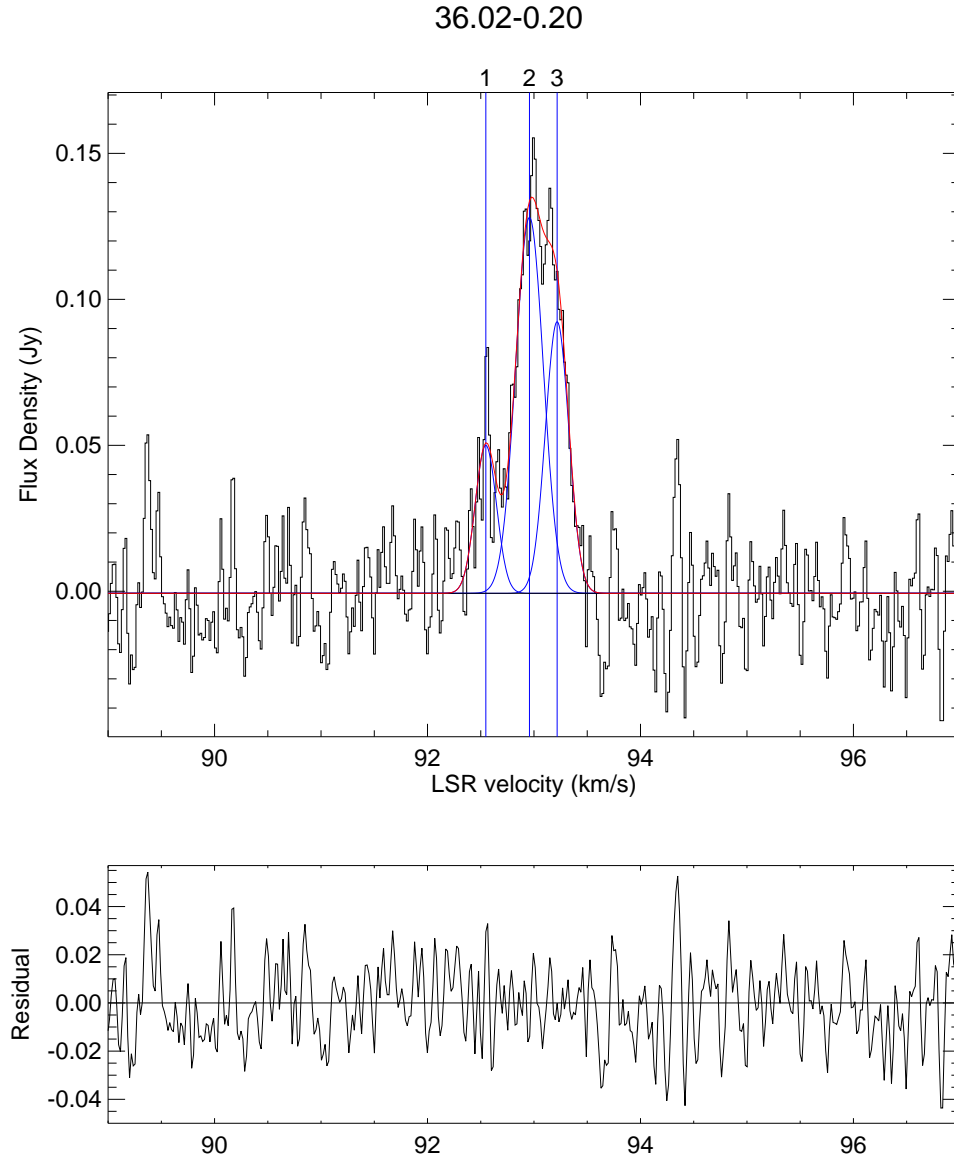


Figure B.5 Gaussian component fit to source 36.02–0.20. The top panel shows the spectrum, and overlays of each Gaussian and its position in blue, and the fit in red. The bottom panel shows the residual. The Gaussians are numbered in the same order as in the corresponding Table.

Table B.6 Gaussian Components of source 36.64–0.21. The columns show the amplitude, S in Jy, center, v_c in km s^{−1} and the FWHM Δv_{FWHM} in km s^{−1} for each component.

No.	S (Jy)	v_c (km s ^{−1})	Δv_{FWHM} (km s ^{−1})
1	0.06	73.63	0.26
2	1.63	77.33	0.23
3	0.23	78.86	0.44

Table B.7 Gaussian Components of source 36.90–0.41. The columns show the amplitude, S in Jy, center, v_c in km s^{−1} and the FWHM Δv_{FWHM} in km s^{−1} for each component.

No.	S (Jy)	v_c (km s ^{−1})	Δv_{FWHM} (km s ^{−1})
1	0.06	81.65	0.14
2	0.06	83.38	0.79
3	0.11	84.45	0.82
4	0.37	84.71	0.35

Table B.8 Gaussian Components of source 36.92+0.48. The columns show the amplitude, S in Jy, center, v_c in km s^{−1} and the FWHM Δv_{FWHM} in km s^{−1} for each component.

No.	S (Jy)	v_c (km s ^{−1})	Δv_{FWHM} (km s ^{−1})
1	0.56	−36.10	0.19
2	1.47	−35.91	0.25

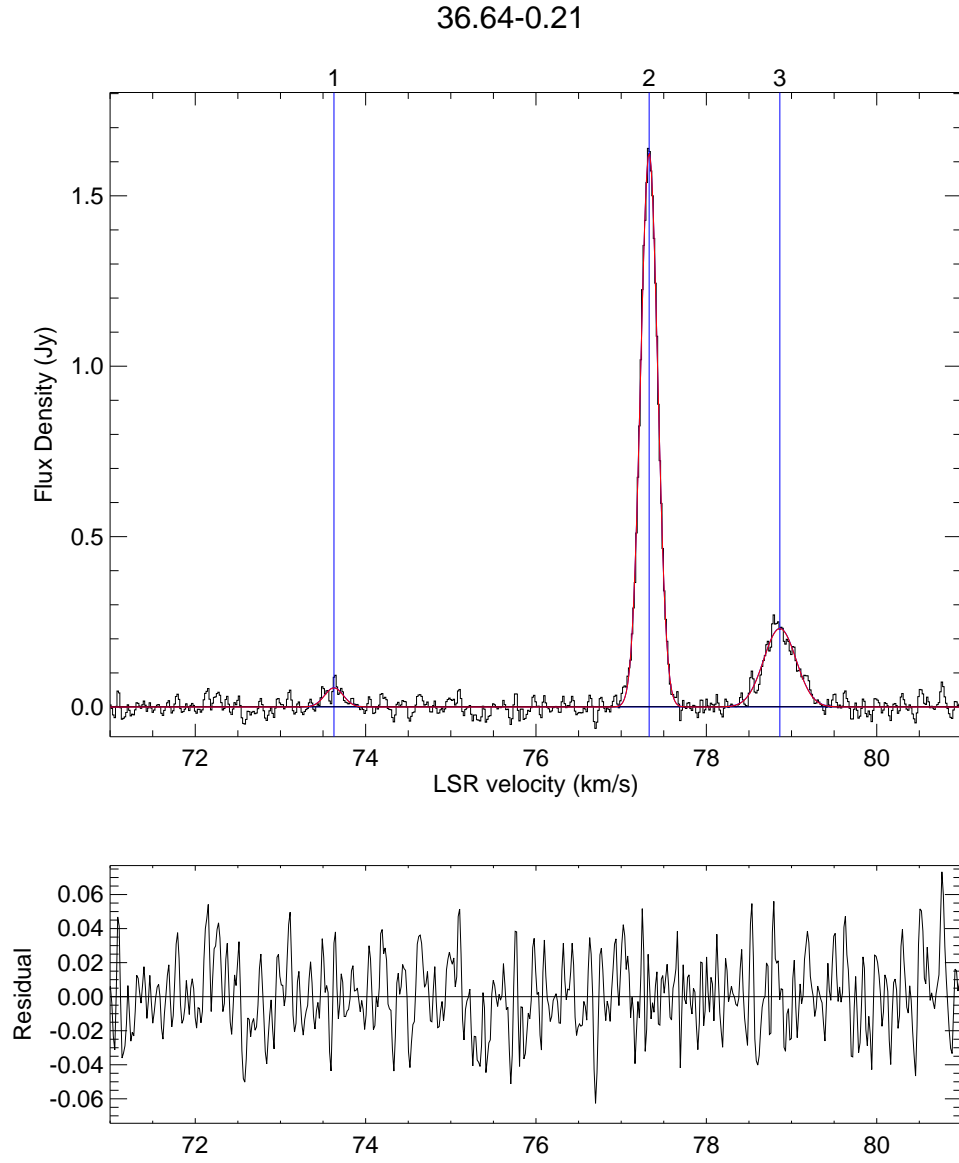


Figure B.6 Gaussian component fit to source 36.64–0.21. The top panel shows the spectrum, and overlays of each Gaussian and its position in blue, and the fit in red. The bottom panel shows the residual. The Gaussians are numbered in the same order as in the corresponding Table.

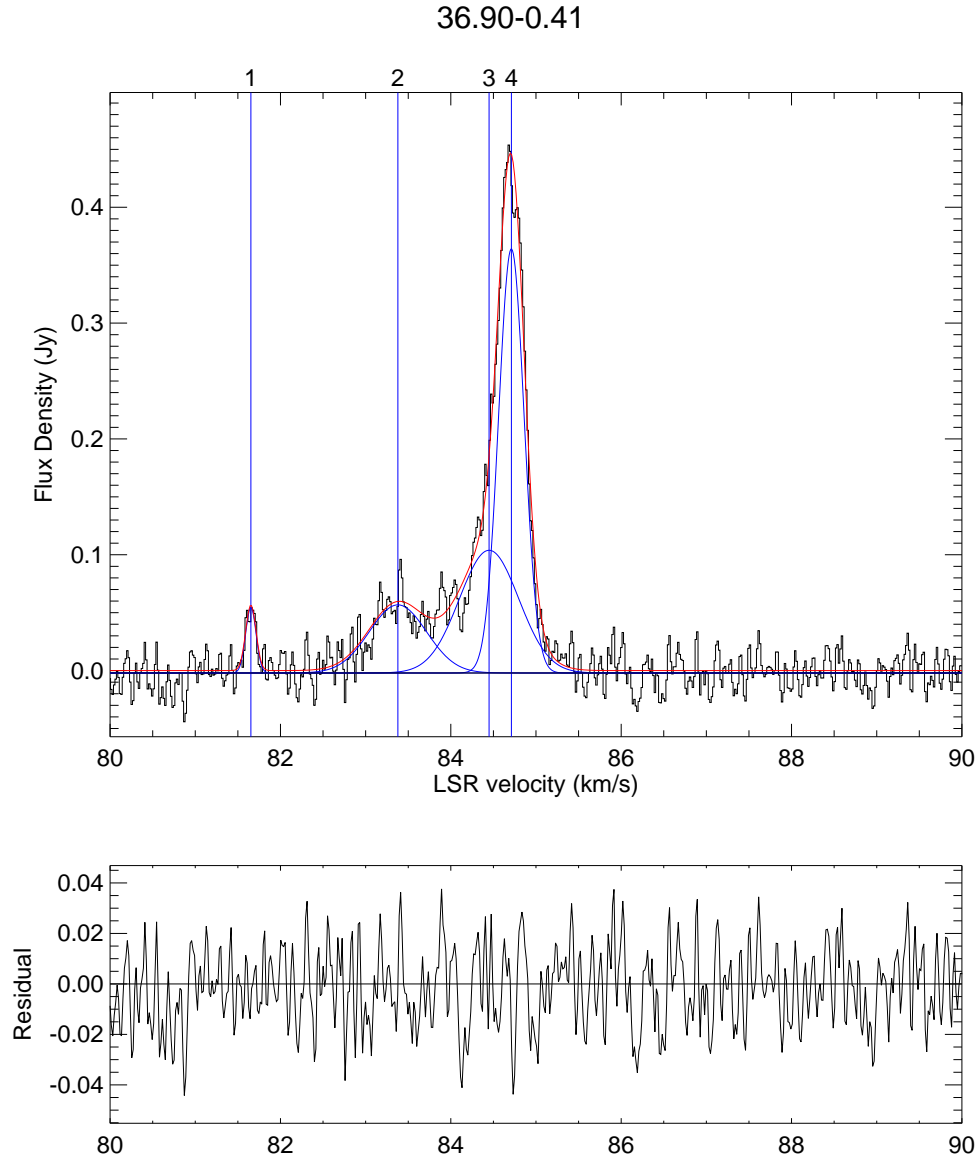


Figure B.7 Gaussian component fit to source 36.90–0.41. The top panel shows the spectrum, and overlays of each Gaussian and its position in blue, and the fit in red. The bottom panel shows the residual. The Gaussians are numbered in the same order as in the corresponding Table.

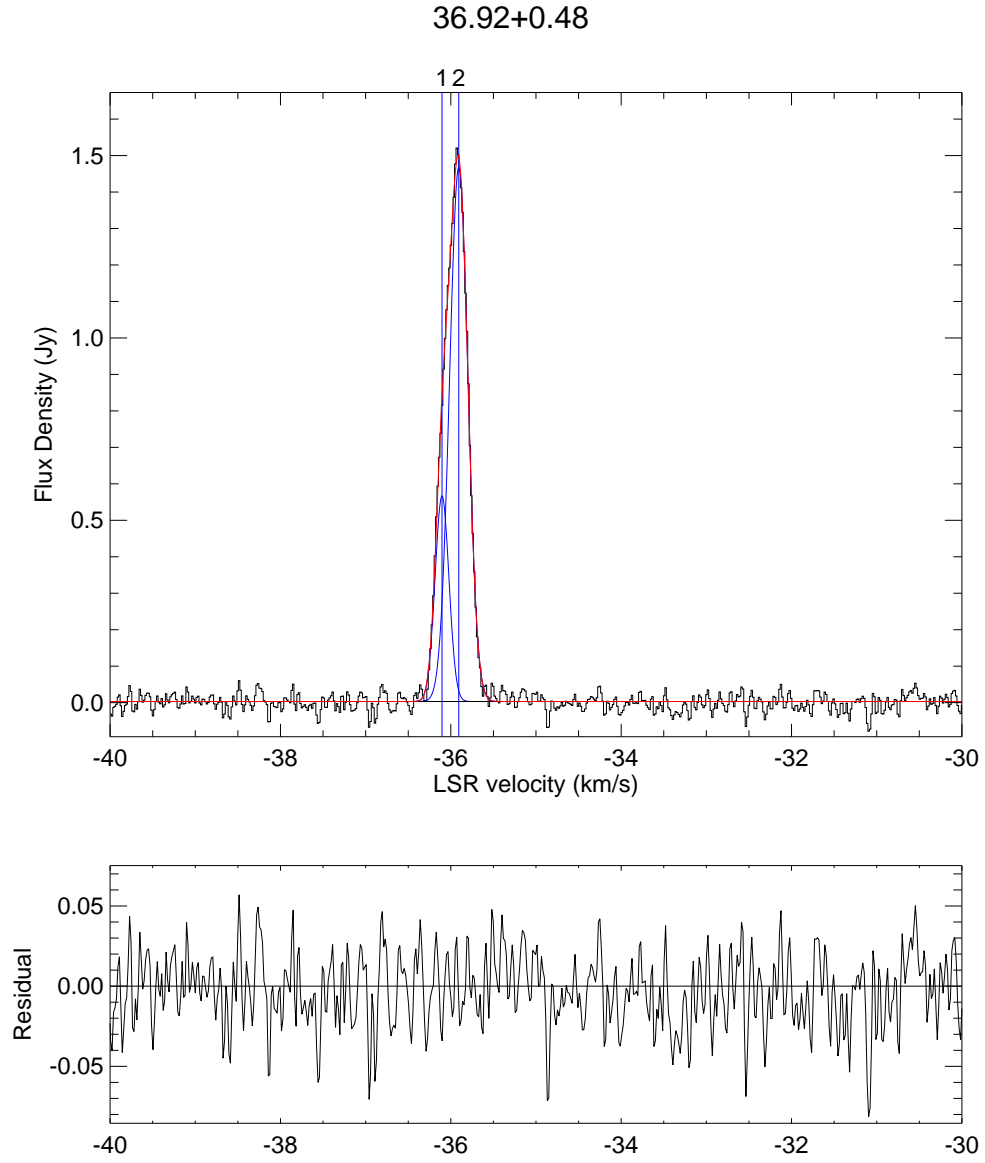


Figure B.8 Gaussian component fit to source $36.92+0.48$. The top panel shows the spectrum, and overlays of each Gaussian and its position in blue, and the fit in red. The bottom panel shows the residual. The Gaussians are numbered in the same order as in the corresponding Table.

Table B.9 Gaussian Components of source 37.02–0.03. The columns show the amplitude, S in Jy, center, v_c in km s⁻¹ and the FWHM Δv_{FWHM} in km s⁻¹ for each component.

No.	S (Jy)	v_c (km s ⁻¹)	Δv_{FWHM} (km s ⁻¹)
1	0.75	78.38	0.85
2	6.37	78.43	0.35
3	2.71	78.88	0.42
4	0.44	79.32	0.34
5	0.32	79.93	0.82
6	0.07	80.76	0.24
7	0.08	84.77	0.23
8	0.10	85.19	0.25

Table B.10 Gaussian Components of source 37.38–0.09. The columns show the amplitude, S in Jy, center, v_c in km s⁻¹ and the FWHM Δv_{FWHM} in km s⁻¹ for each component.

No.	S (Jy)	v_c (km s ⁻¹)	Δv_{FWHM} (km s ⁻¹)
1	0.04	68.16	1.33
2	0.10	70.12	0.97
3	0.13	70.57	0.34

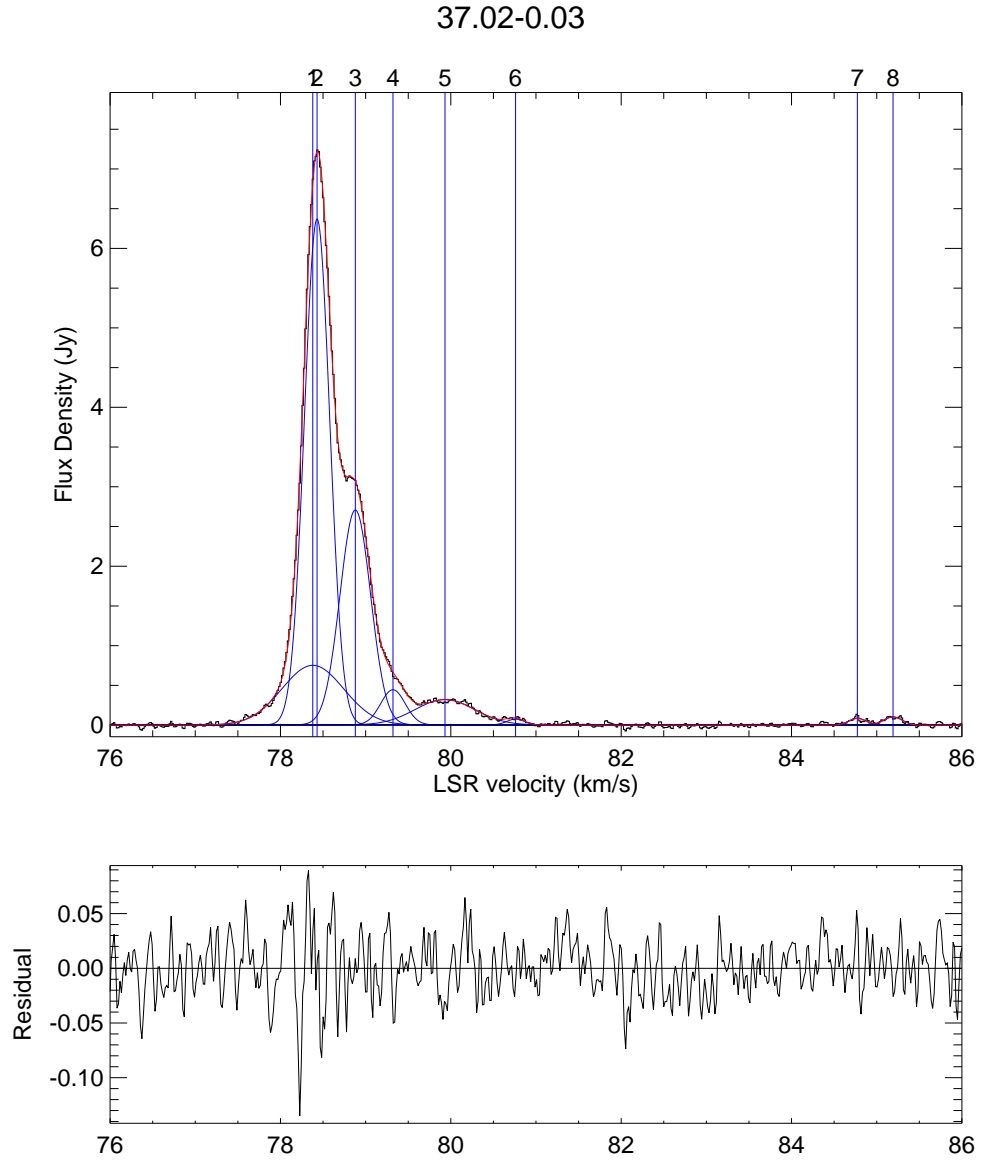


Figure B.9 Gaussian component fit to source 37.02–0.03. The top panel shows the spectrum, and overlays of each Gaussian and its position in blue, and the fit in red. The bottom panel shows the residual. The Gaussians are numbered in the same order as in the corresponding Table.

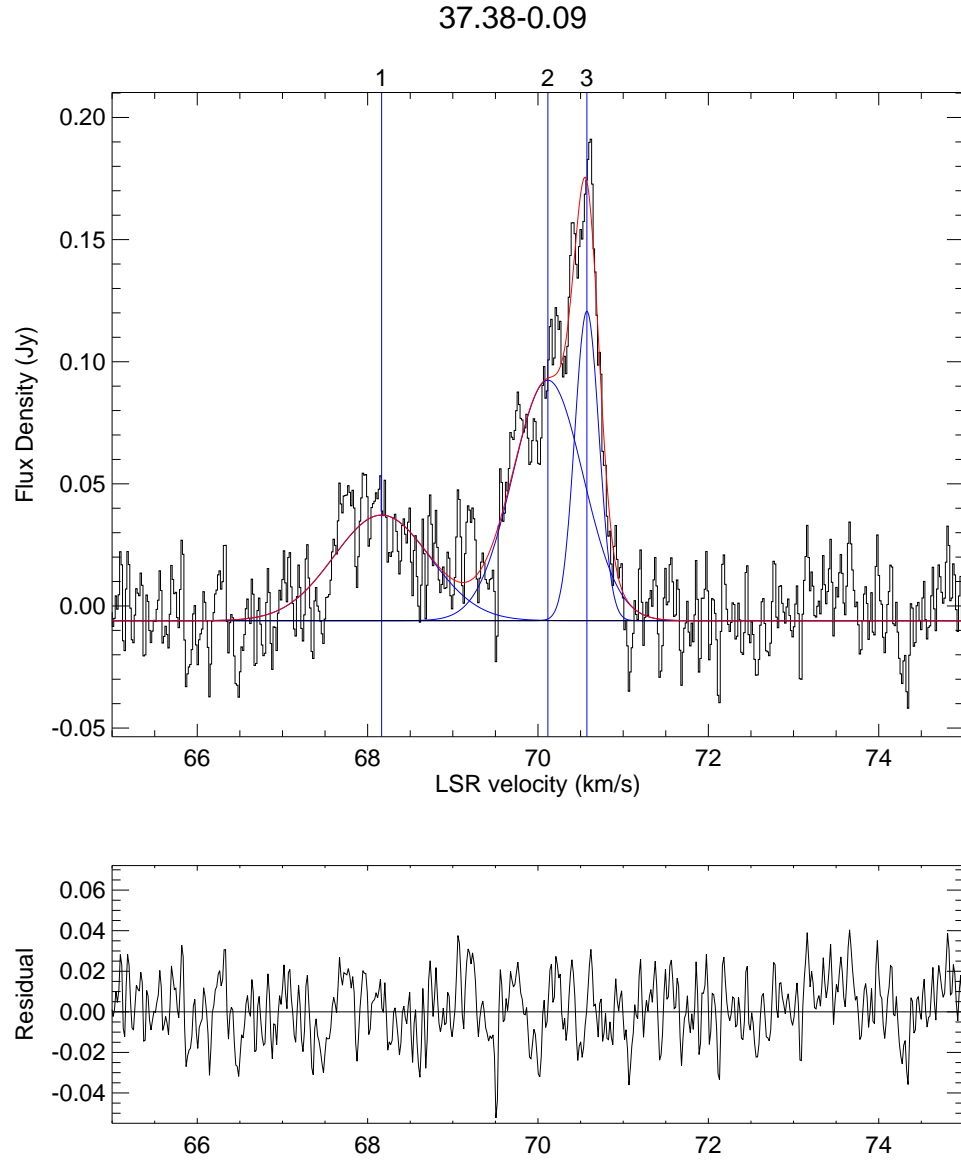


Figure B.10 Gaussian component fit to source 37.38-0.09. The top panel shows the spectrum, and overlays of each Gaussian and its position in blue, and the fit in red. The bottom panel shows the residual. The Gaussians are numbered in the same order as in the corresponding Table.

Table B.11 Gaussian Components of source 37.74–0.12. The columns show the amplitude, S in Jy, center, v_c in km s⁻¹ and the FWHM Δv_{FWHM} in km s⁻¹ for each component.

No.	S (Jy)	v_c (km s ⁻¹)	Δv_{FWHM} (km s ⁻¹)
1	0.21	50.15	0.26
2	0.84	50.29	0.22

Table B.12 Gaussian Components of source 37.76–0.19. The columns show the amplitude, S in Jy, center, v_c in km s⁻¹ and the FWHM Δv_{FWHM} in km s⁻¹ for each component.

No.	S (Jy)	v_c (km s ⁻¹)	Δv_{FWHM} (km s ⁻¹)
1	0.06	54.33	0.25
2	0.57	55.03	0.54
3	0.13	56.36	0.57
4	0.19	57.12	0.64
5	0.06	58.50	0.57
6	0.54	60.55	0.38
7	0.12	61.87	0.37
8	0.15	62.24	1.35
9	0.41	63.50	0.29
10	0.39	64.67	0.43
11	0.34	65.34	0.28
12	0.13	65.71	0.40

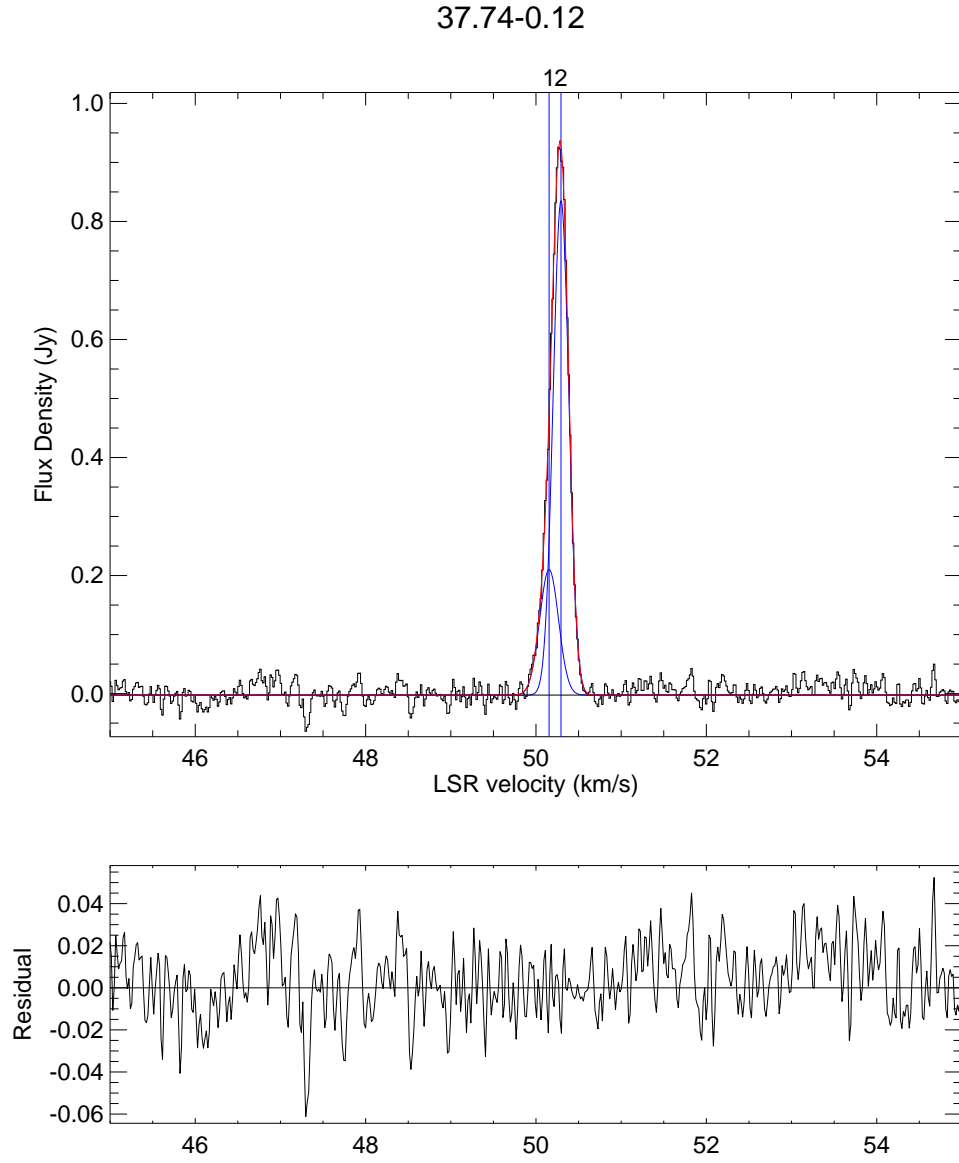


Figure B.11 Gaussian component fit to source 37.74-0.12. The top panel shows the spectrum, and overlays of each Gaussian and its position in blue, and the fit in red. The bottom panel shows the residual. The Gaussians are numbered in the same order as in the corresponding Table.

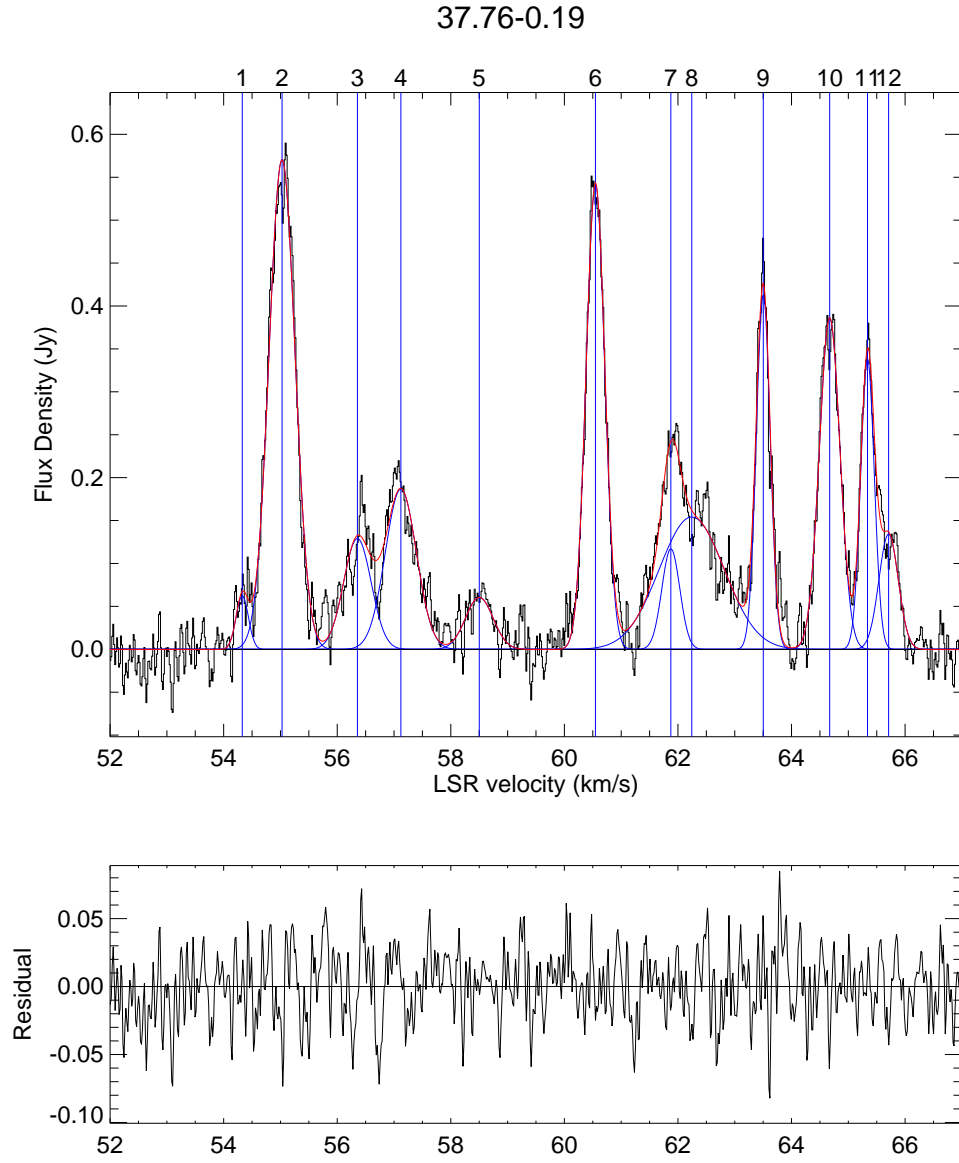


Figure B.12 Gaussian component fit to source 37.76–0.19. The top panel shows the spectrum, and overlays of each Gaussian and its position in blue, and the fit in red. The bottom panel shows the residual. The Gaussians are numbered in the same order as in the corresponding Table.

Table B.13 Gaussian Components of source 37.77–0.22. The columns show the amplitude, S in Jy, center, v_c in km s⁻¹ and the FWHM Δv_{FWHM} in km s⁻¹ for each component.

No.	S (Jy)	v_c (km s ⁻¹)	Δv_{FWHM} (km s ⁻¹)
1	0.11	69.11	0.35
2	0.71	69.57	0.31
3	0.17	69.80	0.50

Table B.14 Gaussian Components of source 38.08–0.27. The columns show the amplitude, S in Jy, center, v_c in km s⁻¹ and the FWHM Δv_{FWHM} in km s⁻¹ for each component.

No.	S (Jy)	v_c (km s ⁻¹)	Δv_{FWHM} (km s ⁻¹)
1	0.04	62.33	0.53
2	0.09	67.03	0.47
3	0.57	67.50	0.23

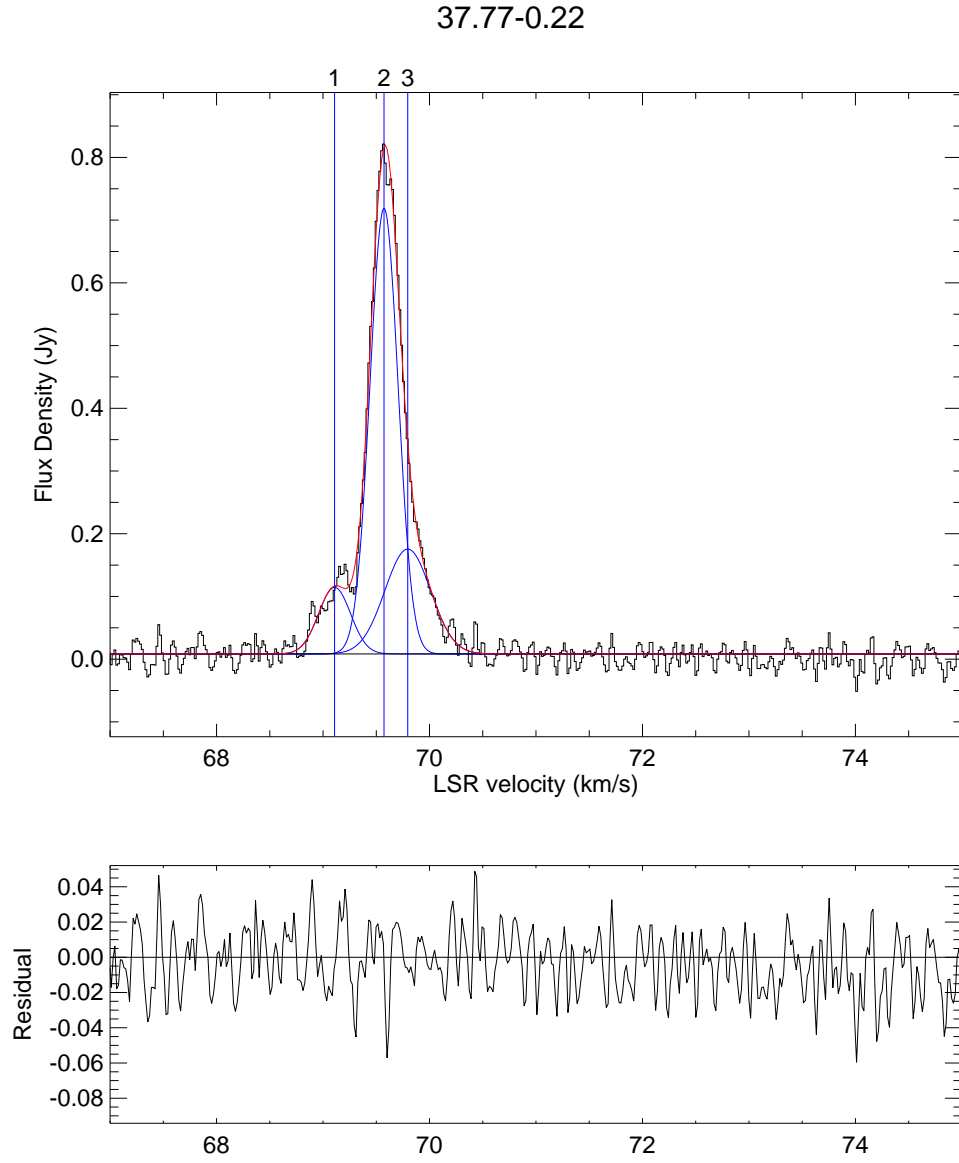


Figure B.13 Gaussian component fit to source 37.77–0.22. The top panel shows the spectrum, and overlays of each Gaussian and its position in blue, and the fit in red. The bottom panel shows the residual. The Gaussians are numbered in the same order as in the corresponding Table.

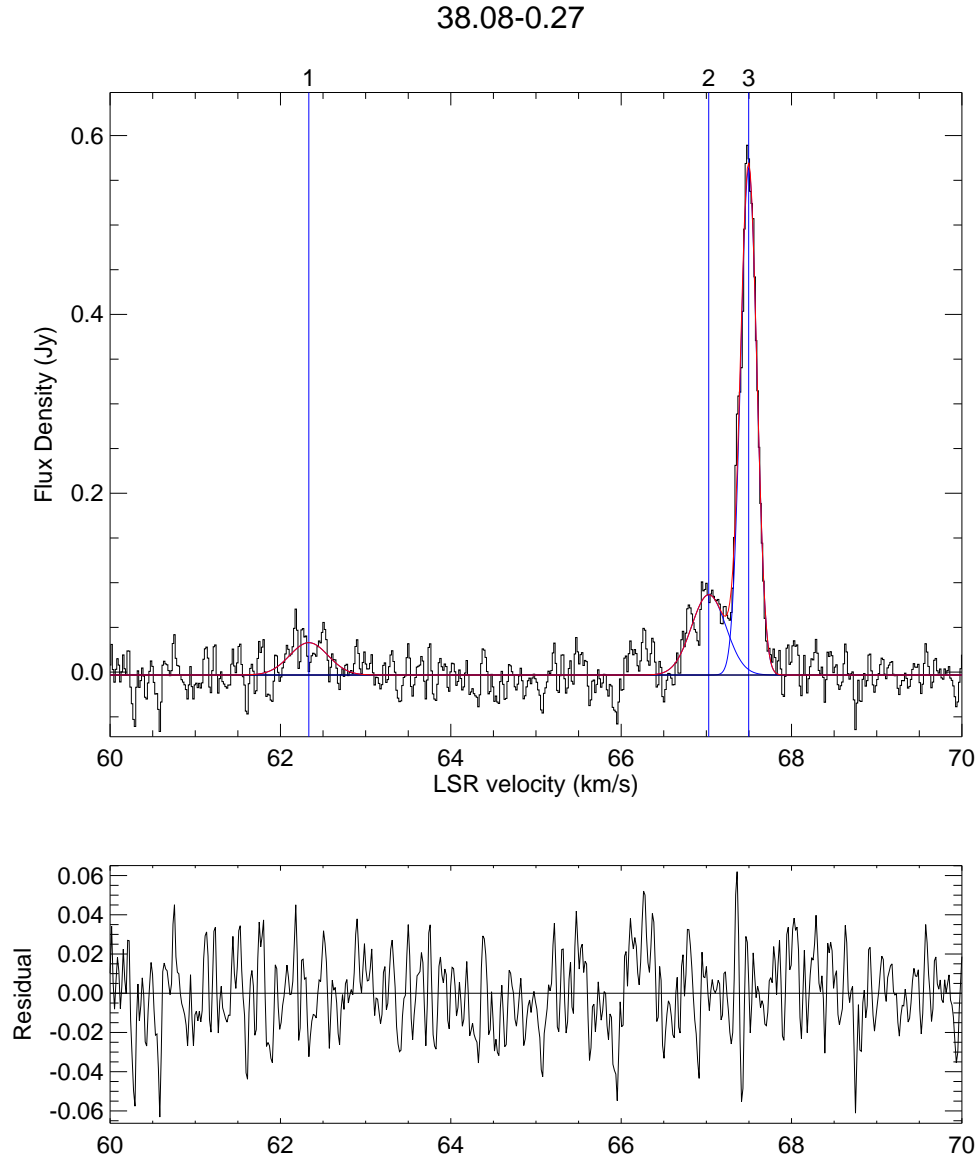


Figure B.14 Gaussian component fit to source 38.08-0.27. The top panel shows the spectrum, and overlays of each Gaussian and its position in blue, and the fit in red. The bottom panel shows the residual. The Gaussians are numbered in the same order as in the corresponding Table.

Table B.15 Gaussian Components of source 38.26–0.20. The columns show the amplitude, S in Jy, center, v_c in km s^{−1} and the FWHM Δv_{FWHM} in km s^{−1} for each component.

No.	S (Jy)	v_c (km s ^{−1})	Δv_{FWHM} (km s ^{−1})
1	0.07	64.31	0.18
2	0.13	64.72	0.78
3	0.19	65.33	0.40
4	0.11	67.75	0.45
5	0.36	68.81	0.41
6	0.58	69.39	0.47
7	0.71	70.20	0.29
8	0.07	70.80	0.41
9	0.15	72.27	0.48
10	0.14	72.88	0.27
11	0.57	73.16	0.39

Table B.16 Gaussian Components of source 38.56+0.15. The columns show the amplitude, S in Jy, center, v_c in km s^{−1} and the FWHM Δv_{FWHM} in km s^{−1} for each component.

No.	S (Jy)	v_c (km s ^{−1})	Δv_{FWHM} (km s ^{−1})
1	0.06	21.95	0.15
2	0.12	23.27	0.30
3	0.03	29.71	0.46
4	0.07	30.97	0.36
5	0.16	31.48	0.40

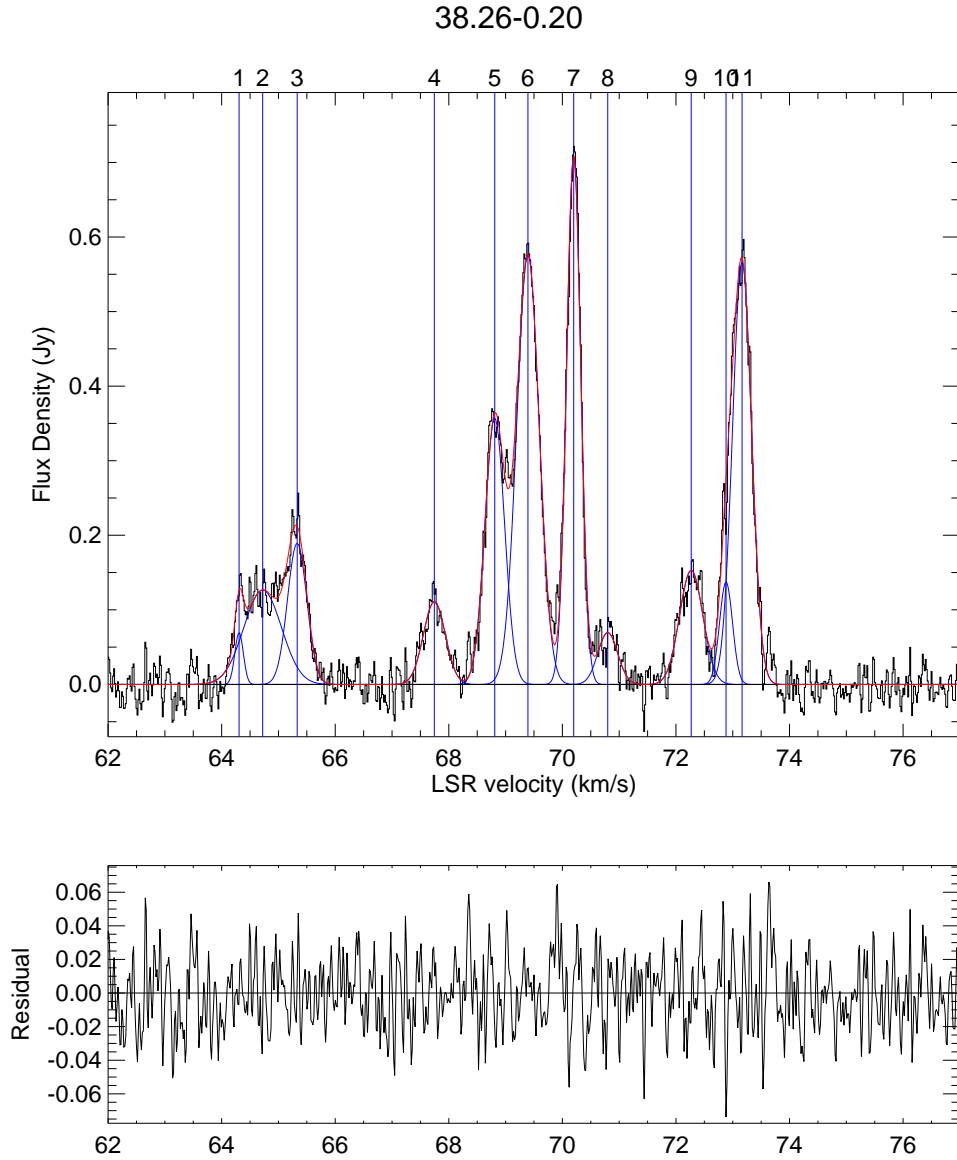


Figure B.15 Gaussian component fit to source 38.26–0.20. The top panel shows the spectrum, and overlays of each Gaussian and its position in blue, and the fit in red. The bottom panel shows the residual. The Gaussians are numbered in the same order as in the corresponding Table.

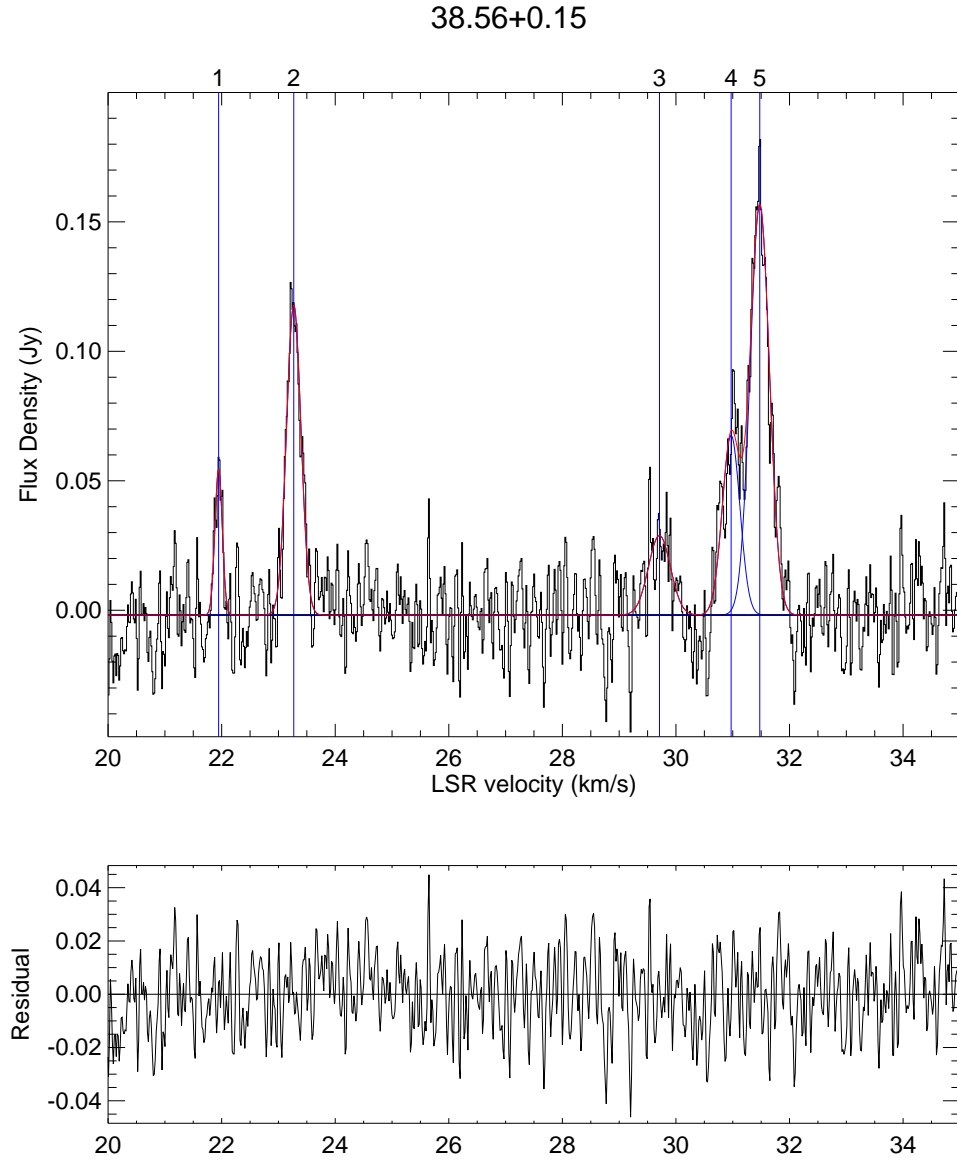


Figure B.16 Gaussian component fit to source 38.56+0.15. The top panel shows the spectrum, and overlays of each Gaussian and its position in blue, and the fit in red. The bottom panel shows the residual. The Gaussians are numbered in the same order as in the corresponding Table.

Table B.17 Gaussian Components of source 38.60–0.21. The columns show the amplitude, S in Jy, center, v_c in km s^{−1} and the FWHM Δv_{FWHM} in km s^{−1} for each component.

No.	S (Jy)	v_c (km s ^{−1})	Δv_{FWHM} (km s ^{−1})
1	0.17	61.69	0.34
2	0.13	61.88	0.13
3	0.40	62.49	0.20
4	0.29	62.62	0.25
5	0.33	63.08	0.39
6	0.05	63.77	0.44
7	0.06	68.23	0.66
8	0.09	68.83	0.31
9	0.34	69.04	0.28
10	0.04	69.11	1.00

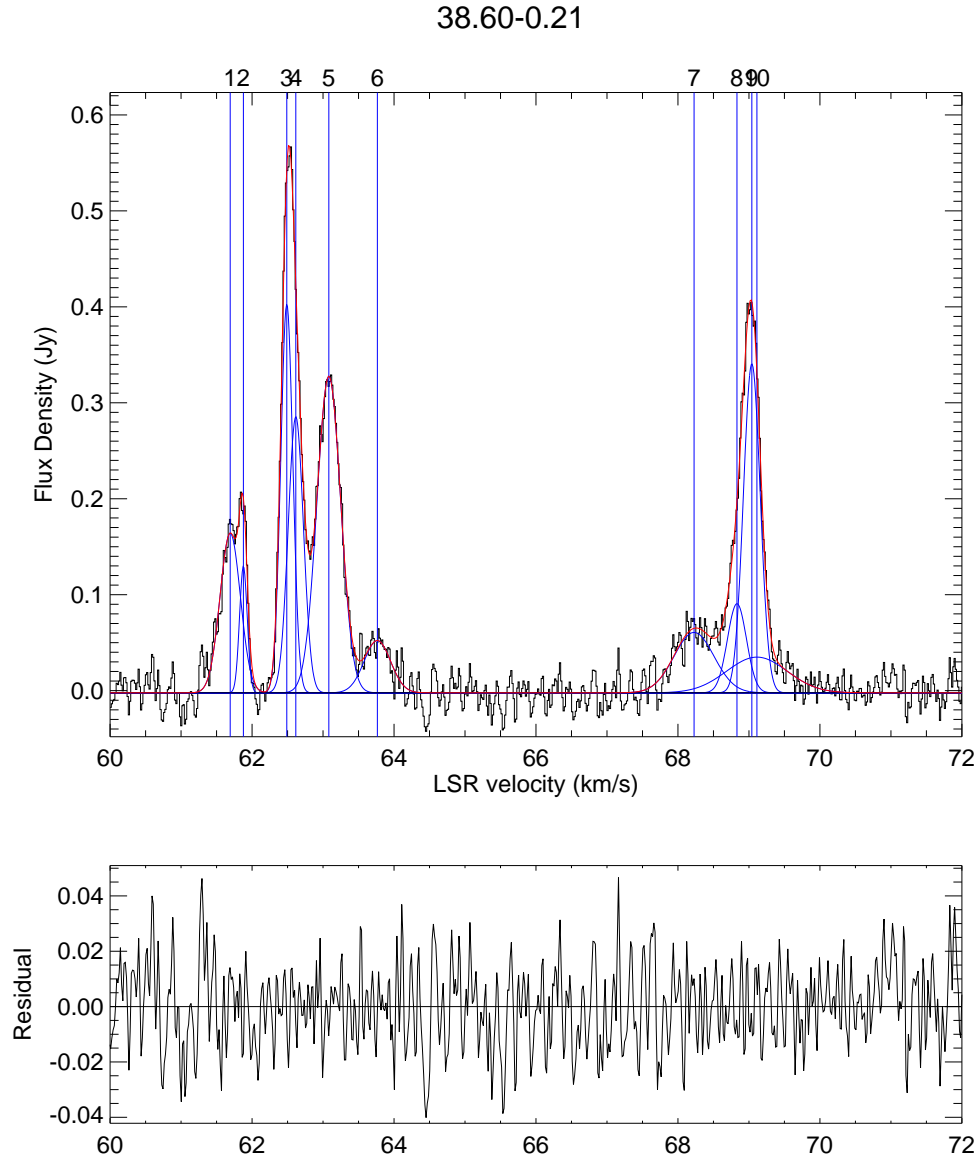


Figure B.17 Gaussian component fit to source 38.60–0.21. The top panel shows the spectrum, and overlays of each Gaussian and its position in blue, and the fit in red. The bottom panel shows the residual. The Gaussians are numbered in the same order as in the corresponding Table.

Table B.18 Gaussian Components of source 38.66+0.08. The columns show the amplitude, S in Jy, center, v_c in km s⁻¹ and the FWHM Δv_{FWHM} in km s⁻¹ for each component.

No.	S (Jy)	v_c (km s ⁻¹)	Δv_{FWHM} (km s ⁻¹)
1	1.53	-31.49	0.24
2	0.91	-31.37	0.31

Table B.19 Gaussian Components of source 38.92-0.36. The columns show the amplitude, S in Jy, center, v_c in km s⁻¹ and the FWHM Δv_{FWHM} in km s⁻¹ for each component.

No.	S (Jy)	v_c (km s ⁻¹)	Δv_{FWHM} (km s ⁻¹)
1	0.34	31.15	0.34
2	0.59	31.63	0.44
3	0.99	31.91	0.34
4	0.73	32.26	0.32
5	0.40	32.76	0.61
6	0.08	33.25	0.31

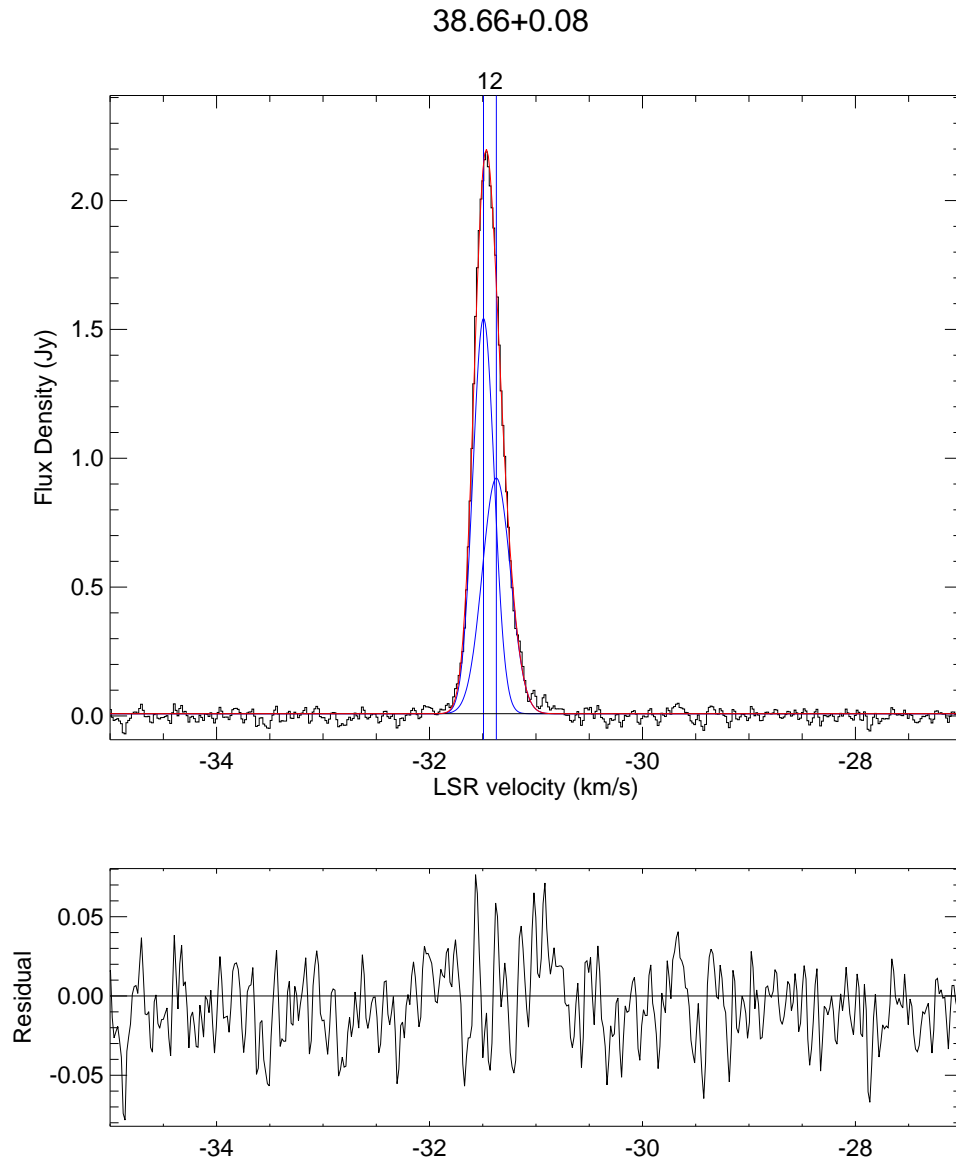


Figure B.18 Gaussian component fit to source 38.66+0.08. The top panel shows the spectrum, and overlays of each Gaussian and its position in blue, and the fit in red. The bottom panel shows the residual. The Gaussians are numbered in the same order as in the corresponding Table.

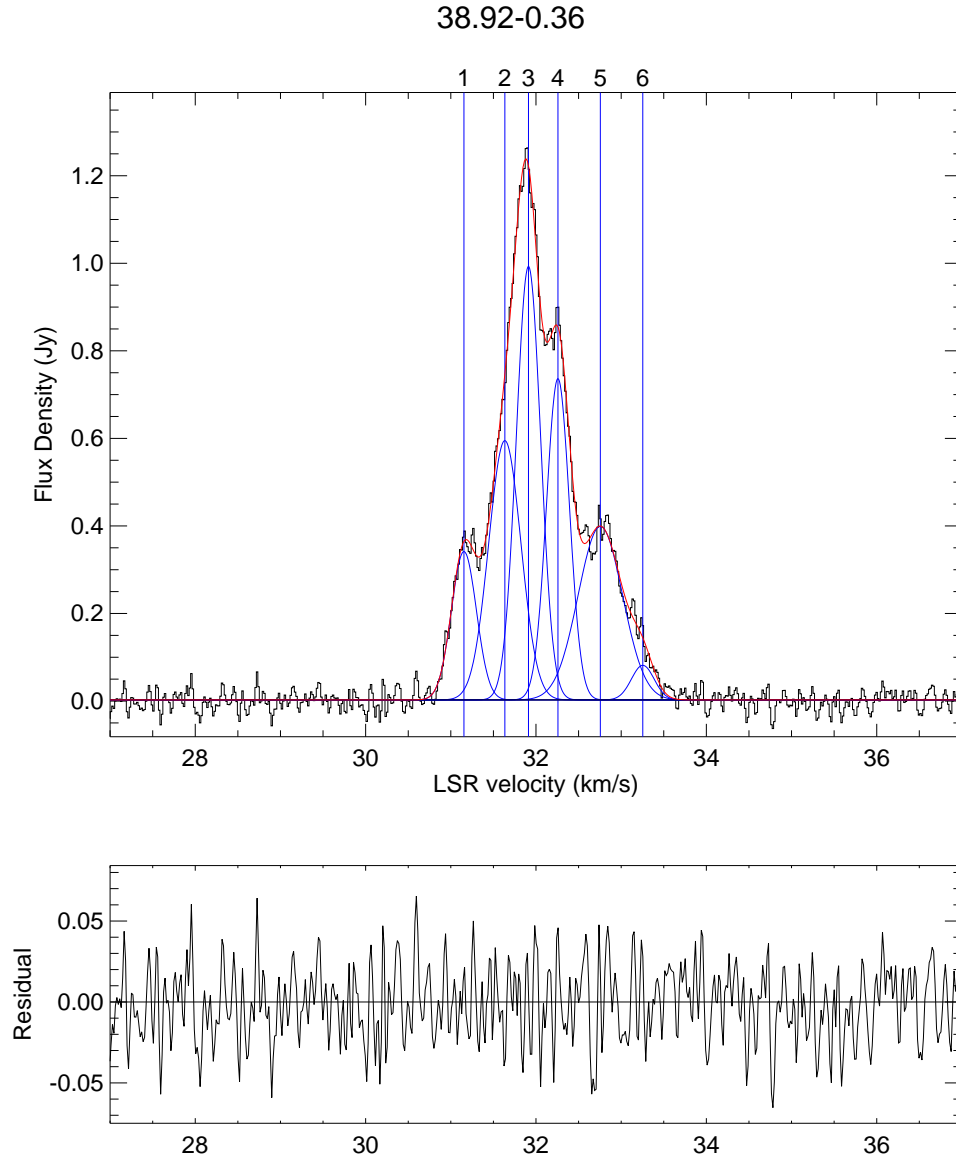


Figure B.19 Gaussian component fit to source 38.92–0.36. The top panel shows the spectrum, and overlays of each Gaussian and its position in blue, and the fit in red. The bottom panel shows the residual. The Gaussians are numbered in the same order as in the corresponding Table.

Table B.20 Gaussian Components of source 39.39–0.14. The columns show the amplitude, S in Jy, center, v_c in km s⁻¹ and the FWHM Δv_{FWHM} in km s⁻¹ for each component.

No.	S (Jy)	v_c (km s ⁻¹)	Δv_{FWHM} (km s ⁻¹)
1	0.20	58.49	0.35
2	0.14	58.89	0.28
3	0.06	59.37	0.44
4	0.22	60.11	0.62
5	1.02	60.40	0.25
6	0.05	64.65	0.28
7	0.16	68.57	0.48
8	0.16	69.41	0.58
9	0.03	70.34	0.86
10	0.19	71.81	0.25
11	0.07	75.36	0.29

Table B.21 Gaussian Components of source 39.54–0.38. The columns show the amplitude, S in Jy, center, v_c in km s⁻¹ and the FWHM Δv_{FWHM} in km s⁻¹ for each component.

No.	S (Jy)	v_c (km s ⁻¹)	Δv_{FWHM} (km s ⁻¹)
1	0.19	47.72	0.45
2	0.17	48.31	0.48
3	0.09	48.90	0.63

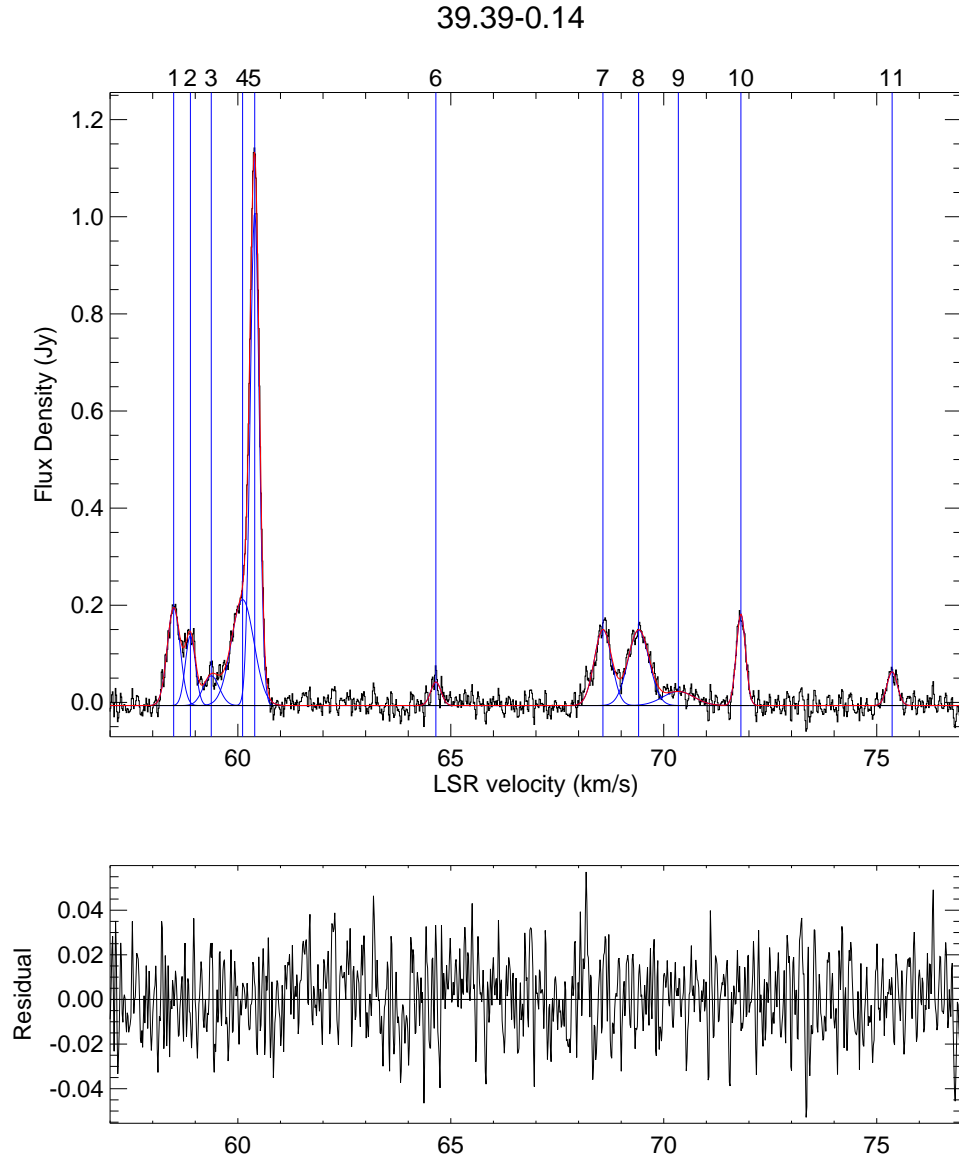


Figure B.20 Gaussian component fit to source 39.39–0.14. The top panel shows the spectrum, and overlays of each Gaussian and its position in blue, and the fit in red. The bottom panel shows the residual. The Gaussians are numbered in the same order as in the corresponding Table.

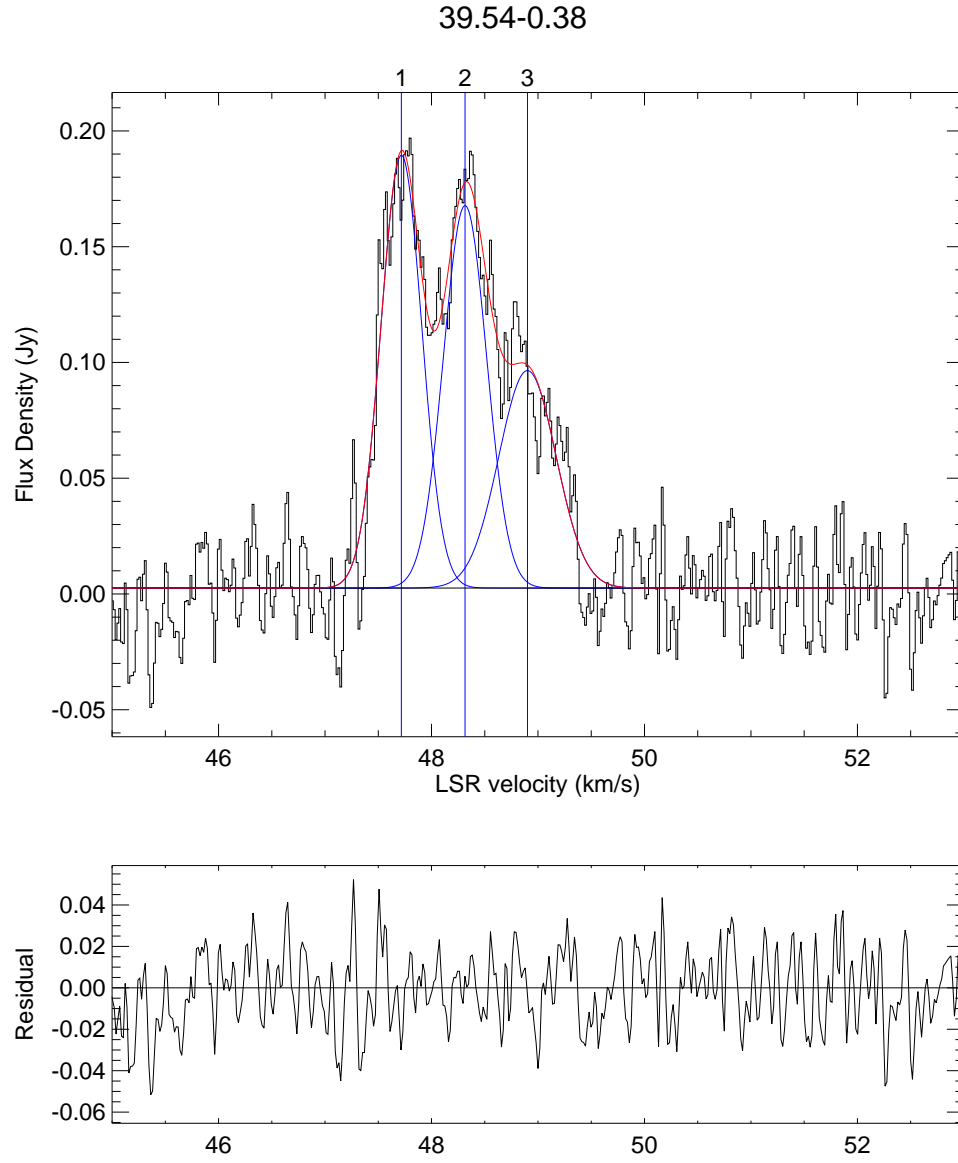


Figure B.21 Gaussian component fit to source 39.54-0.38. The top panel shows the spectrum, and overlays of each Gaussian and its position in blue, and the fit in red. The bottom panel shows the residual. The Gaussians are numbered in the same order as in the corresponding Table.

Table B.22 Gaussian Components of source 40.62–0.14. The columns show the amplitude, S in Jy, center, v_c in km s^{−1} and the FWHM Δv_{FWHM} in km s^{−1} for each component.

No.	S (Jy)	v_c (km s ^{−1})	Δv_{FWHM} (km s ^{−1})
1	1.01	30.02	0.28
2	0.70	30.23	0.31
3	0.43	30.80	0.38
4	4.47	30.95	0.25
5	12.89	31.11	0.22
6	4.51	31.26	0.17
7	0.81	31.52	0.72
8	0.07	35.72	0.22
9	1.15	36.08	0.24
10	0.76	36.22	0.39

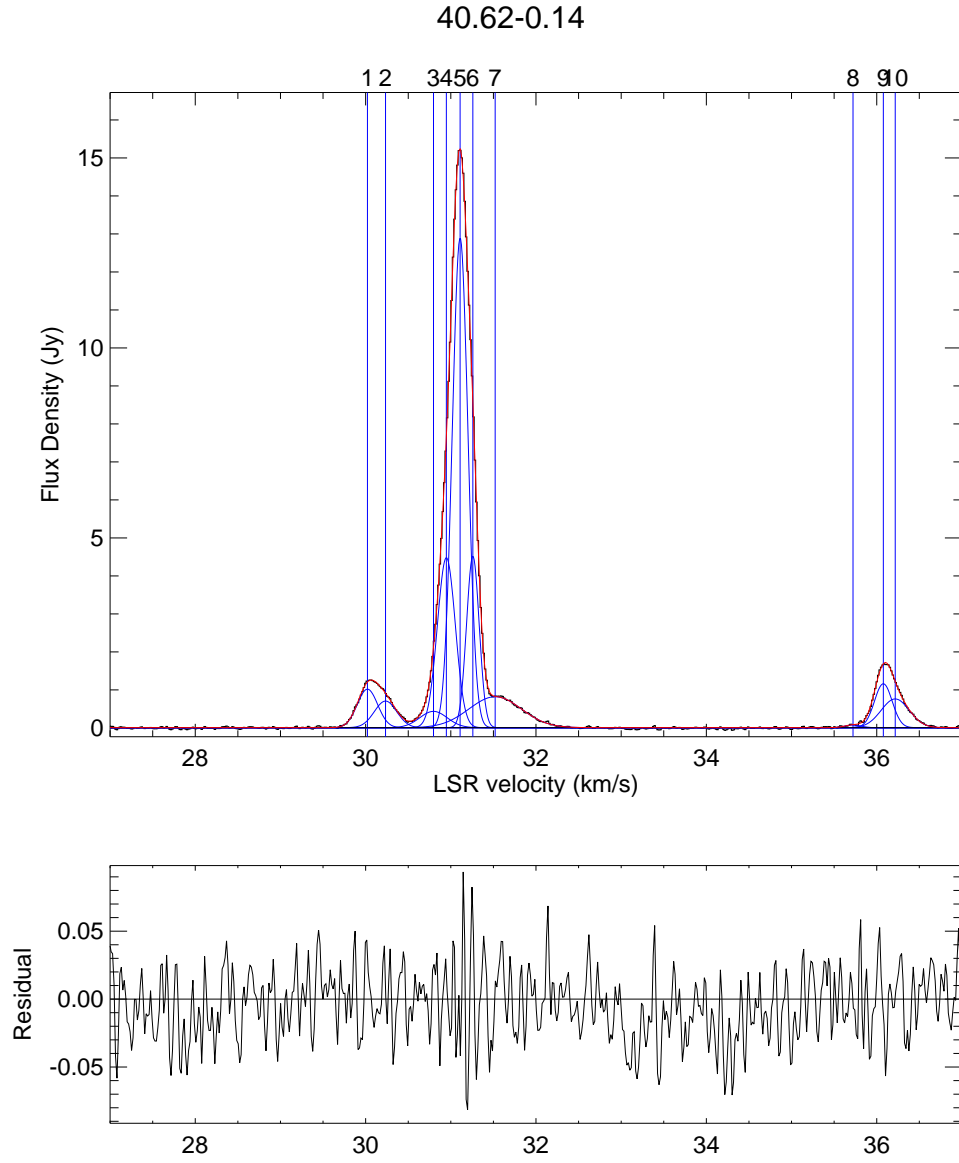


Figure B.22 Gaussian component fit to source 40.62-0.14. The top panel shows the spectrum, and overlays of each Gaussian and its position in blue, and the fit in red. The bottom panel shows the residual. The Gaussians are numbered in the same order as in the corresponding Table.

Table B.23 Gaussian Components of source 40.94–0.04. The columns show the amplitude, S in Jy, center, v_c in km s⁻¹ and the FWHM Δv_{FWHM} in km s⁻¹ for each component.

No.	S (Jy)	v_c (km s ⁻¹)	Δv_{FWHM} (km s ⁻¹)
1	2.21	36.61	0.32
2	0.78	36.84	0.27
3	0.43	37.32	0.29
4	0.23	40.83	0.41
5	0.72	40.97	0.22
6	0.20	41.26	0.35
7	0.07	42.40	0.08
8	0.14	43.63	0.22

Table B.24 Gaussian Components of source 41.08–0.13. The columns show the amplitude, S in Jy, center, v_c in km s⁻¹ and the FWHM Δv_{FWHM} in km s⁻¹ for each component.

No.	S (Jy)	v_c (km s ⁻¹)	Δv_{FWHM} (km s ⁻¹)
1	0.80	57.52	0.30
2	0.14	58.06	0.49
3	0.04	59.36	0.37

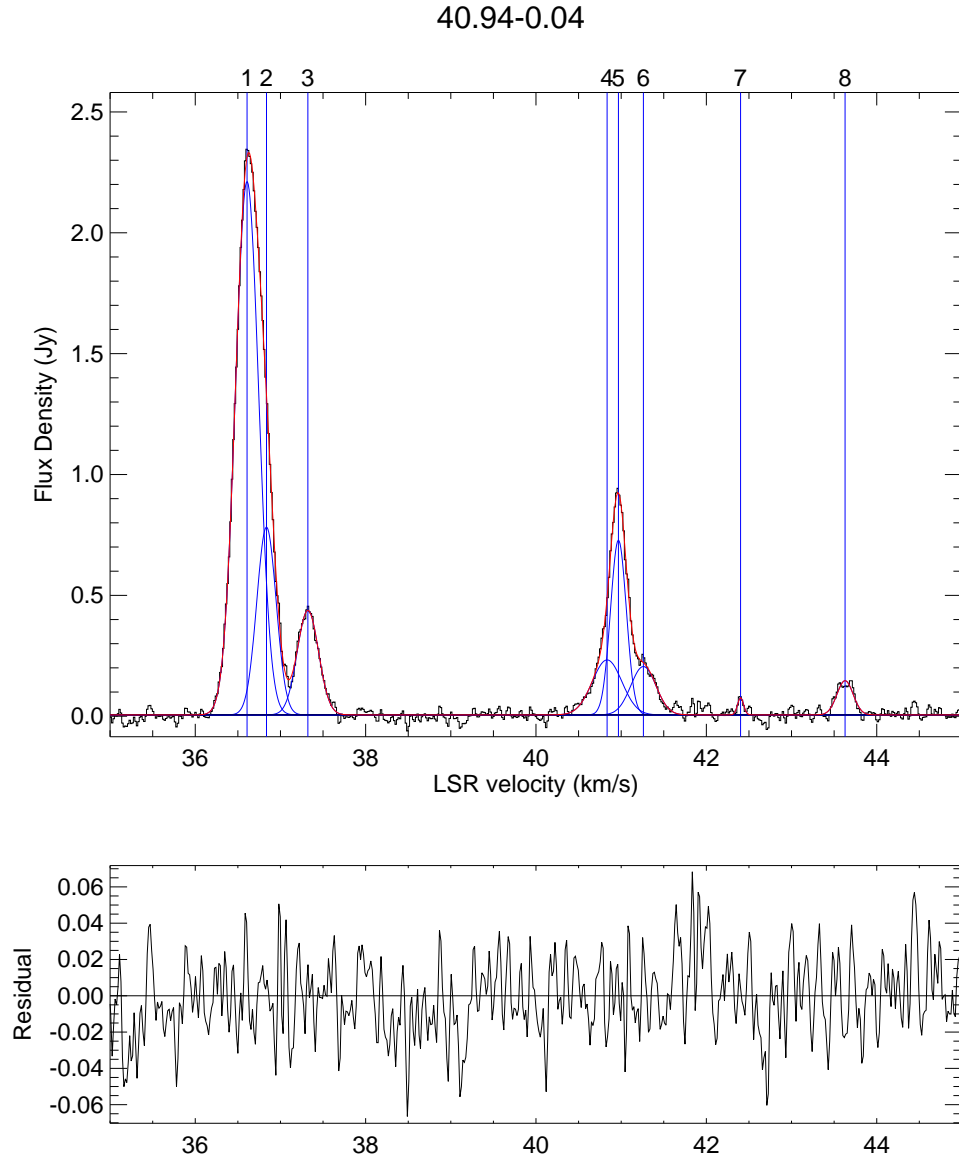


Figure B.23 Gaussian component fit to source 40.94-0.04. The top panel shows the spectrum, and overlays of each Gaussian and its position in blue, and the fit in red. The bottom panel shows the residual. The Gaussians are numbered in the same order as in the corresponding Table.

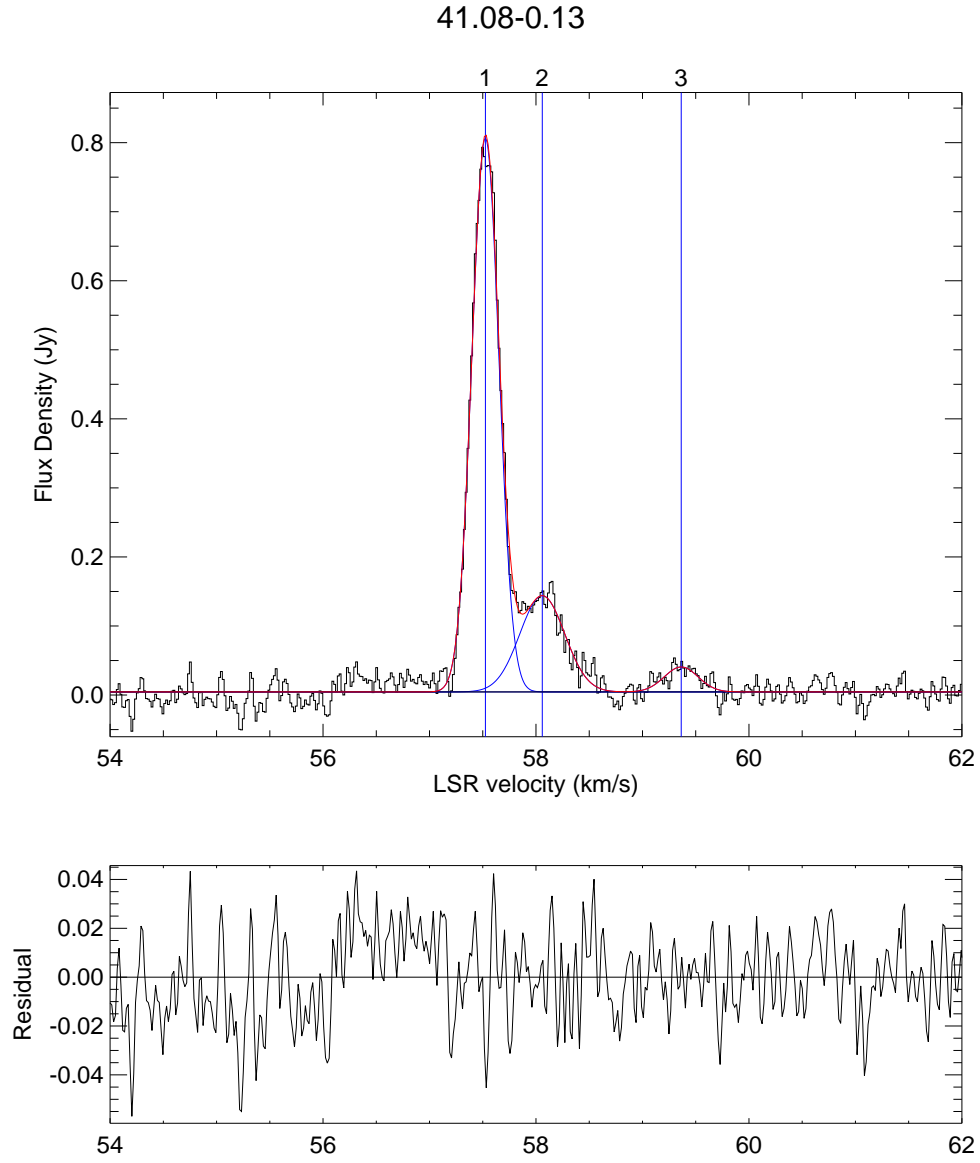


Figure B.24 Gaussian component fit to source 41.08–0.13. The top panel shows the spectrum, and overlays of each Gaussian and its position in blue, and the fit in red. The bottom panel shows the residual. The Gaussians are numbered in the same order as in the corresponding Table.

Table B.25 Gaussian Components of source 41.12–0.11. The columns show the amplitude, S in Jy, center, v_c in km s⁻¹ and the FWHM Δv_{FWHM} in km s⁻¹ for each component.

No.	S (Jy)	v_c (km s ⁻¹)	Δv_{FWHM} (km s ⁻¹)
1	0.04	33.28	0.29
2	0.05	33.52	0.13
3	0.12	35.55	0.29
4	0.23	35.91	0.32
5	1.13	36.54	0.32
6	0.21	37.04	0.45

Table B.26 Gaussian Components of source 41.12–0.22. The columns show the amplitude, S in Jy, center, v_c in km s⁻¹ and the FWHM Δv_{FWHM} in km s⁻¹ for each component.

No.	S (Jy)	v_c (km s ⁻¹)	Δv_{FWHM} (km s ⁻¹)
1	0.25	55.25	0.24
2	0.25	62.76	0.38
3	1.96	63.45	0.47
4	0.16	63.99	0.36
5	0.08	66.43	0.27

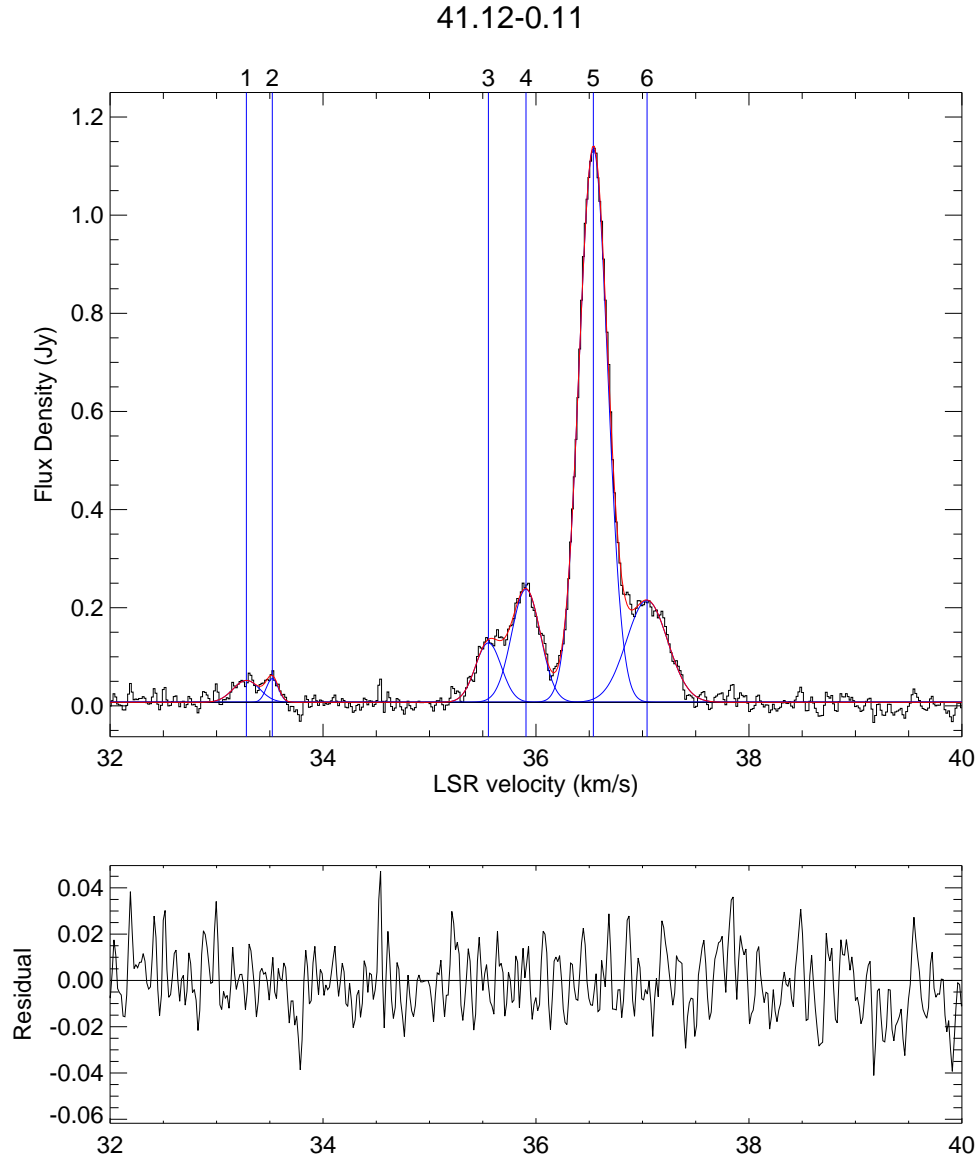


Figure B.25 Gaussian component fit to source 41.12-0.11. The top panel shows the spectrum, and overlays of each Gaussian and its position in blue, and the fit in red. The bottom panel shows the residual. The Gaussians are numbered in the same order as in the corresponding Table.

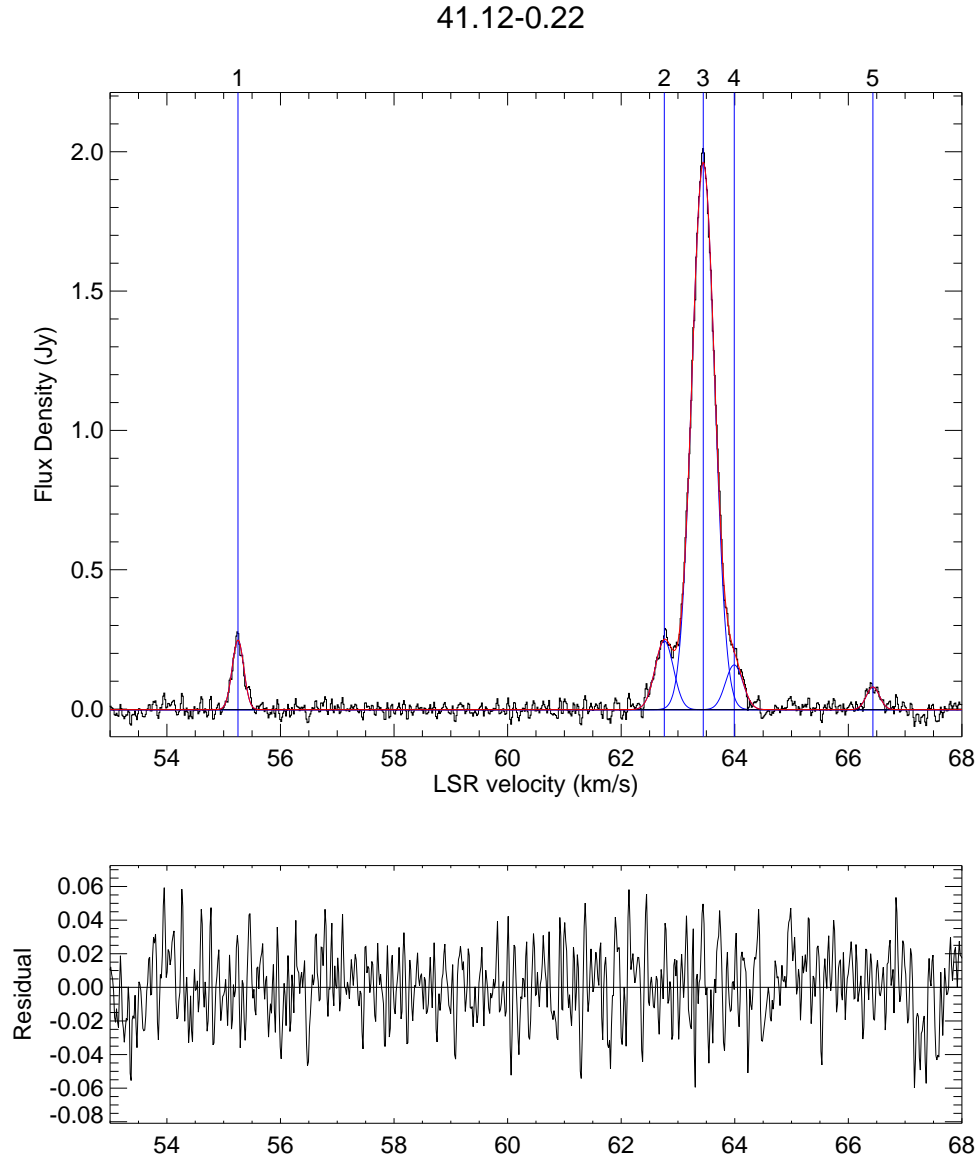


Figure B.26 Gaussian component fit to source 41.12-0.22. The top panel shows the spectrum, and overlays of each Gaussian and its position in blue, and the fit in red. The bottom panel shows the residual. The Gaussians are numbered in the same order as in the corresponding Table.

Table B.27 Gaussian Components of source 41.16–0.20. The columns show the amplitude, S in Jy, center, v_c in km s^{−1} and the FWHM Δv_{FWHM} in km s^{−1} for each component.

No.	S (Jy)	v_c (km s ^{−1})	Δv_{FWHM} (km s ^{−1})
1	0.08	61.73	0.32
2	0.10	62.16	0.33
3	0.07	62.57	0.54
4	0.27	63.52	0.35

Table B.28 Gaussian Components of source 41.27+0.37. The columns show the amplitude, S in Jy, center, v_c in km s^{−1} and the FWHM Δv_{FWHM} in km s^{−1} for each component.

No.	S (Jy)	v_c (km s ^{−1})	Δv_{FWHM} (km s ^{−1})
1	0.04	19.32	0.56
2	0.22	20.04	0.46
3	0.18	20.35	0.23

Table B.29 Gaussian Components of source 41.58+0.04. The columns show the amplitude, S in Jy, center, v_c in km s^{−1} and the FWHM Δv_{FWHM} in km s^{−1} for each component.

No.	S (Jy)	v_c (km s ^{−1})	Δv_{FWHM} (km s ^{−1})
1	0.05	10.68	0.44
2	0.47	11.91	0.38

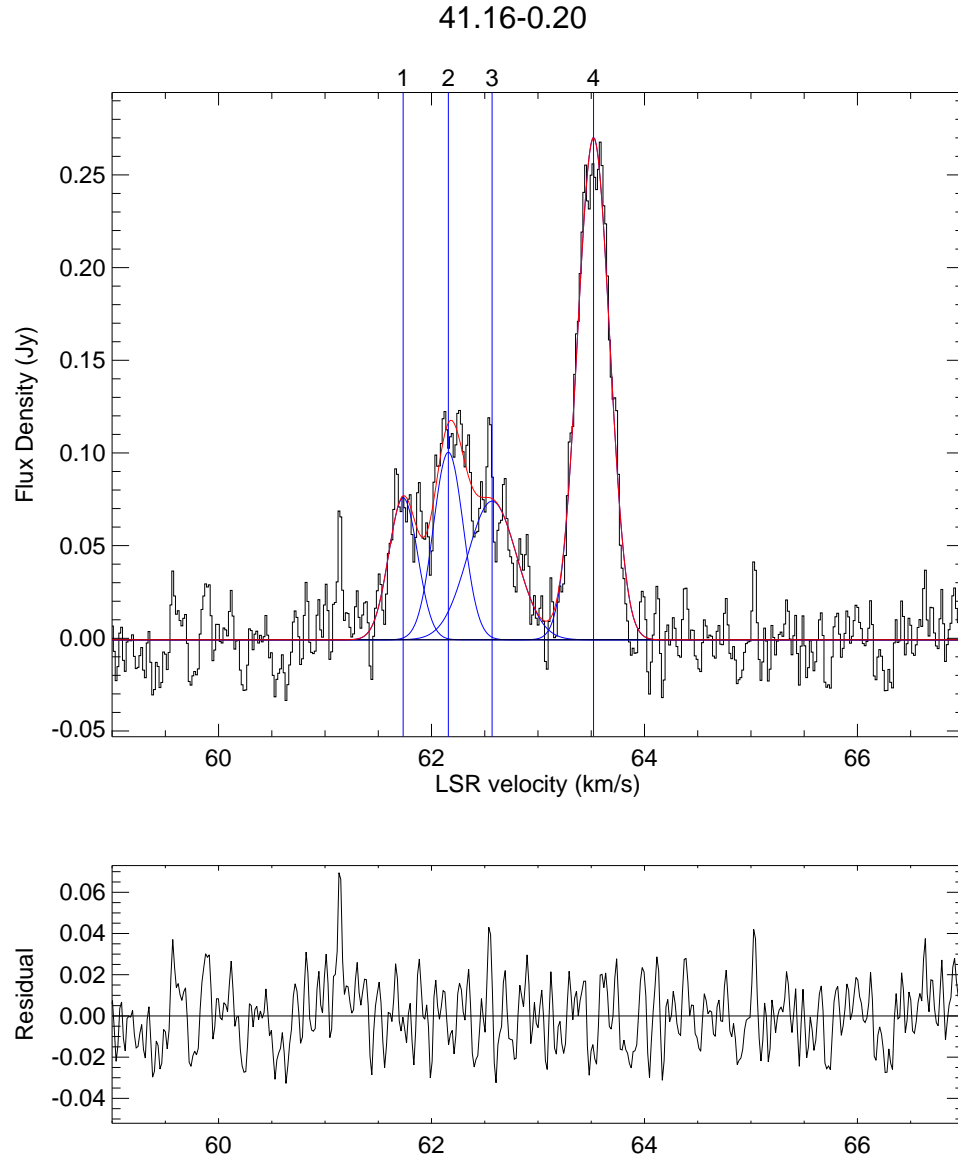


Figure B.27 Gaussian component fit to source 41.16–0.20. The top panel shows the spectrum, and overlays of each Gaussian and its position in blue, and the fit in red. The bottom panel shows the residual. The Gaussians are numbered in the same order as in the corresponding Table.

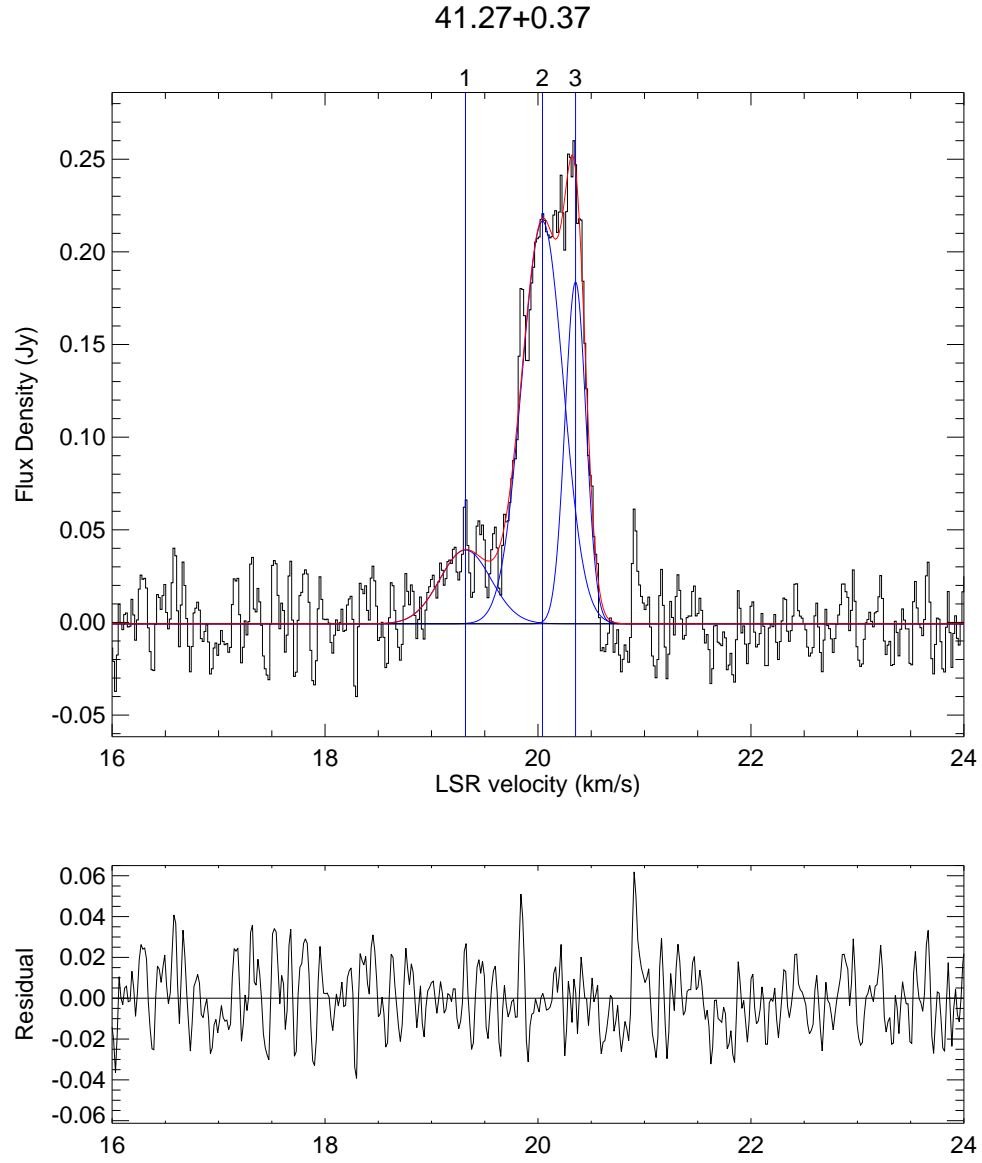


Figure B.28 Gaussian component fit to source 41.27+0.37. The top panel shows the spectrum, and overlays of each Gaussian and its position in blue, and the fit in red. The bottom panel shows the residual. The Gaussians are numbered in the same order as in the corresponding Table.

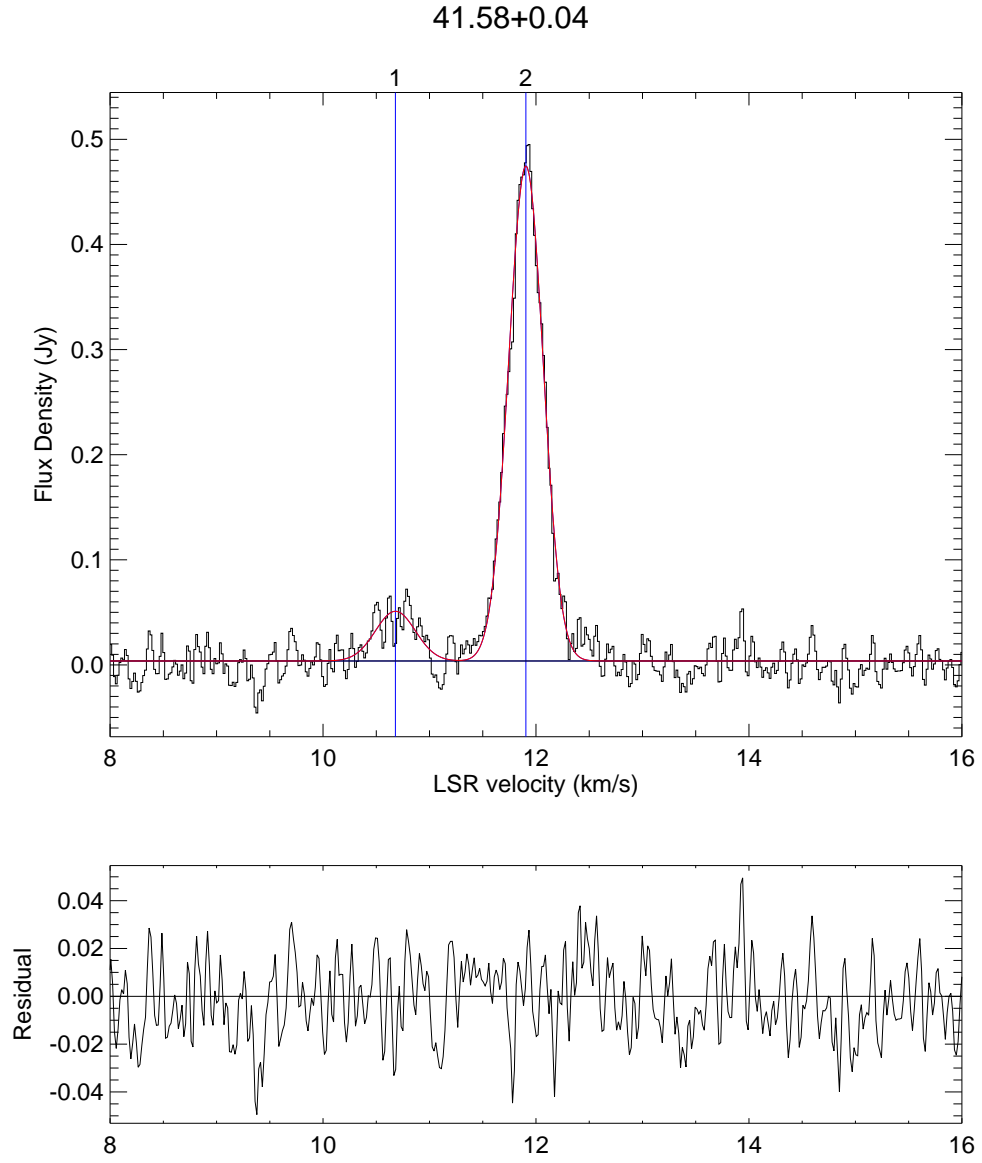


Figure B.29 Gaussian component fit to source 41.58+0.04. The top panel shows the spectrum, and overlays of each Gaussian and its position in blue, and the fit in red. The bottom panel shows the residual. The Gaussians are numbered in the same order as in the corresponding Table.

Table B.30 Gaussian Components of source 41.87–0.10. The columns show the amplitude, S in Jy, center, v_c in km s⁻¹ and the FWHM Δv_{FWHM} in km s⁻¹ for each component.

No.	S (Jy)	v_c (km s ⁻¹)	Δv_{FWHM} (km s ⁻¹)
1	0.18	15.81	0.29
2	0.06	20.70	0.40
3	0.07	23.50	0.34

Table B.31 Gaussian Components of source 43.08–0.08. The columns show the amplitude, S in Jy, center, v_c in km s⁻¹ and the FWHM Δv_{FWHM} in km s⁻¹ for each component.

No.	S (Jy)	v_c (km s ⁻¹)	Δv_{FWHM} (km s ⁻¹)
1	0.52	10.08	0.41
2	8.56	10.19	0.33
3	1.30	10.49	0.26
4	0.63	10.82	0.41
5	0.20	13.94	0.28

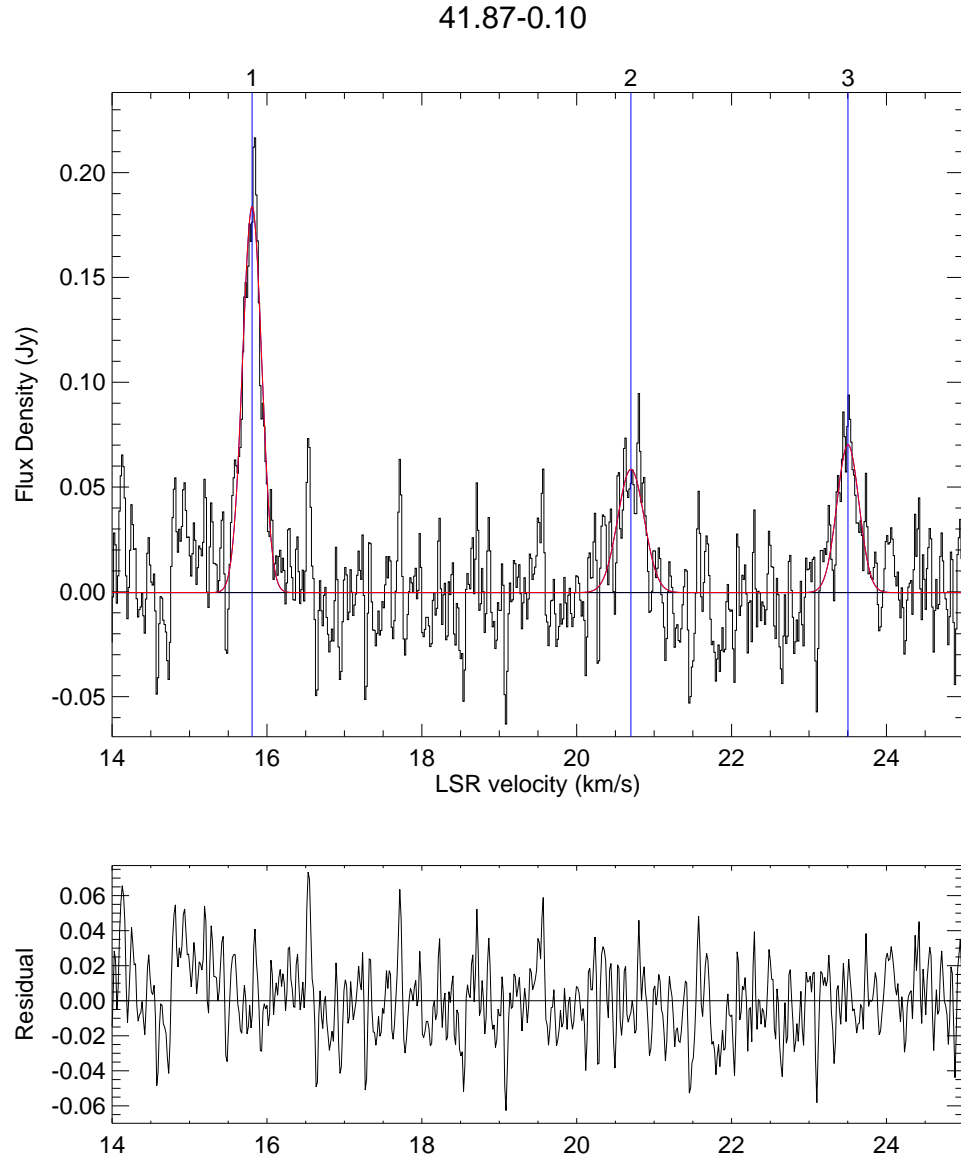


Figure B.30 Gaussian component fit to source 41.87–0.10. The top panel shows the spectrum, and overlays of each Gaussian and its position in blue, and the fit in red. The bottom panel shows the residual. The Gaussians are numbered in the same order as in the corresponding Table.

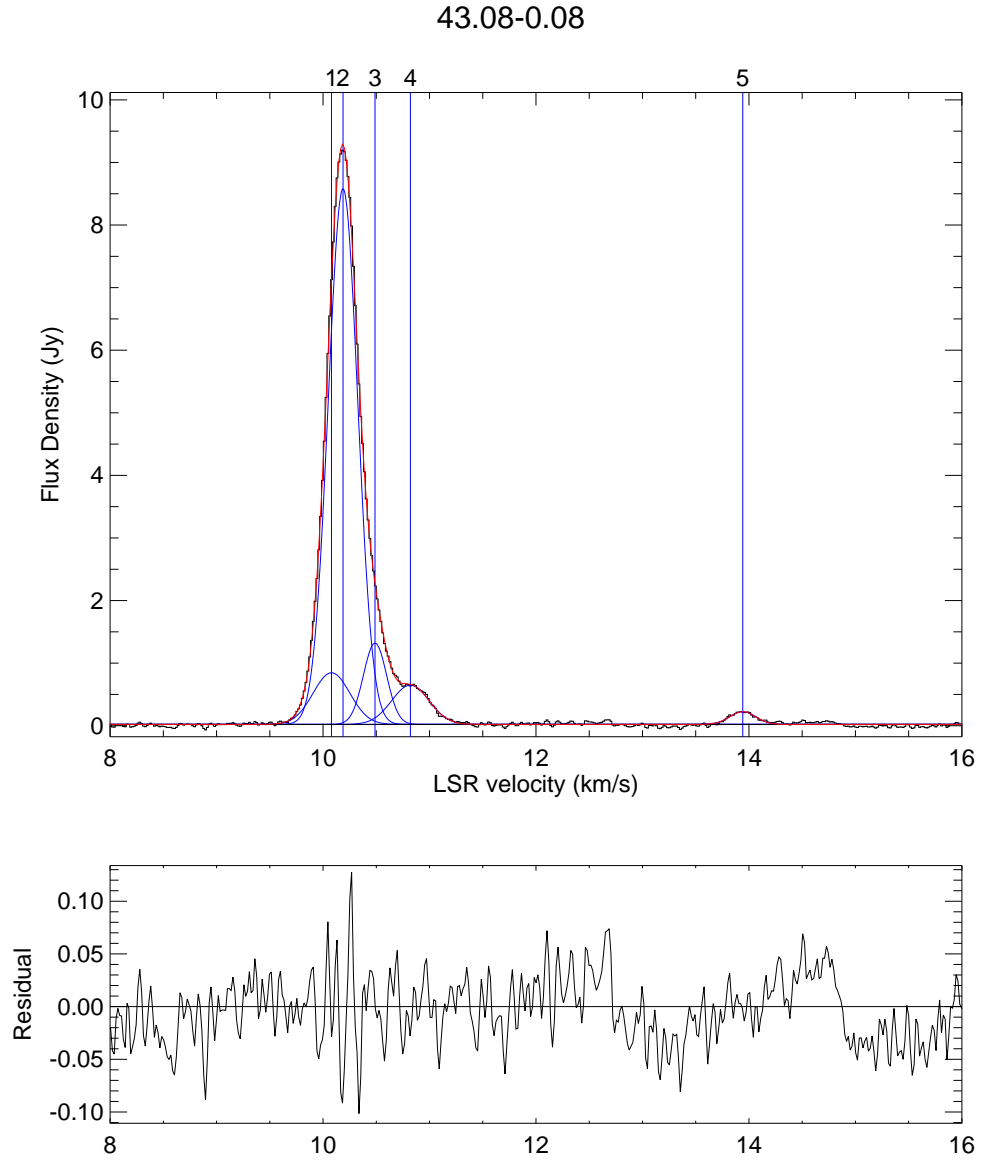


Figure B.31 Gaussian component fit to source 43.08–0.08. The top panel shows the spectrum, and overlays of each Gaussian and its position in blue, and the fit in red. The bottom panel shows the residual. The Gaussians are numbered in the same order as in the corresponding Table.

Table B.32 Gaussian Components of source 43.17–0.00. The columns show the amplitude, S in Jy, center, v_c in km s^{−1} and the FWHM Δv_{FWHM} in km s^{−1} for each component.

No.	S (Jy)	v_c (km s ^{−1})	Δv_{FWHM} (km s ^{−1})
1	0.17	−1.39	0.41
2	1.87	−1.22	0.20
3	1.83	−1.06	0.23
4	0.82	−0.68	0.49
5	0.05	1.29	0.22
6	0.13	1.89	0.42
7	0.06	3.55	0.55
8	0.18	4.02	0.31

Table B.33 Gaussian Components of source 43.18–0.01. The columns show the amplitude, S in Jy, center, v_c in km s^{−1} and the FWHM Δv_{FWHM} in km s^{−1} for each component.

No.	S (Jy)	v_c (km s ^{−1})	Δv_{FWHM} (km s ^{−1})
1	0.07	8.18	0.29
2	0.08	9.17	0.73
3	0.55	10.93	0.69
4	0.54	11.23	0.46
5	0.07	13.03	0.26
6	0.09	13.55	0.50

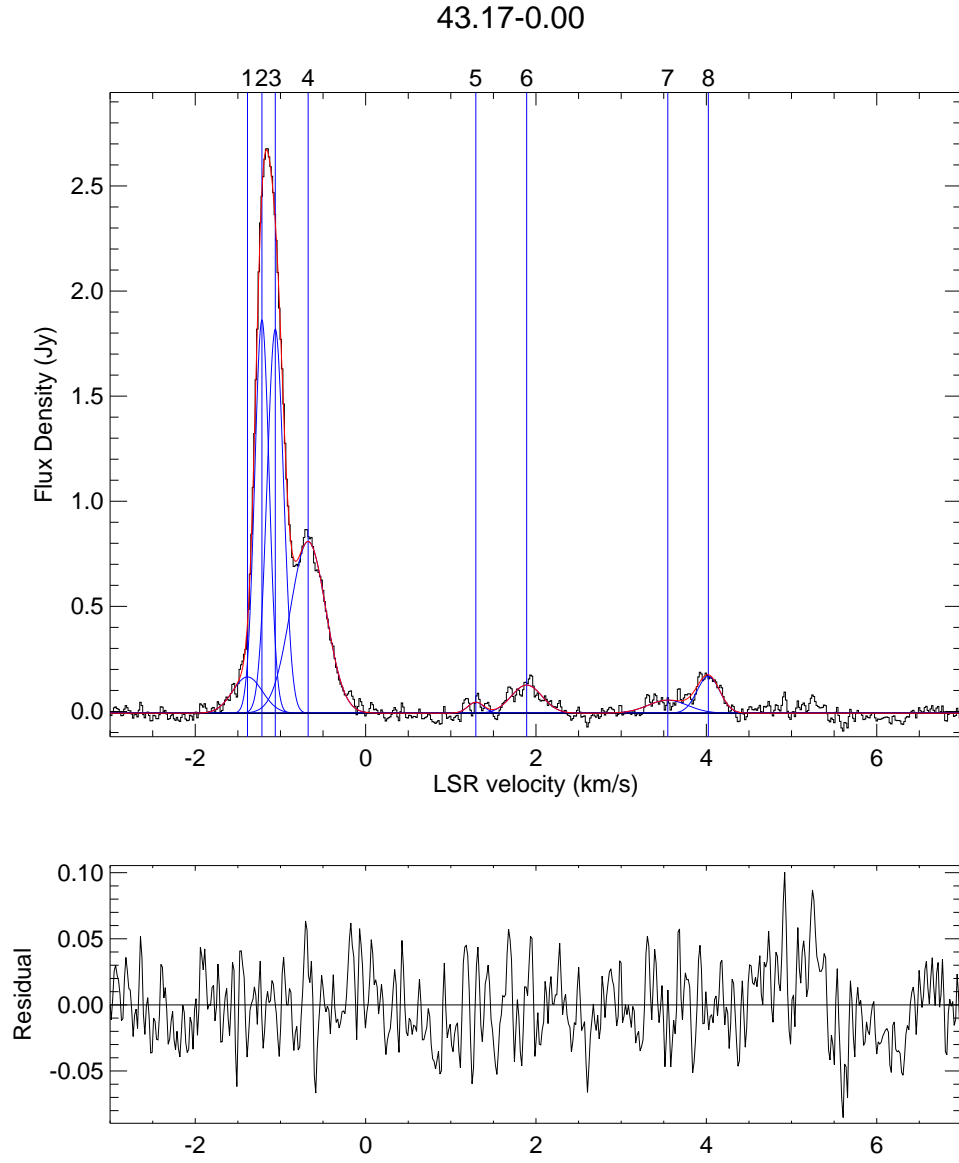


Figure B.32 Gaussian component fit to source 43.17-0.00. The top panel shows the spectrum, and overlays of each Gaussian and its position in blue, and the fit in red. The bottom panel shows the residual. The Gaussians are numbered in the same order as in the corresponding Table.

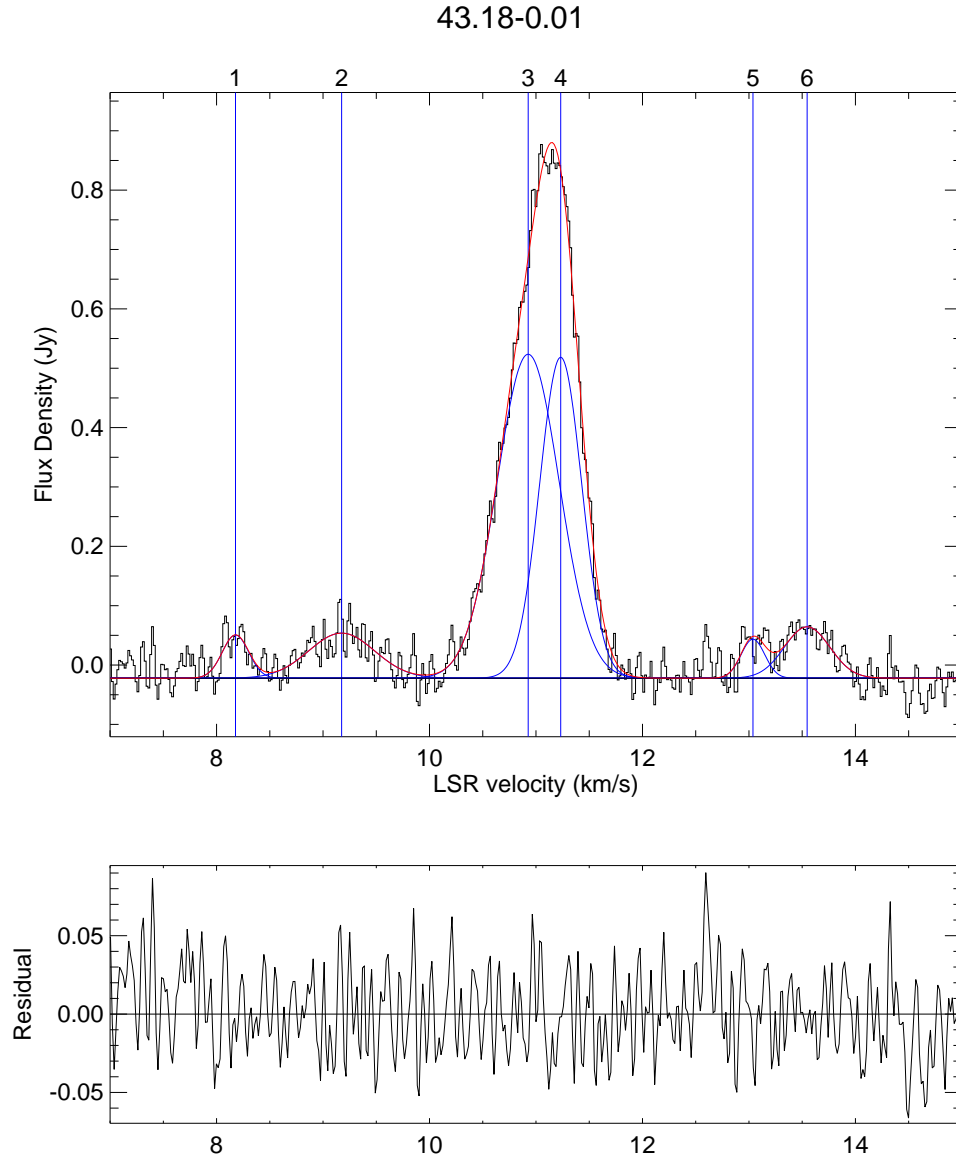


Figure B.33 Gaussian component fit to source 43.18-0.01. The top panel shows the spectrum, and overlays of each Gaussian and its position in blue, and the fit in red. The bottom panel shows the residual. The Gaussians are numbered in the same order as in the corresponding Table.

Table B.34 Gaussian Components of source 44.31+0.04. The columns show the amplitude, S in Jy, center, v_c in km s⁻¹ and the FWHM Δv_{FWHM} in km s⁻¹ for each component.

No.	S (Jy)	v_c (km s ⁻¹)	Δv_{FWHM} (km s ⁻¹)
1	0.22	55.32	0.37
2	0.65	55.77	0.39
3	0.28	56.17	0.25

Table B.35 Gaussian Components of source 44.64-0.52. The columns show the amplitude, S in Jy, center, v_c in km s⁻¹ and the FWHM Δv_{FWHM} in km s⁻¹ for each component.

No.	S (Jy)	v_c (km s ⁻¹)	Δv_{FWHM} (km s ⁻¹)
1	0.02	47.78	0.50
2	0.18	49.11	0.39
3	0.47	49.37	0.30
4	0.24	49.60	0.25

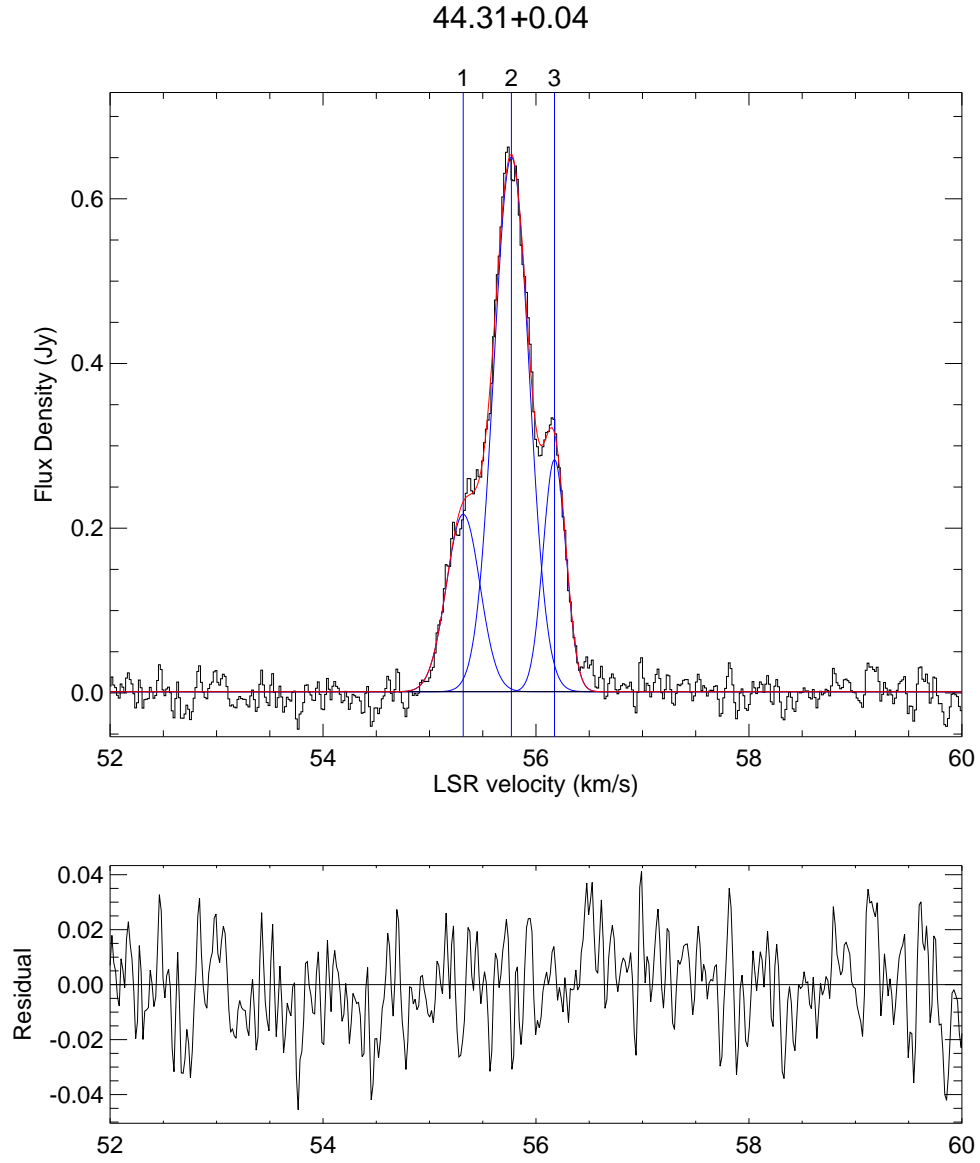


Figure B.34 Gaussian component fit to source 44.31+0.04. The top panel shows the spectrum, and overlays of each Gaussian and its position in blue, and the fit in red. The bottom panel shows the residual. The Gaussians are numbered in the same order as in the corresponding Table.

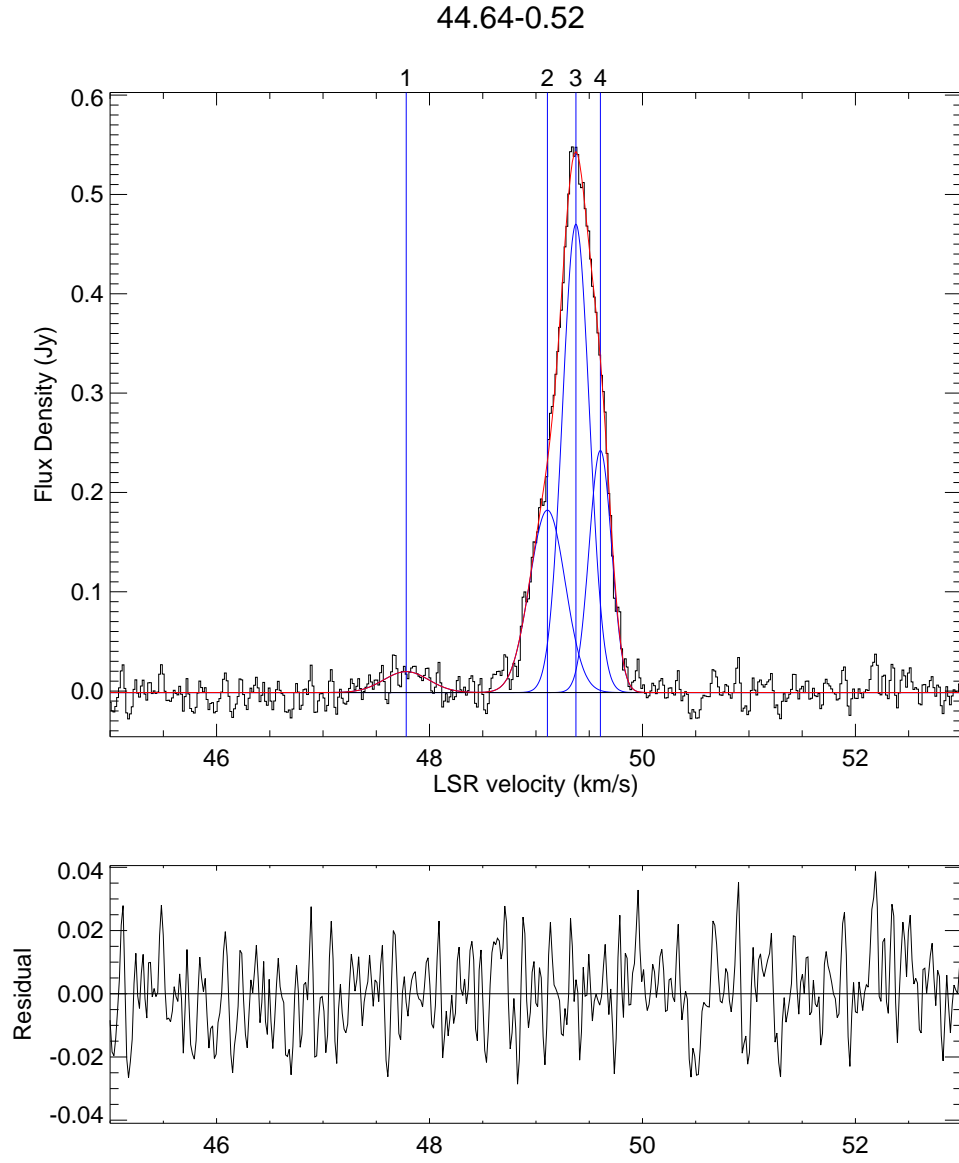


Figure B.35 Gaussian component fit to source 44.64–0.52. The top panel shows the spectrum, and overlays of each Gaussian and its position in blue, and the fit in red. The bottom panel shows the residual. The Gaussians are numbered in the same order as in the corresponding Table.

Table B.36 Gaussian Components of source 45.07+0.13. The columns show the amplitude, S in Jy, center, v_c in km s⁻¹ and the FWHM Δv_{FWHM} in km s⁻¹ for each component.

No.	S (Jy)	v_c (km s ⁻¹)	Δv_{FWHM} (km s ⁻¹)
1	0.18	57.31	0.52
2	14.05	57.65	0.25
3	40.50	57.79	0.32
4	8.54	58.08	0.30
5	4.03	58.23	0.37
6	0.16	58.78	0.48
7	0.58	59.67	0.29

Table B.37 Gaussian Components of source 45.44+0.07. The columns show the amplitude, S in Jy, center, v_c in km s⁻¹ and the FWHM Δv_{FWHM} in km s⁻¹ for each component.

No.	S (Jy)	v_c (km s ⁻¹)	Δv_{FWHM} (km s ⁻¹)
1	0.80	49.76	0.45
2	0.79	50.07	0.31
3	0.31	50.40	0.20

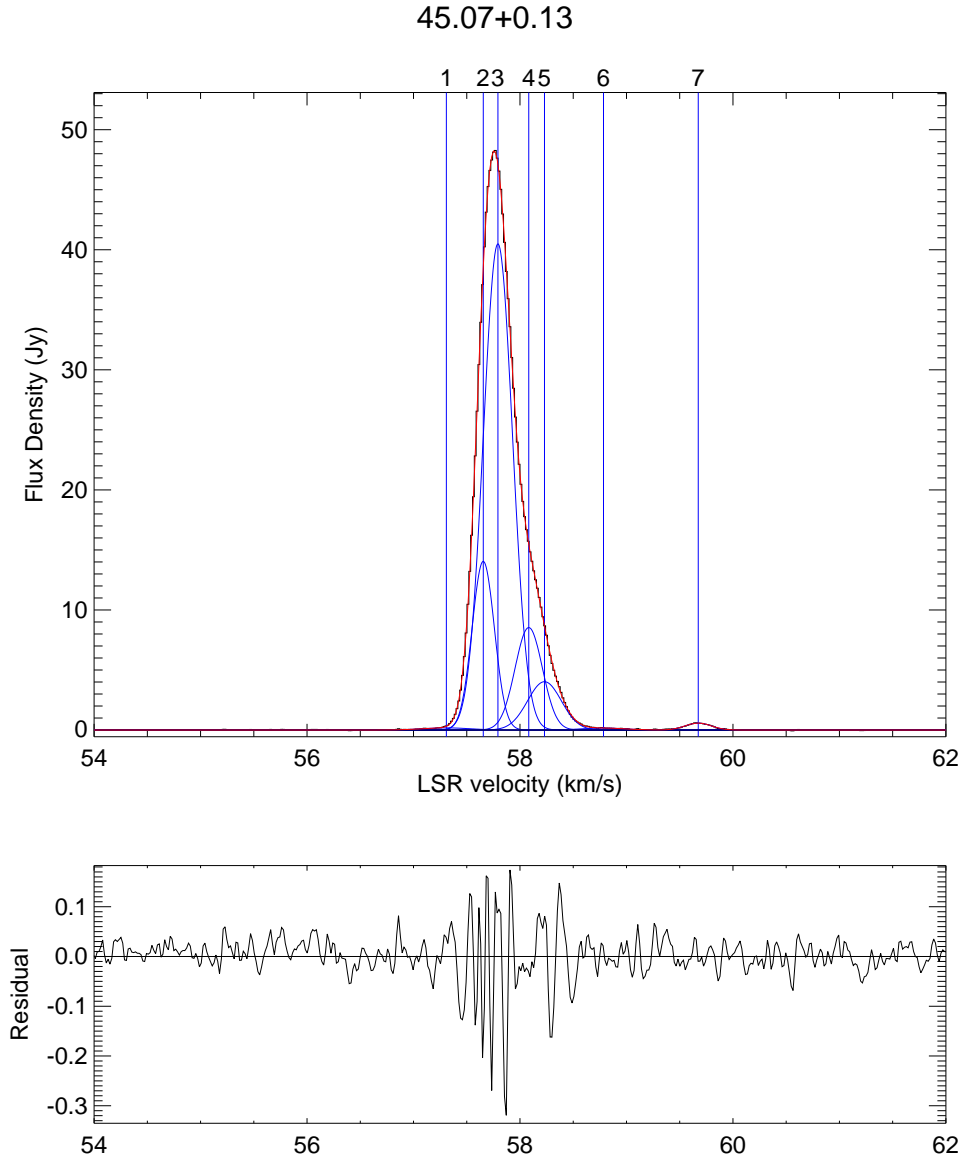


Figure B.36 Gaussian component fit to source 45.07+0.13. The top panel shows the spectrum, and overlays of each Gaussian and its position in blue, and the fit in red. The bottom panel shows the residual. The Gaussians are numbered in the same order as in the corresponding Table.

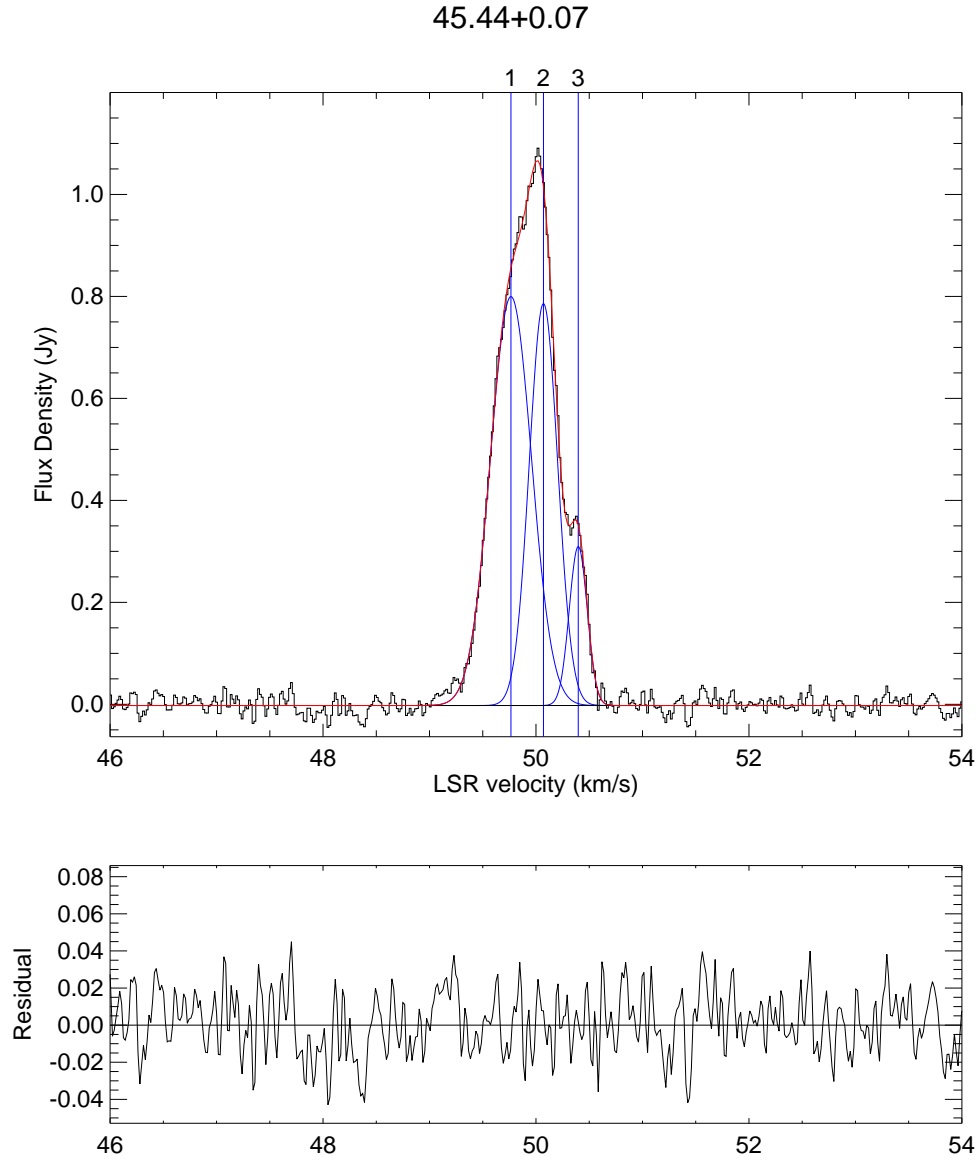


Figure B.37 Gaussian component fit to source 45.44+0.07. The top panel shows the spectrum, and overlays of each Gaussian and its position in blue, and the fit in red. The bottom panel shows the residual. The Gaussians are numbered in the same order as in the corresponding Table.

Table B.38 Gaussian Components of source 45.49+0.13. The columns show the amplitude, S in Jy, center, v_c in km s^{-1} and the FWHM Δv_{FWHM} in km s^{-1} for each component.

No.	S (Jy)	v_c (km s^{-1})	Δv_{FWHM} (km s^{-1})
1	4.98	57.09	0.19
2	3.75	57.24	0.25
3	4.05	57.36	0.43
4	2.53	57.71	0.31
5	0.70	57.88	0.21
6	0.05	64.29	0.36
7	0.04	65.20	0.65
8	0.17	65.64	0.23
9	0.07	65.87	0.89

Table B.39 Gaussian Components of source 45.57–0.12. The columns show the amplitude, S in Jy, center, v_c in km s^{-1} and the FWHM Δv_{FWHM} in km s^{-1} for each component.

No.	S (Jy)	v_c (km s^{-1})	Δv_{FWHM} (km s^{-1})
1	0.12	1.45	0.34
2	0.31	1.64	0.33
3	0.14	3.10	0.32
4	0.05	3.44	0.57
5	0.22	4.17	0.23
6	0.11	9.60	0.28

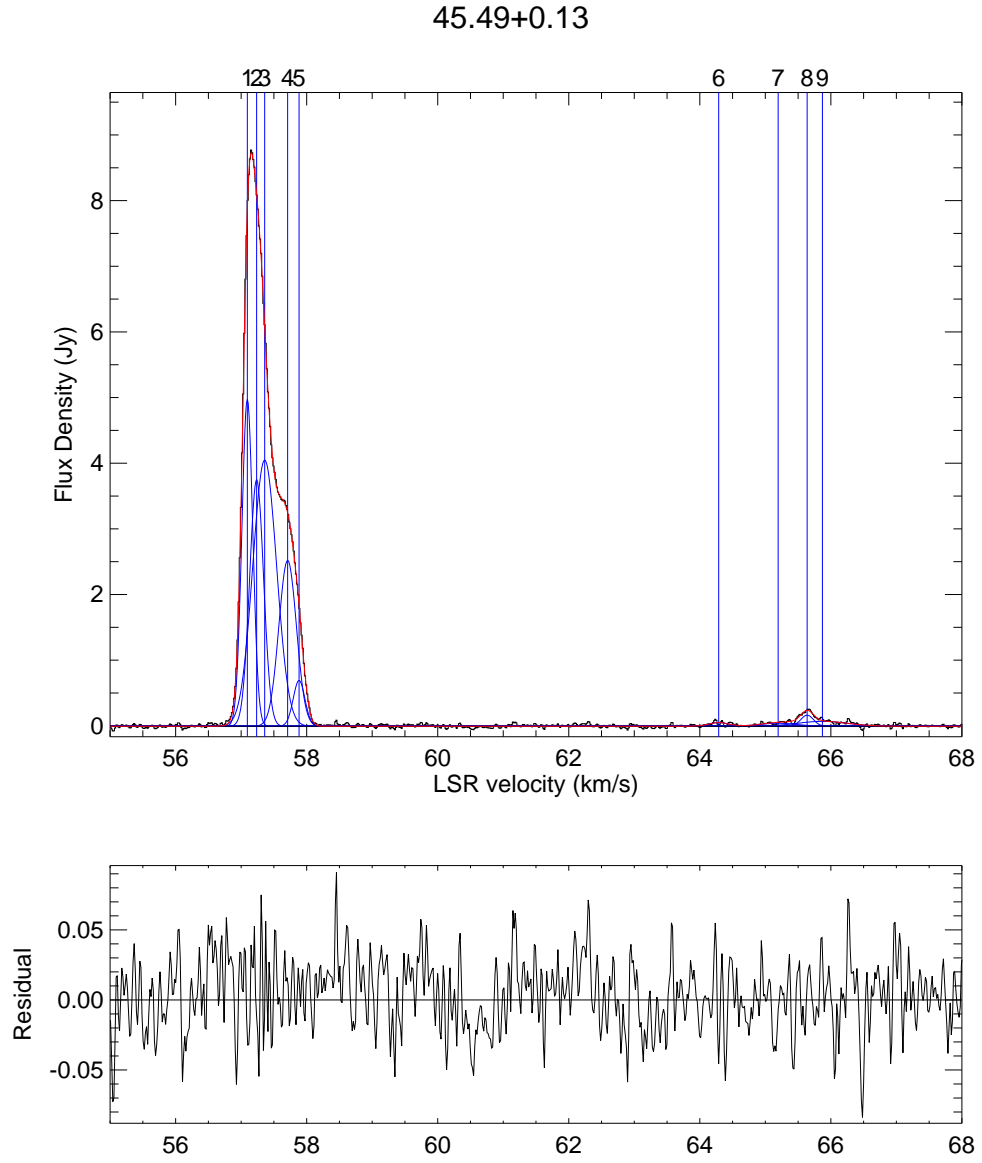


Figure B.38 Gaussian component fit to source 45.49+0.13. The top panel shows the spectrum, and overlays of each Gaussian and its position in blue, and the fit in red. The bottom panel shows the residual. The Gaussians are numbered in the same order as in the corresponding Table.

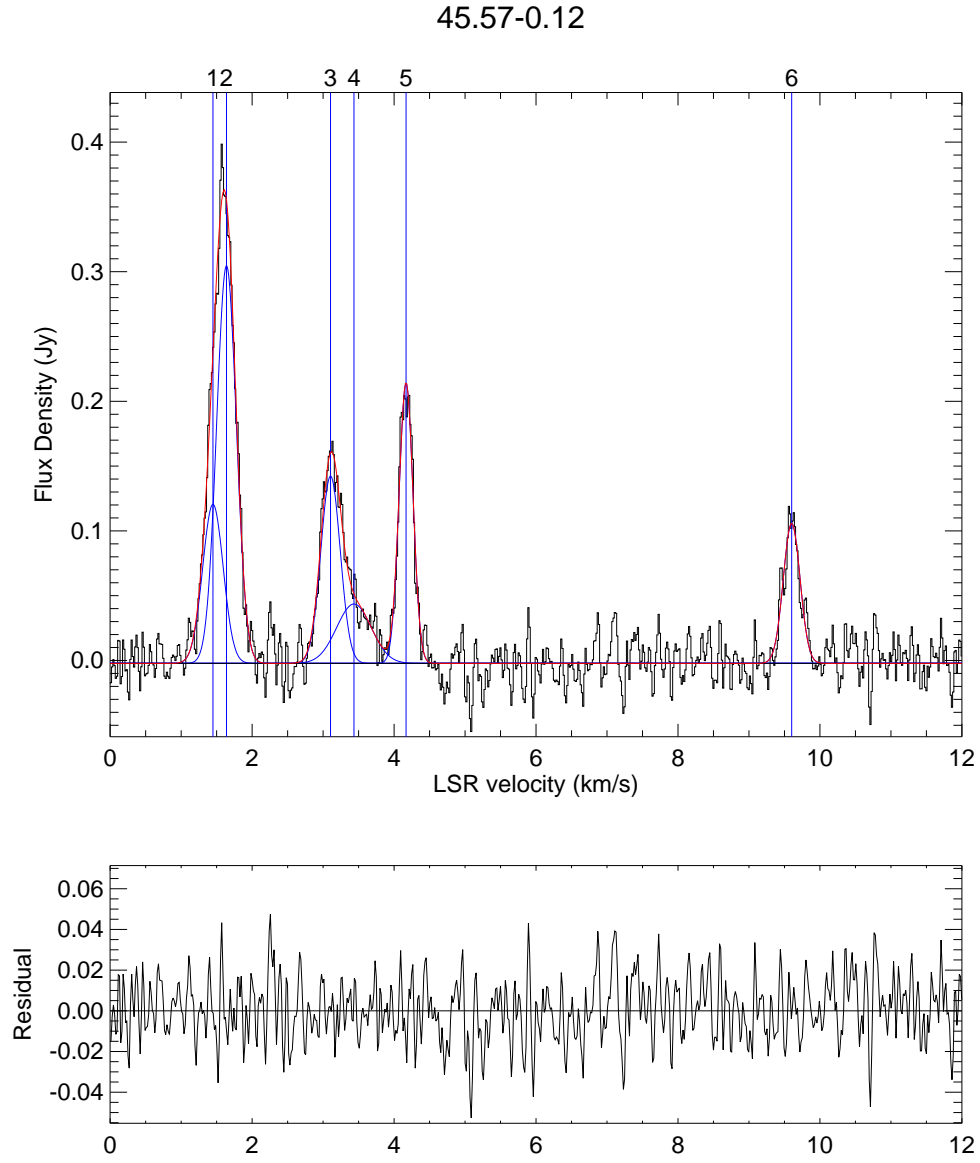


Figure B.39 Gaussian component fit to source 45.57–0.12. The top panel shows the spectrum, and overlays of each Gaussian and its position in blue, and the fit in red. The bottom panel shows the residual. The Gaussians are numbered in the same order as in the corresponding Table.

Table B.40 Gaussian Components of source 46.07+0.22. The columns show the amplitude, S in Jy, center, v_c in km s⁻¹ and the FWHM Δv_{FWHM} in km s⁻¹ for each component.

No.	S (Jy)	v_c (km s ⁻¹)	Δv_{FWHM} (km s ⁻¹)
1	0.05	22.65	0.60
2	1.17	23.25	0.50
3	0.68	23.64	0.40
4	0.11	24.10	0.34
5	0.43	24.44	0.46

Table B.41 Gaussian Components of source 48.89-0.17. The columns show the amplitude, S in Jy, center, v_c in km s⁻¹ and the FWHM Δv_{FWHM} in km s⁻¹ for each component.

No.	S (Jy)	v_c (km s ⁻¹)	Δv_{FWHM} (km s ⁻¹)
1	0.12	57.33	0.17

Table B.42 Gaussian Components of source 48.90-0.27. The columns show the amplitude, S in Jy, center, v_c in km s⁻¹ and the FWHM Δv_{FWHM} in km s⁻¹ for each component.

No.	S (Jy)	v_c (km s ⁻¹)	Δv_{FWHM} (km s ⁻¹)
1	0.11	63.75	0.34
2	0.04	69.22	0.18
3	0.63	71.79	0.54
4	0.50	72.11	0.34

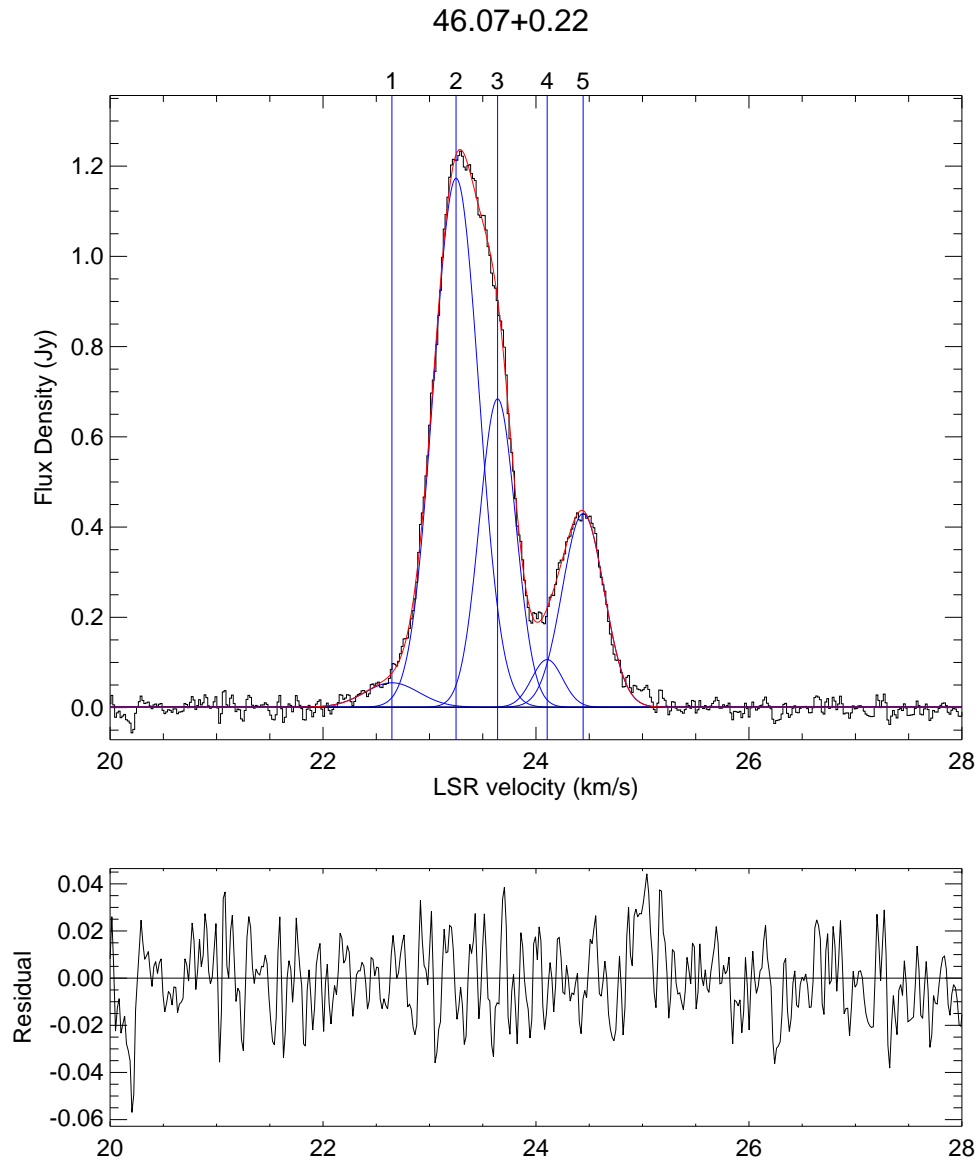


Figure B.40 Gaussian component fit to source 46.07+0.22. The top panel shows the spectrum, and overlays of each Gaussian and its position in blue, and the fit in red. The bottom panel shows the residual. The Gaussians are numbered in the same order as in the corresponding Table.

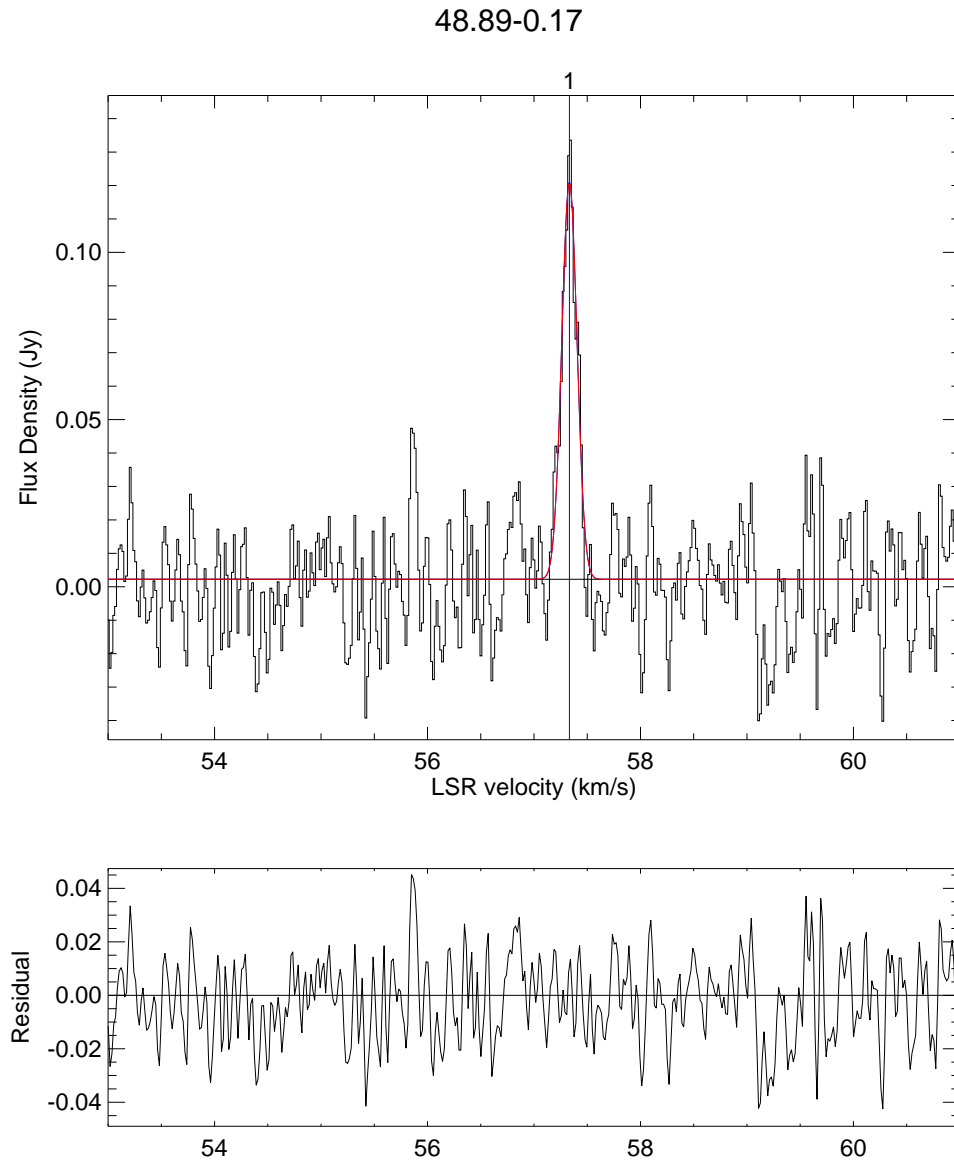


Figure B.41 Gaussian component fit to source 48.89–0.17. The top panel shows the spectrum, and overlays of each Gaussian and its position in blue, and the fit in red. The bottom panel shows the residual. The Gaussians are numbered in the same order as in the corresponding Table.

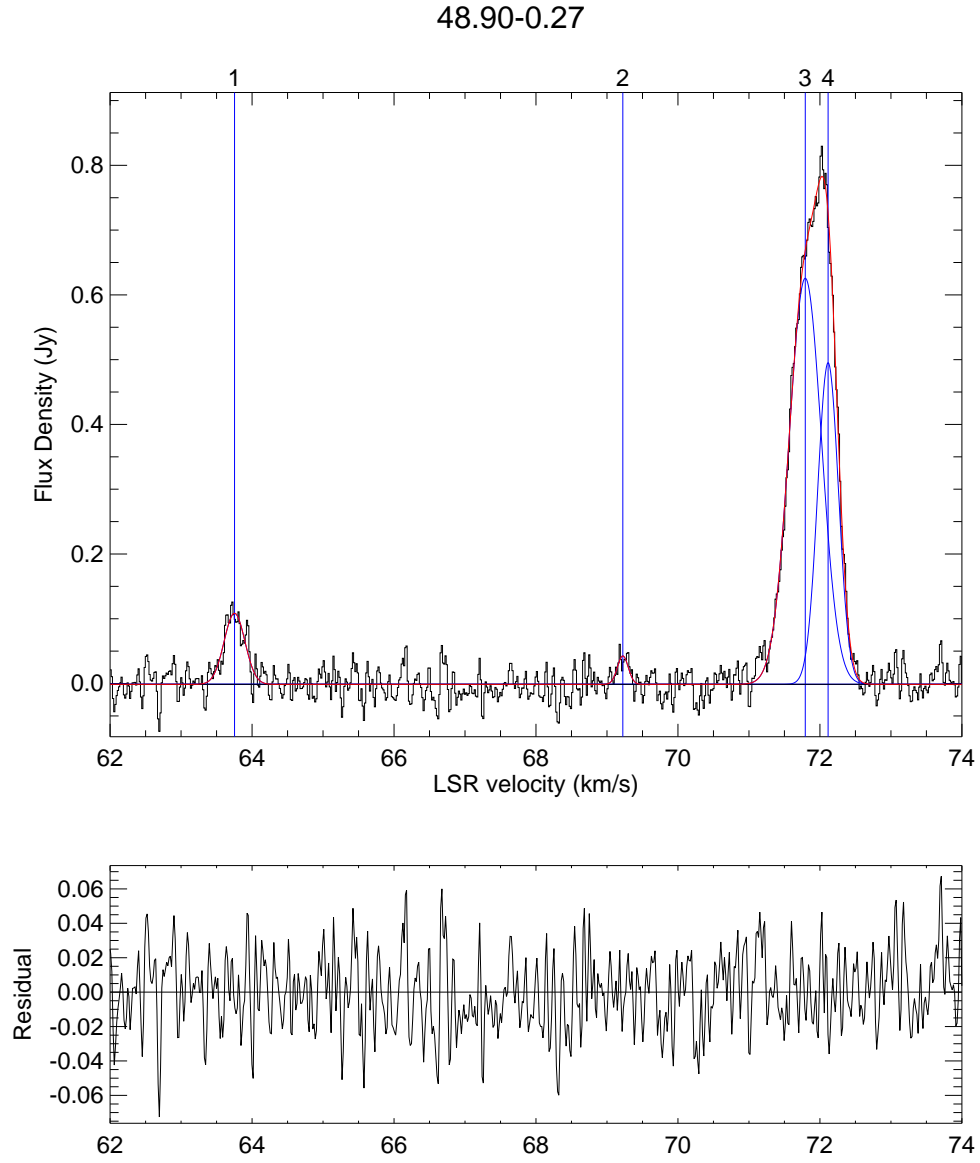


Figure B.42 Gaussian component fit to source 48.90–0.27. The top panel shows the spectrum, and overlays of each Gaussian and its position in blue, and the fit in red. The bottom panel shows the residual. The Gaussians are numbered in the same order as in the corresponding Table.

Table B.43 Gaussian Components of source 48.99–0.30. The columns show the amplitude, S in Jy, center, v_c in km s⁻¹ and the FWHM Δv_{FWHM} in km s⁻¹ for each component.

No.	S (Jy)	v_c (km s ⁻¹)	Δv_{FWHM} (km s ⁻¹)
1	0.04	61.22	0.63
2	0.10	62.67	0.24
3	0.18	63.09	0.37
4	0.03	66.79	0.40
5	0.14	67.26	0.32
6	0.12	67.61	0.34
7	0.04	69.28	0.57
8	0.04	70.47	0.25
9	0.15	71.49	0.31
10	0.47	71.63	0.61
11	0.08	72.39	0.37

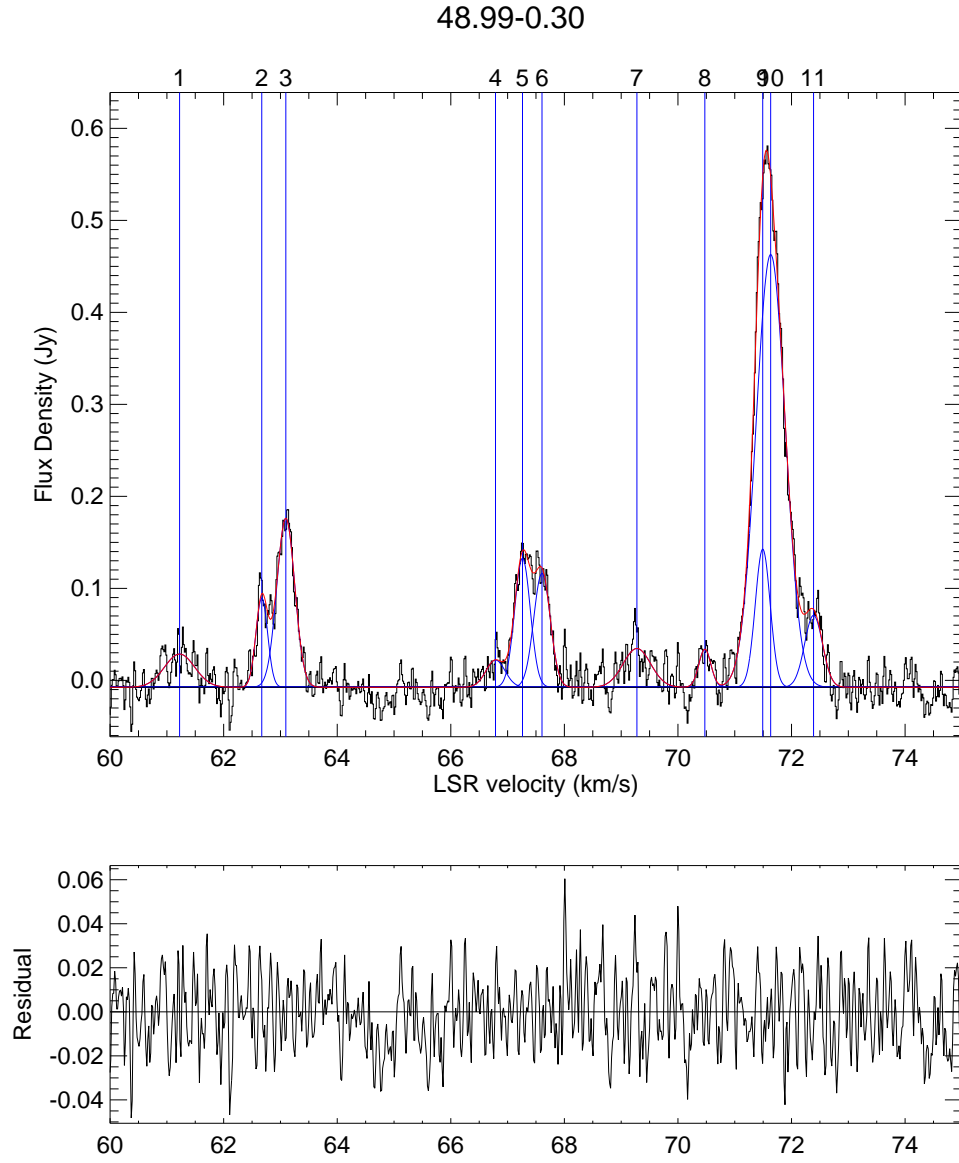


Figure B.43 Gaussian component fit to source 48.99–0.30. The top panel shows the spectrum, and overlays of each Gaussian and its position in blue, and the fit in red. The bottom panel shows the residual. The Gaussians are numbered in the same order as in the corresponding Table.

Table B.44 Gaussian Components of source 49.62–0.36. The columns show the amplitude, S in Jy, center, v_c in km s^{−1} and the FWHM Δv_{FWHM} in km s^{−1} for each component.

No.	S (Jy)	v_c (km s ^{−1})	Δv_{FWHM} (km s ^{−1})
1	1.21	49.26	0.32
2	0.24	49.47	0.18
3	0.34	49.72	0.51
4	0.42	50.10	0.32
5	0.10	50.33	0.24
6	0.09	58.06	0.54
7	0.15	59.15	0.89
8	0.31	59.32	0.31
9	0.05	59.84	0.57

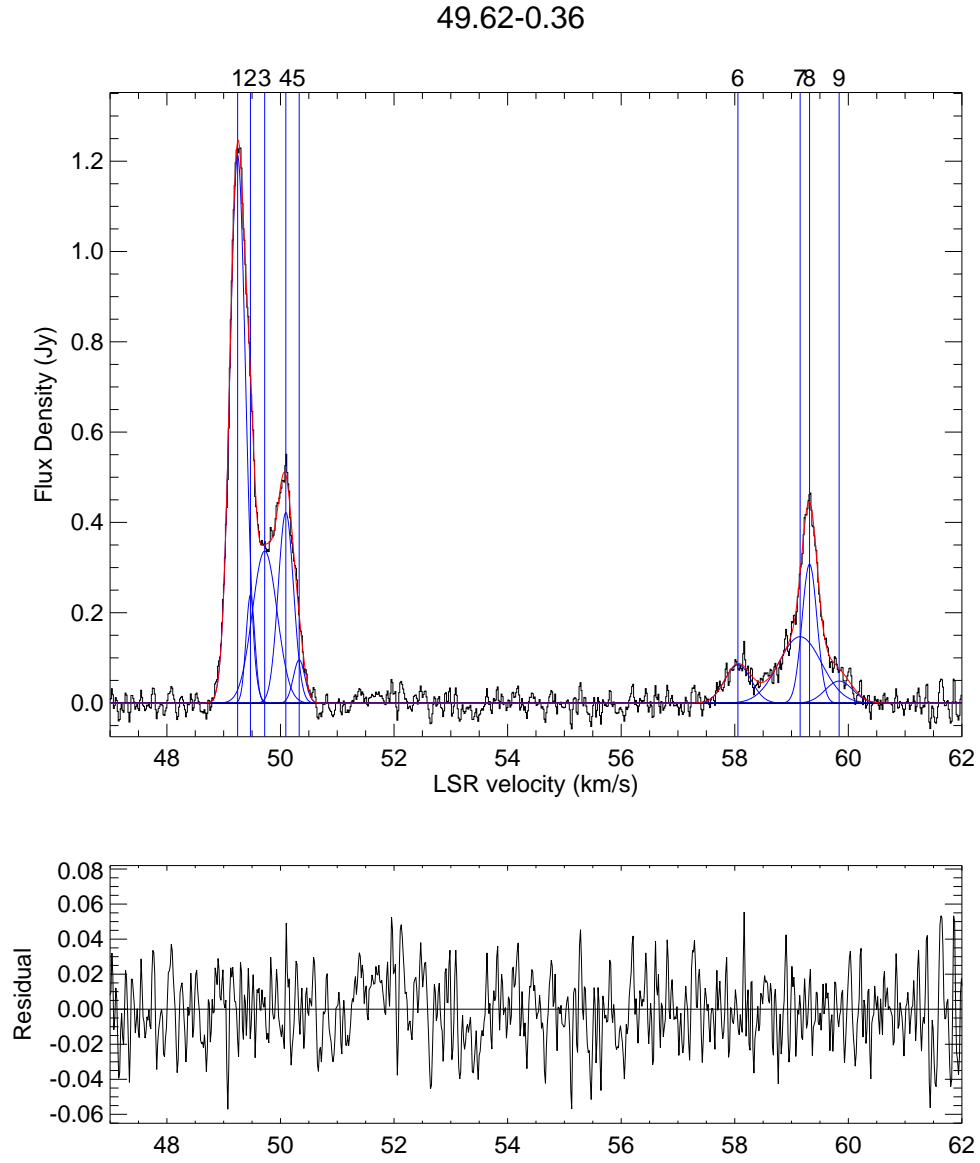


Figure B.44 Gaussian component fit to source 49.62–0.36. The top panel shows the spectrum, and overlays of each Gaussian and its position in blue, and the fit in red. The bottom panel shows the residual. The Gaussians are numbered in the same order as in the corresponding Table.

Table B.45 Gaussian Components of source 50.78+0.15. The columns show the amplitude, S in Jy, center, v_c in km s⁻¹ and the FWHM Δv_{FWHM} in km s⁻¹ for each component.

No.	S (Jy)	v_c (km s ⁻¹)	Δv_{FWHM} (km s ⁻¹)
1	0.05	47.66	0.49
2	0.98	48.71	0.47
3	1.23	48.91	0.34
4	4.23	49.06	0.25
5	0.26	49.35	0.23
6	1.60	49.78	0.32
7	0.16	50.10	0.21
8	0.12	50.56	0.54

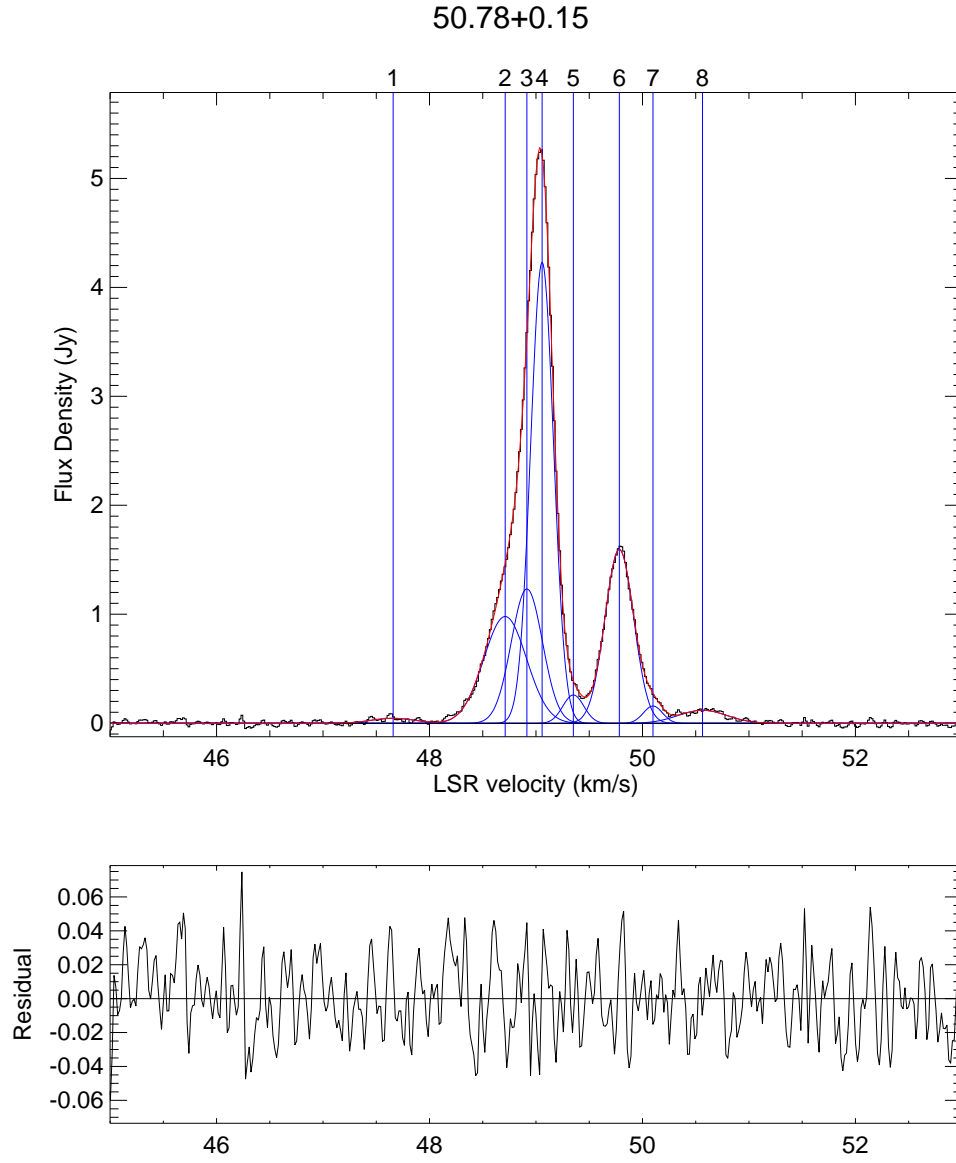


Figure B.45 Gaussian component fit to source 50.78+0.15. The top panel shows the spectrum, and overlays of each Gaussian and its position in blue, and the fit in red. The bottom panel shows the residual. The Gaussians are numbered in the same order as in the corresponding Table.

Table B.46 Gaussian Components of source 52.92+0.41. The columns show the amplitude, S in Jy, center, v_c in km s⁻¹ and the FWHM Δv_{FWHM} in km s⁻¹ for each component.

No.	S (Jy)	v_c (km s ⁻¹)	Δv_{FWHM} (km s ⁻¹)
1	4.96	39.09	0.21
2	1.97	39.21	0.17
3	2.47	39.38	0.48
4	1.82	39.67	0.24
5	0.16	40.01	0.21
6	0.14	40.23	0.19
7	0.16	40.50	0.32
8	0.04	41.07	0.32
9	1.16	42.61	0.24
10	2.83	44.59	0.35

Table B.47 Gaussian Components of source 53.04+0.11. The columns show the amplitude, S in Jy, center, v_c in km s⁻¹ and the FWHM Δv_{FWHM} in km s⁻¹ for each component.

No.	S (Jy)	v_c (km s ⁻¹)	Δv_{FWHM} (km s ⁻¹)
1	1.33	9.87	0.18
2	0.64	9.99	0.12
3	1.62	10.13	0.20

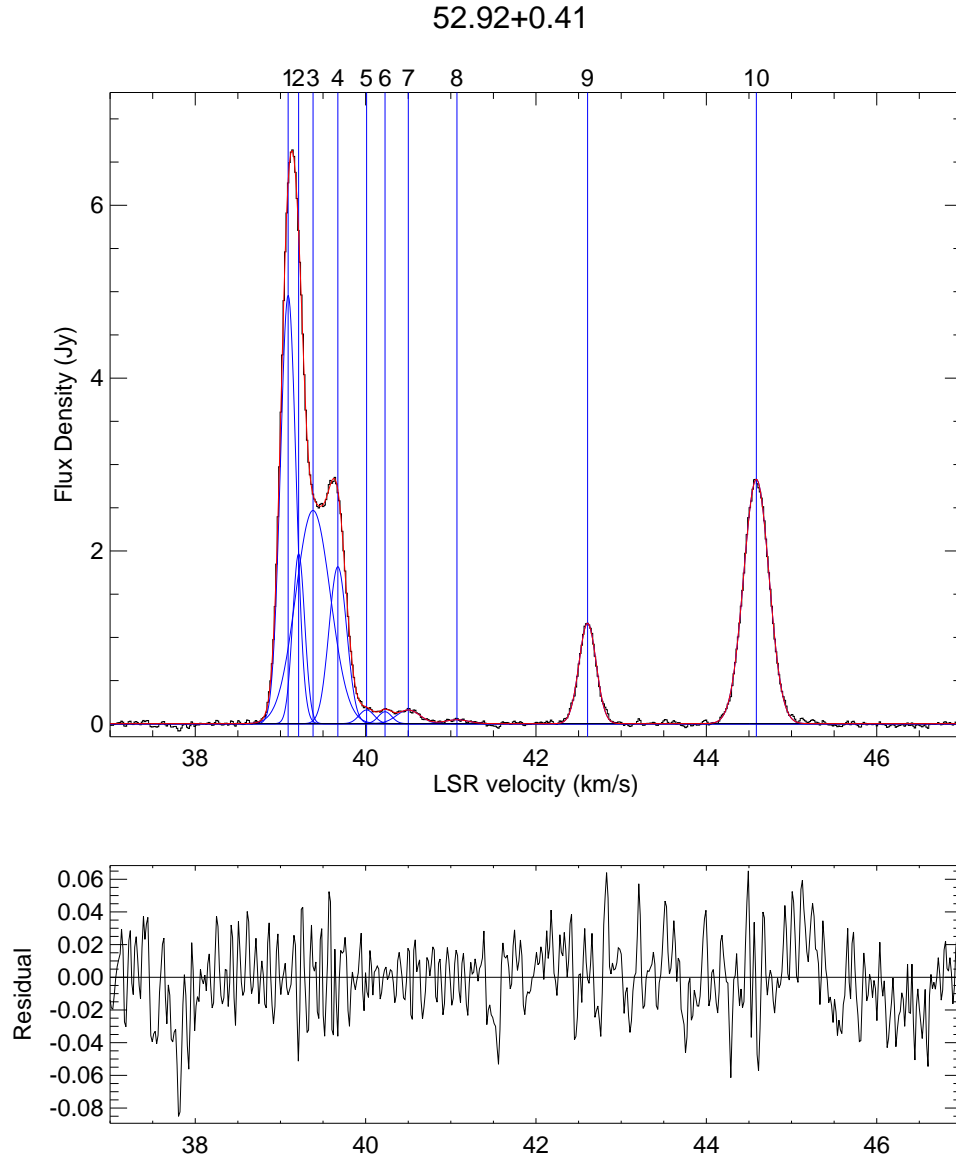


Figure B.46 Gaussian component fit to source 52.92+0.41. The top panel shows the spectrum, and overlays of each Gaussian and its position in blue, and the fit in red. The bottom panel shows the residual. The Gaussians are numbered in the same order as in the corresponding Table.

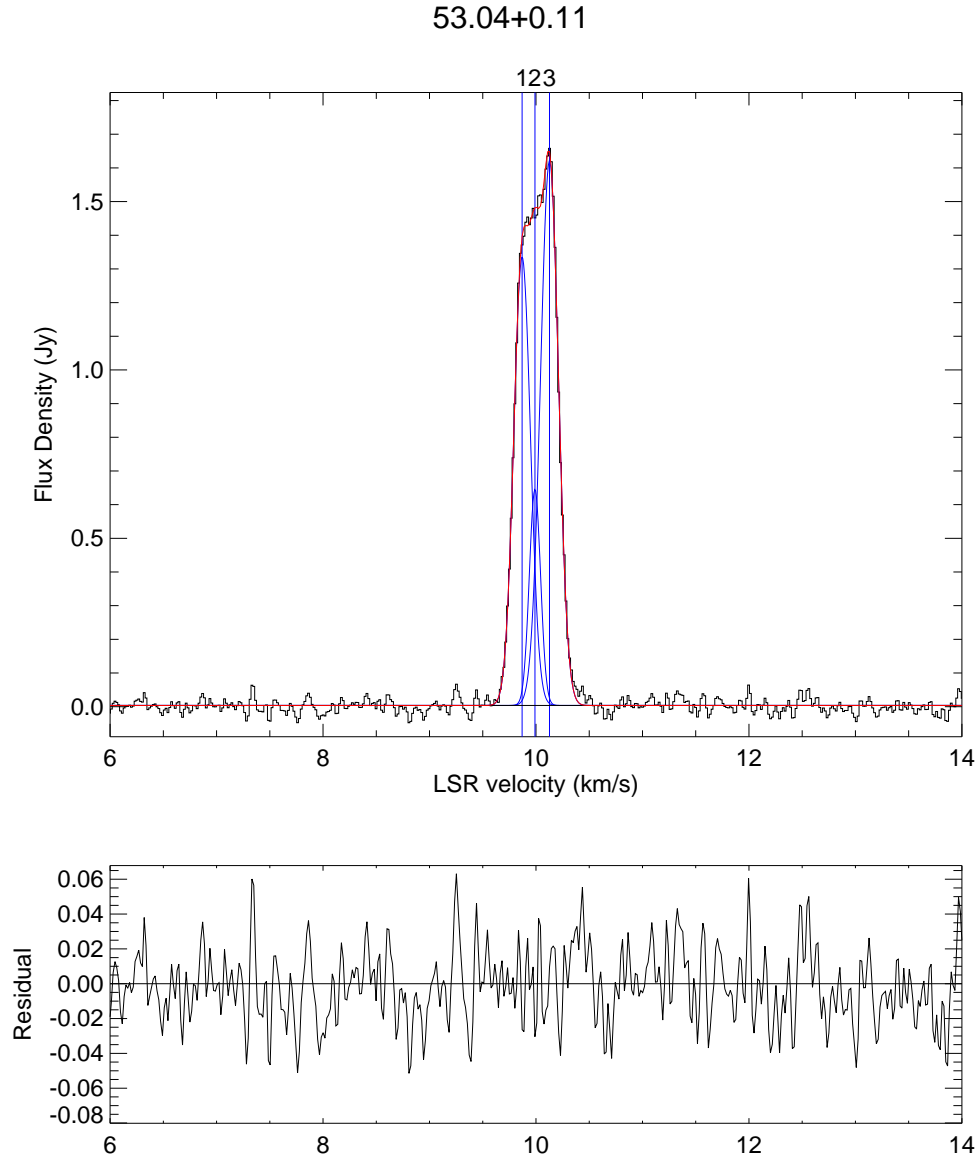


Figure B.47 Gaussian component fit to source 53.04+0.11. The top panel shows the spectrum, and overlays of each Gaussian and its position in blue, and the fit in red. The bottom panel shows the residual. The Gaussians are numbered in the same order as in the corresponding Table.

Table B.48 Gaussian Components of source 53.14+0.07. The columns show the amplitude, S in Jy, center, v_c in km s⁻¹ and the FWHM Δv_{FWHM} in km s⁻¹ for each component.

No.	S (Jy)	v_c (km s ⁻¹)	Δv_{FWHM} (km s ⁻¹)
1	0.66	23.81	0.27
2	0.10	24.28	0.73
3	0.93	24.56	0.24
4	0.08	24.78	0.23
5	0.04	25.21	0.38

Table B.49 Gaussian Components of source 53.62+0.04. The columns show the amplitude, S in Jy, center, v_c in km s⁻¹ and the FWHM Δv_{FWHM} in km s⁻¹ for each component.

No.	S (Jy)	v_c (km s ⁻¹)	Δv_{FWHM} (km s ⁻¹)
1	2.67	18.49	0.17
2	6.03	18.59	0.17
3	2.32	18.78	0.18
4	16.69	18.95	0.24
5	3.03	19.01	0.13
6	1.08	19.18	0.29

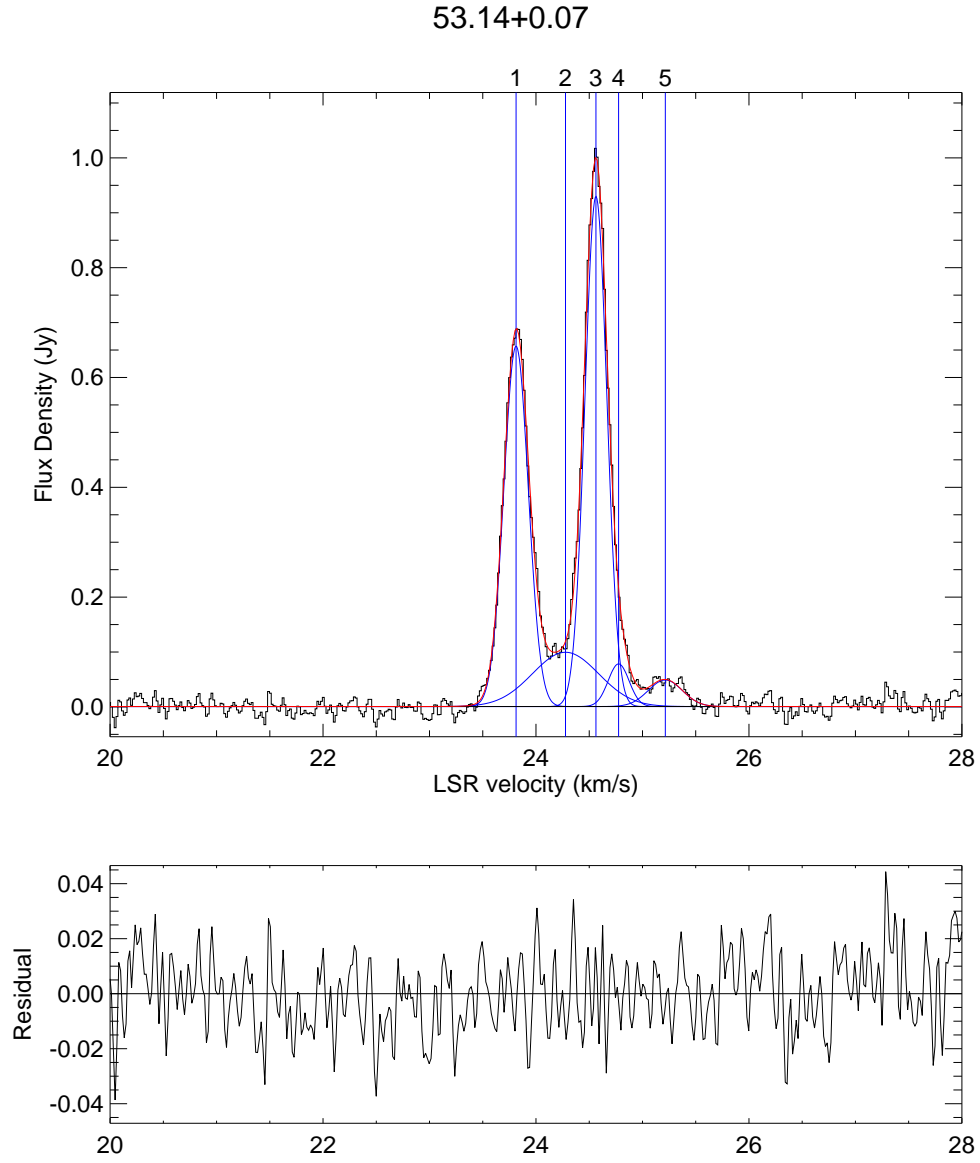


Figure B.48 Gaussian component fit to source 53.14+0.07. The top panel shows the spectrum, and overlays of each Gaussian and its position in blue, and the fit in red. The bottom panel shows the residual. The Gaussians are numbered in the same order as in the corresponding Table.

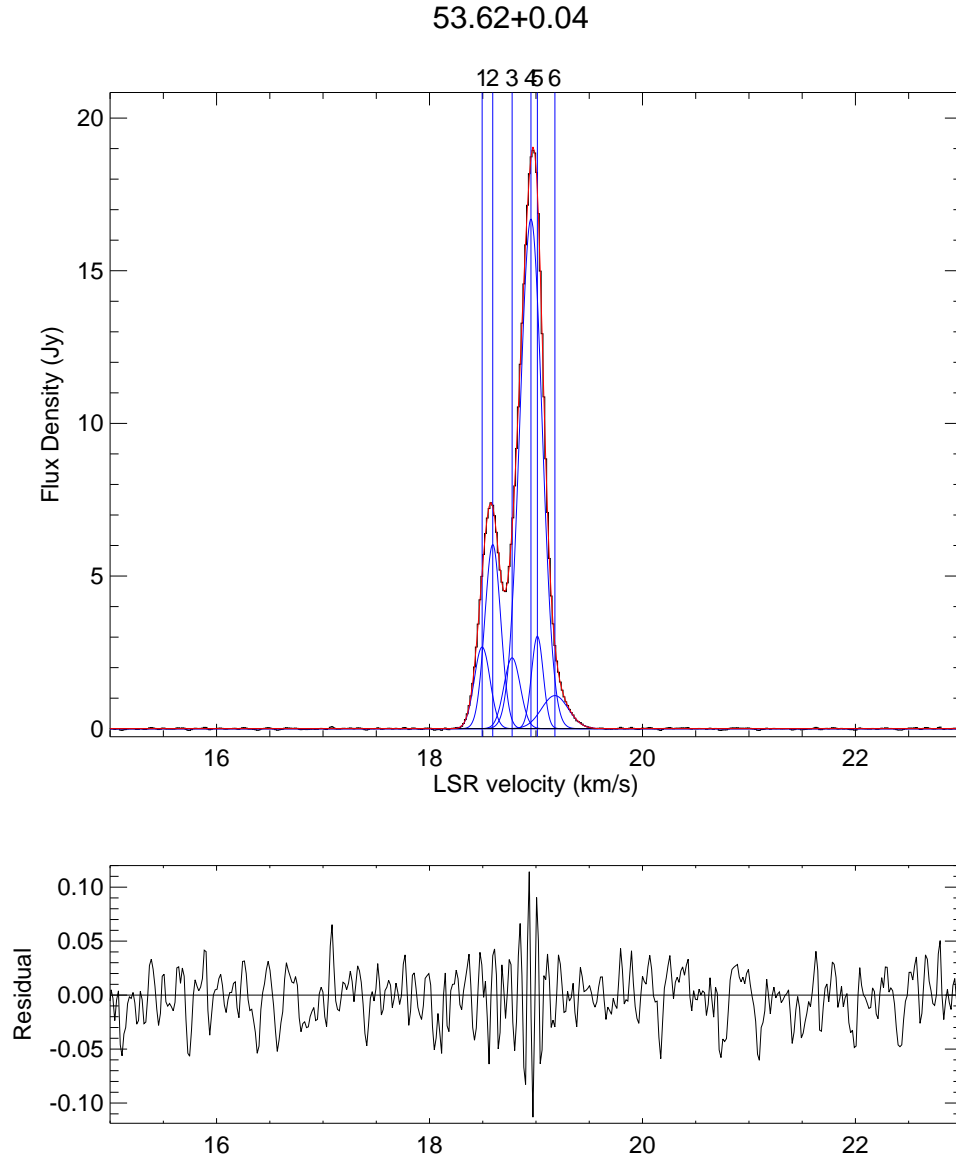


Figure B.49 Gaussian component fit to source 53.62+0.04. The top panel shows the spectrum, and overlays of each Gaussian and its position in blue, and the fit in red. The bottom panel shows the residual. The Gaussians are numbered in the same order as in the corresponding Table.

REFERENCES

- Altenhoff, W., Mezger, P. G., Wendker, H., & Westerhout, G. 1960, Veröff Sternwarte Bonn
- Bachiller, R., Gomez-Gonzalez, J., Barcia, A., & Menten, K. M. 1990, *Astronomy and Astrophysics*, 240, 116
- Ball, J. A., Gottlieb, C. A., Lilley, A. E., & Radford, H. E. 1970, *The Astrophysical Journal*, 162, L203
- Barrett, A. H., Schwartz, P. R., & Waters, J. W. 1971, *The Astrophysical Journal*, 168, L101
- Batrla, W., Matthews, H. E., Menten, K. M., & Walmsley, C. M. 1987, *Nature*, 326, 49
- Batrla, W. & Menten, K. M. 1988, *The Astrophysical Journal*, 329, L117
- Beasley, A. J., Ellingsen, S. P., Claussen, M. J., & Wilcots, E. 1996, *The Astrophysical Journal*, 459, 600
- Behrens, G., Campbell, W., Williams, D., & White, S. 1997, Guidelines for the Design of Cryogenic Systems, Electronics division internal report, NRAO
- Bertin, E. & Arnouts, S. 1996, *A&AS*, 117, 393
- Blaauw, A., Gum, C. S., Pawsey, J. L., & Westerhout, G. 1959, *The Astrophysical Journal*, 130, 702
- Brand, J. & Blitz, L. 1993, *Astronomy and Astrophysics*, 275, 67
- Breckenridge, S. M. & Kukolich, S. G. 1995, *The Astrophysical Journal*, 438, 504
- Bronfman, L., Nyman, L. A., & May, J. 1996, *A&AS*, 115, 81
- Burkhard, D. G. & Dennison, D. M. 1951, *Physical Review*, 84, 408
- Busfield, A. L., Purcell, C. R., Hoare, M. G., Lumsden, S. L., Moore, T. J. T., & Oudmaijer, R. D. 2006, *Monthly Notices of the Royal Astronomical Society*, 366, 1096
- Caswell, J. L. 1996, *Monthly Notices of the Royal Astronomical Society*, 279, 79
- . 1997, *Monthly Notices of the Royal Astronomical Society*, 289, 203
- Caswell, J. L., Vaile, R. A., Ellingsen, S. P., Whiteoak, J. B., & Norris, R. P. 1995, *Monthly Notices of the Royal Astronomical Society*, 272, 96

- Chattopadhyay, G. & Carlstrom, J. E. 1999, *IEEE Microwave and Guided Wave Lett.*, 9, 339
- Churchwell, E., Wolfire, M. G., & Wood, D. O. S. 1990, *The Astrophysical Journal*, 354, 247
- Clarricoats, P. J. B. & Oliver, A. D. 1984, *Corrugated Horns for Microwave Antennas*, 18 (London: IEEE Electromagnetic Waves)
- Clemens, D. P. 1985, *The Astrophysical Journal*, 295, 422
- Codella, C., Testi, L., & Cesaroni, R. 1997, *Astronomy and Astrophysics*, 325, 282
- Cordes, J. M. & Lazio, T. J. W. 2002, *ArXiv Astrophysics e-prints*
- Corruccini, R. J. & Gnievek, J. J. 1960, *NBS Monograph*, 21
- Cragg, D. M., Johns, K. P., Godfrey, P. D., & Brown, R. D. 1992, *Monthly Notices of the Royal Astronomical Society*, 259, 203
- Cragg, D. M., Sobolev, A. M., & Godfrey, P. D. 2005, *Monthly Notices of the Royal Astronomical Society*, 360, 533
- Darling, J., Goldsmith, P., Li, D., & Giovanelli, R. 2003, *The Astronomical Journal*, 125, 1177
- De Buizer, J. M. 2003, *Monthly Notices of the Royal Astronomical Society*, 341, 277
- De Buizer, J. M. & Minier, V. 2005, *The Astrophysical Journal*, 628, L151
- De Buizer, J. M., Radomski, J. T., Telesco, C. M., & Piña, R. K. 2005, *The Astrophysical Journal Supplement Series*, 156, 179
- Dodson, R., Ojha, R., & Ellingsen, S. P. 2004, *Monthly Notices of the Royal Astronomical Society*, 351, 779
- Elitzur, M. 1992, *Astronomical masers* (Astronomical masers Kluwer Academic Publishers (Astrophysics and Space Science Library. Vol. 170), 365 p.)
- Ellingsen, S. P. 2002, in *IAU Symposium*, ed. V. Migenes & M. J. Reid, 151–+
- Ellingsen, S. P. 2005, *Monthly Notices of the Royal Astronomical Society*, 359, 1498
- . 2006, *The Astrophysical Journal*, 638, 241
- Ellingsen, S. P., Norris, R. P., & McCulloch, P. M. 1996a, *Monthly Notices of the Royal Astronomical Society*, 279, 101

- Ellingsen, S. P., von Bibra, M. L., McCulloch, P. M., Norris, R. P., Deshpande, A. A., & Phillips, C. J. 1996b, *Monthly Notices of the Royal Astronomical Society*, 280, 378
- Engargiola, G., Plambeck, R. L., Rosolowsky, E., & Blitz, L. 2003, *The Astrophysical Journal Supplement Series*, 149, 343
- Flynn, E. S., Jackson, J. M., Simon, R., Shah, R. Y., Bania, T. M., & Wolfire, M. 2004, in *ASP Conf. Ser. 317: Milky Way Surveys: The Structure and Evolution of our Galaxy*, ed. D. Clemens, R. Shah, & T. Brainerd, 44
- Freedman, W. L., Wilson, C. D., & Madore, B. F. 1991, *The Astrophysical Journal*, 372, 455
- Gaylard, M. J. & MacLeod, G. C. 1993, *Monthly Notices of the Royal Astronomical Society*, 262, 43
- Goedhart, S., Gaylard, M. J., & van der Walt, D. J. 2004, *Monthly Notices of the Royal Astronomical Society*, 355, 553
- Goldsmith, P. F. 1996, *IEEE Potentials Magazine*, 15, 38
- . 2001, *Calculation of Atmospheric Emission Measured by Gregorian Feed Horns*, Internal memo, NAIC
- Haschick, A. D. & Baan, W. A. 1989, *The Astrophysical Journal*, 339, 949
- Haschick, A. D., Baan, W. A., & Menten, K. M. 1989, *The Astrophysical Journal*, 346, 330
- Haschick, A. D., Menten, K. M., & Baan, W. A. 1990, *The Astrophysical Journal*, 354, 556
- Hewlett-Packard. 1989, *HP 8753C Network Analyzer Operating Manual*
- Hogerheijde, M. R. & van der Tak, F. F. S. 2000, *Astronomy and Astrophysics*, 362, 697
- Hughes, V. A. & MacLeod, G. C. 1989, *The Astronomical Journal*, 97, 786
- Ivash, E. V. & Dennison, D. M. 1953, *Journal of Chemical Physics*, 21, 1804
- Kalenskii, S. V., Dzura, A. M., Booth, R. S., Winnberg, A., & Alakoz, A. V. 1997, *Astronomy and Astrophysics*, 321, 311
- Kemball, A. J., Gaylard, M. J., & Nicolson, G. D. 1988, *The Astrophysical Journal*, 331, L37
- Kemble, E. C. 1937, *The fundamental principles of quantum mechanics* (McGraw-Hill)

- Kildal, P. S., Baker, L. A., & Hagfors, T. 1994, *Proceedings of the IEEE*, 82, 714
- Kim, M., Kim, E., Lee, M. G., Sarajedini, A., & Geisler, D. 2002, *The Astronomical Journal*, 123, 244
- Kirtman, B. 1962, *Journal of Chemical Physics*, 37, 2516
- Koehler, J. S. & Dennison, D. M. 1940, *Physical Review*, 57, 1006
- Kolpak, M. A., Jackson, J. M., Bania, T. M., Clemens, D. P., & Dickey, J. M. 2003, *The Astrophysical Journal*, 582, 756
- Koo, B.-C., Williams, D. R. D., Heiles, C., & Backer, D. C. 1988, *The Astrophysical Journal*, 326, 931
- Kurokawa, K. 1965, *Microwave Theory and Techniques*, *IEEE Transactions on*, 13, 194
- Lee, M. G., Kim, M., Sarajedini, A., Geisler, D., & Gieren, W. 2002, *The Astrophysical Journal*, 565, 959
- Lees, R. M. 1973, *The Astrophysical Journal*, 184, 763
- Lees, R. M. & Baker, J. G. 1968, *Journal of Chemical Physics*, 48, 5299
- Lin, C. C. & Swalen, J. D. 1959, *Reviews of Modern Physics*, 31, 841
- Liszt, H. S., Burton, W. B., & Bania, T. M. 1981, *The Astrophysical Journal*, 246, 74
- Lockman, F. J. 1989, *The Astrophysical Journal Supplement Series*, 71, 469
- Lovas, F. J. 2004, *Journal of Physical and Chemical Reference Data*, 33, 177
- Mac Low, M.-M., van Buren, D., Wood, D. O. S., & Churchwell, E. 1991, *The Astrophysical Journal*, 369, 395
- MacLeod, G. C. & Gaylard, M. J. 1992, *Monthly Notices of the Royal Astronomical Society*, 256, 519
- MacLeod, G. C., Gaylard, M. J., & Nicolson, G. D. 1992, *Monthly Notices of the Royal Astronomical Society*, 254, 1P
- Marquardt, E. D., Le, J. P., & Radebaugh, R. 2002, 11-th International Cryocooler Conference
- Menten, K. 1991a, in *ASP Conf. Ser. 16: Atoms, Ions and Molecules: New Results in Spectral Line Astrophysics*, ed. A. D. Haschick & P. T. P. Ho, 119–+
- Menten, K. M. 1991b, *The Astrophysical Journal*, 380, L75

- Menten, K. M., Reid, M. J., Moran, J. M., Wilson, T. L., Johnston, K. J., & Batrla, W. 1988a, *The Astrophysical Journal*, 333, L83
- Menten, K. M., Reid, M. J., Pratap, P., Moran, J. M., & Wilson, T. L. 1992, *The Astrophysical Journal*, 401, L39
- Menten, K. M., Walmsley, C. M., Henkel, C., & Wilson, T. L. 1986a, *Astronomy and Astrophysics*, 157, 318
- . 1988b, *Astronomy and Astrophysics*, 198, 253
- Menten, K. M., Walmsley, C. M., Henkel, C., Wilson, T. L., Snyder, L. E., Hollis, J. M., & Lovas, F. J. 1986b, *Astronomy and Astrophysics*, 169, 271
- Minier, V., Booth, R. S., & Conway, J. E. 2000, *Astronomy and Astrophysics*, 362, 1093
- Minier, V., Burton, M. G., Hill, T., Pestalozzi, M. R., Purcell, C. R., Garay, G., Walsh, A. J., & Longmore, S. 2005, *Astronomy and Astrophysics*, 429, 945
- Minier, V., Conway, J. E., & Booth, R. S. 2001, *Astronomy and Astrophysics*, 369, 278
- Minier, V., Ellingsen, S. P., Norris, R. P., & Booth, R. S. 2003, *Astronomy and Astrophysics*, 403, 1095
- Nagai, T., Kaifu, N., Nagane, K., & Akaba, K. 1979, *Publications of the Astronomical Society of Japan*, 31, 317
- Nielsen, H. H. 1932, *Physical Review*, 40, 445
- Norris, R. P., Caswell, J. L., Gardner, F. F., & Wellington, K. J. 1987, *The Astrophysical Journal*, 321, L159
- Norris, R. P., Caswell, J. L., Wellington, K. J., McCutcheon, W. H., & Reynolds, J. E. 1988, *Nature*, 335, 149
- Norris, R. P., Whiteoak, J. B., Caswell, J. L., Wieringa, M. H., & Gough, R. G. 1993, *The Astrophysical Journal*, 412, 222
- Pandian, J. D., Baker, L., Cortes, G., Goldsmith, P. F., Deshpande, A. A., Ganesan, R., Hagen, J., Locke, L., Wadefalk, N., & Weinreb, S. 2006, *IEEE Microwave Magazine*, 7, 74
- Pandian, J. D., Goldsmith, P. F., & Deshpande, A. A. 2007a, *The Astrophysical Journal*, accepted
- . 2007b, under preparation

- Pei, C. C., Gou, Q. Q., & Zeng, Q. 1988, *A&AS*, 76, 35
- Peng, R. S. & Whiteoak, J. B. 1993, *Monthly Notices of the Royal Astronomical Society*, 260, 529
- Pestalozzi, M., Minier, V., Booth, R., & Conway, J. 2002, in *IAU Symposium*, ed. V. Migenes & M. J. Reid, 139
- Pestalozzi, M. R., Minier, V., & Booth, R. S. 2005, *Astronomy and Astrophysics*, 432, 737
- Phillips, C. J., Norris, R. P., Ellingsen, S. P., & McCulloch, P. M. 1998, *Monthly Notices of the Royal Astronomical Society*, 300, 1131
- Plambeck, R. L. & Menten, K. M. 1990, *The Astrophysical Journal*, 364, 555
- Plambeck, R. L. & Wright, M. C. H. 1988, *The Astrophysical Journal*, 330, L61
- Schutte, A. J., van der Walt, D. J., Gaylard, M. J., & MacLeod, G. C. 1993, *Monthly Notices of the Royal Astronomical Society*, 261, 783
- Sinclair, M. W., Carrad, G. J., Caswell, J. L., Norris, R. P., & Whiteoak, J. B. 1992, *Monthly Notices of the Royal Astronomical Society*, 256, 33P
- Slysh, V. I., Kalenskii, S. V., & Val'tts, I. E. 1992, *The Astrophysical Journal*, 397, L43
- Slysh, V. I., Kalenskij, S. V., & Val'tts, I. E. 1993, *The Astrophysical Journal*, 413, L133
- Slysh, V. I., Val'tts, I. E., Kalenskii, S. V., Voronkov, M. A., Palagi, F., Tofani, G., & Catarzi, M. 1999, *A&AS*, 134, 115
- Sobolev, A. M., Cragg, D. M., & Godfrey, P. D. 1997, *Astronomy and Astrophysics*, 324, 211
- Sobolev, A. M. & Deguchi, S. 1994, *Astronomy and Astrophysics*, 291, 569
- Stil, J. M., Taylor, A. R., Dickey, J. M., Kavars, D. W., Martin, P. G., Rothwell, T. A., Boothroyd, A. I., Lockman, F. J., & McClure-Griffiths, N. M. 2006, *The Astronomical Journal*, 132, 1158
- Szymczak, M., Hrynek, G., & Kus, A. J. 2000, *A&AS*, 143, 269
- Szymczak, M. & Kus, A. J. 2000, *Astronomy and Astrophysics*, 360, 311
- Szymczak, M., Kus, A. J., Hrynek, G., Kępa, A., & Pazderski, E. 2002, *Astronomy and Astrophysics*, 392, 277

- Townes, C. H. & Schawlow, A. L. 1975, *Microwave Spectroscopy* (Dover Publications, Inc.: New York)
- Vallee, J. P. 1995, *The Astrophysical Journal*, 454, 119
- Val'tts, I. E., Dzura, A. M., Kalenskii, S. V., Slysh, V. I., Booth, R. S., & Winnberg, A. 1995, *Astronomy and Astrophysics*, 294, 825
- van der Walt, D. J., Churchwell, E., Gaylard, M. J., & Goedhart, S. 2003, *Monthly Notices of the Royal Astronomical Society*, 341, 270
- van der Walt, D. J., Gaylard, M. J., & MacLeod, G. C. 1995, *A&AS*, 110, 81
- van der Walt, D. J., Retief, S. J. P., Gaylard, M. J., & MacLeod, G. C. 1996, *Monthly Notices of the Royal Astronomical Society*, 282, 1085
- van der Walt, J. 2005, *Monthly Notices of the Royal Astronomical Society*, 360, 153
- Voronkov, M. A., Sobolev, A. M., Ellingsen, S. P., & Ostrovskii, A. B. 2005, *Monthly Notices of the Royal Astronomical Society*, 362, 995
- Wadefalk, N. & Weinreb, S. 2005, *IEEE MTT-S Int. Microw. Symp./Very Large Microw. Arrays Radio Astron. Space Commun. Workshop*, Long Beach, CA
- Walsh, A. J., Hyland, A. R., Robinson, G., & Burton, M. G. 1997, *Monthly Notices of the Royal Astronomical Society*, 291, 261
- Walsh, A. J., Macdonald, G. H., Alvey, N. D. S., Burton, M. G., & Lee, J.-K. 2003, *Astronomy and Astrophysics*, 410, 597
- Watson, C., Araya, E., Sewilo, M., Churchwell, E., Hofner, P., & Kurtz, S. 2003, *The Astrophysical Journal*, 587, 714
- Weaver, H., Williams, D. R. W., Dieter, N. H., & Lum, W. T. 1965, *Nature*, 208, 29
- Weinreb, S., Barrett, A. H., Meeks, M. L., & Henry, J. C. 1963, *Nature*, 200, 829
- White, G. K. & Meeson, P. 1968, *Experimental Techniques in Low-Temperature Physics* (Clarendon: Oxford University Press)
- Wilson, T. L., Johnston, K. J., & Mauersberger, R. 1991, *Astronomy and Astrophysics*, 251, 220
- Wilson, T. L., Walmsley, C. M., Jewell, P. R., & Snyder, L. E. 1984, *Astronomy and Astrophysics*, 134, L7
- Wilson, T. L., Walmsley, C. M., Menten, K. M., & Hermsen, W. 1985, *Astronomy and Astrophysics*, 147, L19

- Wood, D. O. S. & Churchwell, E. 1989, *The Astrophysical Journal*, 340, 265
- Xu, Y., Reid, M. J., Zheng, X. W., & Menten, K. M. 2006, *Science*, 311, 54
- Zeng, Q. 1992, in *IAU Symp. 150: Astrochemistry of Cosmic Phenomena*, ed. P. D. Singh, 341